Improving robustness of continuous-gravitational-wave searches against signal-like instrumental artefacts

and a concept for an octahedral gravitational-wave detector in space

Dipl.-Phys. David Keitel

geboren am 27. September 1985 in Siegburg

2014

Abstract

Gravitational waves (GWs) are one of the few remaining predictions of Einstein's theory of general relativity for which no direct evidence has yet been discovered. They promise to open up a completely new window for astronomy. GW signals are expected to be very weak, so that highly sensitive detectors and data-analysis methods are required.

Currently, laser-interferometric detectors provide the most promising way for direct GW detection, although the first generation of these detectors has not detected any GWs yet. A second generation with increased sensitivity will come online in the next few years, making these exciting times in GW research.

The majority of this thesis is concerned with data analysis for continuous gravitational waves (CWs) with ground-based detectors: long-lasting, narrow-band signals which could be produced by rotating neutron stars with non-axisymmetric deformations. Most CW data-analysis methods assume a Gaussian distribution for the detector noise. Non-Gaussian artefacts of instrumental and environmental origin can decrease the performance of these methods if they are "signal-like", i.e. also narrow-band and sufficiently long-lasting. Such artefacts are referred to as "lines".

The main research work presented in this thesis consists of the development of a Bayesian model-selection approach to mitigate this problem and to increase the line-robustness of CW searches. An explicit, yet simple, "signal-like" line model is used to derive new line-robust detection statistics. Simple approaches to tuning these new detection statistics for improved performance are presented, along with extensive numerical tests both on synthetic data sets and with injections of simulated CW signals into real data from the LIGO (*Laser-Interferometric Gravitational-wave Observatory*) detectors.

These newly developed methods for CW data analysis are already in use on the distributed-computing project Einstein@Home.

Additional research work presented in this thesis covers an extended investigation of the behaviour of these line-robust statistics under extreme conditions, such as large differences in the relative sensitivities of different detectors. Preliminary results are presented for an alternative line model based on unmodulated sinusoids.

This thesis also contains a concept study for a space-based GW detector with six spacecraft in an octahedron-shaped constellation, allowing for displacement-noise-cancelling measurements of long-wavelength GWs.

Keywords: gravitational waves, neutron stars, data analysis

Kurzfassung

Gravitationswellen (GW) sind eine der wenigen verbleibenden Vorhersagen aus Einsteins Allgemeiner Relativitätstheorie, für die es noch keine direkten Nachweise gibt. Ihre zukünftige Entdeckung verspricht, der Astronomie ein völlig neues Beobachtungsfenster zu öffnen. Man erwartet, dass GW-Signale sehr schwach sind, sodass äußerst empfindliche Detektoren und Datenanalysemethoden benötigt werden.

Laser-interferometrische Detektoren bieten den derzeit vielversprechendsten Ansatz zur direkten GW-Messung, jedoch hat die erste Generation solcher Detektoren noch keine Signale nachweisen können. Eine zweite Generation mit verbesserter Messgenauigkeit wird in den folgenden Jahren die Beobachtung aufnehmen, sodass eine spannende Zeit in der GW-Forschung ansteht.

Der Großteil dieser Doktorarbeit behandelt die Datenanalyse kontinuierlicher Gravitationswellen (engl.: *continuous waves*, CWs) mit terrestrischen Detektoren: langandauernde, in der Frequenz schmalbandige Signale, die von rotierenden Neutronensternen mit nicht-axisymmetrischen Verformungen ausgestrahlt werden können. Die meisten CW-Datenanalysemethoden basieren auf der Annahme einer Gauß-Verteilung des Detektorrauschens. Nicht-Gaußsche Störsignale oder "Artefakte", die im Detektor selbst oder seinem Umfeld entstehen, können jedoch die Detektionswahrscheinlichkeit dieser Methoden verringern, falls diese Artefakte "signal-artig" ausfallen, also ebenfalls schmalbandig und hinreichend langandauernd sind. Derartige Artefakte werden auch als *"Lines"* bezeichnet.

Das Hauptforschungsergebnis dieser Dissertation ist ein Ansatz zur Minderung dieses Problems und Verbesserung der *Line*-Robustheit von CW-Analysen mittels Bayesscher Modellauswahl. Ein explizites, dabei einfaches, "signal-artiges" *Line*-Modell dient der Herleitung neuer, *Line*-robuster Teststatistiken. Außerdem werden einfache Ansätze zur Anpassung dieser Statistiken präsentiert, die die Detektionswahrscheinlichkeit erhöhen, sowie ausführliche numerische Tests mit synthetischen Daten und Injektionen simulierter CW-Signale in echte Messdaten der LIGO-Detektoren (engl.: *Laser-Interferometric Gravitational-wave Observatory*). Diese neuentwickelten Methoden zur CW-Datenanalyse werden bereits im Verteiltes-Rechnen-Projekt Einstein@Home verwendet.

Zusätzliche Forschungsarbeiten, die in dieser Dissertation beschrieben werden, beinhalten eine Untersuchung des Verhaltens der *Line*-robusten Statistiken unter extremen Bedingungen wie sehr ungleichen relativen Messgenauigkeiten mehrerer Detektoren, sowie vorläufige Ergebnisse für ein alternatives *Line*-Modell mittels unmodulierter harmonischer Funktionen.

Diese Arbeit enthält außerdem eine Konzeptstudie für einen GW-Detektor aus sechs in Form eines Oktaeders angeordneten Weltraumsonden, der das "Verschiebungsrauschen" (engl.: *displacement noise*) bei der Messung langwelliger GW eliminieren kann.

Schlagworte: Gravitationswellen, Neutronensterne, Datenanalyse

Contents

1 Introduction

Gravitational waves (GWs) are one of the few remaining predictions of Einstein's theory of general relativity for which no direct evidence has yet been discovered, and they promise to open up a completely new window to astronomy.

GWs can be understood as ripples in space-time, propagating at the speed of light. Produced by high-energy astrophysical phenomena, their direct detection could provide information that is complementary to that from observations in "photon astronomy" and particle astrophysics.

Gravity is a weak force, when compared to electro-magnetism or nuclear forces, and space-time can be considered as a very "stiff fabric", which even for huge energy inputs only carries small GW amplitudes. Hence, practical research on GW detection has focussed for decades on the construction of highly sensitive detectors, and on the development of data-analysis methods that can extract the extremely weak signals from the measurements of these detectors.

The most sensitive GW detectors constructed so far are laser interferometers with arm-lengths of hundreds of meters to several kilometres, including the *Laser-Interferometric Gravitational-wave Observatory* (LIGO). The first generation of these detectors has provided interesting upper limits on the GW emission for a variety of source types, but has not detected any GWs yet. A second generation of interferometric detectors, with increased sensitivity, will come online in the next few years, making these exciting times in GW research.

The majority of this thesis is concerned with the specific topic of *continuous-wave data analysis*. Continuous gravitational waves (CWs) are a class of possible astrophysical signals that are narrow-band in frequency and can typically be described by a relatively stable signal model over years of observation. In the frequency band covered by terrestrial interferometric detectors, such as LIGO, CWs could be produced by rotating *neutron stars* – extremely compact remnants of massive stars – if they have sufficiently large non-axisymmetric deformations.

Most CW data-analysis methods assume a Gaussian distribution for the detector noise. Indeed, in current interferometers this is a good description over most of the observation time and frequency range. However, the detector data also contains non-Gaussian disturbances and *artefacts* of instrumental and environmental origin. Transient disturbances are typically only relevant in searches for equally transient signals, while CW searches

are mainly affected by so-called "lines": narrow-band disturbances that are present for a sizeable fraction of the observation time.

Line artefacts are so problematic because they can be "signal-like" in the sense of being more similar to a CW signal than to Gaussian noise. Hence, they can cause significant outliers in a CW search that is based on the comparison of the signal model to Gaussian noise only, leading to false alarms and therefore to decreased chances of confidently detecting an actual signal.

Many ad-hoc approaches to mitigate the problem of lines have been developed in the past. The main research work presented in this thesis is the development of a Bayesian model-selection approach to line mitigation. The idea is to use a simple "signal-like" model for line disturbances, which does not require additional information about the characteristics of GW detectors, but only uses the main data stream already in use by the standard search methods. This way, *line-robust detection statistics* can be defined that reproduce the performance of standard methods in Gaussian data, but work better in line-affected frequency bands. This is intended as a "first line of defence" against the most common noise artefacts, but still assuming that additional post-processing steps will handle other types.

This thesis is structured as follows, with an introductory summary of background knowledge followed by several parts containing the results of original research work, conducted together with several collaborators.

Secs. 2–5 give a summary of established knowledge that is necessary as a background for the work presented later on: general relativity, astrophysical GW sources, GW detectors, probability theory and statistics, as well as standard methods of CW data analysis. The material in these chapters is based on standard literature, and contains no original results. I usually point the reader towards a few comprehensive books or review articles at the beginning of each chapter or section, and give additional references where they are relevant for the specific content.

The central part of the thesis, Secs. 6–10, presents the first stage of results from the line-robustness project described above. This material is based on the publication "Search for continuous gravitational waves: Improving robustness versus instrumental artifacts", by D. Keitel in collaboration with R. Prix, M. A. Papa, P. Leaci and M. Siddiqi, Phys. Rev. D 89.6, 064023 (2014), abbreviated as KPPLS14 in the following.

The material in this thesis is an extension of that in the original paper, including additional details of the derivations and the tuning procedures. I also present more comprehensive versions of the original numerical tests, covering both synthetic draws of detection statistics and injections of simulated CW signals into real data from the fifth science run of the LIGO detectors. Sec. 6 also contains a more detailed justification of the specific simple line model used here and by KPPLS14.

The following Secs. 11–13 cover additional material from this research project. In Sec. 11, I briefly summarise my contributions to the distributed computing project Ein-

stein@Home with relation to line robustness. Results from these Einstein@Home searches will be the subject of upcoming publications by the LIGO Scientific Collaboration and the Virgo Collaboration.

In Sec. 12, I investigate a generalisation of the assumptions made in KPPLS14 and the preceding chapters on line-robustness: if a CW analysis uses data from two or more detectors with very different sensitivities, the line-robust statistics could be less effective. I investigate the boundaries within which they are still safe to use, and also explore a simple idea on improving their behaviour. Tests with synthetic draws indicate that this new approach is of limited practical use, but that the optimally-tuned version of the original line-robust statistic is already safe in most cases of practical interest. Since the original submission of this thesis in August 2014, a paper based very closely on the results and text of Sec. 12 has been published in Class. Quant. Grav. 32:035004, titled "Line-robust statistics for continuous gravitational waves: safety in the case of unequal detector sensitivities" (Keitel & Prix 2015).

An independent, though formally similar approach to line-robustness is presented in Sec. 13, based on the modelling of lines as unmodulated sinusoids. This project is still in early stages, with no corresponding publication yet. Here, I only present preliminary analytical results and some thoughts on the related topic of marginalising detection statistics over the phase-evolution parameter space of CW signals.

The two projects mentioned last, unequal-sensitivity investigations and the unmodulated-sinusoid line-model, are based on ideas originally proposed to me by R. Prix, and he has played an important role in discussing the implementation and results.

Concluding this thesis, Sec. 14 presents a contribution to another central topic of GW research: the development of new detector concepts. This is an idea originally developed by Y. Wang, myself and other Ph. D. students from AEI Hannover and then expanded into a research paper titled "Octahedron configuration for a displacement noise-canceling gravitational wave detector in space" by Y. Wang, D. Keitel, S. Babak et al., published in Phys. Rev. D 88.10, 104021 (2013). The material in this chapter is reproduced from that paper with only minor modifications. I give a summary of my contributions to this project in Sec. 14.1.2.

2 Gravitational Waves

This chapter is intended as a quick introduction to the most important concepts around the topic of gravitational waves (GWs). It contains neither full derivations of all mathematical relations, nor an exhaustive discussion of these concepts, nor an extensive literature review. However, I give references to more detailed review articles and textbooks wherever possible.

After a short survey of the history of GW research in Sec. 2.1, I present a bare minimum of theoretical foundations in Secs. 2.2–2.4. I also describe possible astrophysical sources for GWs in Sec. 2.5, as well as concepts for GW detection, and their practical implementation, in Secs. 2.6 and 2.7.

2.1 History of GW research

2.1.1 Before Einstein

Most modern accounts of the historical development of GW research begin with Albert Einstein's prediction of this phenomenon (Einstein 1916, 1918) based on his theory of general relativity (GR, Einstein 1915). However, Einstein was already using the term "Gravitationswellen" (gravitational waves) in such an offhand manner that it was clearly an established term at this time.

And in fact, the concept (or, more exactly, *some* concept, as we will see) of GWs was so widespread, before Einstein, that it even made its way into popular science-fiction novels:

> Die Martier hatten entdeckt, daß die Gravitation, ebenso wie das Licht, die Wärme, die Elektrizität, sich in Form einer Wellenbewegung durch den Weltraum und die Körper fortpflanzt. Während aber die Geschwindigkeit der strahlenden Energie, die wir als Licht, Wärme und Elektrizität beobachten, 300 000 Kilometer in der Sekunde beträgt, ist diejenige der Gravitation eine millionenmal größere. – Laßwitz (1897)
> *Translation: The Martians had discovered that gravitation, just as light, warmth and electricity, propagates through space and through bodies in the form of a wave motion. But while the speed of the radiative energy that we observe as light, warmth and electricity is 300 000 km per second, that of gravitation is a million times higher.*

Apart from this egregious claim about the speed of GWs, the novel also has the Martians building an entire technology on GW manipulation, and invokes GWs as the basis of normal gravitational attraction as well:

> Die Körper sind darum schwer, weil sie die Gravitationswellen absorbieren. Körper ziehen sich nur dann gegenseitig an, wenn sie die von ihnen wechselseitig ausgehenden Gravitationswellen nicht durch sich hindurchtreten lassen.
> – Laßwitz (1897)
> *Translation: Bodies are heavy because they absorb gravitational waves. Bodies attract each other only when they do not let the mutually emitted gravitational waves pass through each other.*

These properties are completely incompatible with a modern understanding of gravity and of GWs, as we will see in the following section based on Einstein's GR. However, they are a nice summary of primitive ideas about GWs that circulated in the centuries before Einstein.

Whereas the phenomenological aspects of gravity were sufficiently well-described by Newton's laws (Newton 1687) for almost 300 years, the underlying mechanism of gravitational attraction and the actual physical source of gravitational potentials were always matters for debate. Newton's inverse-square law implicitly required instantaneous action-at-a-distance, though he himself sometimes expressed discomfort with that concept (Newton 1692).

Analogies between gravity and light soon brought on the idea that gravitational force was mediated by finite-speed perturbations in an "æthereal" medium. Hooke (1705) introduced the idea of a "propagated pulse" as "the Cause of the Descent of Bodies towards the Earth" (p. 185), which is probably the first instance of GW-like language and concepts.

Later, Laplace (1805) also considered the propagation of gravity, itself understood as a fluid, at finite speed. To avoid orbital decay due to friction between planets and the "gravity fluid", he found it necessary that the GW speed should be orders of magnitude higher than the speed of light. This notion became commonplace for a century, as evidenced by the Laßwitz quote.

Similar æther-based ideas for explaining gravitational attraction by the exchange of GWs reached their height in the 19th century with a multitude of "mechanical" or "kinetic" theories of gravity. A contemporary review was given by Taylor (1877), who also cites Hooke as the originator of the concept, an another example is the work by Challis (1869).

But these theories were never very successful at actually describing gravitational phenomena in the laboratory or in celestial mechanics, and today they appear to us as very ad-hoc and unphysical. When the experiment of Michelson & Morley (1887) and Einstein's theory of special relativity (Einstein 1905) did away with the related concept of a "luminiferous æther" as the medium for electromagnetic radiation, mechanical gravity theories also became untenable.

2.1.2 Einstein and the theoretical era

Attempts to unify gravity with a finite speed of light, and thus with special relativity, again hinted at the existence of gravitational waves, as mentioned for example by Poincaré (1905). Einstein then developed the first true successor to Newtonian gravity, general relativity (Einstein 1915), which is still the standard classical theory of gravity today. I will briefly describe that theory, or at least the parts directly relevant to GW science, in the following sections, but for now I continue with the 20th and early 21st century history of GWs. For more details about this era, see §3 of Damour (1983), Sec. 9.1.2 of Thorne (1987), as well as the more sociological work by Collins (2004).

Einstein's first GR-based publication on GWs (Einstein 1916) still contained errors: he later called it "nicht genügend durchsichtig und außerdem durch einen bedauerlichen Rechenfehler verunstaltet", *not sufficiently penetrating, and also marred by a deplorable error in calculation* (Einstein 1918). But he followed it up with the correct results two years later (Einstein 1918). In this modern understanding of GWs, there are (at least) three fundamental differences to the 19th-century ideas:

1. GWs require no medium to propagate, being "ripples" in space-time itself, and in vacuum they move at the same speed as electromagnetic waves.

2. GWs are neither responsible for nor directly related to the mutual attraction of heavy bodies. Whereas Newton's law of attraction can be derived from the weak-field limit of a static solution of Einstein's field equations, GWs are propagating solutions and can be produced only by time-varying mass distributions.

3. Due to the very weak coupling strength of gravity, compared to other fundamental forces, GWs of detectable strength can only be emitted by very massive and energetic astrophysical objects, and will still be extremely weak.

In fact, in the first few decades after Einstein's work on GWs, it was expected that they must be too weak to ever be detectable. There was even still debate on the question whether GWs could actually carry energy and deposit it in a detector, or if they were just a coordinate-dependent mathematical artefact (e.g. Infeld & Scheidegger 1951).

Nonetheless, fundamental theoretical work on GW emission, propagation and interaction was carried out in the 1920s and 1930s, e.g. by Weyl (1922) and Eddington (1924). Consistent results about the energy content of GWs became available with work by Bondi (1957), Bondi, Pirani & Robinson (1959), Bondi (1960) and Bondi, van der Burg & Metzner (1962), and with further papers of that series. Thus, the coordinate-independent existence of GWs and their in-principle detectability was considered established after the 1962 Jablonna/Warsaw GR3 conference – see Infeld (1964) for the original proceedings and Ashtekar (2014) for a retrospective. Another essential development was the high-frequency-limit formalism of Isaacson (1968a,b) and his introduction of the GW stress-energy tensor.

2.1.3 The era of GW searches

Practical work on GW detection only began with the work of Joseph Weber, who first tried to detect GWs from astrophysical sources with resonant metal-bar detectors (Weber 1960, 1966, see also Sec. 2.7.2). Weber claimed the detection of GW events several times (Weber 1969, 1970, 1986), based on simultaneous excitations of spatially-separated detectors. Additional resonant-mass detectors, operated by independent groups, followed through the 1980s and 1990s, but could not verify Weber's results.

However, despite the discovery of strong indirect evidence for the existence of GWs from the orbital decay of a binary pulsar (Hulse & Taylor 1975, Taylor & Weisberg 1982), a direct detection by resonant-mass detectors looked increasingly unlikely, as the astrophysical predictions for expected signal strengths and event rates were corrected ever downwards during these decades.

The best prospects for detection were then seen in large-scale laser-interferometric detectors, a concept pioneered by Weiss (1972). I will discuss these in more detail in Sec. 2.6. The first generation of ground-based interferometers, in operation during the 2000s, did not detect any gravitational waves so far. The main results are upper limits on source populations, which in several cases have reached informative levels when compared to the astrophysical predictions. Some data is still undergoing analysis, with the work presented in this thesis being part of that effort. Improved sensitivity, and therefore realistic chances of detection, are expected from the second generation currently under construction.

Space-based interferometric detectors (see Sec. 2.7.1) have been under discussion since the 1990s as well, but are still a long-term project: the most mature proposal, LISA, is currently scheduled for a launch in the 2030s. On a shorter time-scale, pulsar timing arrays (see Sec. 2.7.3) offer an alternative approach to GW detection.

Meanwhile, an indirect detection of primordial GWs through the observation of primordial B-mode polarisation in the cosmic microwave background (CMB) was claimed by the BICEP2 collaboration (Ade et al. 2014). However, Planck measurements (Adam et al. 2014) and many other studies seem to indicate that the signal can be explained purely by galactic dust foregrounds.

2.2 General relativity

The theory of general relativity (Einstein 1915) describes the dynamical interaction between space-time, energy and matter. What has been known classically as the "gravitational force" is, in this picture, the effect of the space-time curvature on the movement of masses, particles and energy flows. This curvature of space-time, in turn, is determined by its energy content. GR is based on the principle of equivalence and usually expressed in the language of differential geometry pioneered by Gauss, Riemann and others.

Here, I only very briefly summarise the central properties of the full theory of GR, and then I will specialise my discussion to two cases of particular relevance to GW science in Secs. 2.3 and 2.4. In this summary, I follow the classic texts by Weinberg (1972) and Misner, Thorne & Wheeler (1973), hereafter referred to as MTW73.

Like special relativity, GR works with a four-dimensional space-time consisting of the familiar three spatial dimensions, together with a time direction, conventionally used as the 0-coordinate. In any covariantly transformed coordinate frame, where space and time coordinates can be mixed, distances can be measured locally with a *metric tensor* $g_{\mu\nu}$:

$$\mathrm{d}s^2 = g_{\mu\nu}\,\mathrm{d}x^\mu\,\mathrm{d}x^\nu = \sum_{\mu=0}^{3}\sum_{\nu=0}^{3} g_{\mu\nu}\,\mathrm{d}x^\mu\,\mathrm{d}x^\nu\,. \tag{2.1}$$

I use the common notation with Greek indices $\mu,\nu,\dots$ running over all four space-time coordinates, while Latin indices $i,k,\dots$ are restricted to the three spatial dimensions. Repeated indices, Greek or Latin, at "opposite positions" (one covariant, one contravariant) automatically imply summation over their respective range, as in the example above. My sign conventions are those of Weinberg (1972), so that for example the flat *Minkowski metric* of special relativity is given by

$$g_{\mu\nu}|_{\mathrm{SRT}} = \eta_{\mu\nu} \equiv \begin{pmatrix} -1 & 0 & 0 & 0 \\ 0 & 1 & 0 & 0 \\ 0 & 0 & 1 & 0 \\ 0 & 0 & 0 & 1 \end{pmatrix}\,. \tag{2.2}$$

The central quantity in differential geometry is the four-index *Riemann tensor*, which fully describes the curvature of a manifold. However, for the field equations of GR we actually only need a contracted form, the two-index *Ricci tensor*

$$R_{\mu\nu} \equiv R^\sigma{}_{\mu\sigma\nu} = \partial_\nu \Gamma^\sigma_{\mu\sigma} - \partial_\sigma \Gamma^\sigma_{\mu\nu} + \Gamma^\rho_{\mu\sigma}\Gamma^\sigma_{\nu\rho} - \Gamma^\rho_{\mu\nu}\Gamma^\sigma_{\sigma\rho}\,, \tag{2.3}$$

where $\partial_\mu \equiv \frac{\partial}{\partial x^\mu}$ is a shorthand for partial derivatives and the second part of this equation is written explicitly in terms of the *affine connection* Γ, also called the *Christoffel symbol*. This quantity is defined through its usage in the *geodesic equation* for the movement of a test particle along a 4-D world-line parametrised by the *proper time* τ:

$$\frac{\mathrm{d}^2 x^\sigma}{\mathrm{d}\tau^2} + \Gamma^\sigma_{\mu\nu}\frac{\mathrm{d}x^\mu}{\mathrm{d}\tau}\frac{\mathrm{d}x^\nu}{\mathrm{d}\tau} = 0\,. \tag{2.4}$$

Its components are related to those of the metric through

$$\Gamma^\sigma_{\mu\nu} = \frac{1}{2}g^{\rho\sigma}\left(\partial_\mu g_{\nu\rho} + \partial_\nu g_{\mu\rho} - \partial_\rho g_{\mu\nu}\right)\,. \tag{2.5}$$

Further contraction of the Ricci tensor yields the *curvature scalar*, $R \equiv R^\mu{}_\mu$.

Using these quantities, the central finding of GR is that the metric $g_{\mu\nu}$ for a general curved space-time must be a solution of *Einstein's field equations*,

$$R_{\mu\nu} - \frac{1}{2}g_{\mu\nu}R - \Lambda g_{\mu\nu} = -\frac{8\pi G}{c^4}T_{\mu\nu}\,, \tag{2.6}$$

where c is the speed of light, G is Newton's constant and $T_{\mu\nu}$ is the stress-energy tensor, related to the mass-energy density ρ of all particles and fields through

$$\rho = u^\mu T_{\mu\nu} u^\nu \tag{2.7}$$

for an observer with four-velocity u. The *cosmological constant* Λ is not relevant in the following applications and will be considered zero.

Even though these field equations look deceptively simple, they are very hard to solve analytically, and GR is a theory with an abundant phenomenology. I will not go into the details of classical strong-field solutions such as the Schwarzschild metric for spherical and point masses (Schwarzschild 1916) and the Kerr metric for rotating black holes (Kerr 1963), nor into cosmological applications. Instead, in the following two sections I discuss only two of the limits of GR most relevant for GW science: the weak-field, linearised gravity regime for GW propagation and detection, and the quadrupole formalism which can describe GW emission from a variety of sources. For more detailed studies of GW waveforms, especially when considering binary inspirals (see Sec. 2.5.1), the *post-Newtonian approximation* is also very important; but it is not needed in this thesis.

Note that I have used somewhat sloppy notation and language throughout this section, for example equating a tensor with its components, using "covariant" and "contravariant" simply as labels for "upstairs" and "downstairs" indices instead of properly referring to the different spaces for each type of vector, and so on. As I will now turn to a simplified, strictly coordinate-dependent description of GWs, these subtleties, although very important in the general picture, are of no acute concern.

2.3 GW propagation: linearised gravity

A fully coordinate-invariant treatment of propagating GWs and their interaction with a detector is possible (see Koop & Finn 2014), as well as a non-linear treatment including back-reaction of the GWs on the "background" space-time (see §35.8 of MTW73 and references therein). However, in almost all cases of interest, the treatment of GWs does not require the full formalism of GR. Mostly due to the weakness of typical GWs, several approximations and simplifications can be made, so that a linear treatment on a flat background is sufficient. I only present the most essential steps, while more detailed versions of this standard derivation can be found, for example, in chapter 10 of Weinberg (1972), chapter 18 of MTW73 or chapter 1 of Jaranowski & Królak (2009), hereafter referred to as JK09.

Let us first assume that the GW is so weak that there exists a coordinate system where the metric is close to Minkowski, with a small correction $|h_{\mu\nu}| \ll 1$:

$$g_{\mu\nu} = \eta_{\mu\nu} + h_{\mu\nu} \,. \tag{2.8}$$

Thus, terms of order h^2 can safely be ignored, including those arising in raising and lowering indices: we can therefore use $\eta_{\mu\nu}$ for that purpose, instead of the full $g_{\mu\nu}$. For example, the trace of $h_{\mu\nu}$ is simply $h = \eta^{\mu\nu} h_{\mu\nu}$.

The linearised field equations and the expressions for the GWs themselves take on a particularly simple form if we use the gauge invariance of GR to choose a particular coordinate system which is *harmonic* and *transverse-traceless* ("TT").

First introducing the quantity $\bar{h}_{\mu\nu} \equiv h_{\mu\nu} - \frac{1}{2}\eta_{\mu\nu}h$, with the trace $h \equiv h^{\mu}{}_{\mu}$, the harmonic gauge condition is $\partial_{\nu}\bar{h}^{\mu\nu} = 0$. It already fixes four of the ten degrees of freedom that $h_{\mu\nu}$, as a symmetric 4×4 matrix, could have.

In harmonic coordinates, the field equations from Eq. (2.6) reduce to a linear form:

$$\Box \bar{h}_{\mu\nu} \equiv \partial^{\sigma}\partial_{\sigma}\bar{h}_{\mu\nu} = -\frac{16\pi G}{c^4}T_{\mu\nu}\,. \tag{2.9}$$

Propagating GWs are vacuum solutions of GR, i.e. $T_{\mu\nu} = 0$. Just as in Maxwellian electromagnetism, we therefore have a simple 4-D wave equation, whose simplest solutions are *plane waves*. Any more complicated GWs of arbitrary shape and spectral structure can be expressed as a superposition of monochromatic plane waves.

The combined harmonic and TT gauges give the constraints that the metric is purely spatial, $h_{\mu 0} = 0$, that the wave is excited transversely to its direction of propagation, $\partial_j h_{ij} = 0$, and that it is "traceless", $h^i{}_i = 0$. They reduce the degrees of freedom in $h_{\mu\nu}$ to only two. Aligning the coordinate system so that the wave propagates in the $+z$ direction, we arrive at a simple expression for the metric perturbation of a plane wave:

$$h_{\mu\nu} = \begin{pmatrix} 0 & 0 & 0 & 0 \\ 0 & h_+ & h_\times & 0 \\ 0 & h_\times & -h_+ & 0 \\ 0 & 0 & 0 & 0 \end{pmatrix}, \tag{2.10}$$

where h_+ and $h_\times$ are the two remaining degrees of freedom. These are also called "plus" and "cross" *polarisations* of the GW. As basic solutions of the wave equation Eq. (2.9), they can be expressed by periodic functions

$$h_+(t,z) \equiv A_+ \cos\left(\omega\left(t - \frac{z}{c}\right) + \phi_+\right), \tag{2.11a}$$

$$h_\times(t,z) \equiv A_\times \cos\left(\omega\left(t - \frac{z}{c}\right) + \phi_\times\right), \tag{2.11b}$$

with angular frequency ω, amplitudes A_+, $A_\times$ and phases ϕ_+, $\phi_\times$.

Each of $h_+(t,z)$, $h_\times(t,z)$ by itself corresponds to a *linearly polarised* wave. A general, *elliptically-polarised* GW as in Eq. (2.10) can be expressed as

$$h(t,z) = h_+(t,z)\,e_+ + h_\times(t,z)\,e_\times\,, \tag{2.12}$$

with a basis of *polarisation tensors* defined by unit vectors $\widehat{x}$, $\widehat{y}$:

$$e_+ \equiv \widehat{x} \otimes \widehat{x} - \widehat{y} \otimes \widehat{y} \,, \tag{2.13a}$$

$$e_\times \equiv \widehat{x} \otimes \widehat{y} + \widehat{y} \otimes \widehat{x} \,. \tag{2.13b}$$

Alternatively, a *circular polarisation basis* is given by

$$e_{\mathrm{r}} \equiv \frac{1}{\sqrt{2}} (e_+ + \mathrm{i} e_\times) \,, \tag{2.14a}$$

$$e_{\mathrm{l}} \equiv \frac{1}{\sqrt{2}} (e_+ - \mathrm{i} e_\times) \,. \tag{2.14b}$$

2.4 GW emission: quadrupole formalism

The amplitude of a GW decreases linearly with the distance between source and observer (while the power decreases quadratically, just as optical luminosities do). We know that there are no very strong GWs reaching Earth, since we would already have detected them by experiments such as those by Weber. So any GWs we hope to observe are weak, and linearised gravity is a good description for the observation, far from any strong gravitational field sources. However, distances to astronomical objects are huge, and hence for the GW to be detectable at all, the source must indeed have a strong field. Therefore, we need a different formalism to describe GW emission.

This task still does not require full GR: it turns out that a treatment of GW emission only requires knowledge of the field at distances from the centre of the source where the field is already weakened, but still dominates over contributions from the rest of the universe. This is called the "local wave zone" by Thorne (1987). Similar approximations are known for the emission of dipole antennas in electromagnetism. Since gravitation is a spin-2 field with a quadrupole as the lowest moment in a multipole expansion, this approach is called the *quadrupole formalism*. It is described in detail in Sec. 9.3.2 of Thorne (1987), chapter 36 of MTW73, Sec. 3 of Maggiore 2008 and Sec. 1.7 of JK09.

The central quantity here is the (traceless) *quadrupole moment* of the mass distribution, which in the Newtonian limit – for sources with weak internal fields and slow internal motions – is given by

$$\mathcal{I}_{ij}(t) \equiv \int \rho(t, \vec{x}) \left(x_i x_j - \frac{1}{3} r^2 \delta_{ij} \right) \mathrm{d}^3 x \,, \tag{2.15}$$

at a distance r from the centre of the source with a mass distribution ρ.

To leading quadrupole order, it is then relatively straightforward to compute the local GW amplitude, which in the TT gauge is found as

$$h_{ij} = \frac{1}{r} \frac{2G}{c^4} \, \partial_t^2 \, \mathcal{I}_{ij} \left(t - \frac{r}{c} \right) \,. \tag{2.16}$$

On average over several cycles of the GW-generation process, the emitted luminosity is

$$L = \frac{G}{5c^5} \sum_{ij} \left\langle \left(\frac{\mathrm{d}^3 \mathcal{I}_{ij}}{\mathrm{d}t^3} \right)^2 \right\rangle . \qquad (2.17)$$

Eqs. (2.16) and (2.17) remain valid for sources with a strong internal field, as long as the internal motions are slow. It is only necessary to replace $\mathcal{I}$ from Eq. (2.15) with the quadrupole coefficient from an expansion of the Newtonian potential, with the dipole term vanishing in the centre-of-mass frame of the source (Thorne 1980),

$$\Phi = -G\frac{M}{r} - \frac{3G}{2}\frac{\mathcal{I}_{ij}(t)x^i x^j}{r^5} - \frac{5G}{2}\frac{\mathcal{I}_{ijk}(t)x^i x^j x^k}{r^7} + \ldots \qquad (2.18)$$

and, possibly, to include higher-order terms for the amplitude and luminosity.

Here, I am glossing over the issue of *radiation reaction*, i.e. the effects of the emitted GW on the source itself, which is discussed briefly in Sec. 9.3.2 of Thorne (1987), and in more detail in Damour (1983) and in the references therein.

The most relevant example for this thesis is the GW emission from a spinning compact object, such as a neutron star (see Sec. 3), with rotational frequency f_{rot} and "ellipticity"

$$\epsilon \equiv \frac{|I_{xx} - I_{yy}|}{I_{zz}} , \qquad (2.19)$$

where I is the moment-of-inertia tensor. More precisely, this corresponds to the deviation from axisymmetry around the spin axis. At a distance d from the observer, the quadrupole formalism predicts a GW amplitude (at $f_{\mathrm{GW}} = 2f_{\mathrm{rot}}$, Prix 2009) of

$$h_0 = \frac{4\pi^2 G}{c^4} \frac{\epsilon\, I_{zz} f_{\mathrm{rot}}{}^2}{d} . \qquad (2.20)$$

2.5 Astrophysical sources of gravitational waves

Although gravity is the force of nature which is most directly experienced in everyday life, as well as the dominant force over cosmic scales, it is in fact a much weaker force than electromagnetism - in other words, the coupling between gravitation and matter is weak. Hence, GWs tend to be much weaker than electromagnetic waves. Emitters of non-negligible GW energy must be extremely massive and energetic systems, making GWs an intrinsically astrophysical topic.

Furthermore, the results of Sec. 2.4 tell us that any GW source must have a time-varying mass quadrupole. Spherically symmetric sources, such as a simple radially-pulsating star, cannot produce GWs. The simplest systems which fulfil the quadrupole requirement are (i) two or more orbiting objects and (ii) rotating individual objects with non-axisymmetric deformations. Promising candidates are typically compact objects

with high masses, where the density is high enough to create strong-field effects, and with high orbital or rotation speeds.

This line of reasoning leads us to two of the most interesting candidate sources for terrestrial GW detectors: compact binaries and rotating compact stars. In the following, I describe these sources, and some others which are also relevant for terrestrial interferometric GW detectors (see Sec. 2.6). I refer only tangentially to sources for other types of detectors (see Sec. 2.7).

2.5.1 Compact binaries

The most promising sources for the detection of GWs with ground-based interferometers are compact binary systems. "Compact" here refers both to small separations of the system components and to the components themselves. For ground-based interferometric detectors, these include neutron stars (NSs) and stellar-mass black holes (BHs). (See Abadie et al. 2010c, and Secs. II.A, B of Andersson et al. 2013.) Both are remnants of supernova explosions of massive stars. I will give some details about NS properties and physics in Sec. 3, but will not go into any details about BHs in this thesis.

When two such objects orbit each other, this constitutes a time-varying mass quadrupole, and the system will radiate away energy in GWs. This emission is compensated by a reduction in gravitational binding energy, which corresponds to a shrinking orbital separation and, according to Kepler's laws, to increased orbital speed.

This orbital evolution can in some cases be observed directly by conventional electromagnetic astronomy. The observation of orbital decay in the binary system PSR B1913+16, consisting of a pulsar (see Sec. 3.3) and another NS, by Hulse & Taylor (1975) and Taylor & Weisberg (1982) gave the first indirect evidence for GWs, as the measured orbital tightening matches the predictions of GR very well.

However, a GW signal strong enough for direct detection is expected only from the final phase of an inspiral, much later than the current stage of PSR B1913+16. This final phase, shortly before and including the actual collision of the two objects, is called *coalescence*. Hence, this type of signal is referred to as a "compact binary inspiral" or "compact binary coalescence" (CBC). The typical signal shape before coalescence is a "chirp", since the increasing orbital speed produces an increasing GW frequency. CBCs are short, *transient* events, as the signal frequencies in the final inspiral phase evolve rapidly when entering the sensitive range of terrestrial detectors.

Long-arm-length detectors, such as the third-generation ground-based ET (see Sec. 2.6.3) or space missions (see Sec. 2.7.1), are more sensitive towards lower frequencies. Hence, they could observe earlier phases of binary inspirals, as well as binaries containing white dwarfs – the burned-out remnants of stars not massive enough to ignite supernovae (Sathyaprakash et al. 2012, Amaro-Seoane et al. 2013). Space-based detectors, as well as pulsar-timing arrays (PTAs, see Sec. 2.7.3), could also observe, at even lower frequencies,

the coalescences of super-massive black holes (SMBHs), which can follow a galaxy merger (Begelman, Blandford & Rees 1980, Volonteri, Haardt & Madau 2003).

2.5.2 Rotating compact stars

Among solitary objects, the only promising candidates for GW detection with ground-based detectors are neutron stars. These are heavy, extremely compact and, from electro-magnetic observations, some of them are known to rotate rapidly (Owen, Reitze & Whit-comb 2009, Prix 2009). The missing piece of evidence is for quadrupolar deformations, though models predict that NSs can support significant asymmetries (Johnson-McDaniel & Owen 2013).

The GW emission of a rotating NS would typically have a much slower frequency evolution than a CBC event, as even over long observation times only a small part of the rotational energy is converted to GW emission, and since there is no self-enhancing effect as for CBCs – on the contrary, a GW-emitting NSs will "spin down" and hence become a less efficient GW emitter over time. This is the reason why GW emission from rotating NS is referred to as "continuous waves" (CWs): the signals last for a long time, with only slow changes in frequency.

Hence, the data analysis problem is very different from the CBC case: one looks for long-lasting, narrow-band signals instead of short, broad-band transients. Integration over long observation times can increase the signal-to-noise rate of the intrinsically very weak signals.

As CWs are the main topic of this thesis, Sec. 3 gives more details about NS physics, and Sec. 5 contains an introduction to CW data analysis.

2.5.3 Stellar explosions

Supernova (SN) explosions at the end of the life of massive stars are among the most energetic events known in the universe. Models of SN explosion mechanisms require asymmetries, which indicates that some fraction of this energy will get converted into GWs (Janka et al. 2007). SNe would produce transient signals, similar to CBCs (see Sec. II.C of Andersson et al. 2013). However, due to the complicated internal physics, the shape of waveforms is much harder to predict. Therefore, "unmodelled" searches for excess strain power are the usual method, which are also called *burst searches*.

Even more energetic phenomena have been discovered as *gamma-ray bursts* (GRBs). Long-duration GRBs are thought to be extremely powerful SN explosions ("hypernovae", see Woosley & Bloom 2006, Hjorth & Bloom 2012), while the leading scenario for short GRBs is the collision of two NSs, i.e. a coalescence event (Perna & Belczynski 2002, Belczynski et al. 2006, Troja, Rosswog & Gehrels 2010). Hence, burst and CBC searches share a common target.

2.5.4 Early universe

A completely different class of expected GW signals is of cosmological origin (Brustein et al. 1995, Turner 1997, Maggiore 2000a, Ananda, Clarkson & Wands 2007). According to the hot big bang model, the early universe was so energetic that many processes leading to GW emission can be imagined. Most importantly, such *primordial* GWs are expected as the tensor component of initial quantum fluctuations, complementing the scalar density perturbations which seeded the large-scale cosmic structure and are still observable today as anisotropies in the cosmic microwave background (CMB). After the rapid cosmic expansion during the inflationary phase, these GWs would propagate, almost without interaction, to the present day and, though diluted by expansion, could still be detectable. An indirect detection of such a signal, imprinted on the B-mode polarisation component of the CMB, was recently claimed by the BICEP2 team (Ade et al. 2014).

Together with the superposition of signals from binary systems and rotating NS which are not resolvable as individual sources (Rosado 2011, 2012), the primordial GWs constitute a *stochastic background* (Allen & Romano 1999). This is another very promising source for direct detection with PTAs and space-based interferometric GW detectors (Phinney et al. 2004, Jenet et al. 2005, Amaro-Seoane et al. 2013). It is most likely too weak at the frequencies of terrestrial detectors, but chances of detection are still non-zero and are pursued by stochastic search techniques, such as cross-correlation of the strain from multiple detectors.

2.5.5 Exotic sources

As GWs open a completely new window of observations, they also have the potential to discover exotic sources unknown to electromagnetic astronomy. Among these candidates, the most "mundane" are *intermediate-mass black holes* (IMBHs, see Miller & Colbert 2004), for which no direct electromagnetic evidence exists yet. These could show up as CBC or burst events, either from IMBH binaries (Fregeau et al. 2006), or when a single IMBH captures a smaller (stellar) object, or is in turn captured by a SMBH (Mandel et al. 2008).

Getting more exotic, *phase transitions* in the early universe could yield stronger and sharper signatures than the tensor-perturbation background. Another often-discussed class of exotic sources are *cosmic strings* – one-dimensional topological defects, not to be confused with the elementary superstrings of string theory. These could emit GWs when rearranging their shape (e.g. spontaneous straightening of "kinks" in the string, see Damour & Vilenkin 2001) or colliding with each other.

Finally, GW detectors, especially through the unmodelled searches of the burst and stochastic types, are also looking out for the vast class of "unknown unknowns".

Figure 2.1: Schematic illustration of the effect of an incident GW with + polarisation, and with a $h(t)$ dependence as given by the top panel, on a ring of test particles in a plane perpendicular to the propagation direction. Superimposed on the ring is a simplistic sketch of a Michelson interferometer. Figure credit: LIGO Scientific Collaboration, Abbott et al. (2009e).
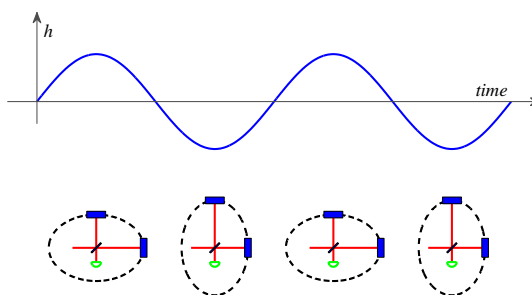
2.6 Terrestrial laser-interferometric detectors

The main part of this thesis is concerned with data analysis for terrestrial laser-interferometric detectors, so I will focus on those here. However, there are some other classes of GW detectors that deserve at least a short description, which I will give in Sec. 2.7: non-terrestrial, i.e. space-based, interferometric detectors, as well as terrestrial non-interferometric detectors, and a more indirect approach, pulsar timing arrays (PTAs). The following introduction to terrestrial interferometers is based on the much more thorough treatments in classic texts by Drever (1983) and Saulson (1994) and the more recent reviews by Maggiore (2008) and Pitkin et al. (2011).

2.6.1 General concepts

In principle, the passage of a GW of sufficient amplitude could be detected by monitoring the relative distances of any set of spatially separated test masses. The classical thought experiment to visualise the effect of the two linear GW polarisations given in Eqs. (2.12)–(2.13) requires a ring of test particles. In Fig. 2.1, imagine a GW with + polarisation travelling perpendicularly to the plane of the figure. If the ring is perfectly circular in the absence of a GW (not pictured), it gets stretched along alternating axes at each half-phase of the wave. For the × polarisation, imagine the same effect, but rotated by 45 degrees.

Fig. 2.1 also includes a simplistic sketch of a Michelson interferometer. This demonstrates that a whole ring of test masses is not required, but that the distorting effect of a GW can also be measured by the differential arm-length change ΔL between the two arms of such an L-shaped detector. For an interferometer of arm-length L, the relation of ΔL to a GW strain h, given for example by Eq. (2.20), is

$$h = \frac{\Delta L}{L}\,. \tag{2.21}$$

Sensitivity to arbitrarily-polarised GWs from arbitrary directions can be increased with a global network of L-shaped detectors or with different shapes, such as a triangle.
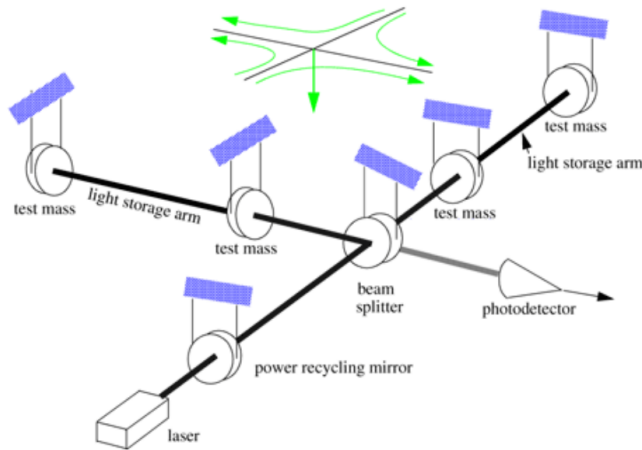
Figure 2.2: Schematic of a LIGO-type interferometric GW detector, with suspensions of all main components indicated.
Figure credit:
LIGO Scientific Collaboration, Abbott et al. (2004a).

An L-shaped Michelson geometry is the basis of the *Laser-Interferometric Gravitational Observatory* (LIGO, see Abbott et al. 2009e), which I discuss here as a representative for all terrestrial interferometers. Just as in the original experiment by Michelson & Morley (1887), an interferometer allows very sensitive measurements by converting a length change to a phase modulation of the propagating light beam. A laser provides a high-coherence, high-power light source, which is important for stable phase measurements and for low noise levels (see Sec. 2.6.2).

A more detailed schematic of a LIGO-type Michelson interferometer is given in Fig. 2.2, although this does not include most details of the optical and isolation systems. The laser beam is sent into two 4 km-length arms by means of a beam splitter, with the two mirrors at the remote ends of the arms serving as *test masses* for the GW measurement. After returning through the beam splitter, the received power at a photo detector, positioned at 90 degrees from the laser source, yields the main output signal. All of these components are suspended, to isolate the detector from its environment.

Three additional mirrors are used to increase the sensitivity of the interferometer. The *power-recycling mirror* between the laser and the beam splitter forms a resonant cavity with the main part of the interferometer, which for this purpose can be considered as an "effective mirror". This is used to increase the incident power on the beam splitter without having to actually increase the laser power. Similarly, the additional, partially transmissive test-mass mirrors in the arms, close to the beam splitter, allow the build-up of enhanced light power in *arm cavities* and also increase the effective arm-length, thereby enhancing the measurable phase modulation. The varying widths of the schematic laser beams in Fig. 2.3 illustrate the circulating power in the different parts of the interferometer.

In the classical readout scheme for the LIGO detectors, the interferometer is configured such that destructive interference of the laser carrier mode occurs at the photo detector. It is therefore referred to as operating at a "dark port" or "dark fringe". Thus, even when all cavities are in resonance, the received power at the photo detector is very small,

Figure 2.3: Schematic of a LIGO-
type interferometric GW de-
tector, with power build-up in
the sub-system cavities indicated
by the width of the laser beams.
Figure credit:
LIGO Scientific Collaboration,
Abadie et al. (2010a).
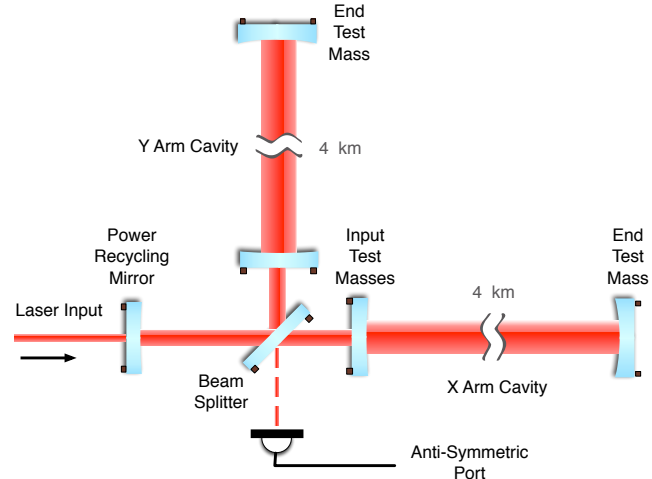
providing tenable working conditions for a high-sensitivity photo detector. Incident GWs
induce phase modulations in the arms, producing constructive interference at the photo
detector. The interferometer is kept near the dark operating point, which is also referred
to as "locking", by feedback controls on the mirrors and the beam-splitter and by phase-
modulation of the incident laser beam. The associated "error signal" also provides the GW
strain measurement, extracted by *heterodyning* with a radio-frequency (RF) oscillator
(see Abbott et al. 2009e, and Sec. 5.4 of Pitkin et al. 2011).

2.6.2 Noise sources

To measure low-amplitude GWs, we need a very sensitive detector, meaning that all
non-GW contributions to differential phase-modulations in the interferometer arms must
be minimised. However, there are several influences from the terrestrial environment of
the detector and from the involved components, as well as from fundamental physical
properties of laser light, which make any detector a noisy system.

Most of these noise sources have frequency-dependent contributions, so that together
with the optical properties of the interferometer (its *transfer function*) they dictate a
sensitivity curve for the detector, in the sense of an equivalent strain from Eq. (2.21) as a
function of frequency. A measured LIGO sensitivity curve, compared with the expected
contributions from various noise sources, is shown in Fig. 2.4. The relative contributions
from each noise source are different for different detectors and configurations, so I only
describe them qualitatively. A more formal definition of noise spectra in terms of power
spectral densities follows in Sec. 5.1.

Following Abbott et al. (2009e), let me first list sources of *displacement noise* that couple
to differential motions of the test masses:

19
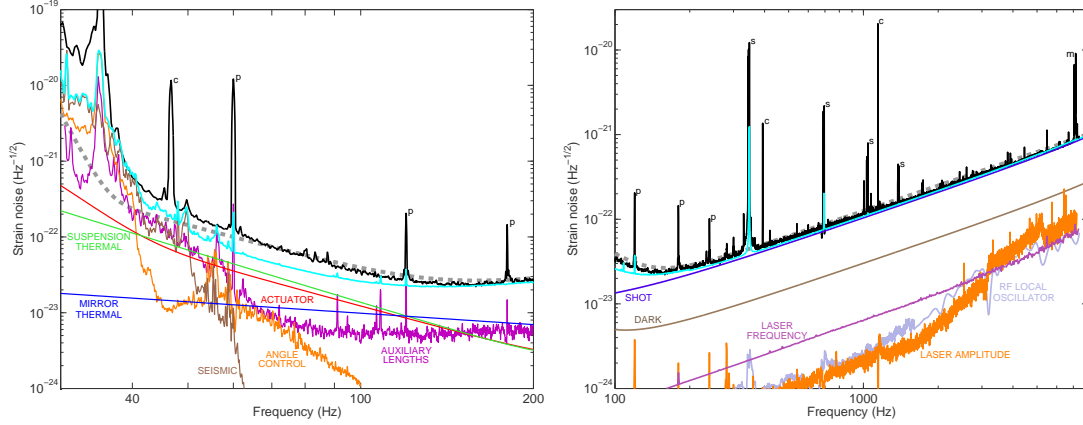
Figure 2.4: Typical noise spectrum of the LIGO H1 detector during its fifth science run (S5, see Sec. 2.6.3), along with the major known noise components. In the low-frequency part (left panel), displacement-noise contributions dominate, while for higher frequencies (right panel) mostly sensing-noise sources are relevant. The black curve is the total measured strain noise, the dashed grey curve the theoretical design goal and the cyan curve the root-square-sum of all the labelled components. The letters identify the strongest narrow line artefacts, which I will discuss in Sec. 6.2: c, calibration line; p, power line harmonic; s, suspension wire vibrational mode; m, mirror (test mass) vibrational mode. Figure credit: LIGO Scientific Collaboration, Abbott et al. (2009e).

- *Seismic noise* includes all kinds of environmental vibrations coupling into the detector, such as seismic activity of the Earth itself, but also coming from the weather and human activity. It can be reduced by many orders of magnitude by using *suspensions*, i.e. by hanging all major detector components on wires and multi-stage pendulums, and possibly with active control. Still, this is the main limiting factor at low frequencies, producing a steep increase of noise power below $\approx 45\,\text{Hz}$ for LIGO and in general limiting the lowest sensitive frequencies of current-technology terrestrial interferometers to a few tens of Hz.

- *Thermal noise* is present in all components of a detector, most notably in the mirrors and the suspensions. Thermal fluctuations cause the excitation of resonant modes, but also, through dissipation, a broad-band noise contribution.

- *Auxiliary length noise*, *angle control noise* and *actuator noise* are all related to the sensors and control loops used in locking the interferometer and damping other types of noise. Even though these loops improve the overall sensitivity of the detector, they also introduce additional, sub-dominant noise components.

Not pictured is *gravity gradient noise* from fluctuations of the terrestrial gravitational field, which gives a fundamental limit to low-frequency sensitivity at a few Hz. This is not yet relevant for current interferometers, due to the dominant seismic noise. However, with

improved seismic isolation, this can become more important, and is of central interest for third-generation detectors.

Another class is *sensing noise*, influencing the phase-modulation measurement:

- *Shot noise* is due to the quantum nature of the laser beam, or more specifically to the intrinsically random fluctuations of the number of photons in the beam. Thus, it can be suppressed by using a high laser power and resonant cavities. Shot noise is the main limiting factor at high frequencies, so that the astrophysically interesting range of sensitivity ends at a few kHz.

- The laser itself contributes additional *laser-frequency noise* and *laser-amplitude noise* components. These couple to both arms, but still yield differential noise due to unavoidable small differences in the mirror properties.

- *RF local-oscillator noise* is contributed by electronics that produce modulated radio-frequency side-bands, used for generation of the "error signals".

- The photo diode contributes a *dark noise* due to its internal thermal fluctuations.

Apart from shot noise, another fundamental quantum contribution is *radiation-pressure noise*, which increases with laser power and mainly affects sensitivity at low frequencies. It is expected to become relevant only in future interferometer generations.

Besides these broad-band noise components, which mostly are relatively stable over time, there are also transient disturbances (called "glitches") and persistent, but narrow-band features ("lines"), which I will discuss in Sec. 6.

2.6.3 Existing and planned detectors

The first generation of interferometric GW detectors was constructed in the 1990s and produced first scientific results in the 2000s. The largest of these are the LIGO detectors (Abbott et al. 2004a, 2009e) at Hanford (Washington, USA; one with 4 km arms, labelled H1, and one with 2 km arms, labelled H2) and Livingston (Louisiana, USA; 4 km, L1) as well as the Virgo detector at Cascina (Italy, 3 km, V1, see Bradaschia et al. 1990, Acernese et al. 2008). Smaller detectors include GEO600 near Hannover (Germany, 600 m, G1, see Grote 2010) and TAMA in Tokyo (Japan, 300 m, see Tsubono 1995, Kuroda 1997, Ando et al. 2001).

All of these detectors follow the basic Michelson layout, but with significant differences in the practical implementation. For example, Virgo uses a special seismic isolation system called "super-attenuators" (Braccini et al. 1993), GEO600 uses squeezed light to reduce shot noise (Abadie et al. 2011a, Khalaidovski et al. 2012, Grote et al. 2013) and TAMA was placed in underground tunnels to reduce environmental effects. For most of this thesis, I will concentrate on the two LIGO detectors H1 and L1.
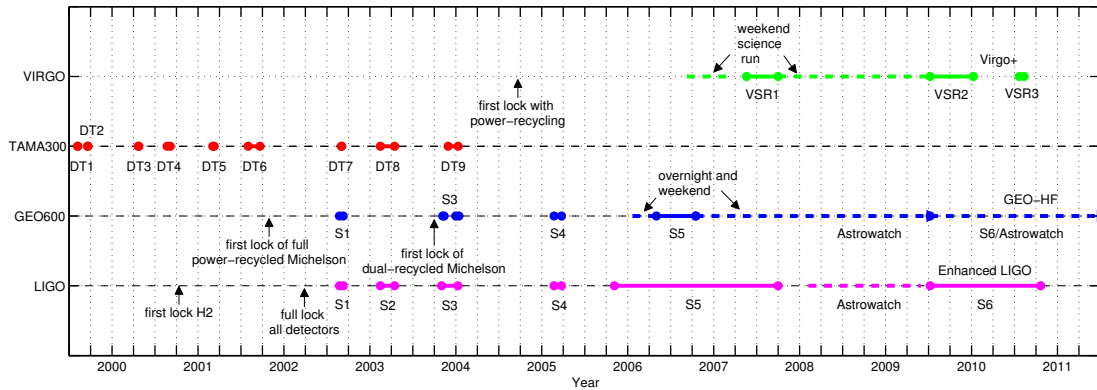
Figure 2.5: Time-line of science runs, or data-taking periods, of the first-generation interferometric GW detectors. Figure credit: Pitkin et al. (2011).

A time-line of all *science runs* of first-generation detectors is shown in Fig. 2.5, and details for initial-LIGO science runs follow below. The references variously give run descriptions, detector status reports or descriptions of calibration and sensitivity.

S1: 2002/08/23 – 2002/09/09 (Abbott et al. 2004a)

S2: 2003/02/14 – 2003/04/14 (Secs. II, IV, II of Abbott et al. 2005a,b,d, respectively)

S3: 2003/10/31 – 2004/01/09 (Sec. II of Abbott et al. 2007b)

S4: 2005/02/22 – 2005/03/23 (Sigg 2006)

S5: 2005/11/04 – 2007/09/30 (Sigg 2008, Abadie et al. 2010d)

S6: 2009/07/07 – 2010/10/20 (Abadie et al. 2012e, Aasi et al. 2014c)

The second-generation network of terrestrial interferometric GW detectors is currently under construction. While GEO600 keeps running in an "Astrowatch" mode for nearby supernovae or GRBs, the larger LIGO and Virgo detectors are receiving upgrades towards their Advanced LIGO (Shoemaker et al. 2011, Aasi et al. 2014a) and Advanced Virgo (Acernese et al. 2009, 2015) configurations. Plans exist for an additional LIGO detector in India (Aasi et al. 2013c). Another completely new detector is being built in Japan: the cryogenic 3-km interferometer KAGRA (*Kamioka Gravitational wave detector*, previously also called LCGT, see Somiya 2012, Aso et al. 2013, Punturo & Somiya 2013). The respective first science runs can be expected in 2015–2020 (Aasi et al. 2013c).

Several concepts for third-generation detectors are under investigation (Punturo et al. 2010b, Punturo & Lück 2011). The most mature proposal is called the *Einstein Telescope* (ET, see Punturo et al. 2010a, Abernathy et al. 2011, Punturo, Lück & Beker 2014). It would yield an order-of-magnitude increase in sensitivity over the second generation. With longer arms and better seismic isolation, it would also significantly bring down the low-frequency end of the sensitive range, opening a new window for additional sources, some of them shared with space-based detectors (Sathyaprakash et al. 2011, 2012).
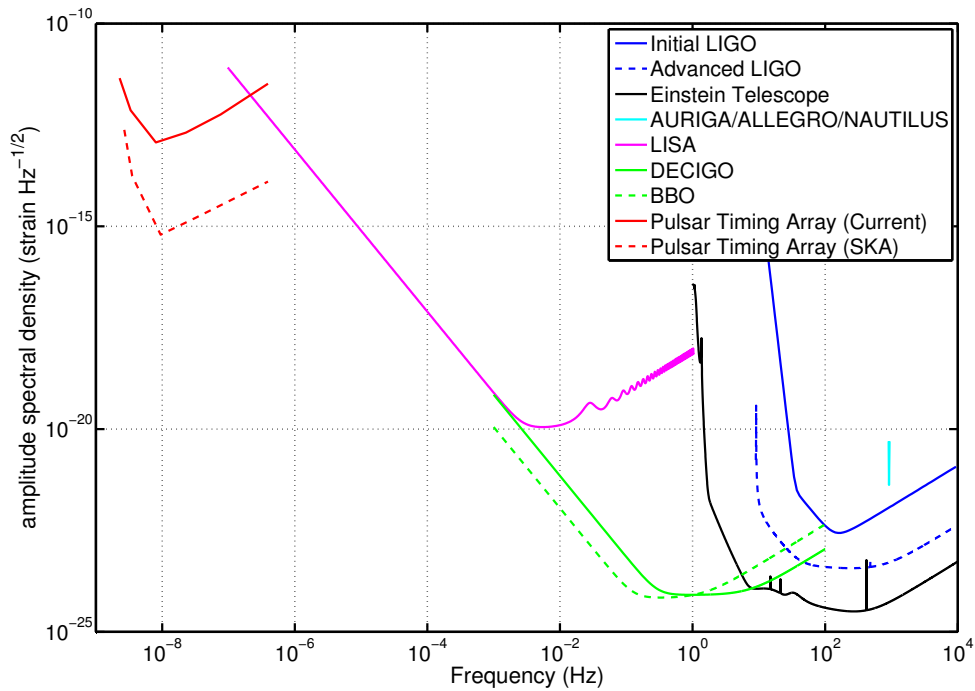
Figure 2.6: Estimated sensitivity curves for various GW detectors and concepts. Figure credit and references for the individual curves: Pitkin et al. (2011).

2.7 Other GW-detector types

2.7.1 Space-based laser-interferometric detectors

Laser-interferometric detectors in space can avoid terrestrial noise sources, most importantly the "seismic barrier" which fundamentally limits the low-frequency sensitivity of terrestrial detectors at a few Hz to tens of Hz. Space-based interferometers can also have longer arms, as no vacuum tubes are needed – instead, the laser beams propagate freely through space itself. On the other hand, spacecraft hardware is much more difficult and expensive to build and cannot be serviced and tuned on site, which makes it very challenging to equal the absolute sensitivities of ground-based detectors. Yet, the expected GW sources in the lower frequency band of such detectors, especially super-massive black-hole (SMBH) binaries, should be so strong that comparatively lower sensitivities (see Fig. 2.6) would be enough to reach much higher signal-to-noise ratios than current ground-based detectors.

The earliest and most mature concept for a GW detector in space is the *Laser Interferometer Space Antenna* (LISA, see Danzmann et al. 2003, 2011), currently scheduled for

launch as an ESA L3 mission around 2034. Variations of the concept were and are known as eLISA (for "European LISA" or "evolved LISA", see Amaro-Seoane et al. 2013) and NGO ("New Gravitational-wave Observatory", see Jennrich et al. 2012). The basic idea is a triangle of three spacecraft exchanging laser light, where the original plan included three identical spacecraft with six links, and the scaled-down version one mother and two daughter spacecraft with four links only.

With an arm-length of millions of km, either a heliocentric or geocentric orbit and a target peak sensitivity of $\sim 10^{-21}\sqrt{\text{Hz}}$, LISA would be an enormously powerful observatory for SMBH binaries, for EMRIs and IMRIs (*extreme/intermediate mass-ratio inspirals*), for white-dwarf and neutron-star binaries and cosmological backgrounds.

Even more ambitious concepts are the Japanese *Decimeter Gravitational Observatory* (DECIGO, see Kawamura et al. 2006, Ando et al. 2010a, Kawamura et al. 2011) and the American *Big Bang Observer* (BBO, see Phinney et al. 2004, Harry et al. 2006).

Another concept for a space-based detector is the *Octahedral Gravitational Observatory* (OGO) by Wang, Keitel, Babak et al. (2013), referred to in the following as OGO13. This is not at the stage of a full mission study, but a concept mostly motivated by theoretical considerations. Based on the displacement-noise-free interferometry concept of Kawamura & Chen (2004), Chen & Kawamura (2006) and Chen et al. (2006), a constellation of six spacecraft in the form of an octahedron provides 24 measurement channels. Time-delayed combinations of these measurements can be used to construct GW strain channels that analytically cancel displacement-noise contributions, which most importantly includes acceleration and laser-frequency noise. As I have contributed significantly to this work, in parallel to the projects described in the main part of this thesis (Secs. 6–13), a detailed description of this concept follows in Sec. 14, essentially reproducing the content from OGO13.

2.7.2 Non-interferometric detectors

There is another GW detector concept, older than interferometric detectors, which I have already mentioned in Sec. 2.1: resonant-mass detectors. In principle, GWs can directly excite the internal mechanical modes of any extended object. As the expected GW amplitudes are weak, this effect could be very hard to measure. Low-dissipation detectors using large test masses, very good isolation, cryogenic temperatures and electronic readout have made the approach viable, typically with resonance frequencies in the kHz regime. For an early review of the physics of such detectors, see Blair (1983).

After the original attempts by Weber (1960, 1966, 1969, 1970, 1986), more recent examples of resonant-bar detectors include the American experiment ALLEGRO (Mauceli et al. 1996) and the three Italian detectors AURIGA (Cerdonio et al. 1997), EXPLORER (Astone et al. 1993, 2008) and NAUTILUS (Astone et al. 1997, 2008). Nowadays, however, interferometric detectors reach much better sensitivities over a wider frequency bandwidth, and are generally considered the more promising approach.

A variation of the resonant-mass concept are spherical detectors such as the Dutch MiniGRAIL (de Waard et al. 2003, Gottardi et al. 2007) and the Brazilian "Mario Schenberg" (Aguiar et al. 2002, 2006). Recently, torsion-bar antennas (TOBAs, see Ando et al. 2010b) have also been investigated.

Yet another concept for high-frequency GW detection makes use of radio-frequency electromagnetic cavities. (Pegoraro, Picasso & Radicati 1978, Pegoraro et al. 1978, Bernard et al. 2001, Ballantini et al. 2003). In contrast to mechanical resonators, this could allow for dynamical tuning of the resonance range. So far, however, only small prototypes exist.

2.7.3 Pulsar timing arrays

At the moment, the most promising alternative way for GW detection is provided by *pulsar timing arrays* (PTAs, see Foster & Backer 1990). The term refers to the long-time observation of several ("an array of") millisecond radio pulsars (see Sec. 3.3). The central idea for GW detection with PTAs (Jenet et al. 2005) relies on the modulation of the *times of arrival* of pulses from each individual pulsar on Earth by any GWs interacting with the radio waves along their trajectory. In a simplified picture, a PTA can therefore be imagined as replacing the km-scale arms of terrestrial interferometers, or the million-km arms of missions like LISA, with galaxy-scale arms. Hence, PTAs are sensitive to GWs of much lower frequencies than even space-based interferometers, aiming mostly for the range from 10^{-9} Hz to 10^{-6} Hz.

On the other hand, PTAs do not require space missions, as the pulsars can simply be observed by terrestrial radio telescopes. Current efforts on the establishment of sufficiently sensitive PTAs are distributed over an European (EPTA, see Ferdman et al. 2010), a North American (NANOGrav, see Jenet et al. 2009) and an Australian (PPTA, see Manchester et al. 2013) collaboration. Intercontinental collaboration is in preparation under the IPTA project (Hobbs et al. 2010).

The detection of GWs from cosmological sources, especially from SMBH binaries (Rajagopal & Romani 1995, Jaffe & Backer 2003, Wyithe & Loeb 2003), with PTAs is considered realistic in the current decade, although it is unclear yet whether the most likely first detection would be a single, strong source or a stochastic background (Maggiore 2000b, Sesana, Vecchio & Colacino 2008, Rosado 2011) – this question is discussed by Sesana, Vecchio & Volonteri (2009), Mingarelli et al. (2013), Sesana (2013) and Rosado & Sesana (2014). Future large-scale radio-telescope networks, especially the *Square Kilometer Array* (SKA, see Carilli & Rawlings 2004, Dewdney et al. 2013), are expected to bring an enormous increase in PTA sensitivity.

3 Neutron stars and pulsars

Among the possible GW sources discussed in Sec. 2.5, neutron stars (NSs) are the most relevant for this thesis, as they can potentially produce continuous-wave emission that would be detectable by terrestrial interferometers. NSs are characterised by the extreme density and compactness of the matter in their interior, with masses in the range of 1 to 2 $M_\odot$ (solar masses) compressed into $\sim 10\,$km radii, resulting in extreme densities. Their strong surface gravity makes them promising GR laboratories and GW emitters, and their strong magnetic fields create a rich phenomenology in electromagnetic observations – especially the appearance of many NSs as *pulsars*.

In this chapter, I give a short introduction to the formation of NSs, as well as the current understanding of their internal structure and of the most relevant emission processes. For more details, I refer the reader to the references given in each section, as well as the general references Lorimer & Kramer (2004), Haensel, Potekhin & Yakovlev (2006) and Becker (2009).

3.1 Formation

The idea of extremely compact stellar-mass objects, which have densities similar to that of atomic nuclei and therefore should actually be composed of nuclear matter, originated in the early 1930s with Landau (1932) and Baade & Zwicky (1934a,b). A historical perspective can be found in Baym (1982).

NSs are created in supernova (SN) explosions of massive stars, a notion which goes back to Baade & Zwicky. When a heavy star has exhausted its fuel of light elements, it suffers *core collapse* because fusion no longer provides enough pressure to counteract gravity and to stabilise the core. This collapse increases the central density by so much that, in a simplified picture, most protons and electrons are converted to neutrons, leading to an extremely neutron-rich remnant, the *proto-neutron star*. The outer layers of the star bounce back from this stiff, compact core and are blown off, although additional mechanisms, including asymmetry, neutrino interactions and hydrodynamics, are believed to be required for successful modelling of such a SN explosion (Janka et al. 2007).

The ejecta expand and thin out to form a *supernova remnant* (SNr) nebula. The remaining NS is initially even much hotter than its stellar-core progenitor and though it cools very rapidly, mostly through neutrino emission (Yakovlev & Pethick 2004), surface temperatures can still still exceed $10^6\,$K after hundreds of years (Yakovlev et al. 2011). The

discovery of several young, hot NSs in SNrs is currently the best proof for this formation scenario (Pavlov, Sanwal & Teter 2004).

NSs can only be formed by progenitor stars in a certain mass range. The viable fusion chains in a star depend on the nuclear binding energies of different nuclei and the star's ability to ignite the various steps in each chain, in turn depending on its mass (and initial composition). For masses $\lesssim 8\,M_\odot$, the final stages of nuclear fusion towards iron-group elements never ignite, and no SN follows. (Iron-group elements have the most-tightly-bound nuclei, with nickel-56 and the stable iron-56 being produced most efficiently, see Sec. 4.7 of Woosley & Weaver 1995, and Woosley & Janka 2005.) Instead, at the end of the red-giant phase, the outer shells are shed and the core remains as a white dwarf (WD), which is not nearly as compact as a NS.

On the other hand, for much higher masses – above several dozen $M_\odot$, though the exact boundary depends on chemical composition and stellar-wind losses – the proto-NS which forms at the centre of a SN becomes too massive and continues collapsing into a black hole. Very high-mass stars can also be completely disintegrated by powerful SNe.

An important aspect of NS formation is the behaviour of stellar *magnetic fields*. It is usually assumed that during the SN most of the initial magnetic field remains attached to the dense core, and gets amplified by several orders of magnitude by the collapse, reaching up to 10^{12} G. However, in a field-line picture, these can get "buried" inside the remnant NS during the core collapse (Ho 2011), and according to current models are expected to re-emerge on time-scales of thousands of years. Young NSs found in SNrs and with low magnetic fields, which therefore lack some of the electromagnetic phenomena discussed in Sec. 3.3, are also known as *central compact objects* (Pavlov, Sanwal & Teter 2004, de Luca 2008).

Even higher magnetic fields have been found in a class of NSs called *magnetars*, exceeding 10^{14} G. These can be explained by dynamo processes during the NS formation (Duncan & Thompson 1992, Thompson & Duncan 1993, Spruit 2008).

The evolution of NSs in binary systems is more complicated than for isolated stars, as mass transfer between the stellar components and orbital effects have to be taken into account (Canal, Isern & Labay 1990). SNe can also deliver a "kick" to the forming NS, potentially disrupting the binary (Lyne & Lorimer 1994, Brandt & Podsiadlowski 1995, Podsiadlowski et al. 2004).

3.2 Structure

The modern understanding of NS structure is much more sophisticated than the original "giant nucleon" ideas by Landau (1932) and Baade & Zwicky (1934a,b). Generally, NSs are assumed to have a multi-layered structure, as illustrated in Fig. 3.1. Still, the details are an active matter of research with many competing models. For general reviews, see Haensel, Potekhin & Yakovlev (2006) and Weber, Negreiros & Rosenfield (2009).

Figure 3.1: Schematic illustration of neutron star structure.
Figure credit: M. Baym, from Baym & Lamb (2005).
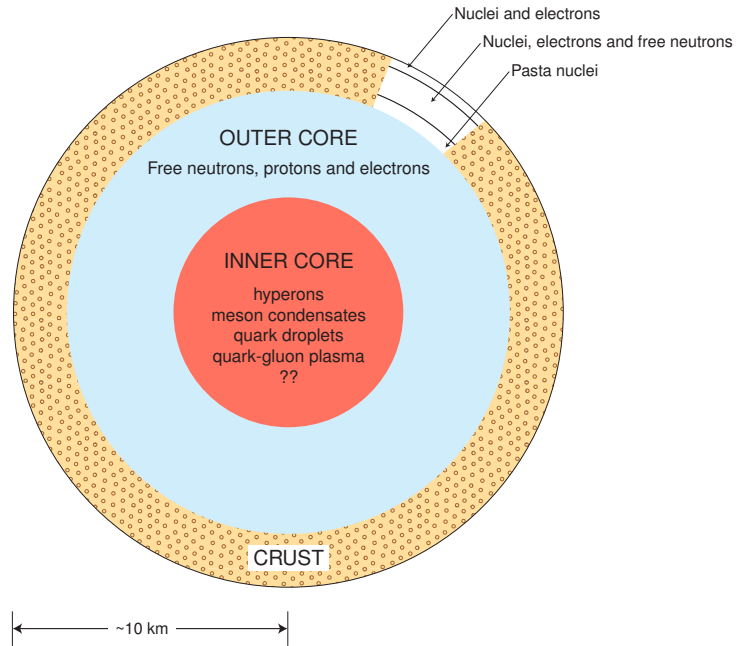
The surface layer consists of relatively standard matter, mostly heavy nuclei, though with their electrons removed and forming a degenerate gas – similar to the interior of WDs, and with metal-like properties. With increasing depth and density, the neutron content of these nuclei increases, at at some point gets so high that "neutron drip" occurs, where free neutrons outside the nuclei appear. Going further down, the admixture of these free neutrons increases.

Below this *crust* lies the main interior part of the NS, its *core*. The outer core is conventionally believed to be dominated by neutrons, with only a small proton and electron fraction. Between the crust and core might exist a boundary layer in a "pasta phase", consisting of extremely deformed nuclei embedded in a liquid neutron phase (Pethick & Potekhin 1998, Newton, Gearheart & Li 2013).

The outer core has very interesting properties from a condensed-matter point of view: the majority component of neutrons is most likely in a *superfluid* state (Baym, Pethick & Pines 1969, Pines & Alpar 1985, Lombardo & Schulze 2001), while the proton admixture may be *superconducting* (Glampedakis, Andersson & Samuelsson 2011, Lander 2013).

The most uncertain region is the inner core. In the most conservative model, the neutron phase reaches all the way to the centre of the NS. However, alternative models predict the existence of more exotic phases, including heavier baryons (or "hyperons", Schaffner & Mishustin 1996), meson condensates (Haensel & Proszynski 1982) or pure quark matter in a variety of models, including "colour superconductors" (Alford et al. 2008) and "strange stars" (Weber 2005). In some exotic models, these phases might even reach to the NS surface (Alford et al. 2006). Models with both conventional and exotic phases are also referred to as *hybrid stars* (Alford, Han & Prakash 2013).

The difference between the various models is important mostly because they predict different *equations of state* (EoS) for the NS, relating pressure and density. Different EoS also imply different mass-radius relations (Lattimer & Prakash 2001). A generic property is that neutron star radii *decrease* with increasing mass, because the strong gravity compresses heavy NSs even more.

Direct measurements of NS masses constrain the allowed range of EoS, and thereby can select between the different models. Notably, many exotic models have difficulties explaining the discovery of NSs with $M \gtrsim 2\,M_\odot$ (Demorest et al. 2010, Lattimer & Prakash 2011, Antoniadis et al. 2013). For reviews of NS equations of state, the observed NS mass distribution and their relation, as well as mass determination techniques, see Lorimer & Kramer (2004), Stairs (2006), Lattimer (2012) and Kiziltan et al. (2013).

3.3 Electromagnetic emission

Young NSs have thermal emission from their surface in the keV range, making them bright X-ray sources. For NSs close to Earth, thermal emission is detectable across a wide range of the electromagnetic spectrum, including infra-red, optical, UV and X-rays (Kaplan 2004). However, older NSs, which have already cooled down significantly, are very difficult to observe as thermal sources at larger distances.

Yet there are several kinds of strong non-thermal emission that a NS can produce. The first extra-galactic X-ray source, *Scorpius X-1*, was discovered by Giacconi et al. (1962) and first interpreted as a NS by Shklovsky (1967), though this was not widely recognised at the time. Today, its emission is known to be powered by accretion off a companion star, so that it is classified as a *low-mass X-ray binary* (LMXB, Benacquista & Downing 2013). Meanwhile, the first *radio pulsar* was discovered (PSR B1919+21, discovered in 1967 and published as Hewish et al. 1968). These rapidly and regularly pulsed sources were connected to rotating magnetised NSs by Gold (1968), with a similar model previously published by Pacini (1967). For details of the early observational history, see chapter 10 of Shapiro & Teukolsky (1983) and Sec. 1.2 of Haensel, Potekhin & Yakovlev (2006).

The details of the pulsar emission process are intricate (see Kramer et al. 1997, and the general descriptions in Lorimer & Kramer 2004, Lorimer 2008), but the general picture is as follows: The strong rotating magnetic field of a pulsar accelerates charged particles away from the surface, in a beam formed by the field lines. Electromagnetic radiation is then produced by these particles and emitted along the magnetic field axis. If this beam points towards Earth, but the magnetic field axis and the rotational axis do not coincide, we observe pulsed radiation with a frequency equal to that of the rotation.

Most pulsars are observed to *spin down* over time, as rotational energy is converted into heat, particles and radiation. However, this loss is dominated not by the pulsed radio or high-energy emission, but by low-frequency dipole radiation (Graham-Smith 2003).
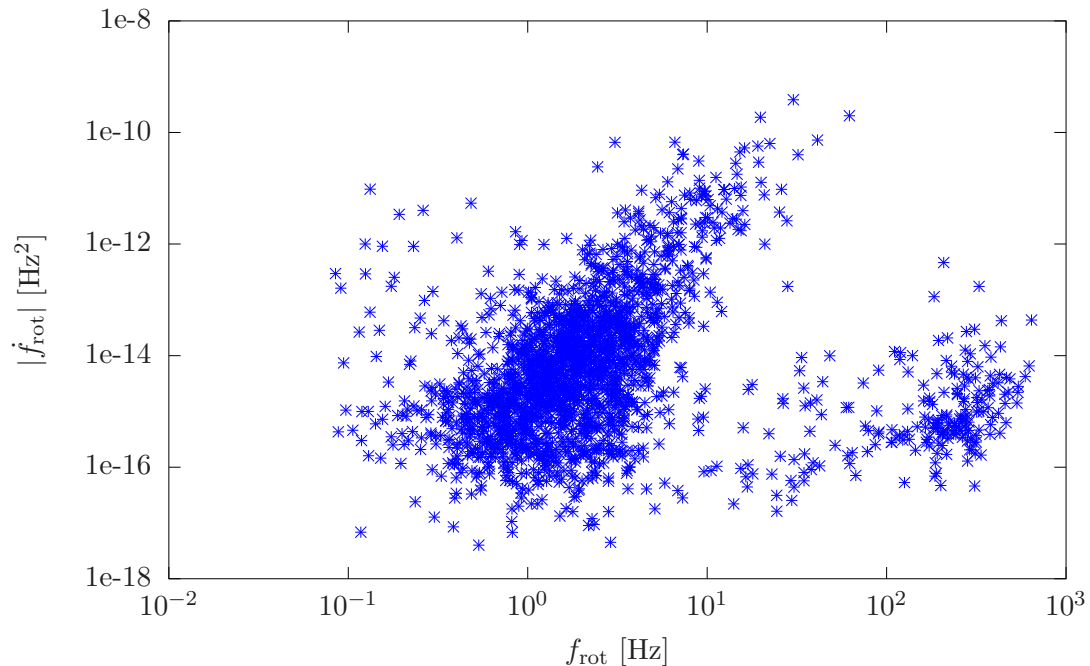
Figure 3.2: Population of currently-known pulsars in the frequency-spin-down plane. The sub-population in the lower right-hand corner are the millisecond pulsars. Data for this plot was taken from the ATNF catalogue (Manchester et al. 2005) on July 18, 2014. 2011 pulsars are shown, while 317 with missing $\dot{f}_{\mathrm{rot}}$ measurements were omitted.

Today, over 2300 pulsars are known (Manchester et al. 2005). Their frequency-spin-down distribution is shown in Fig. 3.2. A special class of pulsars are the *millisecond pulsars* (MSPs), which have the shortest known periods (in the ms range, hence the name; see Lorimer 2008 for a review). They reside, predominantly, in binary systems, as the standard evolution scenario requires accretion from a companion which "spins up" an old NS to these high frequencies (Alpar et al. 1982). MSPs also have extremely regular pulsations, making them ideally suited for pulsar-timing arrays (see Sec. 2.7.3). Double-NS binaries, with one or both components observable as pulsars, are especially valuable for high-precision tests of general relativity (Kramer et al. 2006, Kramer 2014).

Although the frequency evolution of most older pulsars is very regular, with a slow and continuous spin-down, some young pulsars exhibit so-called *glitches*, sudden increases in frequency. These events are not fully understood yet, with competing models relating them to "star-quakes" in the NS crust, rearrangements of the magnetic field, superfluid vortices in the interior or two-stream instabilities (Ruderman, Zhu & Chen 1998, Larson & Link 2002, Link & Cutler 2002, Andersson, Comer & Prix 2003).

Pulsed emission from some NSs is also observed in the optical (Shearer & Golden 2002), X-ray (Caballero & Wilms 2012) and gamma-ray bands (Abdo et al. 2013). Emission

mechanisms vary – for example, gamma-ray beams can be much broader than radio beams, and their emission region is usually considered to be higher in the magnetosphere than for radio emission (Abdo et al. 2009). Hence, the observed pulsar populations in the various bands are not identical, with an increasing number of *radio-quiet* pulsars discovered in other bands.

The pulsar population also includes exotic classes which are related to magnetars, with their pulsations powered by magnetic-field decay instead of rotational energy: *soft gamma repeaters* and *anomalous X-ray pulsars* (Mereghetti 2008). NSs can also produce a variety of transient electromagnetic phenomena, including glitch-associated outbursts, *magnetar flares* (Hurley et al. 2005) and X-ray burst events in accreting binaries (Lewin, van Paradijs & Taam 1993).

3.4 Gravitational-wave emission

The most popular model for a non-axisymmetric NS that could produce observable GWs involves a quadrupolar deformation referred to as a "mountain", sustained either mechanically or by magnetic forces (Ushomirsky, Cutler & Bildsten 2000). For a NS rotating with a frequency f_{rot}, this model predicts GW emission at $f_{GW} = 2f_{rot}$, and a strength given by Eq. (2.20).

The maximum ellipticity, defined as in Eq. (2.19), that a NS could realistically support depends on the complex modelling of its internal structure and magnetic field. These estimates have changed significantly over recent years, with the current state of knowledge (Johnson-McDaniel & Owen 2013) favouring $\epsilon_{max} \sim 10^{-5}$ for the standard nucleon-only NS model. More exotic structures could support higher ellipticities: $\epsilon_{max} \sim 10^{-3}$ for quark-baryon hybrid stars and $\epsilon_{max} \sim 10^{-1}$ for colour-superconducting quark stars.

For very young NSs, such mountains could simply be residuals of the intrinsic asymmetries of the SN creating the NS (Janka et al. 2007). For older NSs, possible physical reasons for deformations could be episodes of accretion in binary systems (Ushomirsky, Cutler & Bildsten 2000, Watts et al. 2008) and spontaneous breaking of the crust due to spin-down-induced stress (Ruderman 1969, 1976, Carter, Langlois & Sedrakian 2000).

An additional component to CW emission can come from free precession (Zimmermann & Szedenits 1979, Zimmermann 1980, Cutler & Jones 2001, Jones & Andersson 2002) in the case of misaligned rotational and symmetry axes. This would produce additional signals at $f_{GW} = f_{rot} + f_{prec}$ and $f_{GW} = 2(f_{rot} + f_{prec})$ (Van Den Broeck 2005).

Alternatively, CW-type emission could also be produced by oscillatory modes in the NS interior. Several classes of such modes are known, including f-, g-, p- and r-modes (Kokkotas & Schmidt 1999, Stergioulas 2003). Of these, r-modes (rotational modes, Andersson, Kokkotas & Stergioulas 1999, Friedman & Lockitch 1999) are the most promising GW emitters (Owen 2000, Owen & Lindblom 2002). These circulatory fluid modes are relevant mostly in very rapidly rotating NSs (hundreds of Hz and upwards), i.e. young

NSs shortly after their birth, or in recently spun-up old NSs. As GW emission can actually drive the r-modes through the CFS instability (Chandrasekhar 1970, Friedman & Schutz 1978), r-modes could result in strong CW emission at $f_{\text{GW}} \approx \frac{4}{3} f_{\text{rot}}$. However, the physical details of these modes, especially of damping processes, and therefore the actual predictions are quite uncertain (Ho, Andersson & Haskell 2011). Some of these modes could also be associated with short burst-like events, or intermediate-duration transients (Prix, Giampanis & Messenger 2011).

Furthermore, NSs in close binary systems can accrete matter from their companion, leading to a temporary asymmetry and possibly to associated GW emission (Bildsten 1998, Melatos & Payne 2005, Payne & Melatos 2006, Watts et al. 2008, Watts & Krishnan 2009). The most promising sources of this type are those binaries known from X-ray observations as LMXBs (Ushomirsky, Bildsten & Cutler 2000, Chakrabarty et al. 2003, Benacquista & Downing 2013).

Returning to the simple model of CW emission due to simple non-axisymmetries, two simple arguments can be made to obtain upper limit estimates for realistically expected CW signal strengths. An argument first put to record by Thorne (1987) and credited to Blandford (1984), makes use of statistics for the Milky Way pulsar population and of a hypothetical class of as-of-yet unobserved NSs. These *gravitars* would convert almost all of their spin-down power into GWs, instead of most of it going into EM emission as for the observed pulsar population. An updated version of this argument (Abbott et al. 2007a) leads to the estimate that, with 50% probability, one could expect a strongest CW signal of $h_0^{\max} \approx 4 \cdot 10^{-24}$ – if all NSs were gravitars. Knispel & Allen (2008) have considered more realistic assumptions for this argument, arriving at more realistic estimates in the range of $\sim 10^{-26}$ to $\sim 10^{-24}$, depending on the typical frequencies and ellipticities of the NS population.

Another important upper limit can be obtained for individual NSs, if their distance d, rotational frequency f_{rot} and frequency derivative $\dot{f}_{\text{rot}}$ are known from electromagnetic observations. If the entire spin-down energy loss were converted into GWs, Eq. (2.20) would yield (Prix 2009)

$$h_0 \leq \frac{1}{d} \sqrt{\frac{5 G I_{zz}}{2 c^3} \frac{|\dot{f}_{\text{rot}}|}{f_{\text{rot}}}} \qquad (3.1)$$

as an upper limit. The spin-down upper limits for several known pulsars are comparable to the sensitivity of first- and second-generation interferometric GW detectors (Aasi et al. 2014e), and for the Crab and Vela pulsars have already been beaten by LIGO and Virgo searches (Abbott et al. 2008b, Abadie et al. 2011b).

More extensive reviews of GW emission from NSs can be found in Owen, Reitze & Whitcomb (2009) and Prix (2009). Those references also cover the topic of continuous wave data analysis, which I will discuss in Sec. 5.

4 Probability theory and statistics

This thesis belongs to the field of data analysis, which makes use of mathematical statistics to derive knowledge from measured data. In this chapter, I will briefly introduce those concepts from probability theory, statistics and inference that will be used in the main part of this work, along with the corresponding notation. This does not constitute a full review of standard statistical methods, but is only intended as the minimum set of knowledge needed for the discussions in the ensuing chapters.

Statisticians, both theoretical and applied, are often divided into two camps, *frequentists* and *Bayesians*. The principal difference is one of philosophical interpretation of probability: while frequentist probability is understood as the idealised fractional occurrence over infinitely repeated trials, Bayesian probability is a subjective "degree of plausibility". This immediately leads to a more practical distinction: while frequentists may assign probabilities only to measurable quantities and must frame problems such as hypothesis testing in a different language, Bayesians also talk about the probability of hypotheses or, in general, of any kind of statements about the data. More on the philosophical differences between the schools can be found in Loredo (1989) and Jaynes (2003).

Thus, I first give some comments on the general notion of "probability" from both approaches (Sec. 4.1) and a slightly longer introduction to Bayesian statistics and hypothesis testing (Sec. 4.2). Using this framework, I introduce the general concepts of detection statistics (Sec. 4.3) and likelihood-ratio tests (Sec. 4.4), focussing on the application to time-series analysis. Then, I focus on the special case of the detection of periodic signals in time series (Sec. 4.5), which leads naturally to the topic of continuous gravitational wave data analysis in Sec. 5. I also include, in Sec. 4.6, definitions of some elementary probability distributions which will be used later on.

4.1 Elementary probability theory

The concepts of randomness and probability have long been some of the thorniest in the history of mathematics and philosophy of science. Traditional, intuition-based definitions of probability run into many difficulties and paradoxes. In a strict Bayesian approach for the purpose of scientific inference, probability can be derived entirely as a generalisation of Boolean logic when allowing for incomplete information. Such an approach is presented in great clarity in chapters 1 and 2 of Jaynes (2003), based on Cox (1946, 1961).

Alternatively, a robust framework for defining probabilities comes from *measure theory*, the branch of mathematical analysis concerned with assigning "sizes" to sets. This can serve as a foundation for frequentist statistics, where the sets are taken as the repeated trials of the intuitive picture. However, it is also fully compatible with the Bayesian interpretation and can indeed be used for a more formal foundation of Bayesianism (Chang & Pollard 1997, Orbanz & Teh 2010, Culbertson & Sturtz 2014) than the one by Jaynes. I will skip the details here, as in-depth treatments can be found in many standard textbooks, for example in Bass (1966) and DeGroot (1970).

Here, as a tool for "translation" between the two interpretations, I will give the central results of any definition of probability: the *rules* or *axioms of probability*, usually attributed to Kolmogorov (1933). These are obtained from the measure-theoretical approach by identifying a *random variable A* with a mapping from a *probability space* to a *target space*, for example the real numbers. The outcome of A taking on any specific value can be considered a *random event*, and its probability $P(A)$ is a function (induced by a probability measure) that fulfills $P(A) \in [0, 1]$. For ease of notation, I do not distinguish explicitly between a random variable and its values.

From the Bayesian point of view, these rules can be considered as simple corollaries to what Jaynes called the three "desiderata" for a useful definition of probability, with random variables reinterpreted as objects of inference and assumed implicit dependence of all probabilities on prior information – see Sec. 4.2 and Jaynes (2003) for details.

The first important law about probabilities is the *law of unitarity*: If $\mathcal{I} = \{A_i\}$ is the (discrete) set of all possible outcomes of a random experiment, and $P(A_i)$ is the probability of event A_i, then the total probability must be unity:

$$\sum_{\mathcal{I}} P(A_i) = 1 \,. \tag{4.1}$$

For continuous sets of events and under the assumption that a *probability density function* (pdf) $p(x)$ exists, the equivalent is

$$\int_{x \in \mathcal{I}} \mathrm{d}x \, p(x) = 1 \,. \tag{4.2}$$

From the differential $p(x)$, the *cumulative distribution function* $F(x)$ is obtained (in the one-dimensional case) as

$$F(x) \equiv \int_{x' \leq x} \mathrm{d}x' \, p(x') \,. \tag{4.3}$$

However, $F(x)$ can exist even in cases where $p(x)$ does not, i.e. when it is non-differentiable – it must then be redefined straight from measure theory. The term *probability distribution function* can be used to mean either $p(x)$ or $F(x)$, depending on the source. I will generally use it for $p(x)$ in this work.

The second important rule is the additivity of probabilities for *independent* events:

$$P\left(\bigcup_{i \in I} A_i\right) = \sum_{i \in I} P(A_i).$$
(4.4)

Additivity does not hold for events which are not independent - that is, in general

$$P(A \cup B) = P(A) + P(B) - P(AB),$$
(4.5)

where $P(AB)$ is the *joint probability* of A and B, sometimes also written as $P(A, B)$, corresponding to the overlap in the supports of the two events.

This is related to the *conditional probability* $p(B|A)$ of B given A by

$$P(B|A) = \frac{p(AB)}{p(A)} \quad \text{and} \quad p(A|B) = \frac{p(AB)}{p(B)}.$$
(4.6)

4.2 Bayesian inference

The Bayesian concept of assigning probabilities to *hypotheses*, in the sense of "how likely is it that a statement $\mathcal{H}$ is true?", leads to a specialised nomenclature in the case of *inference* problems, that is when we want to *infere* a physical statement from a set of observed data x.

The probability $P(\mathcal{H})$ which we assign to a hypothesis $\mathcal{H}$ *without taking into account the data*, based either purely on theoretical considerations or also on previous data, is called the *prior* on $\mathcal{H}$. In principle, it should be written more explicitly as a conditional probability $P(\mathcal{H}|\mathcal{I})$, where $\mathcal{I}$ contains all prior information. However, for simplicity of notation I will, after this initial discussion, omit the $\mathcal{I}$ dependence and simply use $P(\mathcal{H})$ as a shortcut for $P(\mathcal{H}|\mathcal{I})$, and similarly $P(A|B)$ for conditional probabilities, which in full notation would always read $P(A|B, \mathcal{I})$. Note that, in this sense, Bayesian probabilities are *always* conditional.

In contrast to the prior, the new assessment of a hypothesis *when considering the data* is the *posterior probability* $P(\mathcal{H}|x)$ or, more explicitly, $P(\mathcal{H}|x, \mathcal{I})$. It is often useful to think of the step from prior to posterior as an "update" of the degree of belief.

4.2.1 Bayes' theorem

The relation that tells us how the data "updates" the prior to the posterior is called *Bayes' theorem* and follows directly from the definition of conditional probability, Eq. (4.6):

$$P(\mathcal{H}|x, \mathcal{I}) = \frac{P(\mathcal{H}|\mathcal{I}) P(x|\mathcal{H}, \mathcal{I})}{P(x|\mathcal{I})}.$$
(4.7)

Here, $P(x|\mathcal{H},\mathcal{I})$ is called the *likelihood* of the data under $\mathcal{H}$ and the denominator $P(x|\mathcal{I})$ is sometimes called the *evidence*. For a *complete* set of hypotheses $\{\mathcal{H}_i\}$, defined by the hypotheses being *mutually exclusive*, $P(\mathcal{H}_i, \mathcal{H}_j | \mathcal{I}) = \delta_{ij} P(\mathcal{H}_i | \mathcal{I})$, and *exhaustive*, $\sum_i P(\mathcal{H}_i|\mathcal{I}) = 1$, the evidence can be expressed as

$$P(x|\mathcal{I}) = \sum_i P(x|\mathcal{H}_i\,\mathcal{I}) \, P(\mathcal{H}_i|\mathcal{I}) \,. \tag{4.8}$$

In applications in parameter estimation and hypothesis testing (see Sec. 4.2.3), it can often be ignored as a proportionality factor, and in some quantities of interest, such as the odds ratios later considered in Sec. 4.2.3, it cancels out.

4.2.2 Priors

Proper treatment of priors is an important part of Bayesian data analysis. Ideally, a prior includes all knowledge available about the problem without looking at the data, including mathematical constraints, predictions from theoretical physics and the results of other measurements. However, in practice often no previous measurements may exist, and theoretical guidance may be vague. In such cases, priors are often chosen to represent the state of "ignorance", meaning that they should not put any stringent bounds on the support of the posterior, and should be weak enough so that even moderately constraining data sets can easily dominate the posterior.

Within the freedom of this requirement, specific priors can often be chosen based on considerations of simplicity. Therefore, some of the most popular priors are simple flat and uniform distributions.

Uniform priors can, however, be disadvantageous in the inference of *scale parameters*, such as the width of a distribution. Without additional constraints, it should intuitively be equally likely to be very narrow or very wide – but a uniform prior puts little weight on values close to zero. For such scale parameters, $\theta \in (0, \infty)$, it is often more appropriate to use a *log-uniform prior* , which can be expressed as $P(\theta|\mathcal{I}) \propto 1/\theta$ and assigns equal prior probability to equal intervals in $\log(\theta)$.

In fact, this is a special case of the *Jeffreys prior* (Jeffreys 1946, and see also Secs. 6.15 and 12 of Jaynes 2003), which is designed to express maximum ignorance in a reparametrisation-invariant way. Letting θ stand for a whole set of model parameters, it is given by

$$P(\theta|\mathcal{I}) \propto \sqrt{\det F(\theta)}, \tag{4.9}$$

where $\det F(\theta)$ is the determinant of the *Fisher information matrix* of the θ parameters:

$$F_{ij} \equiv -E\left[\frac{\partial^2 \log(P(x|\theta\,\mathcal{I}))}{\partial\theta_i\,\partial\theta_j}\right] \tag{4.10}$$

Here, $E[\,]$ denotes an *expectation value*, given for a pdf $p(x)$ and some function $f(x)$ by

$$E\left[f(x)\right] = \int f(x)\,p(x)\,\mathrm{d}x\;.\tag{4.11}$$

The Jeffreys prior is reparametrisation-invariant in the sense that, if $P\left(\theta|\mathcal{I}\right) \propto \sqrt{\det F(\theta)}$ for some θ, then also $P\left(\vartheta|\mathcal{I}\right) \propto \sqrt{\det F(\vartheta)}$ for some transformed parameters $\vartheta(\theta)$.

4.2.3 Hypothesis testing

The problem of hypothesis testing, or, more specifically, of *binary hypothesis testing*, can be stated as the following question: When two hypotheses are given, which one provides a better fit to the data?

In the Bayesian approach, hypothesis testing can be stated extremely simply as the computation of a single quantity: The ratio of probabilities between the competing hypotheses. Traditionally, due to the usage in betting, this is also referred to as their relative *odds* or *odds ratio*.

After measuring some data x, the *prior odds*

$$o_{12} \equiv \frac{P\left(\mathcal{H}_1|\mathcal{I}\right)}{P\left(\mathcal{H}_2|\mathcal{I}\right)}\tag{4.12}$$

are updated to the *posterior odds*

$$O_{12} \equiv \frac{P\left(\mathcal{H}_1|x,\mathcal{I}\right)}{P\left(\mathcal{H}_2|x,\mathcal{I}\right)} = o_{12}\,\frac{P\left(x|\mathcal{H}_1,\mathcal{I}\right)}{P\left(x|\mathcal{H}_2,\mathcal{I}\right)} = o_{12}\,B_{12}\;,\tag{4.13}$$

where B_{12} is often called the *Bayes factor* between the two hypotheses and corresponds simply to the likelihood ratio

$$B_{12} \equiv \frac{P\left(x|\mathcal{H}_1,\mathcal{I}\right)}{P\left(x|\mathcal{H}_2,\mathcal{I}\right)}\;.\tag{4.14}$$

Hence, the Bayes factor tells us directly how much more likely (or unlikely) $\mathcal{H}_1$ has become in contrast to $\mathcal{H}_2$ by virtue of the data, and O_{12} gives the best current estimate of which hypothesis should be preferred.

The machinery and formalism for hypothesis testing is thus very simple; all the real work lies in formalising the competing hypotheses and their respective likelihoods, in the honest and comprehensive compilation of priors and in the actual likelihood computations. This approach also remains valid for *composite hypotheses*, with model functions depending on some parameters θ. If the likelihood under $\mathcal{H}(\theta)$ for fixed θ is $P\left(x|\mathcal{H}(\theta),\mathcal{I}\right)$, then the likelihood for the composite hypothesis $\mathcal{H}$ is given by a *marginalisation* integral

$$P\left(x|\mathcal{H},\mathcal{I}\right) = \int P\left(x,\theta|\mathcal{H},\mathcal{I}\right)\,\mathrm{d}\theta = \int P\left(x|\mathcal{H}(\theta),\mathcal{I}\right)\,P\left(\theta|\mathcal{H},\mathcal{I}\right)\,\mathrm{d}\theta\;.\tag{4.15}$$

Likelihood computation can be very computationally expensive for real-world data analysis problems, especially for hypotheses with large parameter spaces.

4.3 Detection statistics and Neyman–Pearson optimality

A special case of binary hypothesis testing is the so-called *detection problem*. In the simplest and, at the same time, most idealised case, there is a data set x, a *noise hypothesis* corresponding to a model including all sources of instrumental and physical noise, and a *signal hypothesis* for a tentative signal, which is often a composite hypothesis depending on some parameters.

In this thesis, I am mostly concerned with the detection problem for continuous wave signals and not with more complicated forms of hypothesis testing with several competing signal hypotheses, nor with parameter estimation. Also, this work is not a fully Bayesian analysis, even though it starts from a Bayesian approach in Sec. 7. Instead, the Bayesian odds are used as a stepping stone to a more conventional, frequentism-compatible quantity: a *detection statistic*.

In general, any scalar, orderable quantity computed from the data could be used as a detection statistic. In this sense, the concept is very similar to a *ranking statistic*, with the common understanding that a ranking statistic is an ordered set of integers, whereas a detection statistic could have any arbitrary scaling. The main criterion for a "good" detection statistic in a frequentist sense is that, over many random trials, it should yield a clear separation of noise and signal candidates.

In a practical frequentist approach, a detection statistic can be defined by any ad-hoc method. There are two fundamentally different classes: either the statistic is a function of the data only, and therefore only measures how much of an *outlier* any given data point is from the expected noise distribution; or the statistic also depends on the signal model parameters. I will mostly refer to the latter approach from now on, which usually is computationally expensive, but more informative.

The general problem of constructing a detection statistic consists in finding a one-dimensional function which is a projection of the full noise-and-signal parameter space, but with the detection-statistic values from the two different populations separating as neatly as possible. This would allow to put a *threshold* value on the detection statistic so that most signals fall above and most noise events fall below it.

To formally discuss the performance of a detection statistic $S(x)$, when drawing candidates from a noise distribution (written as $x \sim \mathcal{N}$) and a signal distribution ($x \sim \mathcal{S}$), a *false-alarm probability* associated with a threshold S_{thr} can be defined as

$$p_{\mathrm{FA}} \equiv P\left(S(x) > S_{\mathrm{thr}} | x \sim \mathcal{N}\right) , \qquad (4.16)$$

and a *detection probability* as

$$p_{\mathrm{det}} \equiv P\left(S(x) > S_{\mathrm{thr}} | x \sim \mathcal{S}\right) . \qquad (4.17)$$

A detection statistic $S(x)$ is considered *optimal* if, out of all possible statistics $\{S'(x)\}$, it has the highest p_{det} at a given value of p_{FA}. It may happen that there is a globally

optimal statistic, i.e. that $p_{\text{det}}(p_{\text{FA}})$ for a given $S(x)$ is higher than for all other $S'(x)$ over the whole p_{FA} range, but in general this is not guaranteed and optimality must be stated at a fixed p_{FA}. This criterion is called *Neyman-Pearson optimality* after its introduction by Neyman & Pearson (1933).

The function $p_{\text{det}}(p_{\text{FA}})$ is also commonly called a *ROC*, standing for either *receiver-operating characteristic* or *receiver-operator characteristic*, depending on the source. This name derives from the field of radar engineering, where the $p_{\text{det}}(p_{\text{FA}})$ of airplane and ship detection by radar receivers was considered.

4.4 Likelihood-ratio test

In a detection problem for two simple signal and noise hypotheses, without free parameters, the Neyman-Pearson criterion can be used to show that an optimal statistic is given by a *likelihood-ratio test* between the two hypotheses (see Sec. 3.3 and Appendix B of JK09 and references therein). It therefore agrees with the Bayesian approach from Sec. 4.2.3. Instead of the likelihood ratio Λ itself, which is simply equivalent to the Bayes factor from Eq. (4.14), often the log-likelihood ratio $\log \Lambda$ is used.

From now on, I assume that the data set is a time series $x(t)$ consisting of additive contributions from zero-mean Gaussian noise and from a deterministic signal,

$$x(t) = n(t) + s(t) \,, \tag{4.18}$$

and that it is measured over an interval of $t \in [0, T]$.

A general expression for the log-likelihood ratio follows (see Sec. 3.4.1 of JK09), via the theory of Gaussian stochastic processes (see Sec. V of Lifshits 2012), from a general result of measure theory, the *Cameron-Martin formula* (Cameron & Martin 1944):

$$\log \Lambda(x) = \int_0^T q(t)\, x(t)\, \mathrm{d}t \,-\, \frac{1}{2} \int_0^T q(t)\, s(t)\, \mathrm{d}t \,, \tag{4.19}$$

where $q(t)$ is a function solving the integral equation

$$s(t) = \int_0^T \kappa(t, t')\, q(t')\, \mathrm{d}t' \,, \tag{4.20}$$

which contains the *auto-correlation function*

$$\kappa(t, t') \equiv E\left[n(t)\, n(t')\right] \,. \tag{4.21}$$

As the second term in Eq. (4.19) does not depend on individual noise realisations $n(t)$, a likelihood-ratio-test statistic is given by just

$$G(x) \equiv \int\limits_0^T q(t)\, x(t)\, \mathrm{d}t \; . \tag{4.22}$$

Under the additional assumption that the noise is stationary and therefore the auto-correlation is translation-invariant,

$$\kappa(t, t') = \kappa(t - t')\,, \tag{4.23}$$

the solution of Eq. (4.20) is easily given in the Fourier domain as

$$\widetilde{q}(f) = \begin{cases} 2\, \dfrac{\widetilde{s}(f)}{S(f)} & \text{for } f \geq 0\,, \\[2mm] 2\, \dfrac{\widetilde{s}(f)}{S(-f)} & \text{for } f < 0\,, \end{cases} \tag{4.24}$$

with the *single-sided noise power spectral density* (PSD) given by

$$S(f) \equiv 2 \int\limits_{-\infty}^{\infty} \kappa(\tau)\, \mathrm{e}^{-2\pi \mathrm{i} f \tau}\, \mathrm{d}\tau \; . \tag{4.25}$$

Alternatively, the power spectrum can be defined by the second-order expectation of the Fourier-transformed noise,

$$\frac{1}{2} S(|f|)\, \delta(f - f') = E\left[\widetilde{n}(f)\widetilde{n}^*(f')\right] \; . \tag{4.26}$$

The equivalence of these two definitions is a special case of the *Wiener-Khintchine theorem* (Wiener 1930, Khintchine 1934).

For a time series as in Eq. (4.18), inserting Eq. (4.24) into Eq. (4.19) and using a scalar product on the time-series space defined by

$$\langle x\,|y \rangle \equiv 4\Re \int_0^{\infty} \frac{\widetilde{x}(f)\, \widetilde{y}^*(f)}{S(f)}\, \mathrm{d}f \; , \tag{4.27}$$

a simple result follows for the log-likelihood ratio of signal and noise hypotheses:

$$\log \Lambda(x) = \langle x\,|s \rangle - \frac{1}{2}\, \langle s\,|s \rangle \; . \tag{4.28}$$

This is also often referred to as "matched filtering", since a detection statistic can also be considered as applying a linear-filter operator to the input data, and an optimal statistic corresponds to a filter that maximises the SNR of the transformed output. Through the scalar products, $\log \Lambda(x)$ tests for the "match" between signal model and data. This approach is discussed in Sec. 3.4.3 of JK09.

Adapting the likelihood-ratio test for composite hypotheses $\mathcal{H}(\theta)$ poses a problem in a classical frequentist approach, as the optimality proofs only work for simple hypotheses. A standard solution is *maximum-likelihood estimation*, where the likelihood function $P(x|\mathcal{H}(\theta),\mathcal{I})$ is *maximised* over all parameters θ and the likelihood ratio at this point is used as a detection statistic.

As we have seen in Sec. 4.2.3, the Bayesian approach is completely general when it comes to composite hypothesis, and due to marginalisation over all possible θ can sometimes outperform a maximum-likelihood statistic. When the priors accurately match the actual noise and signal distributions – which of course can only be tested for sure in simulated data sets, often referred to as *Monte-Carlo studies* – the marginalised Bayes factor still gives a Neyman-Pearson optimal statistic. For the specific case of GW data analysis, this point is discussed by Searle (2008) and Prix & Krishnan (2009).

4.5 Detection of quasi-periodic signals

As discussed, for example, in chapters 3 and 4 of JK09, the likelihood-ratio test translates well to such diverse signal types as the "chirped" GW waveform of inspiralling binaries (see Sec. 2.5.1) and stochastic signals. However, in this thesis I am only interested in the detection of *quasi-periodic* signals in time series, for which an extensive discussion based on Bayesian methods is given by Bretthorst (1988). This is also called the problem of *spectral estimation* or *spectral analysis*. For a historical perspective, see Sec. 1.1 of Bretthorst (1988) and the more extensive reviews by Robinson (1982) and Marple (1987).

Most approaches to spectral analysis rely, in one way or the other, on the *Fourier transform*. In its continuous version, it gives the relation between the PSD and auto-correlation function of the noise time series, as in Eq. (4.25). For discretely sampled time series, a *discrete Fourier transform* (DFT) can be used., for which efficient numerical methods exist (the *Fast Fourier Transform*, FFT, popularised by Cooley & Tukey 1965). A simple estimator for the power spectrum of a time series $x(t)$ sampled at N_{samples} points t_n in time is given by the periodogram (Schuster 1898)

$$\widehat{S}(f) \equiv \frac{1}{N_{\text{samples}}} \left| \sum_{n=1}^{N_{\text{samples}}} x(t_n) \, \mathrm{e}^{\mathrm{i} f t_n} \right|^2 \tag{4.29}$$

Peaks of the periodogram can be considered as estimators for signal frequencies in the data. However, this is an *optimal* estimator only under certain conditions, listed in Sec. 2.3 of Bretthorst (1988). Problems with this simple approach occur especially for data sets with non-uniform sampling, a small number of samples, non-Gaussian components or multiple signals.

Classical frequentist modifications to the periodogram include the use of *windowing* (Blackman & Tukey 1958, Harris 1978) or *(multi-)tapering* (Thomson 1982) of the data,

or methods such as the Lomb-Scargle periodogram (Lomb 1976, Scargle 1982). Extensive studies of this problem, focussing on astronomical applications, were conducted by Scargle (1981, 1982, 1989, 1990, 1998).

A Bayesian approach, as presented in Bretthorst (1988), allows to rediscover the periodogram as a frequency estimator, but also to find much more general results, making some of the existing frequentist machinery seem superfluous. However, in many cases of practical application, it is still considered a more robust approach to combine a detection statistic, derived either from a maximum-likelihood or a Bayesian approach, with some classical tools, such as windowing.

For a time series with multiple signals at well-separated frequencies (with respect to the sampling rate of the data), it makes sense intuitively that these can be studied by separating the data into frequency bands and doing separate analyses under the assumption of a single signal. In a rigorous Bayesian formulation, this rule was shown by Jaynes (1987) and is discussed further in chapter 6 of Bretthorst (1988). Continuous-wave data analysis (see Sec. 5) routinely makes use of this property, as it seems very unlikely that two detectable CW sources could be nearby in frequency.

4.6 Probability distributions

In this thesis, I will mostly work with continuous probability distributions. And among these, two famous distributions occur quite often. For reference, I will state here their distribution functions and lower-order moments, along with a brief description of their occurrences and importance.

4.6.1 Gaussian distribution

The *Gaussian* or *normal distribution* is part of the large *exponential family* of probability distributions. Written as

$$p_{\mathcal{N}}(x) \equiv \frac{1}{\sigma\sqrt{2\pi}}\, e^{-\frac{(x-\mu)^2}{2\sigma^2}}\,, \tag{4.30}$$

it is completely defined by its first two moments, the mean of the distribution μ and the variance σ^2. For a random variable A drawn from such a Gaussian distribution, it is customary to write $A \sim \mathcal{N}(\mu, \sigma)$.

The Gaussian distribution is ubiquitous in practical data analysis because of the *central limit theorem*, which in one of its simpler forms tells us that the distribution of any observable which is the sum of sufficiently many independent random variables (from arbitrary distributions) tends towards a Gaussian. It is also special from the point of view of inference as the natural choice when the knowledge about a distribution cannot reasonably be constrained beyond its mean and variance. See Secs. 7.6 and 11 of Jaynes (2003) for a "maximum entropy" justification of this principle.

4.6.2 χ^2-distribution

Another rather simple member of the exponential family is the χ^2-*distribution*, named after the usage by Pearson (1900) in hypothesis testing. In general, the χ^2-distribution pertains to any random variable A which is the sum of k squares of independently Gaussian-distributed variables $\{A_i\}$:

$$A = \sum_{i=1}^{k} \left(\frac{A_i}{\sigma_i} \right)^2 \quad \text{with} \quad A_i \sim \mathcal{N}(0, \sigma_i) \quad \Rightarrow A \sim \chi_k^2 \,. \tag{4.31}$$

Hence, $p(x) = \chi_k^2(x)$ for a χ^2-distributed variable is defined only for $x \geq 0$, and reads

$$\chi_k^2(x) \equiv \frac{x^{\frac{k}{2}-1} \, \mathrm{e}^{-\frac{x}{2}}}{2^{\frac{k}{2}} \, \Gamma\left(\frac{k}{2} \right)} \,. \tag{4.32}$$

The parameter k is called the number of *degrees of freedom* of the distribution. The expectation of a random variable $A \sim \chi_k^2$ is simply $\mu_A = k$ and the variance is $\sigma_A^2 = 2k$. Higher moments also have simple expressions, but will not be needed in this thesis.

An important generalisation is the *non-central χ^2-distribution*, contrasted to the *central* distribution of Eq. (4.32). Here, the Gaussian variables are allowed to have different and non-zero means:

$$A = \sum_{i=1}^{k} \left(\frac{A_i}{\sigma_i} \right)^2 \quad \text{with} \quad A_i \sim \mathcal{N}(\mu_i, \sigma_i) \quad \Rightarrow A \sim \chi_k^2(\lambda) \,. \tag{4.33}$$

The distribution now has two parameters, the degrees of freedom k as before, and also the *non-centrality parameter*

$$\lambda \equiv \sum_{i=1}^{k} \left(\frac{\mu_i}{\sigma_i} \right)^2 \,. \tag{4.34}$$

The mean of $A \sim \chi_k^2(\lambda)$ is $\mu_A = k + \lambda$, the variance is $\sigma_A^2 = 2k + 4\lambda$ and the full distribution function is

$$\chi_k^2(x, \lambda) \equiv \frac{1}{2} \, \mathrm{e}^{-\frac{x+\lambda}{2}} \left(\frac{x}{\lambda} \right)^{\frac{k}{4}-\frac{1}{2}} I_{\frac{k}{2}-1} \left(\sqrt{\lambda x} \right) \,, \tag{4.35}$$

with the modified Bessel function

$$I_\alpha(x) \equiv \sum_{m=0}^{\infty} \frac{1}{m! \, \Gamma(\alpha + m + 1)} \left(\frac{x}{2} \right)^{\alpha + 2m} \,. \tag{4.36}$$

Both variants of χ^2-distributions tend towards a Gaussian for large k, due to the central limit theorem.

5 Continuous-Wave data analysis

While the later parts of this thesis are concerned with a particular advancement in the field of Continuous Wave (CW) data analysis, this chapter should serve as a brief summary of basic concepts and of the state of the art in the field. It is by no means an exhaustive survey, and more ambitious reviews can be found in JK09, Prix (2009) and Jaranowski & Królak (2012).

Many of these concepts were pioneered by Jaranowski, Królak & Schutz (1998), which I will refer to as JKS98 from now on. However, my notation mostly follows the more recent conventions of Cutler & Schutz (2005) and Prix (2007b, 2011b).

The focus of this thesis is on CWs from isolated neutron stars (NSs). For extensions to CWs from NSs in binary systems, see Dhurandhar & Vecchio (2001), Goetz & Riles (2011) and Aasi et al. (2014d).

As the input data set, I always consider a time series of properly calibrated (Abadie et al. 2010a) GW strain from one or more detectors, often referred to as $h(t)$ in the literature. For a single detector, I write this as $x^X(t)$, where the index X indicates the detector. In most cases, I will omit the time dependence.

For multi-detector quantities, I use boldface, so that $\boldsymbol{x}(t)$ is the multi-detector vector of time-series data, $\{\boldsymbol{x}(t)\}^X = x^X(t)$. For example, for two detectors $X \in \{\mathrm{H1, L1}\}$:

$$\boldsymbol{x}(t) \equiv \begin{pmatrix} x^{\mathrm{H1}}(t) \\ x^{\mathrm{L1}}(t) \end{pmatrix} . \tag{5.1}$$

The measured detector strain can be written in terms of a noise and a signal contribution,

$$\boldsymbol{x}(t) = \boldsymbol{n}(t) + \boldsymbol{s}(t) . \tag{5.2}$$

In this chapter, I will first describe the standard Gaussian noise model for $\boldsymbol{n}(t)$ in Sec. 5.1 and possible parametrisations for a CW signal model, $\boldsymbol{s}(t)$, in Sec. 5.2. After the introduction of some technical concepts in Secs. 5.3–5.6, the central part consists of the description of the standard detection statistic for CW searches, the $\mathcal{F}$-statistic, in Sec. 5.7.

Further useful concepts are the notion of a metric on the signal-parameter space, see Sec. 5.8, and various optimisations and generalisations for $\mathcal{F}$-statistic-based searches, described in Secs. 5.9 and 5.10. I conclude this chapter with brief descriptions of the CW data-analysis software package `LALSuite` in Sec. 5.11 and the distributed computing project Einstein@Home in Sec. 5.12.

5.1 Gaussian noise model

As described in Sec. 2.6.2, ground-based laser-interferometric GW detectors, such as LIGO, are subject to a variety of noise sources. The total effect of these contributions, in the absence of a signal, is usually well-described by a simple Gaussian distribution. Strong disturbances are typically well constrained in either time or frequency, so that the Gaussian approximation holds well for the majority of the time-frequency plane.

For CW data analysis, which is concerned with long-duration data sets (from days up to years), transient disturbances are less of a problem. However, narrow-band disturbances that are persistent over long time-scales and that stay in the same frequency region, i.e. *lines* in the sense of Sec. 6.1, reduce the applicability of the Gaussianity assumption for a CW analysis. See Sec. 6.4 for an estimation of the ratio of disturbed to undisturbed bands in recent LIGO data, all of Sec. 6 for a general discussion of the problem of lines, and the remainder of this thesis for a proposal on how to improve data analysis in their presence. For the rest of this chapter, I will concentrate on the more common case of Gaussian or nearly-Gaussian frequency bands.

For a more quantitative justification of the Gaussian noise assumption, see for example Fig. 3 of Abbott et al. (2004b), Fig. 3 of Aasi et al. (2013b) and the detailed discussion of statistical expectations for a search on LIGO S5 data in Sec. 5.8 of Behnke (2013).

A Gaussian distribution, as defined in Sec. 4.6.1, is fully described by its mean and variance. For zero-mean strain data, it is sufficient to specify the standard deviation σ of the distribution, which is directly related to the single-sided *power-spectral density* (PSD) $\mathcal{S}$, for a frequency band of width Δf and a sampling rate Δt, by

$$\mathcal{S} = \frac{\sigma^2}{\Delta f} = 2\sigma^2 \Delta t \,. \tag{5.3}$$

Gaussian noise data is then described by $\boldsymbol{x}(t) = \boldsymbol{n}(t)$ with samples $\boldsymbol{n}_i \sim \mathcal{N}(0, \sigma)$.

Requiring only stationary noise (for example, by considering a single *short Fourier transform*, see Sec. 5.3), but still allowing for arbitrary correlations between detectors, the (single-sided) noise PSD can be expressed as a $N_{\mathrm{det}} \times N_{\mathrm{det}}$ matrix S^{XY} defined, similarly to Eq. (4.25), by

$$S^{XY}(f) \equiv 2 \int_{-\infty}^{\infty} \kappa^{XY}(\tau) \, \mathrm{e}^{-2\pi \mathrm{i} f \tau} \mathrm{d}\tau \,, \tag{5.4}$$

where

$$\kappa^{XY}(\tau) \equiv E\left[n^X(t+\tau) \, n^Y(t) \right] \tag{5.5}$$

is the correlation matrix of the per-detector noise time-series.

It is possible to estimate the noise PSD as a free parameter alongside the main signal detection and parameter estimation steps of a data-analysis pipeline, as described in Chapter 4 of Bretthorst (1988). However, as in most of the CW data-analysis literature,

I will assume from now on that the noise PSD has already been estimated *before* any hypothesis test. This is usually done with a running-median estimator, which I will describe in Sec. 5.4.

Adapting Eq. (4.27) to the multi-detector time-series space, and assuming a finite observation time T, yields a scalar product

$$\langle \boldsymbol{x} \,|\, \boldsymbol{y} \rangle \equiv 4\Re \sum_{X=1}^{N_{\text{det}}} \sum_{Y=1}^{N_{\text{det}}} \int_0^T \tilde{x}^X(f)\, S_{XY}^{-1}(f)\, \tilde{y}^{Y*}(f)\, \mathrm{d}f \;, \tag{5.6}$$

with Fourier-transformed $\tilde{x}^X(f)$, $\tilde{y}^X(f)$, inverse matrix $S_{XY}^{-1}(f)$ to $S^{XY}(f)$.

Assuming uncorrelated noise for the individual detectors X, the cross-terms in $S^{XY}(f)$ vanish, leaving only the per-detector spectra $S^X(f)$. Usually, one considers narrow frequency bands, or scalar products where at least one of the time series is a narrow signal or disturbance. In such cases, the frequency-dependent variation of the "coloured" noise spectra $S^X(f)$ is negligible, so that constant values S^X can be assumed. The scalar product then simplifies, approximately, to the following time-domain integral:

$$\langle \boldsymbol{x} \,|\, \boldsymbol{y} \rangle \approx 2 \sum_{X=1}^{N_{\text{det}}} \frac{1}{S^X} \int_0^T x^X(t)\, y^X(t)\, \mathrm{d}t \;. \tag{5.7}$$

5.2 CW signal model

In Sec. 2.3, we have seen that a weak and monochromatic gravitational wave, expressed in the TT gauge and in a coordinate system where the z direction coincides with the wave's propagation direction, is fully described by only two components, h_+ and $h_\times$. Now we are interested not only in the instantaneous passage of a short GW, but in the continuous observation of a CW signal. Hence, we have to take into account the possible amplitude and frequency modulations from the source evolution and from the relative motion of source and detector, so that the amplitudes and phases of the induced strain in the detector are modulated.

5.2.1 Reference frames and geometry

The full specification of a CW model function requires several geometrical ingredients. Most of the quantities introduced in this section are also illustrated in Fig. 5.1. Additional details can be found, for example, in Sec. 1 of Prix (2011b).

First, consider a reference frame fixed in the *solar system barycentre* (SSB), given by an orthonormal set of vectors $\{\widehat{x}, \widehat{y}, \widehat{z}\}$ corresponding to the *equatorial coordinate system*. I then denote the wave-propagation direction as $-\widehat{n}$ for a unit vector $\widehat{n}$ pointing from the
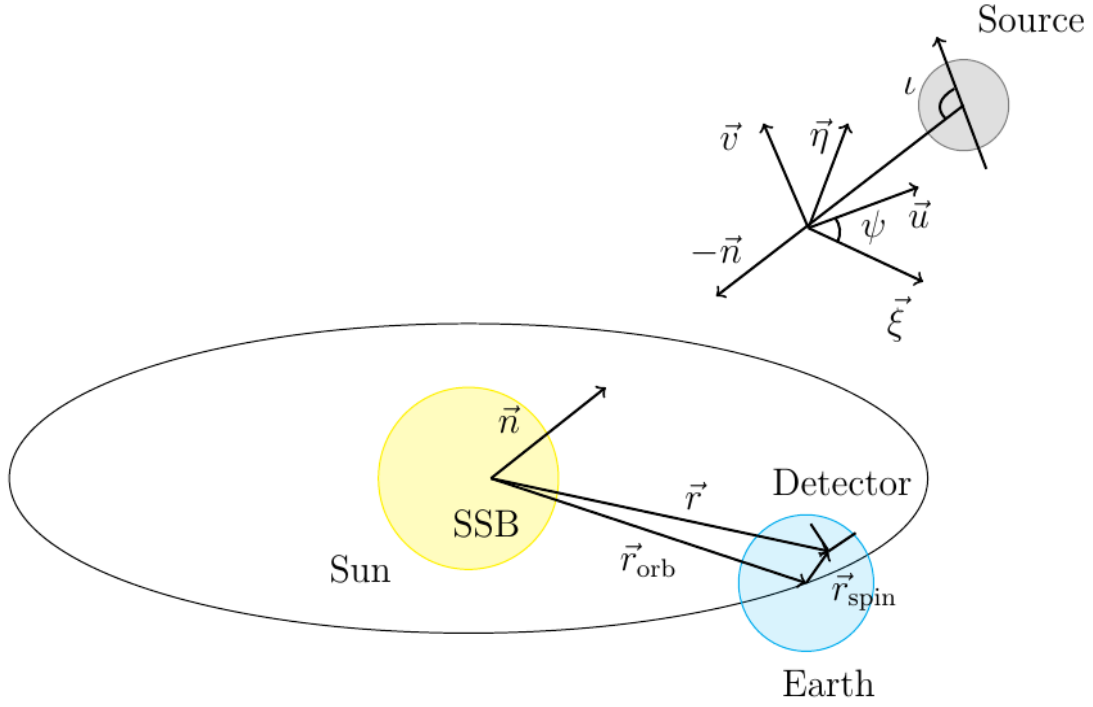
Figure 5.1: Illustration of the SSB, detector, source and wave frames. In addition to the definitions in Sec. 5.2.1, here ι is the inclination angle of the source against the line of sight, and the vector $\vec{r}$ pointing from the SSB to the detector has been decomposed into orbital and spin components.
Figure credit: M. Shaltev (2013).

SSB to the source location. In terms of the equatorial *right ascension* α and *declination* δ of the source, this vector reads:

$$\widehat{n} = \begin{pmatrix} \cos\delta\cos\alpha \\ \cos\delta\sin\alpha \\ \sin\delta \end{pmatrix} . \tag{5.8}$$

A full *wave-frame* basis is given by $\{\widehat{u}, \widehat{v}, -\widehat{n}\}$, where the vectors $\widehat{u}$ and $\widehat{v}$ span a plane transversal to the wave propagation. They also define a tensorial *polarisation basis* for elliptically-polarised GWs, in analogy with Eq. (2.13):

$$e_+ \equiv \widehat{u} \otimes \widehat{u} - \widehat{v} \otimes \widehat{v} \tag{5.9a}$$
$$e_\times \equiv \widehat{u} \otimes \widehat{v} + \widehat{v} \otimes \widehat{u}. \tag{5.9b}$$

Additionally, a polarisation-independent reference frame in the wave plane is $\{\widehat{\xi}, \widehat{\eta}, -\widehat{n}\}$

Figure 5.2: Definition of the polarisation angle ψ in relation to the wave-plane bases $\{\widehat{u}, \widehat{v}\}$ and $\{\widehat{\xi}, \widehat{\eta}\}$.
Figure credit: J. Whelan.
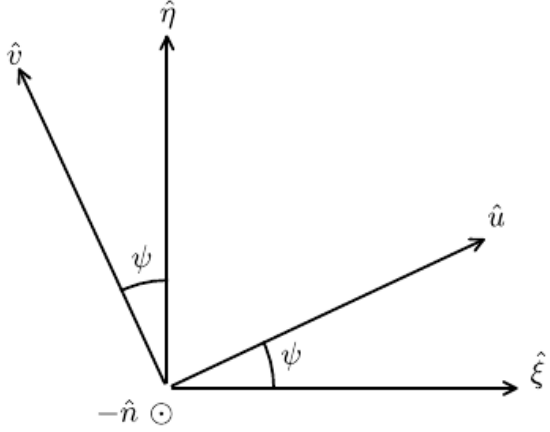
with vectors

$$\widehat{\xi} \equiv \frac{\widehat{n} \times \widehat{z}}{|\widehat{n} \times \widehat{z}|}, \tag{5.10a}$$

$$\widehat{\eta} \equiv \widehat{\xi} \times \widehat{n}, \tag{5.10b}$$

so that $\widehat{\xi}$ is in the equatorial plane and $\widehat{\eta}$ points northwards. These define a second polarisation basis,

$$\epsilon_+ \equiv \widehat{\xi} \otimes \widehat{\xi} - \widehat{\eta} \otimes \widehat{\eta} \tag{5.11a}$$

$$\epsilon_\times \equiv \widehat{\xi} \otimes \widehat{\eta} + \widehat{\eta} \otimes \widehat{\xi}. \tag{5.11b}$$

These wave-plane frames are related by a *polarisation angle* ψ, also illustrated in Fig. 5.2:

$$\sin \psi = \widehat{u} \cdot \widehat{\eta}. \tag{5.12}$$

We also introduce a *detector tensor* d^X depending on the orientation of the detector arms. For an interferometer with arms along the unit vectors $\widehat{l}_1$ and $\widehat{l}_2$, it is given by

$$d^X = \frac{1}{2} \left(\widehat{l}_1 \otimes \widehat{l}_1 - \widehat{l}_2 \otimes \widehat{l}_2 \right). \tag{5.13}$$

When a given wave-front arrives at the position $\vec{r}^X(t)$ of detector X at time t, the *timing relation* for its arrival-time $\tau^X(t)$ at the SSB is given, in first-order Newtonian approximation, by

$$\tau^X(t) \approx t + \frac{\widehat{n} \cdot \vec{r}^X(t)}{c}. \tag{5.14}$$

This transformation, also called the *Rømer delay*, is the basis of *barycentring*, which is the process of translating the measured time series from the detector frame to the SSB. For the full relation, including relativistic terms, see for example the brief discussion in Sec. IV.A of Abbott et al. (2007a), chapter 5 of JK09 as well as a classical reference from the field of radio-pulsar data analysis, Taylor & Weisberg (1989).

5.2.2 Signal waveform and phase-evolution model

If the GW wavelength ℓ is large compared to the detector arm-length, $\ell \gg 2\pi L$, the general plane-wave solution from Eq. (2.12) can be translated into a strain at the detector written as a contraction of the metric perturbation with the detector tensor:

$$h^X(t) = d^X_{ij}(t) \, h^{ij}(\tau^X) = F^X_+(t) \, h_+(\tau^X) + F^X_\times(t) \, h_\times(\tau^X) \,, \tag{5.15}$$

where the *beam-pattern functions* $F^X_+(t)$ and $F^X_\times(t)$ can be expressed in either of the two wave-plane polarisation bases (Eqs. (5.9) and (5.11)) as

$$F^X_+(t,\widehat{n},\psi) \equiv d^X_{ij}(t) \, e^{ij}_+(\widehat{n}) = a^X(t,\widehat{n}) \cos(2\psi) + b^X(t,\widehat{n}) \sin(2\psi) \,, \tag{5.16a}$$

$$F^X_\times(t,\widehat{n},\psi) \equiv d^X_{ij}(t) \, e^{ij}_\times(\widehat{n}) = b^X(t,\widehat{n}) \cos(2\psi) - a^X(t,\widehat{n}) \sin(2\psi) \,, \tag{5.16b}$$

with the *antenna-pattern functions* $a^X(t,\widehat{n})$ and $b^X(t,\widehat{n})$, which I will discuss in more detail in Sec. 5.6, giving the source-location dependence of the detector response:

$$a^X(t,\widehat{n}) \equiv d^X_{ij}(t) \, \epsilon^{ij}_+(\widehat{n}) \,, \tag{5.17a}$$

$$b^X(t,\widehat{n}) \equiv d^X_{ij}(t) \, \epsilon^{ij}_\times(\widehat{n}) \,, \tag{5.17b}$$

Note that Eq. (5.15) is completely general and not limited to CW signals: $h_+(\tau^X)$ and $h_\times(\tau^X)$ could be arbitrary functions. However, I will now specialise to CW waveforms, which can be expressed, in SSB time τ, as

$$h_+(\tau) \equiv A_+ \cos \Phi(\tau) \,, \tag{5.18a}$$

$$h_\times(\tau) \equiv A_\times \sin \Phi(\tau) \,, \tag{5.18b}$$

with a phase-evolution model $\Phi(\tau)$ related to the frequency evolution of the source:

$$\Phi(\tau) = \phi_0 + 2\pi \int_{\tau_{\mathrm{ref}}}^{\tau} f(\tau') \, \mathrm{d}\tau' \,, \tag{5.19}$$

with $\phi_0 \equiv \Phi(\tau_{\mathrm{ref}})$ at an arbitrary *reference time* τ_{ref}. For a typical CW signal with slowly-varying frequency, it can be Taylor-expanded around τ_{ref}:

$$\Phi(\tau) = \phi_0 + 2\pi \sum_{s=0}^{s_{\mathrm{max}}} \frac{f^{(s)}(\tau_{\mathrm{ref}})}{(s+1)!} (\tau - \tau_{\mathrm{ref}})^{s+1} \,. \tag{5.20}$$

The expansion coefficients are the frequency and *spin-down parameters* at τ_{ref},

$$f^{(s)}(\tau_{\mathrm{ref}}) \equiv \left. \frac{\mathrm{d}^s f(\tau)}{\mathrm{d}\tau^s} \right|_{\tau_{\mathrm{ref}}} \,. \tag{5.21}$$

For the lowest-order spin-downs, in the following I also use the shorthands

$$\dot{f} \equiv f^{(1)} \,, \quad \ddot{f} \equiv f^{(2)} \,, \quad \text{and} \quad \dddot{f} \equiv f^{(3)} \,. \tag{5.22}$$

Note that the phase model in Eq. (5.20) is given in the SSB reference frame, whereas for each detector the data is a time series sampled according to the detector-frame time. From the barycentring relation, Eq. (5.14), we see that the translation depends on the sky location of the source, so that the full phase-evolution model is determined by a set $\lambda = \{\alpha, \delta, \{f^{(s)}(\tau_{\mathrm{ref}})\}_{s=0}^{s_{\max}}\}$ of $2 + 1 + s_{\max}$ parameters.

5.2.3 Signal amplitude and JKS factorisation

Now that we have a phase-evolution model, let us consider the *amplitude* of the measured strain $h^X(t)$. As seen from Eqs. (5.15)–(5.18), it depends on four *amplitude parameters*: the polarisation angle ψ, the reference phase ϕ_0 and the coefficients for the two polarisation components, A_+ and $A_\times$. To be more physically explicit, the latter two can be replaced by the scalar signal amplitude h_0 from Eq. (2.20) and the *inclination angle* ι of a triaxial NS with respect to the line of sight:

$$A_+ = h_0(1 + \cos^2 \iota)\,, \tag{5.23a}$$
$$A_\times = h_0 \cos \iota\,. \tag{5.23b}$$

While the full expressions for $h(t)$ in either of these parametrisations are not particularly edifying, JKS98 introduced a particular reparametrisation $\mathcal{A}^\mu = \mathcal{A}^\mu(h_0, \cos \iota, \psi, \phi_0)$, with $\mu = 1 \ldots 4$, that allows for an elegant factorised form for Eq. (5.15):

$$\boldsymbol{h}(t, \mathcal{A}, \lambda) = \mathcal{A}^\mu \, \boldsymbol{h}_\mu(t, \lambda)\,, \tag{5.24}$$

using automatic summation convention over repeated amplitude indices μ. This is often referred to as the *JKS factorisation*.

The four new amplitude parameters $\mathcal{A}^\mu$ are related to the physical source parameters by

$$A^1 \equiv A_+ \cos \phi_0 \cos 2\psi - A_\times \sin \phi_0 \sin 2\psi\,, \tag{5.25a}$$
$$A^2 \equiv A_+ \cos \phi_0 \sin 2\psi + A_\times \sin \phi_0 \cos 2\psi\,, \tag{5.25b}$$
$$A^3 \equiv -A_+ \sin \phi_0 \cos 2\psi - A_\times \cos \phi_0 \sin 2\psi\,, \tag{5.25c}$$
$$A^4 \equiv -A_+ \sin \phi_0 \sin 2\psi + A_\times \cos \phi_0 \cos 2\psi\,, \tag{5.25d}$$

and for each detector the basis functions are given by

$$h_1^X(t) \equiv a^X(t) \cos \phi(\tau^X - \tau_{\mathrm{ref}})\,, \tag{5.26a}$$
$$h_2^X(t) \equiv b^X(t) \cos \phi(\tau^X - \tau_{\mathrm{ref}})\,, \tag{5.26b}$$
$$h_3^X(t) \equiv a^X(t) \sin \phi(\tau^X - \tau_{\mathrm{ref}})\,, \tag{5.26c}$$
$$h_4^X(t) \equiv b^X(t) \sin \phi(\tau^X - \tau_{\mathrm{ref}})\,. \tag{5.26d}$$

5.3 Short Fourier Transforms

For most CW searches, the original strain data $\boldsymbol{x}(t)$ is converted into the frequency domain by the application of *Short-baseline Fourier Transforms*, or simply "Short Fourier Transforms" (SFTs). These are simply discrete Fourier transforms (DFTs) over a short baseline T_{SFT}, with a frequency resolution of $\delta f = 1/T_{\mathrm{SFT}}$. SFTs have the advantage that "narrow-band" subsets of the data, i.e. a limited frequency range Δf, can easily be extracted.

The use of SFTs was introduced by Schutz (1998), Schutz & Papa (1999) and Williams & Schutz (2000). When T_{SFT} is small enough, each SFT can be analysed coherently without "demodulation" for the effects of barycentring and intrinsic source spin-down.

However, the sensitivity of a CW search can be increased by longer *coherence* times, referring to the length for which consistent amplitude and phase-evolution parameters are required. Hence, many search algorithms coherently combine the information from a number N_{SFT} of SFTs. Many quantities, including the noise PSD $\mathcal{S}$, can be assumed as constant over the duration of each SFT. Indexing per-SFT quantities with α, the narrow-band scalar product from Eq. (5.7) can be generalised as

$$\langle \boldsymbol{x} \,|\, \boldsymbol{y} \rangle \approx 2 \sum_{X=1}^{N_{\mathrm{det}}} \sum_{\alpha=1}^{N_{\mathrm{SFT}}^X} \frac{1}{S_\alpha^X} \int_0^{T_{\mathrm{SFT}}} x_\alpha^X(t') \, y_\alpha^X(t') \, \mathrm{d}t' \;, \tag{5.27}$$

defining $x_\alpha^X(t') = x^X(t_\alpha + t')$ for SFTs starting at times t_α.

In searches for isolated NSs, typically $T_{\mathrm{SFT}} = 1800\,\mathrm{s}$ is chosen, whereas some binary searches use much shorter baselines. See Krishnan et al. (2004) and Sec. V.C of Abbott et al. (2007a) for a discussion of the unmodulated-search-per-SFT approach compared to longer coherence times, and for a motivation of the default value of $T_{\mathrm{SFT}} = 1800\,\mathrm{s}$.

SFTs are usually created from "science-quality" data only, i.e. from time stretches when no strong disturbances were found in the auxiliary channels and no other data-quality vetoes apply. The file format used for SFTs in the LIGO and Virgo collaborations is defined in Mendell (2002).

5.4 Noise-PSD estimation

To compute the scalar product from Eqs. (5.7) or (5.27), we need the noise PSDs S^X. In practice, an exact determination according to Eq. (5.4) is impossible, as an expectation value cannot be computed from a single data set. One possible solution, as mentioned in Sec. 5.1, is to consider the PSDs as additional free parameters of a Bayesian analysis. However, the more common approach is to include an explicit noise-estimation step in the search pipeline.

An average of $S^X(f)$ over the whole spectrum would be a bad choice, considering the obviously non-constant noise spectrum of LIGO as illustrated in Fig. 2.4. Instead, the method of choice is a *running-median estimator*, which only assumes that the PSD $S^X(f)$ at each frequency f can be reasonably well approximated by an average over a certain frequency interval around it. Using the median (instead of the arithmetic mean) and a sufficiently wide frequency interval allows for the suppression of narrow spectral features, which are expected from both CW signals and instrumental artefacts.

Formally, the estimator for $S^X(f)$ is defined through a *periodogram*, adapting Eq. (4.29) to SFT-based data:

$$\widehat{S}^X(f') \equiv \frac{1}{N_{\mathrm{SFT}}^X} \sum_{\alpha=1}^{N_{\mathrm{SFT}}^X} \frac{2\left|\tilde{x}_\alpha^X(f')\right|^2}{T_{\mathrm{SFT}}}, \tag{5.28}$$

The median is then computed over N_{rngmed} frequency bins, corresponding to a range $f' \in \left[f - \frac{N_{\mathrm{rngmed}}}{2T_{\mathrm{SFT}}}, f + \frac{N_{\mathrm{rngmed}}}{2T_{\mathrm{SFT}}}\right]$. Throughout this thesis, I use a running median window of $N_{\mathrm{rngmed}} = 101$ SFT bins, which at $T_{\mathrm{SFT}} = 1800\,\mathrm{s}$ corresponds to a band of $\approx 56\,\mathrm{mHz}$.

5.5 Noise weighting

The sensitivity of each detector varies over the length of a science run, and we only need to assume it to be approximately constant over each SFT. Furthermore, sensitivities can be different between detectors. Hence, any detection statistic computed from a coherent length longer than T_{SFT}, and from multiple detectors, may have contributions from SFTs with different S_α^X.

This effect can be naturally absorbed in our formalism by introducing *noise weights* for each detector X and SFT α, defined as

$$w_\alpha^X \equiv \frac{\mathcal{S}}{S_\alpha^X}. \tag{5.29}$$

In this definition, $\mathcal{S}$ could in principle be an arbitrary normalisation constant. However, noise weighting is especially useful when defining the weights in such a way that most quantities in sums and integrals are translated to numerically manageable scales. To achieve this, a normalisation constraint

$$\sum_{X=1}^{N_{\mathrm{det}}} \sum_{\alpha=1}^{N_{\mathrm{SFT}}^X} w_\alpha^X = \sum_{X=1}^{N_{\mathrm{det}}} N_{\mathrm{SFT}}^X = N_{\mathrm{SFT}} \tag{5.30}$$

fixes $\mathcal{S}$ to be the harmonic mean of the per-detector and per-SFT PSDs, which can be interpreted as the overall sensitivity of the data set:

$$\mathcal{S}^{-1} \equiv \frac{1}{N_{\mathrm{SFT}}} \sum_{X=1}^{N_{\mathrm{det}}} \sum_{\alpha=1}^{N_{\mathrm{SFT}}^X} (S_\alpha^X)^{-1}. \tag{5.31}$$

We can then define a noise-weighted time-average of any quantity Q:

$$\langle Q \rangle_{\mathrm{SFTs}} \equiv \frac{1}{N_{\mathrm{SFT}}} \sum_{X=1}^{N_{\mathrm{det}}} \sum_{\alpha=1}^{N_{\mathrm{SFT}}^X} w_\alpha^X \, Q_\alpha^X \, , \tag{5.32}$$

properly normalised so that $\langle 1 \rangle_{\mathrm{SFTs}} = 1$. The same normalisation convention is used for single-detector quantities Q^X in a multi-detector search:

$$\langle Q^X \rangle_{\mathrm{SFTs}} \equiv \frac{1}{N_{\mathrm{SFT}}^X} \sum_{\alpha=1}^{N_{\mathrm{SFT}}^X} w_\alpha^X \, Q_\alpha^X \, . \tag{5.33}$$

Using noise weights, the scalar product from Eq. (5.27) can be rewritten as

$$\langle \boldsymbol{x} \,|\, \boldsymbol{y} \rangle \approx \mathcal{S}^{-1} \sum_{X=1}^{N_{\mathrm{det}}} \sum_{\alpha=1}^{N_{\mathrm{SFT}}^X} w_\alpha^X \int_0^{T_{\mathrm{SFT}}} x_\alpha^X(t) \, y_\alpha^X(t) \, \mathrm{d}t \, . \tag{5.34}$$

5.6 Antenna patterns

An important quantity in CW data analysis is the *antenna-pattern matrix*

$$\mathcal{M}_{\mu\nu} \equiv \langle \boldsymbol{h}_\mu \,|\, \boldsymbol{h}_\nu \rangle \, , \tag{5.35}$$

where $\boldsymbol{h}_\mu = \{h_\mu^X\}$ are the basis functions from Eq. (5.26). $\mathcal{M}_{\mu\nu}$ can be considered as a *metric* on the space of amplitude parameters $\mathcal{A}^\mu$, or as their Fisher matrix (see Sec. 4.2.2), which I will show in Sec. 5.7.

For GWs with $f \gg 1/(1\,\mathrm{day})$, the antenna-pattern matrix is approximately given by

$$\mathcal{M}_{\mu\nu} \approx \mathcal{S}^{-1} T_{\mathrm{data}} \begin{pmatrix} A & C & 0 & 0 \\ C & B & 0 & 0 \\ 0 & 0 & A & C \\ 0 & 0 & C & B \end{pmatrix} , \tag{5.36}$$

where in the spirit of the previously introduced noise-weighting convention the common scaling factor $\mathcal{S}^{-1} T_{\mathrm{data}}$ was pulled out, with

$$T_{\mathrm{data}} \equiv T_{\mathrm{SFT}} N_{\mathrm{SFT}} = T_{\mathrm{SFT}} \sum_{X=1}^{N_{\mathrm{det}}} N_{\mathrm{SFT}}^X \tag{5.37}$$

denoting the total amount of data from all detectors. The quantities

$$A = \langle a^2 \rangle_{\mathrm{SFTs}} \, , \tag{5.38a}$$
$$B = \langle b^2 \rangle_{\mathrm{SFTs}} \, , \tag{5.38b}$$
$$C = \langle a\,b \rangle_{\mathrm{SFTs}} \tag{5.38c}$$
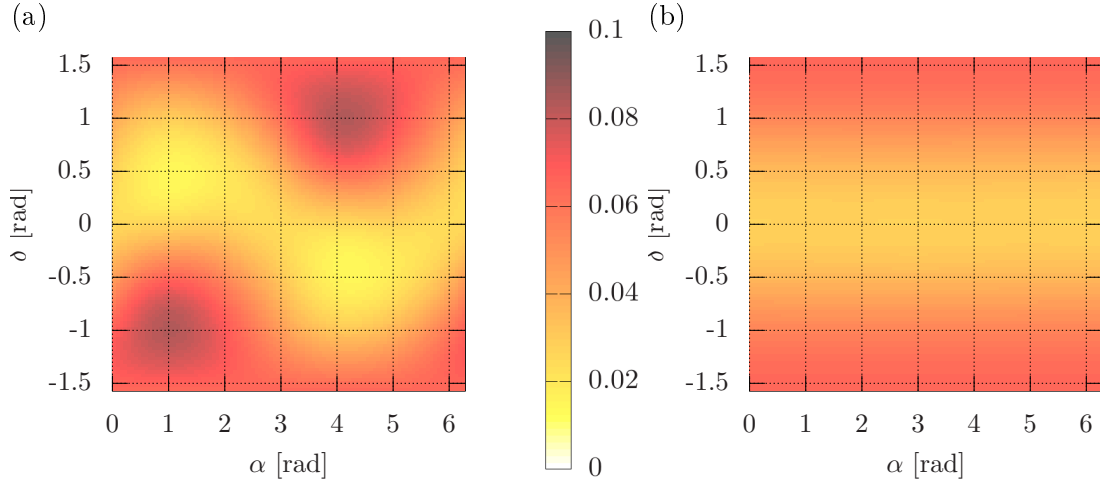
Figure 5.3: Overall antenna-pattern-matrix determinant D for the H1-L1-G1-V1 network, averaged over $T_{\text{data}} = 12\,\text{h}$ (24 SFTs per detector) in panel (a) and $T_{\text{data}} = 24\,\text{h}$ (48 SFTs per detector) in panel (b). T_{data} starts at GPS time 852443819 (Jan 10, 2007, 05:56:45 UTC; start of the S5R5 segment selection from Aasi et al. 2013b).

are called the *antenna-pattern matrix elements*, with the antenna-pattern functions $a(t)$ and $b(t)$ defined in Eq. (5.17) and the noise-weighted averaging from Eq. (5.32).

Defining the determinant of the reduced antenna-pattern matrix,

$$D \equiv AB - C^2\,,\tag{5.39}$$

the determinant of the full matrix is

$$|\mathcal{M}| = \left(\mathcal{S}^{-1}T_{\text{data}}\right)^4 D^2\,.\tag{5.40}$$

This depends on both the quality of the data set at a given frequency, through the factor $\mathcal{S}^{-1}(f)$, and on the sky-dependent detector response, through D. Hence, it gives a measure for the sensitivity of a data set, specific to each template $\lambda = \{\alpha, \delta, f, \dot{f}, \dots\}$. In this role, $|\mathcal{M}|$ will become important in Sec. 12.

For the moment, I conclude the discussion of antenna patterns with a visual representation of the sky-dependent variations of D and the per-detector D^X, depending on the length of observation time. Using the `lalapps_ComputeAntennaPattern` code, I have computed D^X and D for a network of four detectors: LIGO H1 in Hanford, Washington, USA; LIGO L1 in Livingston, Louisiana, USA; GEO600 near Hannover, Germany and Virgo in Cascina, Italy. Here, I assume equal noise PSDs S^X for all detectors.

Sky maps of the multi-detector D, averaged over 30-minute SFTs spanning a total of either 12 hours or 24 hours, are given in Fig. 5.3. The set of four D^X for each time-span is shown in Figs. 5.4 and 5.5, respectively. We see that for a whole day of observation (or integer multiples of a day), most of the variation in right ascension α is averaged out.

H1

L1

G1

V1
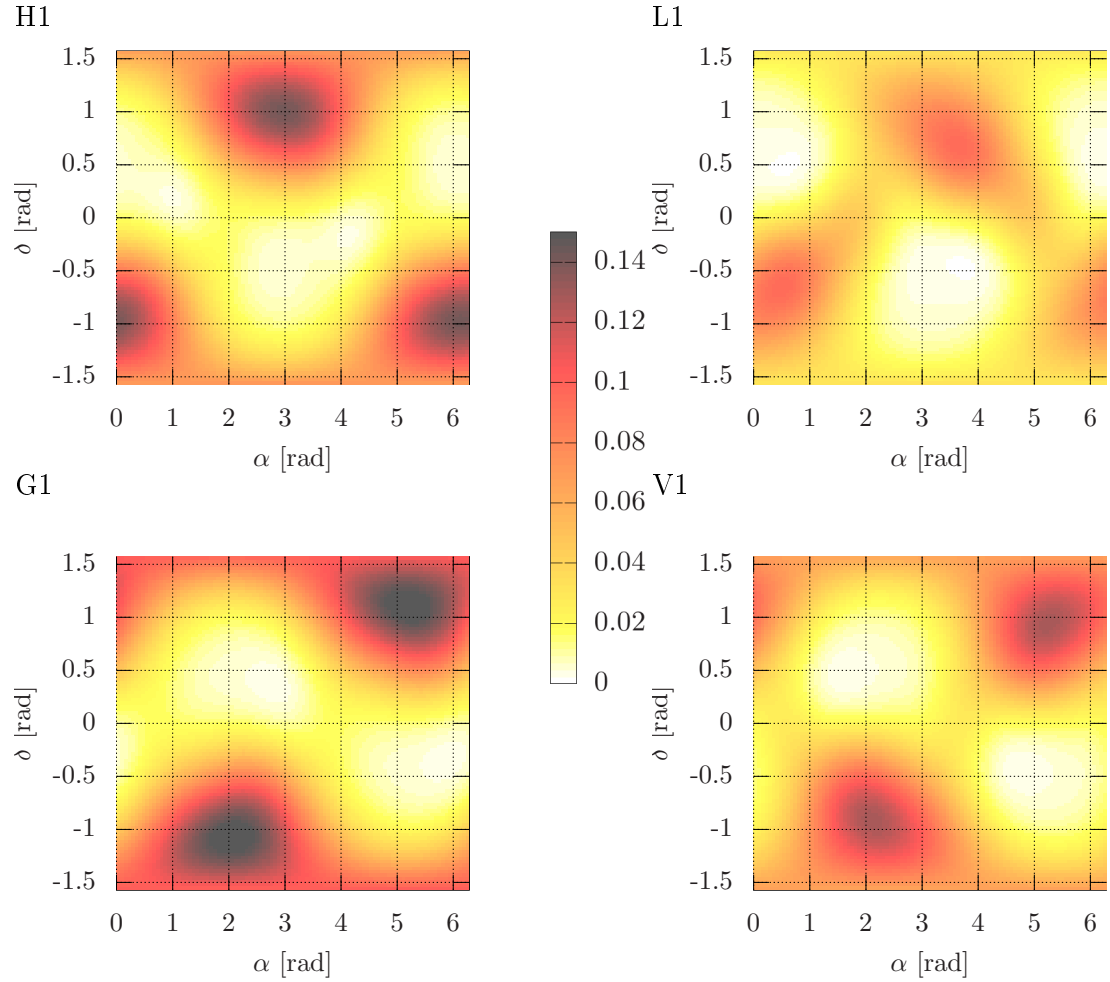
Figure 5.4: Per-detector antenna-pattern-matrix determinant D^X (colour scale), averaged over $T_{\mathrm{data}} = 12\,\mathrm{h}$ (24 SFTs), as a function of sky location (α, δ in rectangular projection) for LIGO Hanford (H1), LIGO Livingston (L1), GEO600, Hannover (G1), Virgo, Cascina (V1).
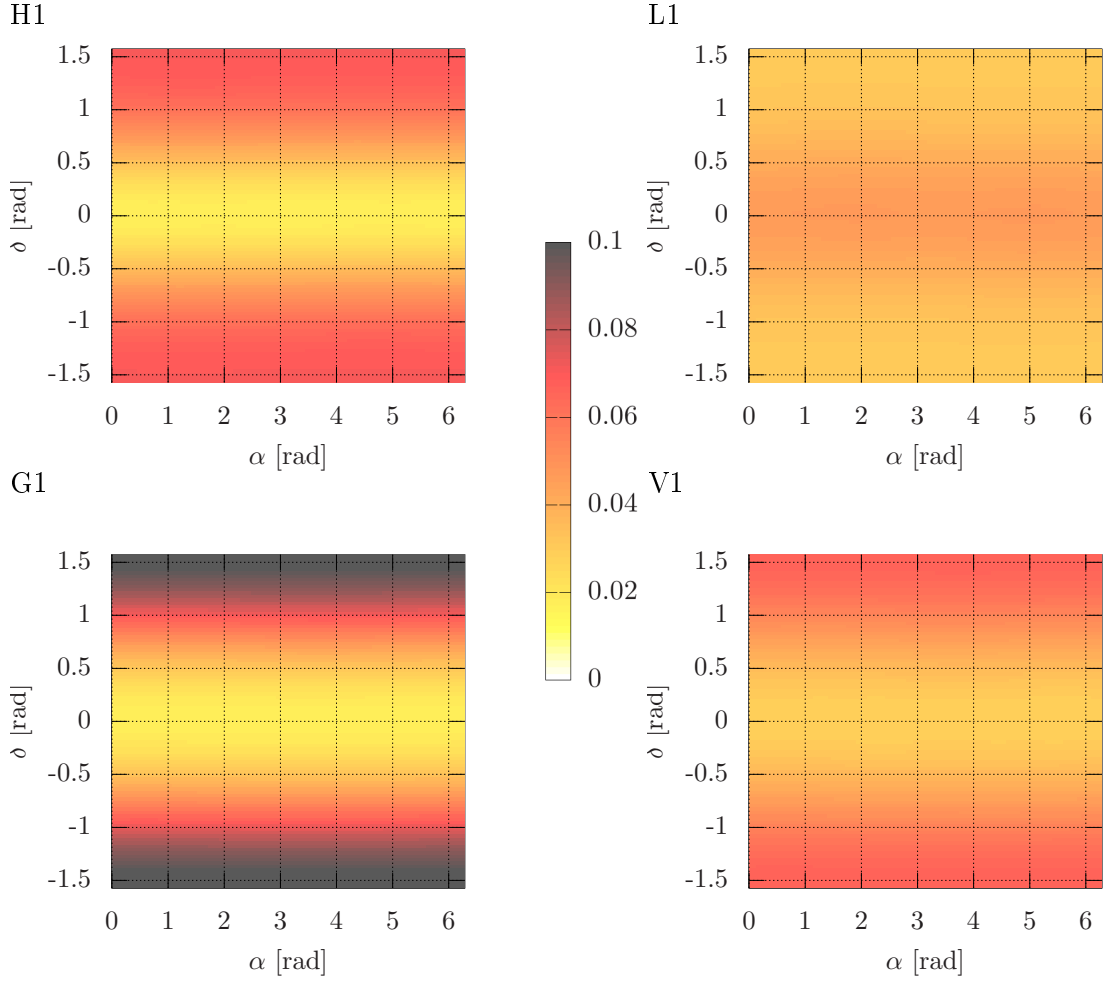
Figure 5.5: Per-detector antenna-pattern-matrix determinant D^X (colour scale), as in Fig. 5.4, but averaged over $T_{\mathrm{data}} = 24\,\mathrm{h}$ (48 SFTs). The small remaining α-dependence would only average out over a *sidereal* day (≈ 23.9344 hours) and when using finer time resolution.

5.7 The $\mathcal{F}$-statistic

Now, all necessary tools are available to introduce one of the standard detection statistics of CW data analysis, the $\mathcal{F}$-*statistic*. Here I will give the classical maximum-likelihood derivation, with a Bayesian re-derivation to follow in Sec. 7.2.1.

This statistic was first introduced by JKS98, and the multi-detector generalisation was given by Cutler & Schutz (2005). As before, I follow the notation of Prix (2011b), but with details of the derivation taken mostly from JK09.

In Sec. 4.4, we have already seen that the log-likelihood ratio between two simple hypotheses gives an optimal test statistic. Specialising to a CW signal with fixed amplitude parameters $\mathcal{A}$ and phase-evolution parameters λ and inserting the JKS factorisation Eq. (5.24) for the signal $\boldsymbol{s}(t)$ into Eq. (4.28), the log-likelihood ratio between the CW signal and Gaussian noise hypotheses follows in terms of scalar products as

$$
\begin{aligned}
\log \Lambda(\boldsymbol{x}, \mathcal{A}, \lambda) &= \langle \boldsymbol{x} \,|\, \mathcal{A}^\mu \, \boldsymbol{h}_\mu(\lambda) \rangle - \frac{1}{2} \langle \mathcal{A}^\mu \, \boldsymbol{h}_\mu(\lambda) \,|\, \mathcal{A}^\nu \, \boldsymbol{h}_\nu(\lambda) \rangle \\
&= \mathcal{A}^\mu \, \langle \boldsymbol{x} \,|\, \boldsymbol{h}_\mu(\lambda) \rangle - \frac{1}{2} \mathcal{A}^\mu \, \langle \boldsymbol{h}_\mu(\lambda) \,|\, \boldsymbol{h}_\nu(\lambda) \rangle \, \mathcal{A}^\nu \\
&= \mathcal{A}^\mu x_\mu(\lambda) - \frac{1}{2} \mathcal{A}^\mu \, \mathcal{M}_{\mu\nu}(\lambda) \, \mathcal{A}^\nu \,.
\end{aligned}
\tag{5.41}
$$

Here we see the previously-defined antenna-pattern matrix $\mathcal{M}_{\mu\nu}$ occurring naturally, along with projections

$$
x_\mu(\lambda) \equiv \langle \boldsymbol{x} \,|\, \boldsymbol{h}_\mu(\lambda) \rangle = \sum_{X=1}^{N_{\mathrm{det}}} \langle x^X \,|\, h_\mu^X \rangle
\tag{5.42}
$$

of the data on the basis functions. Rewriting the antenna-pattern matrix as the scalar product

$$
\mathcal{M}_{\mu\nu} = \langle \boldsymbol{h}_\mu \,|\, \boldsymbol{h}_\nu \rangle = \left\langle \frac{\partial \boldsymbol{h}}{\partial \mathcal{A}^\mu} \,\middle|\, \frac{\partial \boldsymbol{h}}{\partial \mathcal{A}^\nu} \right\rangle ,
\tag{5.43}
$$

a comparison with Eq. (4.10) demonstrates that the antenna-pattern matrix (or, more precisely: its expectation value) is the Fisher matrix for the amplitude parameters $\mathcal{A}$.

If we now generalise to the detection problem for CW signals with unknown parameters, it is $(7 + s_{\max})$-dimensional – with 4 amplitude parameters, 2 sky coordinates and $1 + s_{\max}$ spin-down parameters. This dimensionality can be reduced by analytically *maximizing* Eq. (5.41) over the amplitude parameters. The maximum can be found by solving

$$
\frac{\partial \log \Lambda(\boldsymbol{x}, \mathcal{A}, \lambda)}{\partial \mathcal{A}^\mu} = x_\mu(\lambda) - \mathcal{M}_{\mu\nu}(\lambda) \, \mathcal{A}^\nu \overset{!}{=} 0 \,.
\tag{5.44}
$$

Using the inverse matrix defined by $\mathcal{M}^{\mu\sigma} \, \mathcal{M}_{\sigma\nu} = \delta^\mu{}_\nu$, this yields

$$
\mathcal{A}_{\mathrm{ML}}^\mu(\boldsymbol{x}, \lambda) = \mathcal{M}^{\mu\nu}(\lambda) \, x_\nu(\lambda)
\tag{5.45}
$$

as the maximum-likelihood estimator of the amplitudes, given the data $\boldsymbol{x}$ and a specific set of phase-evolution parameters λ. That this extremum is indeed a maximum follows from $\mathcal{M}_{\mu\nu}$ being positive definite.

Inserting these estimators into Eq. (5.41) gives a maximum-likelihood detection statistic, which is the well-known $\mathcal{F}$-statistic:

$$2\mathcal{F}(\boldsymbol{x}, \lambda) \equiv x_\mu \, \mathcal{M}^{\mu\nu}(\lambda) \, x_\nu \,. \tag{5.46}$$

Note that there is some ambiguity in the literature about whether the term "the $\mathcal{F}$-statistic" refers to $\mathcal{F}$ or $2\mathcal{F}$. Of course, this is only important when discussing specific numerical values, while as detection statistics both are equivalent in the Neyman-Pearson sense (see Sec. 4.3. In this thesis, it usually means $2\mathcal{F}$.

After the maximisation over $\mathcal{A}$, only the phase-evolution parameters λ remain. In the special case of a *targeted search*, where λ is assumed to be fully known from astrophysical priors, computing Eq. (5.46) at this fixed λ would be sufficient. On the other hand, for unknown λ, since we have already started with a maximum-likelihood approach, the logical next step is to also maximise the log-likelihood over λ. However, this can only be done numerically. A simple-minded, yet computationally expensive, search over all possible λ values can deliver the maximum $2\mathcal{F}(\boldsymbol{x}, \lambda)$ over the whole parameter space, together with maximum-likelihood parameter estimates λ_{ML}. I will return to the topic of $\mathcal{F}$-statistic-based searches for unknown CW sources in the next section.

It is important to note that the $\mathcal{F}$-statistic is not actually optimal in the Neyman-Pearson sense as a detection statistic for physical CW signals, even in pure Gaussian noise. As pointed out by Prix & Krishnan (2009), the signal hypothesis is not fully specified when just the model function Eq. (5.24) is given.

The frequentist maximum-likelihood approach used to derive the $\mathcal{F}$-statistic translates, in Bayesian language, to an implicit prior distribution for the amplitude parameters $\mathcal{A}$, which I will discuss in more detail in chapters 7 and 12. This "$\mathcal{F}$-statistic prior" does not correspond to realistic assumptions: the spins of galactic NSs are rather expected to be randomly oriented, described by uniform priors in the angular variables $\cos\iota$ and ψ. Hence, the $\mathcal{F}$-statistic is slightly suboptimal for realistic signal populations.

Prix & Krishnan (2009) have derived a Bayesian "$\mathcal{B}$-statistic" with improved sensitivity, for which however the amplitude parameters cannot be treated analytically, making it computationally more expensive. Further investigation of alternative priors that are physically motivated, yet still allow for analytical treatment, was presented by Whelan et al. (2014).

The statistical properties of the $\mathcal{F}$-statistic can be found by using two useful facts: From the definitions of the correlation matrix, noise PSD and scalar product in Eqs. (5.4)–(5.6), we have $E\left[\langle \boldsymbol{n} | \boldsymbol{p}\rangle \, \langle \boldsymbol{n} | \boldsymbol{q}\rangle\right] = \langle \boldsymbol{p} | \boldsymbol{q}\rangle$ for Gaussian noise $\boldsymbol{n}$ and arbitrary time series $\boldsymbol{p}, \boldsymbol{q}$, so that $E\left[\langle \boldsymbol{n} | \boldsymbol{h}_\mu\rangle \, \langle \boldsymbol{n} | \boldsymbol{h}_\nu\rangle\right] = \langle \boldsymbol{h}_\mu | \boldsymbol{h}_\nu\rangle$. (See Eq. (39) of Prix 2011b for a detailed proof.)

Also, $\mathcal{M}^{\mu\nu}$ does not depend on the data $\boldsymbol{x}$ and can be pulled out of any expectation values.

Hence, the expectation value of $2\mathcal{F}$ in Gaussian noise, defining $n_\mu \equiv \langle \boldsymbol{n} \, | \boldsymbol{h}_\mu \rangle$ in analogy with x_μ from Eq. (5.42), follows as

$$
\begin{aligned}
E\left[2\mathcal{F}\right]_{\mathrm{n}} = E\left[n_\mu \, \mathcal{M}^{\mu\nu} \, n_\nu\right] &= \mathcal{M}^{\mu\nu} \, E\left[n_\mu \, n_\nu\right] \\
&= M^{\mu\nu} \, E\left[\langle \boldsymbol{n} \, | \boldsymbol{h}_\mu \rangle \, \langle \boldsymbol{n} \, | \boldsymbol{h}_\nu \rangle\right] \\
&= \mathcal{M}^{\mu\nu} \, \langle \boldsymbol{h}_\mu \, | \boldsymbol{h}_\nu \rangle = \mathcal{M}^{\mu\nu} \, \mathcal{M}_{\mu\nu} = 4 \, .
\end{aligned}
\tag{5.47}
$$

In the presence of a signal, with $s_\mu \equiv \langle \boldsymbol{s} \, | \boldsymbol{h}_\mu \rangle$, this changes to

$$
\begin{aligned}
E\left[2\mathcal{F}\right]_{\mathrm{s}} &= E\left[(n_\mu + s_\mu) \, \mathcal{M}^{\mu\nu} \, (n_\nu + s_\nu)\right] \\
&= \mathcal{M}^{\mu\nu} \left(E\left[n_\mu \, n_\nu\right] + 2E\left[s_\mu \, n_\nu\right] + E\left[s_\mu \, s_\nu\right]\right) \\
&= 4 + \rho^2 \, ,
\end{aligned}
\tag{5.48}
$$

where the noise-signal cross-term vanishes due to $E\left[n_\mu\right] = \langle E\left[\boldsymbol{n}\right] \, | \boldsymbol{h}_\mu \rangle = 0$. The signal-signal term, with $E\left[s_\mu \, s_\nu\right] = s_\mu \, s_\nu$, yields the *signal-to-noise ratio* (SNR) ρ defined by

$$
\rho^2 \equiv \langle \boldsymbol{s} \, | \boldsymbol{s} \rangle = \mathcal{A}^\mu \, \mathcal{M}_{\mu\nu} \, \mathcal{A}^\nu = s_\mu \, \mathcal{M}^{\mu\nu} \, s_\nu \, .
\tag{5.49}
$$

The $\mathcal{F}$-statistic is a quadratic function in the four Gaussian-distributed noise components n_μ. It can be shown that its distribution in the noise case is given by a central χ^2-distribution with 4 degrees of freedom, $2\mathcal{F}|_{\mathrm{n}} \sim \chi_4^2(0)$, and by a non-central χ^2-distribution with non-centrality parameter ρ^2 in the signal case, $2\mathcal{F}|_{\mathrm{s}} \sim \chi_4^2(\rho^2)$. See Sec. 4.6.2 for the respective probability distribution functions.

For practical computation, the $\mathcal{F}$-statistic can be related to per-SFT quantities through the relations

$$
2\mathcal{F} = \frac{1}{D\mathcal{S}^{-1}T_{\mathrm{data}}} \left(B|x_{\mathrm{a}}|^2 + A|x_{\mathrm{b}}|^2 - 2C\Re(x_{\mathrm{a}}x_{\mathrm{b}}^*)\right)
\tag{5.50a}
$$

$$
= \frac{2}{DN_{\mathrm{SFT}}} \left(B|F_{\mathrm{a}}|^2 + A|F_{\mathrm{b}}|^2 - 2C\Re(F_{\mathrm{a}}F_{\mathrm{b}}^*)\right) \, ,
\tag{5.50b}
$$

with complex projections of the data on the basis functions,

$$
x_{\mathrm{a}} \equiv \langle \boldsymbol{x} \, | \boldsymbol{h}_{\mathrm{a}} \rangle = \langle \boldsymbol{x} \, | \boldsymbol{h}_1 - \mathrm{i}\boldsymbol{h}_3 \rangle \quad \text{and} \quad x_{\mathrm{b}} \equiv \langle \boldsymbol{x} \, | \boldsymbol{h}_{\mathrm{b}} \rangle = \langle \boldsymbol{x} \, | \boldsymbol{h}_2 - \mathrm{i}\boldsymbol{h}_4 \rangle \, ,
\tag{5.51}
$$

and the sum over all SFTs of the so-called $\mathcal{F}$-*statistic atoms* $F_{\mathrm{a},\alpha}^X$, $F_{\mathrm{b},\alpha}^X$:

$$
F_{\mathrm{a}} \equiv \sum_{X=1}^{N_{\mathrm{det}}} \sum_{\alpha=1}^{N_{\mathrm{SFT}}^X} F_{\mathrm{a},\alpha}^X = \sum_{X=1}^{N_{\mathrm{det}}} \sum_{\alpha=1}^{N_{\mathrm{SFT}}^X} \int_0^{T_{\mathrm{SFT}}} y_\alpha^X(t) \sqrt{w_\alpha^X} \, a_\alpha^X(t) \, \mathrm{e}^{-\mathrm{i}\phi_\alpha^X(t)} \, \mathrm{d}t \, ,
\tag{5.52a}
$$

$$
F_{\mathrm{b}} \equiv \sum_{X=1}^{N_{\mathrm{det}}} \sum_{\alpha=1}^{N_{\mathrm{SFT}}^X} F_{\mathrm{b},\alpha}^X = \sum_{X=1}^{N_{\mathrm{det}}} \sum_{\alpha=1}^{N_{\mathrm{SFT}}^X} \int_0^{T_{\mathrm{SFT}}} y_\alpha^X(t) \sqrt{w_\alpha^X} \, b_\alpha^X(t) \, \mathrm{e}^{-\mathrm{i}\phi_\alpha^X(t)} \, \mathrm{d}t \, .
\tag{5.52b}
$$

This definition uses the antenna-pattern matrix elements A, B, C and determinant D from Eqs. (5.38) and (5.39), the noise weights w_α^X from Eq. (5.29), the antenna-pattern functions from Eq. (5.17) and normalised data $y_\alpha^X(t)$ as described in Sec. 4.1 of Prix 2011b.

The phase factors in Eq. (5.52) indicate that the $\mathcal{F}$-statistic, even if its computation is split into per-SFT steps, still is a *coherent* detection statistic in the sense that amplitudes *and* phases of the signal templates are kept consistent across SFT boundaries.

Furthermore, it is useful to rewrite the SNR from Eq. (5.49) in a similar, more explicit way, obtaining the source-orientation dependent relation between h_0 and SNR:

$$\rho^2 = h_0^2 \left(\alpha_1 A + \alpha_2 B + 2\alpha_3 C\right) \mathcal{S}^{-1} T_{\mathrm{data}}, \tag{5.53}$$

with three auxiliary functions

$$\alpha_1(\cos\iota, \psi) \equiv \frac{1}{4}(1 + \cos^2\iota)^2 \cos^2(2\psi) + \cos^2\iota \sin^2(2\psi), \tag{5.54a}$$

$$\alpha_2(\cos\iota, \psi) \equiv \frac{1}{4}(1 + \cos^2\iota)^2 \sin^2(2\psi) + \cos^2\iota \cos^2(2\psi), \tag{5.54b}$$

$$\alpha_3(\cos\iota, \psi) \equiv \frac{1}{4}(1 - \cos^2\iota)^2 \sin(2\psi) \cos(2\psi). \tag{5.54c}$$

5.8 Parameter-space metric and template banks

For a so-called "blind search", where some or all of the phase-evolution parameters λ of putative CW sources are not known, the optimal sampling of the parameter space is a non-trivial problem. Even after the amplitude parameters are analytically maximised over, a brute-force numerical exploration of a *template bank* covering the remaining phase-evolution parameter space is so expensive that blind CW searches are *computationally limited*: the available computing power determines the maximum number of search templates. A template bank must be constructed in a way that gives the maximum sensitivity under this constraint.

The density of a template bank can be quantified by the *mismatch* between the perfectly-matched results – that would be obtained if a search template λ exactly matches the actual physical source parameters λ_{s} – and the result at another point λ, corresponding to a relative loss of squared SNR:

$$m(\lambda_{\mathrm{s}}; \lambda) \equiv \frac{\rho^2(\lambda_{\mathrm{s}}) - \rho^2(\lambda)}{\rho^2(\lambda_{\mathrm{s}})}. \tag{5.55}$$

Note that this is not a symmetric function, and does not define a global distance measure on the (generally curved) parameter space. But at least locally around a given λ_{s}, a Taylor expansion in small parameter offsets $\mathrm{d}\lambda$ allows to express the mismatch through a *metric tensor* g_{ij}:

$$m(\lambda_{\mathrm{s}}; \lambda_{\mathrm{s}} + \mathrm{d}\lambda) \approx g_{ij}(\lambda_{\mathrm{s}})\, \mathrm{d}\lambda^i\, \mathrm{d}\lambda^j + \mathcal{O}\left(\mathrm{d}\lambda^3\right). \tag{5.56}$$

Thus, the metric forms the basis for constructing "efficient" template banks in the sense that the available computing power should be translated into an optimum sensitivity. Template densities in all dimensions must be fine enough to limit the maximum mismatch, while not being "wasteful" in using more templates than necessary.

The concept of a parameter-space metric was first introduced in the CBC context by Balasubramanian, Sathyaprakash & Dhurandhar (1996) and Owen (1996) and translated to the CW field by Brady et al. (1998) and Prix (2007b). For recent developments to find global, numerically well-behaved expressions for the CW metric, see Wette & Prix (2013). For template bank construction, see Prix (2007a) and Messenger, Prix & Papa (2009). Also, for the prediction and optimisation of sensitivities for wide-parameter-space searches, see Prix & Shaltev (2012) and Wette (2012).

I will not go into the, rather complicated, details of the CW metric parametrisations. Suffice it to say that in Sec. 10, I will be using the flat "super-sky metric" from Wette & Prix (2013).

5.9 Semi-coherent searches

The computing cost for a fully coherent $\mathcal{F}$-statistic search for signals with unknown phase-evolution parameters scales at least with $T_{\mathrm{data}}^6 f^2$, for a search over $\lambda = \{\alpha, \delta, f, \dot{f}\}$ (Brady et al. 1998, Prix 2007b, 2009). Hence, a coherent search with fixed computing power over a given parameter space must have a limited data volume T_{data} and parameter-space resolution, leading to a limited sensitivity. To achieve a better sensitivity, the scaling of the cost with T_{data} must be reduced. This can be achieved by *semi-coherent* methods, which for long observation times have been shown to be more sensitive at fixed computing cost (Brady & Creighton 2000, Cutler, Gholami & Krishnan 2005, Prix & Shaltev 2012).

In general, a semi-coherent algorithm computes a coherent detection statistic, for example the $\mathcal{F}$-statistic, over short *segments* of the data $\boldsymbol{x}$, which I denote as $\{\boldsymbol{x}_k\}_{k=1}^{N_{\mathrm{seg}}}$. These are then combined, in the *incoherent step* (typically by summation), to obtain the semi-coherent statistic over the whole data set.

For my work, the most relevant semi-coherent approach is the so-called *StackSlide* method discussed by Brady & Creighton (2000), Cutler, Gholami & Krishnan (2005) and Prix & Shaltev (2012). The name comes from "stacking" the results of the individual segments while "sliding" the templates from each segment to line up with each other. The segments typically consist of many SFTs. In the most general form of a StackSlide search, the semi-coherent statistic $\widehat{\mathcal{F}}\left(\boldsymbol{x}, \widehat{\lambda}\right)$ in a template $\widehat{\lambda}$ can be constructed as a sum over N_{seg} coherent statistics:

$$\widehat{\mathcal{F}}\left(\boldsymbol{x}, \widehat{\lambda}\right) \equiv \sum_{k=1}^{N_{\mathrm{seg}}} \widetilde{\mathcal{F}}_k\left(\boldsymbol{x}_k, \widetilde{\lambda}_k(\widehat{\lambda})\right) . \tag{5.57}$$

The simplest choice would be to compute $\mathcal{F}_k$ on the same template in each segment, i.e. $\widetilde{\lambda}_k(\widehat{\lambda}) = \widehat{\lambda}$. But in fact this is not optimal in terms of sensitivity at fixed computing cost, as can be shown by a semi-coherent extension of the metric approach (Brady & Creighton 2000, Pletsch 2010): this would generally require a very dense template bank, while high sensitivities can also be reached with a *coarse grid* of templates in each segment and a much denser *fine grid* which is only used in the incoherent summing step.

Hence, to fully specify the semi-coherent statistic $\widehat{\mathcal{F}}(\boldsymbol{x}, \widehat{\lambda})$ requires an algorithm to pick the right coarse-grid $\widetilde{\lambda}_k(\widehat{\lambda})$ for each fine-grid point $\widehat{\lambda}$. This can be achieved by picking nearest neighbours with the metric distance of Eq. (5.56), with a semi-coherent metric $\widehat{m}_{ij}$. I will discuss one such approach in the following section. The construction of a fine grid by increasing the resolution of an initial coarse grid along some or all of the phase-evolution parameters is called *refinement*.

Alternative semi-coherent algorithms include the Hough transform (Papa et al. 1998, Krishnan et al. 2004, Krishnan 2005, Sintes & Krishnan 2006), the PowerFlux algorithm (Dergachev 2006, Abbott et al. 2008a, 2009a, Dergachev 2009, 2011), cross-correlation searches (Dhurandhar et al. 2008, Chung et al. 2011) and sliding coherence windows (Pletsch 2011).

A related concept are *hierarchical searches*, which combine multiple semi-coherent and coherent stages with increasing sensitivity, while in each step narrowing down the parameter space. The current state of the art in $\mathcal{F}$-statistic-based searches is to have one main semi-coherent stage over the full parameter space, taking most of the computing power, and several semi-coherent and coherent "follow-up" stages for smaller parameter regions around the most significant candidates (Shaltev & Prix 2013, Shaltev et al. 2014).

5.10 Global-correlations method

An optimal refinement strategy and incoherent combination algorithm for a StackSlide-based semi-coherent search has to be based on the behaviour of the detection statistic, e.g. the $\mathcal{F}$-statistic, over the phase-evolution parameter space. As discussed in Sec. 5.8, the metric gives a good description of the local $\mathcal{F}$-statistic surface, or, equivalently, the mismatch distribution. However, Prix & Itoh (2005) and Pletsch (2008) found, by also analysing the global picture, that strong *global correlations* exist, in the sense that a given CW signal leads to elevated $\mathcal{F}$-statistic values in large regions of the parameter space.

For observation times less than a month and when the parameter space consists of frequency and sky coordinates only (no spin-down parameters), as considered by Prix & Itoh (2005), these regions are (approximately) "circles in the sky". Including the first spin-down parameter, as done by Pletsch (2008), turns these into hypersurfaces in a 4-D parameter space.

Based on the analytical equations for these hypersurfaces, a "global correlations transform" (GCT) to a new set of parameters and the accompanying coherent and semi-coherent metrics were found by Pletsch & Allen (2009) and Pletsch (2010). Most semi-coherent methods, including the current implementation of the Hough transform (Krishnan et al. 2004), use refinement in the parameters (spin-down and sky coordinates). In contrast, the GCT coordinates, under certain approximations and for limited observation time, allow to use one-dimensional refinement in the spin-down parameter only, which leads to increased sensitivity at fixed computing cost.

However, it was later found (Manca et al. 2014) that for longer observation times of a few months or more, the lack of sky-refinement is no longer justified, and that the GCT-based search code `lalapps_HierarchSearchGCT` in its current implementation loses sensitivity in this regime.

5.11 GW data-analysis software: LALSuite

The LIGO scientific collaboration (LSC) has collected many algorithms, helper functions and entire search pipelines in the Free and open-source software package `LALSuite` (*LSC Algorithm Library Suite*). For this thesis, I have used several of the `LALApps` applications and `LALpulsar` library functions contained in this suite, mostly written by other authors, but some also containing my own contributions and extensions. I list these here, along with very brief descriptions of their usage, and the main authors.

- `lalapps_ComputePSD` by B. Krishnan, I. Gholami, R. Prix, A. Sintes, K. Wette, which I use for the computation of noise power spectral densities and normalised SFT power for the line-prior tuning in Sec. 8.1.

- `lalapps_HierarchSearchGCT`, a semi-coherent StackSlide CW search code based on the global correlations method described in Sec. 5.10. The tests on real and simulated LIGO data in Sec. 10 are done with this program. It was written mostly by H. Pletsch, with later contributions by K. Wette, R. Prix, B. Machenschalk and myself.

- `lalapps_Makefakedata_v4` by R. Prix, M. A. Papa, X. Siemens, B. Allen and C. Messenger, which I use in Sec. 10 for the generation of simulated noise time series and CW signals, and the injection of simulated signals into real LIGO data.

- `lalapps_FstatMetric_v2` by R. Prix and K. Wette, which computes coherent and semi-coherent metrics, and which I use in Sec. 10 for the identification of neighbouring sky templates.

- `lalapps_SynthesizeLVStats` for the generation of synthetic statistic draws in Sec. 9, written by myself, based on the `lalapps_SynthesizeTransientStats` code and the `LALpulsar-SynthesizeCWDraws` module, both by R. Prix.

- `lalapps_ComputeAntennaPattern`, a simple stand-alone code for the computation and output of antenna-pattern functions, Eq. (5.17), and matrix elements, Eq. (5.38), written by myself, based on library functions from `LALpulsar` by S. J. Berukoff, R. Prix and J. T. Whelan.

Due to the collaborative nature of the `LALSuite` project, other authors may have contributed as well, and all of these codes also use library functions provided by additional authors. The full author contributions and version history can, as of the writing of this thesis, be found at the following URL:

https://ligo-vcs.phys.uwm.edu/cgit/lalsuite/

5.12 Einstein@Home

As discussed in Secs. 5.8 and 5.9, the sensitivity of large-parameter-space CW searches scales with the available computational power. Resources beyond that of most high-performance computing clusters – like ATLAS at AEI Hannover, which I have used for the studies in Sec. 10 – can be obtained by *distributed computing.* This means running the analysis software on computers across the world, operated both by participating scientific institutions and by volunteers from the general public. The Einstein@Home project (Allen et al. 2005a) does this, based on the BOINC framework (*Berkeley Open Infrastructure for Network Computing*, see Anderson, Walton, Fenton et al. 2002, Anderson 2004).

As of the writing of this thesis, the sustained average computing power of Einstein@Home from over 10^5 actively contributing host computers was in excess of 10^{15} floating point operations per second (one PFLOPS), which would correspond to a place among the upper 40 on the June 2014 Top500 list (Strohmaier et al. 2014).

Wide-parameter CW searches for unknown sources are well-suited to distributed computing, as the computation of a detection statistic over a template bank is a set of mostly independent computations, which therefore is easily parallelised. Hosts are assigned *workunits* of limited run-time and data volume, each covering a subset of the parameter space

After an initial run on LIGO S3 data (Allen, Abbott et al. 2005b), several CW analyses of data sets from the LIGO science runs S4 and S5 (see Sec. 2.6.3) have been published based on Einstein@Home results and different search methods: S4 data was analysed with coherent $\mathcal{F}$-statistic searches on 17 segments of 30 h each, with a simple coincidence criterion over all results (Abbott et al. 2009d). For the first eight months of S5 data, a semi-coherent Hough-based search was performed (Abbott et al. 2009c). The full S5 data set was then also analysed using the Hough-transform method (Krishnan et al. 2004) and the results (Aasi et al. 2013b) are currently the most constraining all-sky upper limits on CW emission from isolated NSs yet, reaching a best sensitivity of $h_0^{90\%} \leq 7.6 \cdot 10^{-25}$ near 152.5 Hz and covering a $[50, 1190]$ Hz frequency range and $[-20, 1.1] \cdot 10^{-10} \, \mathrm{Hz}\, s^{-1}$

spin-down range. Analyses of S6 data using the GCT method are still ongoing, and I will briefly describe these in Sec. 11.

The distributed-computing nature of Einstein@Home brings with it some special challenges. In any CW search over a long time baseline and a large parameter space, the total number of templates needed to cover the parameter space at sufficient sensitivity is huge: for example, in Aasi et al. (2013b), $N_{\mathrm{templ}} \sim 10^{13}$ were required for a single 0.5 Hz band near 100 Hz, and $N_{\mathrm{templ}} \sim 10^{15}$ per band near 1000 Hz. Hence, not all candidates can be returned and used for post-processing, so that the list of candidates gets truncated to the most significant subset, or "toplist". For Einstein@Home searches, this subset has to be particularly restrictive, in order to limit the upload volume from volunteers to the servers. In the case of Aasi et al. (2013b), for each workunit only the top 10^4 candidates were returned.

Furthermore, special care is taken to avoid erroneous or faked results. The host computers which run the Einstein@Home software do not necessarily have hardware of the highest standards, and their operating-system environment is not tightly controlled. Hence, computational errors and corruption of result files on the hosts, or during internet transfer to the Einstein@Home servers, happens at some small rate. For this reason, each workunit is computed by at least two hosts, and a validation code checks for any inconsistencies between the sets of results.

Since 2009, Einstein@Home is also searching electromagnetic data for radio pulsars (see Sec. 3.3), where the detection problem with current technology is much easier than in the GW case. In data from the surveys PMPS (*Parkes Multi-beam Pulsar Survey*, see Manchester et al. 2001) and PALFA (*Arecibo Pulsar Survey Using ALFA*, where ALFA is the *Arecibo L-Band Feed Array*, see Cordes et al. 2006), Einstein@Home has, as of the writing of this thesis, discovered about 50 previously unknown radio pulsars. After additional follow-up from the world-wide network of radio telescopes, 26 have been published by Knispel et al. (2010, 2011), Allen et al. (2013) and Knispel et al. (2013).

A third type of search on Einstein@Home analyses gamma-ray data from the Large Area Telescope (LAT, see Atwood et al. 2009) on board the Fermi Gamma-ray Space Telescope. With methods originally developed for GW searches (Pletsch 2011), and already used successfully before for blind gamma-ray pulsar discovery (Pletsch et al. 2012a,b,c), this search on Einstein@Home has so far found at least 4 new gamma-ray pulsars (Pletsch et al. 2013). Also see Abdo et al. (2013) for the current Fermi gamma-ray pulsar catalogue.

The Einstein@Home project can be found under the following URL:

```
http://www.einsteinathome.org/
```

6 The problem of lines

In this chapter, I provide the main motivation for the work presented in this thesis: while in the previous chapter I had mostly assumed pure Gaussian noise, real data from interferometric GW detectors contains many non-Gaussian artefacts. The type of disturbances most relevant for continuous wave searches are so-called "lines", which I will discuss in detail here. I also briefly review mitigation techniques that have previously been developed to deal with lines.

6.1 What do we mean by "lines"?

When we talk about "lines", the central idea is that these disturbances are similar to continuous wave signals: long-lasting and confined to narrow frequency bands. Hence, these are *spectral* artefacts, which appear as line-like deviations from the background noise distribution in a frequency-domain representation of the data, for example in the power spectrum. These characteristics are in contrast to disturbances which are localised in the time domain, usually called *glitches*. In Fig. 6.1, the prevalence and typical shapes of lines in first-generation interferometer data can be seen.

The simplest type of line is a stationary, *monochromatic* sinusoidal disturbance, so that it contributes noise power at a specific frequency, with both this frequency and the strength of the disturbance remaining constant over time.

Figure 6.1: Representative amplitude spectral density curves for the LIGO detectors H1 and L1 during their sixth science run (S6) and Virgo (V1) during its VSR2-3 runs. Strong lines are visible as peaks in the spectrum.
Figure credit: LIGO Scientific Collaboration and Virgo Collaboration, Abadie et al. (2012e).
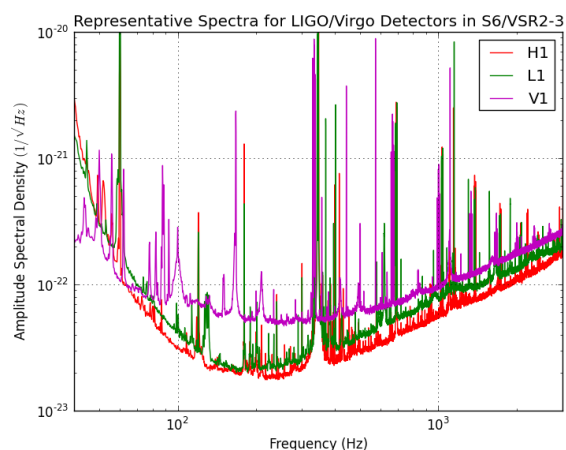
However, in real data, a single line may contain power over a certain band in frequency, its strength may change over time, or even its central frequency may change. The latter effect is called *wandering*. The spectra in Fig. 6.1 already clearly contain a variety of line morphologies.

Furthermore, the population of lines is not limited to those clearly observable in the power spectrum. There are also weaker lines which only show up in the results of highly sensitive CW searches.

For the purpose of this thesis, I will consider as "line-like" any disturbances that are localised in a frequency region smaller than the typical subdivisions of an analysis, and which are present for long enough to have an effect on a given quantity of interest, be this the PSD or a detection statistic. Any line-mitigation techniques should ideally help against this wide class of disturbances, including broad lines and wandering lines.

Two more terms often appear in the context of lines: a collection of several lines at nearby frequencies is called a *forest*, and several lines equally spaced in frequency (including, but not limited to, integer multiples of the same frequency) are called a *comb*. While the lines in a forest do not necessarily share a common physical origin, the lines in a comb are mostly *harmonics* of each other, i.e. a single physical effect couples into the interferometer GW strain channel at the base frequency, but the disturbance also appears in the higher harmonics.

6.2 Physical origin of lines

Lines can have very diverse physical origins, and these are typically known in only a few cases. In general, lines can be considered as the effect of periodic physical processes in the interferometer, or its surrounding, coupling into the GW-strain channel. Here is a list of a few known sources of lines in the initial LIGO detectors:

- *Power lines* (or *mains lines*): Detectors are powered by the standard electrical power grid of their host country, which influences the detector readout through electromagnetic couplings. This produces strong lines at the grid AC frequency and its harmonics. For the LIGO detectors, in the USA, these are at ≈ 60Hz, while for European detectors they are at ≈ 50Hz. Since the power-grid frequency is not exactly stable, and since it couples into the detector through a variety of systems, these lines are usually very broad and non-stationary.

- *Suspension lines* (also called *wire lines* or *violin modes*): These are a side-effect of trying to decouple the detector from environmental vibrations through suspending the mirrors from wires (see Sec. 4.3 of Abbott et al. 2009e and references therein). Even though these are very effective at broad-band noise reduction, there necessarily remain strong disturbances near the resonance frequencies of the suspensions themselves.

- Besides the main suspensions, other components of the detector are also prone to mechanical vibration resonances – for example, the test mass mirrors themselves.

- A large collection of analogue-to-digital converters and other electronics, which are used in the detector control and readout, induce lines at their operating frequencies.

- *Pulsed-heating lines* are another common family of lines where the periodic workings of the thermal compensation system (Ballmer et al. 2005) produce a magnetic coupling with the magnets on the test masses.

- There are also *calibration lines* deliberately injected into the detector data, to allow calibration of the strain-data stream $h(t)$ at known amplitudes. (See Sec. 4.6 of Abbott et al. 2009e, as well as Abadie et al. 2010a, and references in both.)

Some examples of the strongest of these well-known line families (calibration lines, power line harmonics, suspension wire vibrational modes, test mass vibrational modes) are labelled on a typical LIGO H1 spectrum from the fifth science run in Fig. 2.4, taken from Abbott et al. (2009e).

Lines can be either confined to a single detector, or coincident between several detectors. For example, the exact frequency of the wire lines depends on the details of each detector's suspension system, while the power lines are the same for all American detectors. For the rest of this chapter, as well as most of this thesis, I will focus on non-coincident lines only. Coincident lines will be discussed only in Sec. 6.8.

6.3 Line cataloguing

The identification of lines is one of the goals of *detector characterisation* projects at the LIGO, Virgo and GEO600 detectors (Acernese et al. 2007, Christensen 2010, Coughlin 2010, Accadia et al. 2012a), though the main focus of these projects is on improving the overall noise floor and on mitigating glitches that affect time-domain analysis (Blackburn et al. 2008, Abadie et al. 2010d, Aasi et al. 2012, Abadie et al. 2012e).

Lines can be identified either purely on the instrumental side, by analysing the *auxiliary channels*, like magnetometers and vibration sensors, and directly identifying the physical origin of strong spectral peaks. In a complementary approach, peaks in the main $h(t)$ GW-strain channel can be correlated with the auxiliary channels, and significant correlations are considered as lines even if the physical origin remains unclear.

One method employed in the LIGO and Virgo collaborations, called *Fscan*, is based on coincident outliers in the SFT power of $h(t)$ and auxiliary channels. This is similar to the "line flagging" approach which I describe in Secs. 6.5.1 and 8.1.1. A second approach uses the *spectral coherence* between channels. Both are described in Coughlin (2010). For an account of how Fscan identified new lines in early S6 data and how some of these could be removed from the instruments, see Aasi et al. (2014c).

In the past, the most complete line catalogues have been those produced in collaboration between instrument scientists and CW data analysts during the post-processing of CW searches, such as Tables VI and VII of Aasi et al. (2013b) for LIGO S5 data. These combine lines identified by the methods above with those found in the CW searches themselves and then investigated further by instrumentalists.

An advanced noise monitoring framework, specifically designed to catalogue lines and called the *Noise Frequency Event Miner* (NoEMI, see Accadia et al. 2012b), has recently been introduced in the Virgo collaboration. Just as the Fscan and coherence methods, this software uses data from the GW-strain channel as well as from auxiliary channels to identify lines. It then creates a database that can be used to mitigate the lines either at the detector level or later on in the analyses. However, NoEMI has greater flexibility in tracking the frequency evolution of lines over time. NoEMI or similar software is also envisioned to be used at adVirgo, as well as aLIGO, together with the other established methods.

6.4 Influence of lines on CW searches

If lines are present in the data, any CW detection statistic that assumes pure Gaussian noise can produce spurious candidates from signal templates whose frequency evolution crosses a line artefact. Hence, follow-up procedures are needed to separate interesting signal candidates from these line-related false alarms. In addition, some bands of data may be so heavily affected by lines that no astrophysically relevant statements (detection claims or upper limits) may be possible at all.

These effects can be seen, for example, in the results from a recent Einstein@Home analysis of LIGO S5 data (Aasi et al. 2013b), shown in Fig. 6.2. No tenable GW candidates were found in this analysis, and upper limits on the expected astrophysical h_0 at 90% confidence were reported. The plot shows these upper limits as a function of frequency. However, 156 bands of 50mHz width are excluded, indicated by black vertical bars. These bands were too heavily affected by disturbances for the calculation of meaningful upper limits.

Many narrow bands had already been excluded from the analysis beforehand, because of known instrumental artefacts. This usage of the *line cleaning* approach, which I will discuss below in Sec. 6.5, affected a total of 27 Hz of bandwidth. On the other hand, many of the lines resulting in excluded bands in the upper-limits plot were not previously known, and were only identified during follow-up. These led to the exclusion of about 25% of all candidates returned by the search. The full set of all known lines for that search is listed in Tables VI and VII in Aasi et al. (2013b).

Here, and in similar searches, the effect of lines is increased because of the use of *toplists* of candidates, which I have briefly described in Sec. 5.12. If a line is present in a frequency
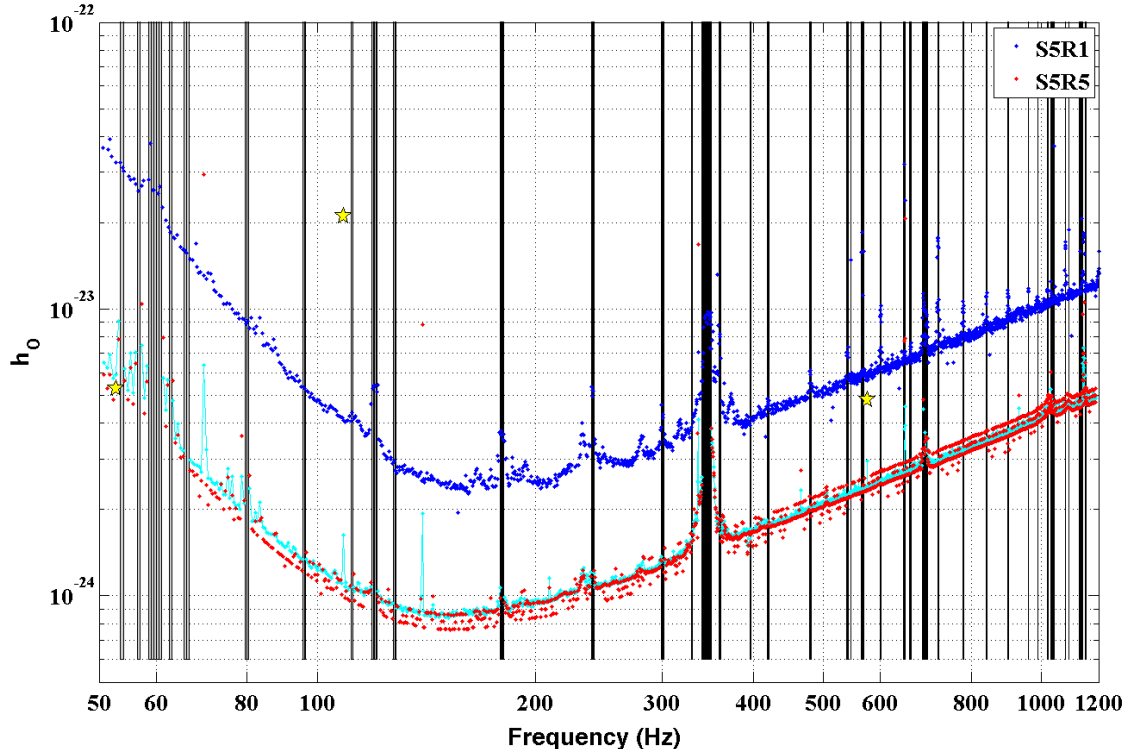
Figure 6.2: Upper limits from the S5R5 Einstein@Home search (Aasi et al. 2013b, red dots), as well from as the previous Einstein@Home search, called S5R1, which used early S5 data (Abbott et al. 2009c, blue dots). The three stars correspond to hardware-injected simulated pulsars which were recovered in the S5R5 search. The curves represent the source strain amplitude h_0 at which 90% of simulated signals would be detected. The vertical bars represent 156 half-Hz frequency bands contaminated by instrumental disturbances for which no upper limits are provided. The cyan curve shows a prediction for the $h_0^{90\%}$ upper limits.
Figure credit: LIGO Scientific Collaboration and Virgo Collaboration, Aasi et al. (2013b).

band, the toplists of all corresponding workunits can easily become *saturated* by line-related candidates. In such a case, even if there were enough unaffected candidates in the band to achieve a detection (or a confident upper-limit statement) after post-processing line removal, this would no longer be possible due to the limited toplist.

As a quantitative estimate of the prevalence of lines in initial LIGO data, consider the lists provided in Tables VI and VII of Aasi et al. (2013b): In a [50.00, 1190.00] Hz frequency band, there are 1060 known individual lines (including harmonics) in H1, and 1035 in L1. The actual width of each line is not perfectly known, but according to the post-processing exclusion limits, these lines span a total of 8.88 Hz in H1 and 8.02 Hz in L1. Note that these are only $\approx 0.78\%$ and $\approx 0.70\%$ of the total bandwidth, respectively, but that they contributed $\approx 25\%$ of the most significant candidates.

Hence, the nominal amount of line-affected bandwidth of GW data is typically small, so that the approach of treating lines as exceptional "disturbances" to an otherwise mostly-Gaussian data set is justified. However, lines can have a disproportionate influence on the set of candidates returned by a search. This makes mitigation strategies important in obtaining meaningful results and improving sensitivity.

6.5 Existing line-mitigation techniques

The ideal method of dealing with lines is to remove their physical sources from the detector system. In Accadia et al. (2012b), this is referred to as "line mitigation". However, here I will concentrate on those cases where detector-level mitigation was not possible, or the lines were not found early enough, and where the mitigation has to take place at the data-analysis level instead.

There are two fundamentally different approaches to artefact mitigation: Bayesian model-selection and ad-hoc, heuristic methods. The former is based on *explicit* alternative models for the noise distribution, extending the standard (Gaussian) broad-band model to include the artefacts. On the other hand, data can be excluded from the analysis on heuristic grounds, and ad-hoc statistics can be constructed to match certain deviations from the GW signal model that have been observed in previous search results. In the Bayesian picture, this latter approach corresponds to a test against *implicit* (and often unknown) alternative hypotheses.

It is also instructive to consider the order in which a search pipeline uses the two properties of *coherence* and *coincidence* between detectors. If the first step in the search is a coherent multi-detector statistic (as is the case for most CW searches), then the noise-artefact-mitigation strategy may use subsequent consistency checks between the individual detectors. On the other hand, if the first step consists of single-detector searches, followed by a selection of coincident triggers between the individual detectors, an additional multi-detector coherent statistic can serve as an artefact-mitigation technique. This is the case in many CBC and burst searches, which I will discuss later on in Secs. 6.6 and 6.7, as well as some early CW searches (Abbott et al. 2009d) and a recent generalisation to CWs from binary systems (Aasi et al. 2014d).

So far, the most commonly used approaches to deal with instrumental lines in CW searches are heuristic. I will briefly describe these in the following.

6.5.1 Line cleaning

One possibility is to completely exclude frequency bands from the search when they are known or believed to be affected by instrumental lines. Different variants of this approach were used in various LIGO and Virgo searches, such as Abbott et al. (2008a), Abadie et al. (2010b, 2012b) and Aasi et al. (2013a,b).

74

The identification of lines for cleaning can be the result of previous detector characterisation work, i.e. from an existing catalogue of "known lines" as discussed in Sec. 6.3. It can also be done through *line flagging* of disturbed frequency bands identified in the data as it is prepared for analysis.

The most popular method for line flagging is based on counting outliers in the normalised average power from the data SFTs. This is described in detail in Sec. 9.3 of Wette (2009) and I will also introduce it in Sec. 8.1.1 of this thesis.

Once line-affected bands (or individual SFT bins) have been identified, the search can either skip these altogether, or they can be replaced by simulated Gaussian noise. In the latter case, bands with a significant contribution of replaced bins cannot be used for astrophysical statements any more, and are used for sensitivity estimates and sanity checks only. However, there may also be templates that, due to their frequency evolution, only overlap with the cleaned bins for short periods. Detection statistics in these templates are still dominated by real detector data, and hence the search can produce valid results with better sensitivity than without the cleaning.

A downside of this method is that it typically eliminates a relatively large fraction of the total frequency band. For example, in the analysis of Abadie et al. (2012b), it excluded a total of 270 Hz out of the 1140 Hz searched, corresponding to $\sim 24\%$ of the data. This problem can be reduced by a *relaxed cleaning* approach introduced by Behnke, Papa & Prix (2014).

Furthermore, this method is either limited to known instrumental lines or, when the line-flagging variant is used, its efficacy is limited to strong disturbances. The reason is that weaker disturbances can often only be identified by using time baselines much longer than those typical for line-flagging algorithms. A simple Fourier-transform-based line-flagging algorithm is also not optimally suited to detect lines with non-constant frequency, which might nevertheless affect CW signal templates.

6.5.2 S-veto

Most astrophysical CW signals will have significant frequency modulation due to the movement of the Earth relative to the source, while lines occur at the location of the detector. Thus, a viable assumption is that lines should be mostly stationary. However, depending on the phase-evolution parameters, some signals can also appear as almost monochromatic in the detector frame, in particular when there is a cancellation between an intrinsic spin-down of the source and the Doppler effect due to the detector motion.

Hence, the idea of the *S-veto* is to veto any candidates which too closely resemble an unmodulated, stationary signal. This amounts to removing any candidates from a frequency and spin-down dependent region of the sky, or equivalently from a sky-dependent part of the frequency-spin-down space.

The S-veto was initially developed for an incoherent PowerFlux analysis (Abbott et al. 2008a) and subsequently adapted to $\mathcal{F}$-statistic searches (Abbott et al. 2009d). In the latter case, it is also known as the *generalised S-veto*.

For a coherent $\mathcal{F}$-statistic search up to first spin-down order $\dot{f}$ only, the veto region is defined by the condition

$$\left| \dot{f} + \frac{(\omega \times \bar{v}) \cdot \hat{n}}{c} f \right| < \epsilon \,, \tag{6.1}$$

where ω is the angular velocity and $\bar{v}$ the average linear velocity of the Earth (both as vectors), $\hat{n}$ is the unit vector from the SSB to the source location (see Sec. 5.2.1) and ϵ is a tolerance defining the veto threshold. This condition can also be derived by specialising the global correlations (see Sec. 5.10) to the case of vanishing spin-down and Doppler modulation, as shown in Sec. VI of Pletsch (2008).

The fraction of the total parameter space vetoed through this approach can again be quite large: for example, about 15% for H1 and 26 % for L1 in Abbott et al. (2008a), as well as $\approx 30\%$ in Abbott et al. (2009d).

A somewhat related idea is used in the Bayesian unmodulated-sinusoid model, for which I present preliminary work in Sec. 13.

6.5.3 $\mathcal{F}$-statistic consistency veto

Whereas the previous two methods work equally well with single- and multi-detector searches and can veto both single-detector and coincident lines, another powerful veto can be obtained by focussing on single-detector lines in multi-detector searches. The idea behind the $\mathcal{F}$-*statistic consistency veto* is that a true CW signal must affect all detectors. The multi-detector $\mathcal{F}$-statistic should therefore be larger than any of the single-detector $\mathcal{F}^X$-statistics. Hence, if $\max\{\mathcal{F}^X\} > \mathcal{F}$, a candidate gets vetoed as a likely instrumental line. This approach was introduced and tested in Aasi et al. (2013a,b), and described in more detail in Sec. 6.3 of Behnke (2013).

The strength of this veto is that it makes no assumptions on which parts of the data or the signal parameter space are contaminated by lines. It only removes candidates which appear, a-posteriori, as incompatible with the signal model. Therefore, the false-dismissal risk is much lower than, for example, with the S-veto. However, this veto is also an ad-hoc prescription and has no tunable threshold, making it somewhat unflexible. A Bayesian generalisation of this idea forms the basis of the main work presented in this thesis, as detailed in Sec. 7. Results on this veto are given in chapters 9 and 10, where I compare its performance to that of the pure $\mathcal{F}$-statistic and to new Bayesian line-robust detection statistics.

6.6 The analogous problem in transient searches: glitches

As discussed in Sec. 2.5, CW signals are not the only interesting targets for GW detection: comparatively strong short-lived GW signals are expected from the late phase of the inspiral of binaries of compact objects such as neutron stars and black holes ("CBCs"), as well as from catastrophic events such as supernovae ("bursts"). Searches for such short-lived signals, or *transients*, have to deal with their own set of instrumental artefacts: short-lived *noise transients* or *glitches* in the time-domain. Similarly to lines in CW searches, these lead to an increase in the false-alarm rates with respect to purely Gaussian noise: for the standard detection statistics, they resemble signals more than Gaussian noise.

6.7 Glitch-mitigation techniques

A number of glitch-mitigation techniques exist for CBC and burst searches. As this thesis focuses on CW searches, I will only briefly mention a few of these, in order to illustrate some parallels to the case of lines. Again, I can divide the existing methods into ad-hoc methods with implicit model assumptions and into explicit, Bayesian noise-modelling approaches.

The most popular methods are ad-hoc glitch-vetos, which are routinely used in typical CBC searches (e.g. Harry & Fairhurst 2011, Abadie et al. 2012d, Babak et al. 2013) and burst searches (e.g. Abbott et al. 2009f, Sutton et al. 2010, Abadie et al. 2012a). These include the χ^2-veto (Allen 2005), where the frequency range of an analysis is split into several subsets and consistency of a candidate across these smaller bands is required. Note that this should not be confused with another "χ^2-veto" in the CW literature (Itoh et al. 2004, Sancho de la Jordana & Sintes 2008, Aasi et al. 2014b), which is concerned with the consistency of a signal across subsets in *time*, for example the segments of a semi-coherent search. The CW version was actually derived from the CBC χ^2-veto. Other standard methods in the CBC field are the null-stream veto (Wen & Schutz 2005) and several varieties of signal-amplitude-consistency vetoes (Abbott et al. 2005c).

It is again instructive to observe the different combinations of coincident and coherent analysis steps. For instance, in current low-mass CBC searches the first step is a separate search in each detector. After a cut on single-detector χ^2 values, glitches are mitigated with a coincidence criterion and the construction of a new multi-detector statistic for the surviving candidates. This new statistic folds in the original single-detector statistics and the χ^2 values. Significance thresholds are set based on Monte-Carlo studies on actual data and injections.

The situation is different in typical "unmodelled" searches for signals for which there is no waveform model ("bursts"). Here, a main statistic is multi-detector-coherent, i.e. it accounts appropriately for time delays and antenna responses of the different detectors

to the same putative GW. This statistic is then augmented by additional statistics (see Sutton et al. 2010 for details) specifically designed for checking signal consistency across the detectors, by means of appropriate veto conditions.

Following the Bayesian approach, various explicit glitch models have been considered, including sine-Gaussians (Clark et al. 2007, Dal Canton et al. 2014) and wavelets (Littenberg & Cornish 2010). Proposals to use these in constructing full glitch-robust search pipelines include those by Clark et al. (2007) and Littenberg & Cornish (2010). Notably, Veitch & Vecchio (2010) have defined a glitch model that describes coincident single-detector candidates with independent amplitude parameters in different detectors. On the other hand, the signal model requires candidates to be both coincident and coherent across all detectors. Both hypotheses would fit a true signal equally well, but the glitch hypothesis would be weighed down by its larger prior volume ("Occam's razor"). In the case of glitches, however, the glitch hypothesis will generally provide a much better fit, allowing it to overcome its larger prior volume. This approach is very similar to the one I will be following in Sec. 7 for lines in CW searches.

6.8 Coincident lines in multiple detectors

The comparison of the approach to line-robustness described in Sec. 7 with the glitch-robust method of Veitch & Vecchio (2010) leads me to the topic of coincident lines. In the standard (incoherent) CBC pipelines, any candidate is already required to be *coincident* between detectors, so the method of Veitch & Vecchio (2010) adds the requirement of multi-detector *coherence* to distinguish GW signals from glitches. On the other hand, in the CW case, we will start from the inherently *coherent* multi-detector $\mathcal{F}$-statistic and introduce an additional *coincidence* requirement to distinguish CW signals from lines.

The method is therefore limited to non-coincident lines, or at least to lines which do not trigger the same templates in multiple detectors. Including coincident lines in the alternative hypothesis, without changing the general approach, would substantially weaken the detection power of this method. Hence, additional work is required to deal with coincident lines, probably involving a different line model, such as the unmodulated sinusoid model which I will briefly introduce in Sec. 13.

However, the present approach of focussing on non-coincident lines can still yield useful results, as the prevalence of coincident lines in actual detector data is quite limited. For example, the lines of known instrumental origin in the LIGO S5 data, as listed in Tables VI and VII of Aasi et al. (2013b) for the H1 and L1 detectors, overlap for a total bandwidth of only 1.6 Hz, corresponding to about 11% of the total contaminated bandwidth and 0.14% of the analysis range.

For another estimate, consider the final high-significance candidates from the Hough-based analysis of Aasi et al. (2013b). In the step before the $\mathcal{F}$-statistic consistency veto

was applied, there were 172 038 candidates. After the veto, a threshold of $2\mathcal{F} = 6.5$ was applied, retaining only 184 candidates.

If I go back to the original candidate lists of that search and permute these two steps, applying the threshold before the $\mathcal{F}$-veto, this yields another 2427 candidates above threshold, but which fail the veto. Hence, only 184 of 2611 candidates above threshold, or 7.05%, had $2\mathcal{F} \geq \max\{2\mathcal{F}^X\}$, and therefore could be due either to CW signals or to coincident lines. After removing the 172 candidates associated with hardware injections (simulated CW signals directly added to the detector data through test mass actuation, as a check of the detector systems and data analysis pipelines), this number is corrected down to 12 candidates out of 2439, or 0.46%. These remaining candidates were ruled out as possible CW signals by follow-ups (Shaltev et al. 2014), and thus are most likely due to coincident lines.

In addition, I can justify the rather simple line model, which does not account for coincident lines, by considering not just a single CW search step, but a full pipeline such as that used in Aasi et al. (2013b). A line-robust statistic only needs to succeed as a cheap and simple "first line of defence" against the most common noise artefacts, in order to reduce the number of spurious candidates, especially avoiding toplist saturation. More sophisticated steps to remove rarer types of artefacts, such as transient disturbances and coincident lines, can be applied to the surviving candidates in later stages of the pipeline, including follow-ups.

7 Line-robust statistics

After the preceding summary of the state of the art in the field of continuous gravitational wave (CW) data analysis, starting with this chapter I present original results of my four-year research project culminating in this thesis. Together with chapters 8, 9 and 10 (and the preceding Secs. 6.5–6.8) it forms an extended version of ideas and results first presented in Keitel et al. (2014), in collaboration with R. Prix, M. A. Papa, P. Leaci and M. Siddiqi. In the following, I refer to that publication as KPPLS14.

In this chapter, I will present – in more detail than in the journal paper – the derivation of a new set of detection statistics for CW data analysis. Compared to the standard $\mathcal{F}$-statistic (see Sec. 5.7), they promise increased robustness against line artefacts, while also relying on a more solid framework than the ad-hoc line-mitigation techniques described in Sec. 6.5. This approach is, however, limited to lines which are not coincident in all detectors.

I will begin by describing, in Sec. 7.1, a set of hypotheses for a given set of GW detector data. These include the standard Gaussian noise and CW signal hypotheses, as briefly introduced before in Secs. 5.1 and 5.2. The novelty here lies in the addition of a simple heuristic hypothesis designed to catch single-detector line-like disturbances. This is not directly guided by physical knowledge about line behaviour, as discussed in Sec. 6.2, but by the observation from previous CW data analyses that non-coincident disturbances cause a large fraction of noise outliers.

Next, I will introduce Bayesian hypothesis tests between these three options, rederiving the $\mathcal{F}$-statistic this way, and obtaining two variations of line-robust statistics, in Sec. 7.2. After first concentrating on the case of a coherent analysis of the whole data set, I will then give the semi-coherent generalisation in Sec. 7.3. In Sec. 7.4, I also present a tangential result about the expectation value of the conventional $\mathcal{F}$-statistic.

As already established in Sec. 5, my notation mostly follows that of Cutler & Schutz (2005) and Prix (2007b, 2011b). Two works which I refer to heavily from here on are those of Prix & Krishnan (2009), hereafter referred to as PK09, and of Prix, Giampanis & Messenger (2011), referred to as PGM11.

7.1 Hypotheses and their likelihoods

Given a multi-detector data set $x^X(t)$ and a model equation for a hypothesis, one can calculate the likelihood of $x^X(t)$ under that hypothesis. I will now present this calculation for a baseline Gaussian noise hypothesis $\mathcal{H}_\mathrm{G}$, the standard CW signal hypothesis $\mathcal{H}_\mathrm{S}$ and a simple single-detector "line" hypothesis $\mathcal{H}_\mathrm{L}$.

7.1.1 The Gaussian noise hypothesis $\mathcal{H}_\mathrm{G}$

As discussed in Sec. 5.1, Gaussian noise is a good model for undisturbed bands of data in a CW analysis. The Gaussian-noise hypothesis $\mathcal{H}_\mathrm{G}$ states that the data $\boldsymbol{x}(t)$ is fully specified by a Gaussian-distributed time series $\boldsymbol{n}(t)$:

$$\mathcal{H}_\mathrm{G} : \boldsymbol{x}(t) = \boldsymbol{n}(t) \,. \tag{7.1}$$

Using the standard Gaussian probability distribution function Eq. (4.30) and the scalar product Eq. (5.7), the probability for measuring a data set $\boldsymbol{x}(t)$ under this hypothesis is given by

$$P\left(\boldsymbol{x}|\mathcal{H}_\mathrm{G}\right) = \kappa\, \mathrm{e}^{-\frac{1}{2}\langle \boldsymbol{x}|\boldsymbol{x}\rangle} \,, \tag{7.2}$$

where κ is a data-independent normalisation constant, and from now on I will suppress the explicit t dependence.

Posterior probability for $\mathcal{H}_\mathrm{G}$

With Bayes' theorem from Eq. (4.7), it immediately follows that the posterior probability for $\mathcal{H}_\mathrm{G}$, given the observed data $\boldsymbol{x}$, is

$$P\left(\mathcal{H}_\mathrm{G}|\boldsymbol{x},\mathcal{I}\right) = \frac{P\left(\mathcal{H}_\mathrm{G}|\mathcal{I}\right) P\left(\boldsymbol{x}|\mathcal{H}_\mathrm{G}\right)}{P\left(\boldsymbol{x}|\mathcal{I}\right)} = \frac{P\left(\mathcal{H}_\mathrm{G}|\mathcal{I}\right)}{P\left(\boldsymbol{x}|\mathcal{I}\right)}\,\kappa\, \mathrm{e}^{-\frac{1}{2}\langle \boldsymbol{x}|\boldsymbol{x}\rangle} \,. \tag{7.3}$$

In general, this cannot be calculated directly, as it also contains the prior probability $P\left(\mathcal{H}_\mathrm{G}|\mathcal{I}\right)$ for the Gaussian-noise hypothesis and a normalisation factor $P\left(\boldsymbol{x}|\mathcal{I}\right)$. Whereas we could make an informed choice for the prior, or at least for its ratio to that for other hypotheses, $P\left(\boldsymbol{x}|\mathcal{I}\right)$ appears to pose a problem. This "probability of the data" would be given by a sum over a complete set of exhaustive and mutually exclusive hypotheses $\{\mathcal{H}_i\}$:

$$P\left(\boldsymbol{x}|\mathcal{I}\right) = \sum_i P\left(\boldsymbol{x}|\mathcal{H}_i\right) P\left(\mathcal{H}_i|\mathcal{I}\right) \,, \tag{7.4}$$

if such a set were known.

However, in practice we usually do not have a complete set of hypotheses. And when we limit ourselves to hypothesis tests between a finite set of hypotheses, we do not need

the absolute values of any posterior probabilities, but only the *odds* between different hypotheses. In such ratios, $P(\boldsymbol{x}|\mathcal{I})$ always cancels. Hence, in the present approach with three hypotheses, we only need the likelihoods and prior ratios to succeed. Eq. (7.3) is thus all we need to know about the Gaussian noise hypothesis.

As a final remark, let me note that for an unknown noise PSD, the hypothesis Eq. (7.1) should be more generally written as

$$\mathcal{H}_{\mathrm{G}} : \boldsymbol{x}(t) = \boldsymbol{n}(t) \quad \text{with prior} \quad P(\mathcal{S}|\mathcal{H}_{\mathrm{G}}) \,. \tag{7.5}$$

Assuming $\mathcal{S}$ to be known beforehand corresponds to a delta prior

$$P(\mathcal{S}|\mathcal{H}_{\mathrm{G}}) = \delta\left(\mathcal{S} - \widehat{\mathcal{S}}\right) \,, \tag{7.6}$$

so that we recover Eq. (7.3) after a marginalisation integral over $\mathcal{S}$ as a nuisance parameter.

In the following, I drop the explicit mention of prior information $\mathcal{I}$, writing $P(\mathcal{H}_{\mathrm{G}})$ for $P(\mathcal{H}_{\mathrm{G}}|\mathcal{I})$, and so on.

7.1.2 The CW signal hypothesis $\mathcal{H}_{\mathrm{S}}$

The presence of an astrophysical CW signal in the data $\boldsymbol{x}$, *in addition to* Gaussian noise, is formally expressed by the signal hypothesis

$$\mathcal{H}_{\mathrm{S}} : \boldsymbol{x}(t) = \boldsymbol{n}(t) + \boldsymbol{h}(t; \mathcal{A}, \lambda) \quad \text{with prior} \quad P(\mathcal{A}, \lambda|\mathcal{H}_{\mathrm{S}}) \,, \tag{7.7}$$

where $\boldsymbol{h}(t; \mathcal{A}, \lambda)$ is the signal waveform as discussed in Sec. 5.2. Again, I have split up the signal parameters into the set of four *amplitude parameters* $\mathcal{A}$ and the remaining *phase-evolution parameters* λ. Prescribing a specific prior distribution $P(\mathcal{A}, \lambda|\mathcal{H}_{\mathrm{S}})$ is an essential part of stating this hypothesis. Also, as a composite hypothesis. $\mathcal{H}_{\mathrm{S}}$ can be considered as the union of simple hypotheses $\mathcal{H}_{\mathrm{S}}(\mathcal{A}, \lambda)$.

Priors

In principle, the priors on $\mathcal{A}$ and λ could be interdependent. For example, a population of down-spinning NS with fixed-size "mountains" would place a specific frequency-dependent prior on the signal strength h_0. However, our present knowledge about the CW source population does not clearly favour any specific assumptions. Hence, we can reasonably simplify the following derivation by assuming that the prior factorises into

$$P(\mathcal{A}, \lambda|\mathcal{H}_{\mathrm{S}}) = P(\mathcal{A}|\mathcal{H}_{\mathrm{S}}) P(\lambda|\mathcal{H}_{\mathrm{S}}) \,. \tag{7.8}$$

The phase-evolution parameters λ are fixed by the search setup in a targeted pulsar search, whereas in a wide-parameter space search, these are free parameters. So for

the general case, we want to obtain any detection statistics as a function of λ, or to marginalise over λ only at the very end of the analysis.

Therefore, it is convenient to follow the approach of PK09 and PGM11 and start by *formally* assuming a single-template search, $\lambda = \lambda_\mathrm{s}$, but to keep the values of λ_s completely arbitrary, so that the results hold for any parameter space. We can formally express this with a delta prior, so that the full parameter space prior is

$$P\left(\mathcal{A}, \lambda | \mathcal{H}_\mathrm{S}\right) = P\left(\mathcal{A} | \mathcal{H}_\mathrm{S}\right) \delta(\lambda - \lambda_\mathrm{s}). \tag{7.9}$$

For increased simplicity, I will drop the phase-evolution parameters λ from all following expressions. Hence, these should be understood as functions of λ, with possible marginalisation or some other evaluation over the whole parameter space to follow at a later stage.

For the amplitude parameters, let us use the reparametrisation of JKS98, going from physical parameters $\{h_0, \cos\iota, \psi, \phi_0\}$ to the new set $\mathcal{A}^\mu = \mathcal{A}^\mu(h_0, \cos\iota, \psi, \phi_0)$, with indices $\mu = 1 \ldots 4$. This allows for factorising the waveform:

$$\boldsymbol{h}(t; \mathcal{A}, \lambda) = \mathcal{A}^\mu \, \boldsymbol{h}_\mu(t; \lambda), \tag{7.10}$$

with four simple basis functions $\boldsymbol{h}_\mu(t; \lambda)$ (see again Sec. 5.2). Note again that here, and in the following, automatic summation over repeated Greek indices is used.

Likelihood for $\mathcal{H}_\mathrm{S}(\mathcal{A})$

Before discussing the amplitude prior $P\left(\mathcal{A} | \mathcal{H}_\mathrm{S}\right)$ in detail, let me proceed one more step towards obtaining the likelihood under the signal hypothesis, which will help in informing the prior choice. In this step, let us assume some arbitrary, but specific values for $\mathcal{A}$, so that we can write down the likelihood for a simple hypothesis $\mathcal{H}_\mathrm{S}(\mathcal{A})$.

From Eq. (7.7), after subtracting the template waveform from the data time series, $\boldsymbol{x} - \boldsymbol{h}(\mathcal{A})$ should be described by Gaussian noise. Thus, adapting the Gaussian likelihood Eq. (7.2) yields the signal likelihood

$$P\left(\boldsymbol{x} | \mathcal{H}_\mathrm{S}, \mathcal{A}\right) = \kappa \, \mathrm{e}^{-\frac{1}{2}\langle \boldsymbol{x} - \boldsymbol{h}(\mathcal{A}) | \boldsymbol{x} - \boldsymbol{h}(\mathcal{A}) \rangle}. \tag{7.11}$$

With the signal factorisation from Eq. (7.10), this yields

$$\begin{aligned} P\left(\boldsymbol{x} | \mathcal{H}_\mathrm{S}, \mathcal{A}\right) &= \kappa \, \mathrm{e}^{-\frac{1}{2}\langle \boldsymbol{x} - \boldsymbol{h}(\mathcal{A}) | \boldsymbol{x} - \boldsymbol{h}(\mathcal{A}) \rangle} \\ &= P\left(\boldsymbol{x} | \mathcal{H}_\mathrm{G}\right) \, \mathrm{e}^{\mathcal{A}^\mu \langle \boldsymbol{x} | \boldsymbol{h}_\mu \rangle - \frac{1}{2}\mathcal{A}^\mu \langle \boldsymbol{h}_\mu | \boldsymbol{h}_\nu \rangle \mathcal{A}^\nu}. \end{aligned} \tag{7.12}$$

Now, we can use the four projections x_μ of the data unto the basis functions and the antenna pattern matrix $\mathcal{M}_{\mu\nu}$, defined as in Secs. 5.2 and 5.6:

$$x_\mu \equiv \langle \boldsymbol{x} | \boldsymbol{h}_\mu \rangle \quad \text{and} \quad \mathcal{M}_{\mu\nu} \equiv \langle \boldsymbol{h}_\mu | \boldsymbol{h}_\nu \rangle. \tag{7.13}$$

These allow us to rewrite Eq. (7.12) as

$$P\left(\boldsymbol{x} | \mathcal{H}_\mathrm{S}, \mathcal{A}\right) = P\left(\boldsymbol{x} | \mathcal{H}_\mathrm{G}\right) \, \mathrm{e}^{\mathcal{A}^\mu x_\mu - \frac{1}{2}\mathcal{A}^\mu \mathcal{M}_{\mu\nu} \mathcal{A}^\nu}. \tag{7.14}$$

Marginal likelihood for $\mathcal{H}_S$

Next, we want to obtain the likelihood of the composite signal hypothesis $\mathcal{H}_S$, which we can get by marginalising over $\mathcal{A}$:

$$P\left(\boldsymbol{x}|\mathcal{H}_S\right) = \int P\left(\boldsymbol{x}, \mathcal{A}|\mathcal{H}_S\right)\,\mathrm{d}\mathcal{A}\,. \tag{7.15}$$

Using Bayes' theorem and the unitarity condition on the prior,

$$\int P\left(\mathcal{A}|\mathcal{H}_S, \ldots\right)\,\mathrm{d}\mathcal{A} = 1\,, \tag{7.16}$$

we can rewrite this as

$$P\left(\boldsymbol{x}|\mathcal{H}_S\right) = \int P\left(\boldsymbol{x}|\mathcal{H}_S, \mathcal{A}\right)\,P\left(\mathcal{A}|\mathcal{H}_S\right)\,\mathrm{d}\mathcal{A}\,. \tag{7.17}$$

Given the $\mathcal{A}$-dependent likelihood $P\left(\boldsymbol{x}|\mathcal{H}_S, \mathcal{A}\right)$ from Eq. (7.14), this integral cannot, in general, be solved analytically. However, such a solution is possible for certain choices of amplitude priors $P\left(\mathcal{A}|\mathcal{H}_S\right)$, as was shown by PK09 and PGM11. A particularly simple, yet somewhat unphysical, choice is a uniform prior in a bounded region in the $\mathcal{A}^\mu$ space, which vanishes outside that region:

$$P\left(\{\mathcal{A}^\mu\}|\mathcal{H}_S\right) = \begin{cases} C & \text{for} \quad h_0(\mathcal{A}) < h_0^* \\ 0 & \text{otherwise}\,. \end{cases} \tag{7.18}$$

Here, C is a normalisation constant to be fixed by the unitarity condition Eq. (7.16), while the cut-off h_0^* need not be a constant, but could for example depend on λ.

In fact, for this and the following few chapters (i.e. the parts of this thesis corresponding to KPPLS14), let us pick a prior which seems rather arbitrary, but allows for the signal-versus-Gaussian hypothesis test to reproduce the standard $\mathcal{F}$-statistic. As was first found by PGM11, this is not achieved by a simple cut-off $h_0^* = h_{\max} = \mathrm{const}$, but by a prior

$$P\left(\{\mathcal{A}^\mu\}|\mathcal{H}_S\right) = \begin{cases} \frac{\sqrt{|\mathcal{M}|}}{(2\pi)^2}\,c_*^{-1} & \text{for} \quad h_0^4(\mathcal{A}) < \frac{70\,c_*}{\sqrt{|\mathcal{M}|}}\,, \\ 0 & \text{otherwise}\,, \end{cases} \tag{7.19}$$

where $|\mathcal{M}|$ is the determinant of the antenna-pattern matrix $\mathcal{M}_{\mu\nu}$ and the remaining free parameter has been absorbed into the constant c_*. Note that this translates to the $\widehat{\rho}_{\max}$ parameter used in PGM11 via $c_* = \frac{1}{70}\,\widehat{\rho}_{\max}^4$.

Such a prior has the advantage that existing numerically efficient implementations of the $\mathcal{F}$-statistic can be used. The alternative of using physical priors on the amplitude-parameter space (uniform in $\cos\iota$, ψ and ϕ_0 and a Jeffreys prior in h_0) has been investigated by PK09 and found to yield a $\mathcal{B}$-statistic with improved sensitivity, yet at an increased computational cost that at the moment does not make this $\mathcal{B}$-statistic appear

preferable. Even with further investigation of alternative priors by Whelan et al. (2014), this issue has not been settled yet.

The point of amplitude priors will be revisited in more detail in Sec. 12.2.1, but for now let us work with the prior Eq. (7.19). Going back to the marginal likelihood Eq. (7.17), it yields a significant simplification:

$$P\left(\boldsymbol{x}|\mathcal{H}_{\mathrm{S}}\right) = \frac{\sqrt{|\mathcal{M}|}}{(2\pi)^2}\, c_*^{-1} \int_{\mathbb{A}} P\left(\boldsymbol{x}|\mathcal{H}_{\mathrm{S}}, \mathcal{A}\right)\, \mathrm{d}\mathcal{A}\,, \qquad (7.20)$$

with the amplitude parameters limited to the set $\mathbb{A} \equiv \left\{ \mathcal{A} : h_0^4(\mathcal{A}) < \frac{70\, c_*}{\sqrt{|\mathcal{M}|}} \right\}$.

Inserting Eq. (7.14) and in the limit of a large integration boundary, $c_* \gg 1$, the integral becomes an analytically solvable Gaussian integral:

$$\int \mathrm{e}^{\mathcal{A}^{\mu} x_{\mu} - \frac{1}{2} \mathcal{A}^{\mu}\, \mathcal{M}_{\mu\nu}\, \mathcal{A}^{\nu}}\, \mathrm{d}^4\mathcal{A} = \sqrt{\frac{(2\pi)^4}{|\mathcal{M}|}}\, \mathrm{e}^{\frac{1}{2} x_{\mu}\, \mathcal{M}^{\mu\nu}\, x_{\nu}}\,. \qquad (7.21)$$

Here, $\mathcal{M}^{\mu\nu}$ is the inverse matrix to $\mathcal{M}_{\mu\nu}$, so that $\mathcal{M}_{\mu\alpha}\, \mathcal{M}^{\alpha\nu} = \delta_{\mu}^{\nu}$.

This is where the introduction of the $\sqrt{|\mathcal{M}|}$ factor in the prior pays off, as it cancels exactly with that from the integral volume. Thus, we obtain the final likelihood of the composite signal hypothesis in the simple form

$$P\left(\boldsymbol{x}|\mathcal{H}_{\mathrm{S}}\right) = P\left(\boldsymbol{x}|\mathcal{H}_{\mathrm{G}}\right)\, c_*^{-1}\, \mathrm{e}^{\frac{1}{2} x_{\mu}\, \mathcal{M}^{\mu\nu}\, x_{\nu}}\,. \qquad (7.22)$$

This looks familiar from the definition of the coherent multi-detector $\mathcal{F}$-statistic in Sec. 5.7,

$$2\mathcal{F}(\boldsymbol{x}) \equiv x_{\mu}\, \mathcal{M}^{\mu\nu}\, x_{\nu}\,, \qquad (7.23)$$

so that we can rewrite it again as

$$P\left(\boldsymbol{x}|\mathcal{H}_{\mathrm{S}}\right) = P\left(\boldsymbol{x}|\mathcal{H}_{\mathrm{G}}\right)\, c_*^{-1}\, \mathrm{e}^{\mathcal{F}(\boldsymbol{x})}\,. \qquad (7.24)$$

Posterior probability for $\mathcal{H}_{\mathrm{S}}$

Under Bayes' theorem, this transforms into the posterior probability for the signal hypothesis as

$$P\left(\mathcal{H}_{\mathrm{S}}|\boldsymbol{x}\right) = o_{\mathrm{SG}}\, c_*^{-1}\, P\left(\mathcal{H}_{\mathrm{G}}|\boldsymbol{x}\right)\, \mathrm{e}^{\mathcal{F}(\boldsymbol{x})}\,, \qquad (7.25)$$

where o_{SG} are the prior odds between the signal and Gaussian-noise hypotheses:

$$o_{\mathrm{SG}} \equiv \frac{P\left(\mathcal{H}_{\mathrm{S}}\right)}{P\left(\mathcal{H}_{\mathrm{G}}\right)}\,. \qquad (7.26)$$

7.1.3 Simple line hypothesis: a CW-like disturbance in a single detector

As already described quantitatively, our simple approach to modelling lines is based on the observation that many lines appear only in one detector, or at least are not exactly coincident in frequency between detectors over long time-scales. Therefore, we focus on single-detector lines which, in that one detector, closely mimic the phase evolution of a CW signal.

This will not be completely true for real lines, as they are associated with the terrestrial reference frame of the detector and not with the astrophysical frame which introduces part of the modulation of a real CW signal. However, such a model can be considered the worst-case scenario for single-detector lines, and will therefore catch those components of a real line which contribute the most power to a false alarm in a CW-signal template.

Single-detector line model: $\mathcal{H}_{\mathrm{L}}^{X}$

Mathematically, we can express such a model by a single-detector line hypothesis identical to the signal hypothesis Eq. (7.7) when restricted to a single detector X:

$$\mathcal{H}_{\mathrm{L}}^{X} = \mathcal{H}_{\mathrm{S}}^{X} : x^{X}(t) = n^{X}(t) + h^{X}(t; \mathcal{A}^{X}) \quad \text{with prior} \quad P\left(\mathcal{A}^{X} | \mathcal{H}_{\mathrm{L}}^{X}\right) . \qquad (7.27)$$

Before deciding on the prior $P\left(\mathcal{A}^{X} | \mathcal{H}_{\mathrm{L}}^{X}\right)$, let me first note that the physical amplitude parameters $\{h_0, \cos\iota, \psi, \phi_0\}$ of an astrophysical CW signal have no physical meaning for an instrumental line. However, we can still use these, or the transformed $\mathcal{A}^{\mu}$, simply as free numerical parameters of the heuristic line model.

The amplitude prior for signals, Eq. (7.19), was not informed by physical knowledge about the CW sources either, but instead chosen to simplify the marginal likelihood computation. As not much is known about the amplitude distribution of lines, either, and to keep to the approach of greatest simplicity, we just use the same prior Eq. (7.19) for $P\left(\mathcal{A}^{X} | \mathcal{H}_{\mathrm{L}}^{X}\right)$.

There remains the possibility to choose a cut-off c_* for the line amplitude prior different from that for signals. Here, we also make the choice to fix these to the same value. This value remains unconstrained for the moment, but will be revisited in Sec. 8.

The calculations of the $\mathcal{A}$-dependent likelihood, marginal likelihood and posterior probability for $\mathcal{H}_{\mathrm{L}}^{X}$ are completely analogous to the signal case. Similarly to Eq. (7.25), the result is

$$P\left(\mathcal{H}_{\mathrm{L}}^{X} | x^{X}\right) = c_*^{-1} P\left(\mathcal{H}_{\mathrm{G}}^{X} | x^{X}\right) o_{\mathrm{LG}}^{X} e^{\mathcal{F}^{X}(x^{X})} . \qquad (7.28)$$

We have already encountered the single-detector $\mathcal{F}$-statistic $\mathcal{F}^{X}(x^{X})$ in Sec. 6.5.3, and it is simply given by Eq. (5.46) restricted to the single detector X.

This posterior contains another prior line-odds factor, namely

$$o_{\mathrm{LG}}^X \equiv \frac{P\left(\mathcal{H}_{\mathrm{L}}^X\right)}{P\left(\mathcal{H}_{\mathrm{G}}^X\right)}. \tag{7.29}$$

Possible ways to quantify our prior knowledge about how often lines occur in a detector X, as opposed to purely Gaussian data, will be another subject of discussion in Sec. 8. Meanwhile, note that all quantities here still depend on the template parameters λ. Therefore, o_{LG}^X represents the prior line-versus-Gaussian odds in a specific template λ, not for the whole parameter space.

Model for a line in an arbitrary detector: $\mathcal{H}_{\mathrm{L}}$

Even though we are using a single-detector line model, we still want to model a line in any *arbitrary* single detector, while also analysing the data from the remaining detectors. Hence, we construct a generalised line hypothesis $\mathcal{H}_{\mathrm{L}}$ as a CW-like disturbance, $\mathcal{H}_{\mathrm{L}}^X$, in any single detector X, while the data from all other detectors, $Y \neq X$, is consistent with Gaussian noise, $\mathcal{H}_{\mathrm{G}}^Y$:

$$\begin{aligned}
\mathcal{H}_{\mathrm{L}} \equiv &\left(\mathcal{H}_{\mathrm{L}}^1 \text{ and } \mathcal{H}_{\mathrm{G}}^2 \text{ and } \mathcal{H}_{\mathrm{G}}^3 \ldots\right) \text{ or} \\
&\left(\mathcal{H}_{\mathrm{G}}^1 \text{ and } \mathcal{H}_{\mathrm{L}}^2 \text{ and } \mathcal{H}_{\mathrm{G}}^3 \ldots\right) \text{ or } \ldots.
\end{aligned} \tag{7.30}$$

As mentioned before, $\mathcal{H}_{\mathrm{L}}$ does not cover coincident lines, which would require $\mathcal{H}_{\mathrm{L}}^X$ and $\mathcal{H}_{\mathrm{L}}^Y$ with $Y \neq X$. Specifically, lines that are present in several detectors for an overlapping data span at least need to have different phase-evolution parameters λ. Otherwise, they might fit the full multi-detector signal hypothesis $\mathcal{H}_{\mathrm{S}}$ better.

It is also worth noting that, if we had allowed for coincident, then even the case were all detectors contain a line, i.e.

$$\left(\mathcal{H}_{\mathrm{L}}^1 \text{ and } \mathcal{H}_{\mathrm{L}}^2 \text{ and } \mathcal{H}_{\mathrm{L}}^3 \ldots\right), \tag{7.31}$$

would not be identical to $\mathcal{H}_{\mathrm{S}}$: for lines, no consistency of amplitude parameters $\mathcal{A}^X$ for all detectors is required, while a signal should have $\mathcal{A}^X = \mathcal{A}^Y \,\forall\, X, Y$.

Posterior probability for $\mathcal{H}_{\mathrm{L}}$

In order to obtain the posterior probability of $\mathcal{H}_{\mathrm{L}}$, we assume – as was already implicitly the case for $\mathcal{H}_{\mathrm{G}}$ and $\mathcal{H}_{\mathrm{S}}$ – that the Gaussian-noise distributions of the individual detectors are independent. Then, as the various alternatives in Eq. (7.30) are mutually exclusive,

the total probability of $\mathcal{H}_\mathrm{L}$ is the sum of these contributions, which in turn factorise into the single-detector probabilities:

$$
\begin{aligned}
P\left(\mathcal{H}_\mathrm{L}|\boldsymbol{x}\right) &= P\left(\mathcal{H}_\mathrm{L}^1|x^1\right) P\left(\mathcal{H}_\mathrm{G}^2|x^2\right) P\left(\mathcal{H}_\mathrm{G}^3|x^3\right) \times \ldots \\
&\quad + P\left(\mathcal{H}_\mathrm{G}^1|x^1\right) P\left(\mathcal{H}_\mathrm{L}^2|x^2\right) P\left(\mathcal{H}_\mathrm{G}^3|x^3\right) \times \ldots \\
&\quad + \ldots \\
&= \sum_X P\left(\mathcal{H}_\mathrm{L}^X|x^X\right) \prod_{Y \neq X} P\left(\mathcal{H}_\mathrm{G}^Y|x^Y\right) .
\end{aligned}
\tag{7.32}
$$

Inserting the single-detector probabilities for $\mathcal{H}_\mathrm{L}^X$ and $\mathcal{H}_\mathrm{G}^X$ from Eq. (7.28) and Eq. (7.3) and simplifying the result by using the relation

$$
\prod_X P\left(\mathcal{H}_\mathrm{G}^X|x^X\right) = P\left(\mathcal{H}_\mathrm{G}|\boldsymbol{x}\right) ,
\tag{7.33}
$$

the full posterior probability for the line hypothesis $\mathcal{H}_\mathrm{L}$ is

$$
P\left(\mathcal{H}_\mathrm{L}|\boldsymbol{x}\right) = c_*^{-1} P\left(\mathcal{H}_\mathrm{G}|\boldsymbol{x}\right) \sum_X o_\mathrm{LG}^X \, \mathrm{e}^{\mathcal{F}^X(x^X)} .
\tag{7.34}
$$

The total prior odds between lines and Gaussian noise are

$$
o_\mathrm{LG} \equiv \sum_X o_\mathrm{LG}^X = \frac{P\left(\mathcal{H}_\mathrm{L}\right)}{P\left(\mathcal{H}_\mathrm{G}\right)} ,
\tag{7.35}
$$

applying again to a given template λ.

As prior odds with their range from zero to infinity can be unintuitive and difficult to handle numerically, a reparametrisation of these quantities is more convenient. For each detector X of a total number N_det of detectors, the quantity

$$
r^X \equiv \frac{o_\mathrm{LG}^X}{o_\mathrm{LG}/N_\mathrm{det}} ,
\tag{7.36}
$$

can be understood as a relative weight of per-detector line probability. These weights are non-negative, with a range of $[0, N_\mathrm{det}]$ and a normalisation condition

$$
\sum_X r^X = N_\mathrm{det} .
\tag{7.37}
$$

If all detectors are equally likely to contain a line, these simplify to $r^X = 1$ for all X.

Instead of the sum in Eq. (7.34), we can also use an average over detectors. For an arbitrary quantity Q^X, let us denote the average as

$$
\left\langle Q^X \right\rangle_X \equiv \frac{1}{N_\mathrm{det}} \sum_X Q^X .
\tag{7.38}
$$

For the prior line-weights, this definition yields $\left\langle r^X \right\rangle_X = 1$.

The rewritten posterior probability for $\mathcal{H}_\mathrm{L}$ from Eq. (7.34) then reads:

$$
P\left(\mathcal{H}_\mathrm{L}|\boldsymbol{x}\right) = c_*^{-1} P\left(\mathcal{H}_\mathrm{G}|\boldsymbol{x}\right) o_\mathrm{LG} \left\langle r^X \, \mathrm{e}^{\mathcal{F}^X(x^X)} \right\rangle_X .
\tag{7.39}
$$

7.1.4 Extended noise hypothesis: Gaussian noise and lines

Instead of treating Gaussian noise and lines as two separate hypotheses, $\mathcal{H}_\mathrm{G}$ and $\mathcal{H}_\mathrm{L}$, we can also combine the two into a single noise hypothesis. After all, the main interest of a CW analysis lies in detecting astrophysical CW signals, and thus lines are just another kind of noise, even if they are distinct from Gaussian noise in their properties and origin.

Formally, we can write this extended noise hypothesis simply as

$$\mathcal{H}_\mathrm{GL} : (\mathcal{H}_\mathrm{G} \text{ or } \mathcal{H}_\mathrm{L}) \, . \tag{7.40}$$

From the definition of $\mathcal{H}_\mathrm{L}$, it is mutually exclusive with $\mathcal{H}_\mathrm{G}$ – except in the limit of zero line amplitudes, which however is a null set and therefore not relevant in probability summations. Hence, the posterior probability for $\mathcal{H}_\mathrm{GL}$ is simply the sum of the two contributions from Eqs. (7.3) and (7.39):

$$
\begin{aligned}
P\left(\mathcal{H}_\mathrm{GL}|\boldsymbol{x}\right) &= P\left(\mathcal{H}_\mathrm{G}|\boldsymbol{x}\right) + P\left(\mathcal{H}_\mathrm{L}|\boldsymbol{x}\right) \\
&= P\left(\mathcal{H}_\mathrm{G}|\boldsymbol{x}\right) \left(1 + c_*^{-1} \, o_\mathrm{LG} \, \left\langle r^X \mathrm{e}^{\mathcal{F}^X(x^X)} \right\rangle_X \right) \, .
\end{aligned}
\tag{7.41}
$$

7.2 Coherent detection statistics

As discussed in Secs. 4.2.3 and 4.3, the posterior odds from a Bayesian hypothesis test can be used as a classical detection statistic. More generally, any monotonic function of the odds is an equivalent detection statistic in the Neyman-Pearson sense, as only the ranking of candidates influences the detection efficiency, and ranking is invariant under monotonic transformations.

With the set of hypotheses just introduced, we can perform three binary hypothesis tests with the goal of detecting CW signals, and then construct the corresponding detection statistics:

1. Testing the CW signal hypothesis $\mathcal{H}_\mathrm{S}$ against the Gaussian noise hypothesis $\mathcal{H}_\mathrm{G}$ reproduces the standard $\mathcal{F}$-statistic, when using the amplitude priors discussed in Sec. 7.1.2. This is already known to have close-to-optimal performance in pure Gaussian noise, limited only by the unphysical prior choice (PK09).

2. Instead, the null hypothesis for pure noise can be replaced by the simple heuristic line hypothesis $\mathcal{H}_\mathrm{L}$. Testing $\mathcal{H}_\mathrm{S}$ against this defines a new *line-veto statistic*. This should be well suited for data sets dominated by strong lines, where the Gaussian-noise contribution is negligible. Also, it could be used in a two-stage approach where a threshold has already been placed on the multi-detector $\mathcal{F}$-statistic to remove most candidates from the bulk of the Gaussian distribution.

3. A more general *line-robust statistic* follows from allowing the noise to contain both a Gaussian contribution and single-detector lines. We achieve this by testing $\mathcal{H}_{\mathrm{S}}$ against the combined hypothesis $\mathcal{H}_{\mathrm{GL}} : (\mathcal{H}_{\mathrm{G}} \text{ or } \mathcal{H}_{\mathrm{L}})$.

In the following, to simplify notation, I will usually neglect the dependencies of multi- or single-detector detection statistics and other posterior quantities on $\boldsymbol{x}$ and x^X, after the quantities are first introduced, and unless there is a specific need to highlight the dependence on the data in some context.

7.2.1 Rederiving the $\mathcal{F}$-statistic

Traditionally, the $\mathcal{F}$-statistic has been derived in a frequentist way by maximising over amplitude parameters, as presented in Sec. 5.7. However, as was first shown by PK09 and as we have seen in Sec. 7.1.2, it also arises naturally from the posterior probability for the CW signal hypothesis, Eq. (7.25). In the posterior odds between $\mathcal{H}_{\mathrm{S}}$ and $\mathcal{H}_{\mathrm{G}}$ (with probability from Eq. (7.3)), the factor $P\left(\mathcal{H}_{\mathrm{G}}|\boldsymbol{x}\right)$ cancels:

$$O_{\mathrm{SG}}(\boldsymbol{x}) \equiv \frac{P\left(\mathcal{H}_{\mathrm{S}}|\boldsymbol{x}\right)}{P\left(\mathcal{H}_{\mathrm{G}}|\boldsymbol{x}\right)} = o_{\mathrm{SG}}\, c_*^{-1}\, \mathrm{e}^{\mathcal{F}(\boldsymbol{x})}\,. \tag{7.42}$$

As the prior odds o_{SG} are fixed before the start of an analysis, the prior cut-off factor c_* is a constant and $\mathrm{e}^{\mathcal{F}}$ is a monotonic function of $\mathcal{F}$, $O_{\mathrm{SG}}(\boldsymbol{x})$ as a detection statistic is equivalent to $\mathcal{F}(\boldsymbol{x})$.

It is notable that the cut-off parameter c_* from the unphysical "$\mathcal{F}$-statistic prior" of Eq. (7.19) (corresponding to non-isotropic spin orientations) appears explicitly in the posterior odds $O_{\mathrm{SG}}(\boldsymbol{x})$. This makes the strangeness of this prior more obvious than in the frequentist derivation, where it was used only implicitly. However, this value does not influence the performance of $O_{\mathrm{SG}}(\boldsymbol{x})$ as a detection statistic, and as noted it is equivalent to $\mathcal{F}(\boldsymbol{x})$ itself.

We also find the corresponding (marginal) likelihood ratio or *Bayes factor* (see Eq. (4.14)),

$$B_{\mathrm{SG}}(\boldsymbol{x}) \equiv \frac{P\left(\boldsymbol{x}|\mathcal{H}_{\mathrm{S}}\right)}{P\left(\boldsymbol{x}|\mathcal{H}_{\mathrm{G}}\right)} = c_*^{-1}\, \mathrm{e}^{\mathcal{F}(\boldsymbol{x})}\,, \tag{7.43}$$

which is again an equivalent detection statistic to $\mathcal{F}$.

7.2.2 Line-veto statistic O_{SL}

Signal-versus-line odds ratio

Next, let us consider the odds between signal and line hypothesis, corresponding to the assumption that all the noise consists of lines. The posterior odds simply follow from the

probabilities in Eqs. (7.25) and (7.39):

$$
O_{\mathrm{SL}}(\boldsymbol{x}) \equiv \frac{P\left(\mathcal{H}_{\mathrm{S}}|\boldsymbol{x}\right)}{P\left(\mathcal{H}_{\mathrm{L}}|\boldsymbol{x}\right)} = o_{\mathrm{SL}}\,\frac{\mathrm{e}^{\mathcal{F}(\boldsymbol{x})}}{\left\langle r^{X}\,\mathrm{e}^{\mathcal{F}^{X}(x^{X})}\right\rangle_{X}}\,. \tag{7.44}
$$

Here another prior odds factor appears,

$$
o_{\mathrm{SL}} \equiv \frac{P\left(\mathcal{H}_{\mathrm{S}}\right)}{P\left(\mathcal{H}_{\mathrm{L}}\right)} = \frac{o_{\mathrm{SG}}}{o_{\mathrm{LG}}}\,. \tag{7.45}
$$

Meanwhile, in contrast to O_{SG}, the amplitude-prior cut-off c_{*} does not appear in O_{SL}, as it cancels out. However, had we used different cut-offs c_{*}^{S} and c_{*}^{L} for the signal and line case, respectively, the result would be

$$
O_{\mathrm{SL}}'(\boldsymbol{x}) = o_{\mathrm{SL}}\,\frac{c_{*}^{\mathrm{L}}}{c_{*}^{\mathrm{S}}}\,\frac{\mathrm{e}^{\mathcal{F}(\boldsymbol{x})}}{\left\langle r^{X}\,\mathrm{e}^{\mathcal{F}^{X}(x^{X})}\right\rangle_{X}}\,. \tag{7.46}
$$

This introduces a mere proportionality factor, so that O_{SL} and O_{SL}' still are equivalent detection statistics.

Log-odds and Bayes factor

While the signal-to-Gaussian-noise test yields the odds $O_{\mathrm{SG}} \propto \mathrm{e}^{\mathcal{F}}$, it is often more convenient to use the $\mathcal{F}$-statistic values themselves, due to numerical difficulties with the huge range of an exponential. To get a quantity that scales similarly to $\mathcal{F}$, let us consider the logarithm of the signal-to-line odds from Eq. (7.44):

$$
\ln O_{\mathrm{SL}} = \ln o_{\mathrm{SL}} + \mathcal{F} - \ln\left\langle r^{X}\mathrm{e}^{\mathcal{F}^{X}}\right\rangle_{X}\,. \tag{7.47}
$$

Recalling that the multi-detector average $\langle\,\rangle_{X}$ from Eq. (7.38) is basically a sum, we can split the last term using the "log-sum-exp formula", which is a common trick in numerical computation (Press et al. 2007):

$$
\ln\left(\sum_{n=1}^{N}\mathrm{e}^{Q_{n}}\right) = \max_{n}\left\{Q_{n}\right\} + \ln\left(\sum_{n=1}^{N}\mathrm{e}^{Q_{n}-\max_{n}\{Q_{n}\}}\right)\,. \tag{7.48}
$$

Thus, defining the maximum single-detector contribution – in terms of $\mathcal{F}^{X}$-statistics weighted by prior line-odds – as

$$
\mathcal{F}_{\max}' \equiv \max_{X}\left\{\mathcal{F}^{X} + \ln r^{X}\right\}\,, \tag{7.49}
$$

the log-odds turn into

$$
\ln O_{\mathrm{SL}} = \ln o_{\mathrm{SL}} + \mathcal{F} - \mathcal{F}_{\max}' - \ln\left\langle r^{X}\mathrm{e}^{\mathcal{F}^{X}-\mathcal{F}_{\max}'}\right\rangle_{X}\,. \tag{7.50}
$$

This form is useful to get an intuitive understanding of how O_{SL} behaves as a function of the multi- and single-detector $\mathcal{F}$- and $\mathcal{F}^X$-statistic values. Per definition, $\mathrm{e}^{\mathcal{F}'_{\max}} \geq r^X \, \mathrm{e}^{\mathcal{F}^X}$, and so all of the terms in the detector-average in Eq. (7.50) are bounded within $[0, 1]$. With N_{det} terms in total, the logarithmic average $\ln \langle \ldots \rangle_X$ is then bounded within $[-\ln N_{\mathrm{det}}, 0]$.

When one of the single-detector terms is much larger than all others,

$$\ln O_{\mathrm{SL}} \approx \ln o_{\mathrm{SL}} + \mathcal{F} - \mathcal{F}'_{\max} \,, \tag{7.51}$$

while when all terms are equal,

$$\ln O_{\mathrm{SL}} = \ln o_{\mathrm{SL}} + \mathcal{F} - \mathcal{F}'_{\max} + \ln N_{\mathrm{det}} \,. \tag{7.52}$$

In all cases of practical interest, when N_{det} is not huge, the logarithmic correction is at most of order 1.

Another interesting case is when $\mathcal{F}$ or $\mathcal{F}'_{\max}$ are very large. In that case, the bounded logarithmic correction is negligible, independent of the relative ratios of the $\mathcal{F}^{X'}$. The full odds ratio is then well approximated by

$$\ln O_{\mathrm{SL}}(\boldsymbol{x}) \approx \ln o_{\mathrm{SL}} + \mathcal{F}(\boldsymbol{x}) - \mathcal{F}'_{\max}(\boldsymbol{x}) \,. \tag{7.53}$$

If there is no prior knowledge about differing line probabilities in each detector, the natural assumption is $r^X = 1$. Then, the leading term is simply $\mathcal{F}'_{\max} = \max\{\mathcal{F}^X\}$ and thus

$$\ln O_{\mathrm{SL}}(\boldsymbol{x}) \approx \mathcal{F}(\boldsymbol{x}) - \max_X\{\mathcal{F}^X(x^X)\} + \ln o_{\mathrm{SL}} \,. \tag{7.54}$$

Considering $\ln O_{\mathrm{SL}}$ as a detection statistic, we can ignore the constant prior odds. In this limit, the computation therefore reduces to a comparison of the multi-detector $\mathcal{F}$-statistic with the highest single-detector contribution.

Again, we can equivalently use the Bayes factor as a detection statistic:

$$B_{\mathrm{SL}}(\boldsymbol{x}) \equiv \frac{P\left(\boldsymbol{x}|\mathcal{H}_{\mathrm{S}}\right)}{P\left(\boldsymbol{x}|\mathcal{H}_{\mathrm{L}}\right)} = \frac{O_{\mathrm{SL}}(\boldsymbol{x})}{o_{\mathrm{SL}}} = \frac{\mathrm{e}^{\mathcal{F}(\boldsymbol{x})}}{\left\langle r^X \, \mathrm{e}^{\mathcal{F}^X(x^X)} \right\rangle_X} \,, \tag{7.55}$$

or, most conveniently for numerical implementations, its logarithm:

$$\ln B_{\mathrm{SL}}(\boldsymbol{x}) = \mathcal{F} - \mathcal{F}'_{\max} - \ln \left\langle r^X \mathrm{e}^{\mathcal{F}^X - \mathcal{F}'_{\max}} \right\rangle_X \,. \tag{7.56}$$

Relation to the $\mathcal{F}$-statistic consistency veto

The limiting behaviour of O_{SL} from Eq. (7.54) is especially interesting because we can use it to re-obtain the $\mathcal{F}$-statistic consistency veto, which has been used as an ad-hoc line mitigation technique before (see Sec. 6.5.3 and also Aasi et al. 2013a,b, Behnke 2013).

Let us consider the limit of large $\mathcal{F}$ and $\mathcal{F}_{\mathrm{max}}^X$ and assume $r^X = 1$ for all X. Fixing the detection threshold on $O_{\mathrm{SL}}(\boldsymbol{x})$ to a value equal to the prior odds o_{SL}, any candidate counts as detected exactly if $\mathcal{F} \geq \mathcal{F}_{\mathrm{max}}^X$.

An equivalent formal prescription is to start with a set of candidates and then to apply a veto at that threshold, i.e.

$$\text{if} \quad \mathcal{F}(\boldsymbol{x}) < \max_X \{\mathcal{F}^X(x)\} \quad \Longrightarrow \quad \text{veto the candidate}\,, \tag{7.57}$$

and to accept all candidates passing this veto step.

We can again turn this into a detection statistic, the $\mathcal{F}^{+\mathrm{veto}}$-statistic, by ranking the unvetoed candidates by their original multi-detector $\mathcal{F}$-statistic, while assigning a zero value to all vetoed candidates:

$$\mathcal{F}^{+\mathrm{veto}}(\boldsymbol{x}) \equiv \begin{cases} \mathcal{F}(\boldsymbol{x}) & \text{if } \mathcal{F}(\boldsymbol{x}) \geq \max_X \{\mathcal{F}^X(x)\}\,, \\ 0 & \text{otherwise}\,. \end{cases} \tag{7.58}$$

There is an important subtlety here: Indeed we can express the single-step $\mathcal{F}$-statistic consistency veto prescription as a special threshold on the O_{SL}-statistic (in a limiting case). However, as a detection statistic $\mathcal{F}^{+\mathrm{veto}}$ is *not in general* equivalent to any form of the O_{SL}-statistic. Specifically, as soon as arbitrary thresholds on both O_{SL} and $\mathcal{F}^{+\mathrm{veto}}$ are allowed, their detection power can be different, as the ranking of candidates is different. The two statistics are not monotonic functions of each other and therefore not equivalent. I will also demonstrate this difference with simulated data in Sec. 9, see for example Fig. 9.8.

7.2.3 Line-robust detection statistic O_{SGL}

Signal-versus-extended-noise odds ratio

Another detection statistic results from testing the signal hypothesis against the combined noise hypothesis $\mathcal{H}_{\mathrm{GL}}$ from Sec. 7.1.4, i.e. when we allow for both Gaussian and line components in the noise model. With the posteriors from Eqs. (7.25) and (7.41), the corresponding odds are

$$O_{\mathrm{SGL}}(\boldsymbol{x}) \equiv \frac{P(\mathcal{H}_{\mathrm{S}}|\boldsymbol{x})}{P(\mathcal{H}_{\mathrm{GL}}|\boldsymbol{x})} = \frac{o_{\mathrm{SG}}\, \mathrm{e}^{\mathcal{F}(\boldsymbol{x})}}{c_* + o_{\mathrm{LG}} \left\langle r^X \mathrm{e}^{\mathcal{F}^X} \right\rangle_X}\,. \tag{7.59}$$

There are some interesting observations to be made about this *line-robust statistic*. First, these odds are the harmonic sum of the two others we have previously considered:

$$O_{\mathrm{SGL}}(\boldsymbol{x}) = \left[O_{\mathrm{SG}}^{-1}(\boldsymbol{x}) + O_{\mathrm{SL}}^{-1}(\boldsymbol{x}) \right]^{-1} . \tag{7.60}$$

This relation illustrates the conceptual difference to an ad-hoc two-stage approach with two independent thresholds on O_{SG} and on O_{SL}: Instead, as O_{SGL} is the straightforward result of a Bayesian derivation, a single threshold on this combined statistic should be preferable in all cases where the data is well described by a mixture of $\mathcal{H}_{\mathrm{G}}$ and $\mathcal{H}_{\mathrm{L}}$.

Second, the amplitude-prior cut-off parameter c_* from Eq. (7.19) becomes interesting at this point. It is only a scale factor in O_{SG} and thus not relevant for the performance as a detection statistic, and it cancels out completely in O_{SL}. However, Eq. (7.59) shows that this parameter does affect the properties of O_{SGL}, since it determines the scaling between the constant denominator term (coming from the $\mathcal{H}_{\mathrm{G}}$ contribution) and the $\mathcal{F}^X$-dependent terms (coming from $\mathcal{H}_{\mathrm{L}}$).

To better understand this effect, let us first rewrite Eq. (7.59) into a clearer form. We introduce the signal-versus-extended-noise prior odds

$$o_{\mathrm{SGL}} \equiv \frac{P\left(\mathcal{H}_{\mathrm{S}}\right)}{P\left(\mathcal{H}_{\mathrm{GL}}\right)} , \tag{7.61}$$

which are related to previously defined prior odds through

$$o_{\mathrm{SG}} = o_{\mathrm{SGL}}\left(1 + o_{\mathrm{LG}}\right) . \tag{7.62}$$

Furthermore, it is useful to define a prior "line probability"

$$p_{\mathrm{L}} \equiv P\left(\mathcal{H}_{\mathrm{L}}|\mathcal{H}_{\mathrm{GL}}\right) = \frac{P\left(\mathcal{H}_{\mathrm{L}}\right)}{P\left(\mathcal{H}_{\mathrm{GL}}\right)} = \frac{o_{\mathrm{LG}}}{1 + o_{\mathrm{LG}}} , \tag{7.63}$$

measuring the relative prior weight of lines versus "lines plus Gaussian noise". Whereas all previously introduced prior odds are unbounded towards positive infinity, p_{L} corresponds to the odds between a hypothesis $\mathcal{H}_{\mathrm{L}}$ and another $\mathcal{H}_{\mathrm{GL}}$ which *contains* the first, so that it is also a true probability, with values in $[0, 1]$. The relation to the corresponding single-detector quantities

$$p_{\mathrm{L}}^X \equiv \frac{P\left(\mathcal{H}_{\mathrm{L}}^X\right)}{P\left(\mathcal{H}_{\mathrm{GL}}^X\right)} = \frac{o_{\mathrm{LG}}^X}{1 + o_{\mathrm{LG}}^X} , \tag{7.64}$$

though, is more complicated than for the prior odds:

$$p_{\mathrm{L}} = \frac{\sum\limits_X \frac{p_{\mathrm{L}}^X}{1 - p_{\mathrm{L}}^X}}{1 + \sum\limits_X \frac{p_{\mathrm{L}}^X}{1 - p_{\mathrm{L}}^X}} , \tag{7.65}$$

using the inverse relations

$$o_{\mathrm{LG}} = \frac{p_{\mathrm{L}}}{1 - p_{\mathrm{L}}} , \quad o_{\mathrm{LG}}^X = \frac{p_{\mathrm{L}}^X}{1 - p_{\mathrm{L}}^X} . \tag{7.66}$$

As a third step, the constant term becomes more similar to the $e^{\mathcal{F}^X}$-like terms when we introduce a new "tuning" or transition scale parameter

$$\mathcal{F}^{(0)}_* \equiv \ln c_* \,. \tag{7.67}$$

Using these three redefinitions, we can then rewrite Eq. (7.59) as

$$O_{\mathrm{SGL}}(\boldsymbol{x}) = o_{\mathrm{SGL}} \, \frac{e^{\mathcal{F}(\boldsymbol{x})}}{(1 - p_{\mathrm{L}}) \, e^{\mathcal{F}^{(0)}_*} + p_{\mathrm{L}} \, \left\langle r^X e^{\mathcal{F}^X(x^X)} \right\rangle_X} \,. \tag{7.68}$$

Limiting cases of O_{SGL}, log-odds and Bayes factor

This new form of O_{SGL} is well-suited to investigate its behaviour as a function of the line prior p_{L} and of the single-detector $\mathcal{F}^X$ values, as well as its limiting cases.

In the limit of a-priori certainty that there are no lines in the data, $p_{\mathrm{L}} \to 0$, comparison of Eq. (7.68) with Eq. (7.42) shows that O_{SGL} reduces to the $\mathcal{F}$-statistic:

$$O_{\mathrm{SGL}}(\boldsymbol{x}) \to O_{\mathrm{SG}}(\boldsymbol{x}) \propto e^{\mathcal{F}(\boldsymbol{x})} \quad \text{for} \quad p_{\mathrm{L}} \to 0 \,. \tag{7.69}$$

In the other extreme, when believing for certain that the noise is completely dominated by lines, it reduces to the pure line-veto statistic of Eq. (7.44):

$$O_{\mathrm{SGL}}(\boldsymbol{x}) \to O_{\mathrm{SL}}(\boldsymbol{x}) \quad \text{for} \quad p_{\mathrm{L}} \to 1 \,. \tag{7.70}$$

Complementarily, we can consider any fixed p_{L} value in $(0, 1)$ and analyse the transition between these two extremes depending on the data, that is on the $\mathcal{F}^X(x^X)$ values compared to the prior parameter $\mathcal{F}^{(0)}_*$. To illustrate this behaviour more clearly, Eq. (7.68) can be rewritten in yet another form, using the relations $o_{\mathrm{SGL}} = p_{\mathrm{L}} \, o_{\mathrm{SL}}$ and $(1 - p_{\mathrm{L}})/p_{\mathrm{L}} = o_{\mathrm{LG}}^{-1}$. Introducing a "transition scale"

$$\mathcal{F}_* \equiv \mathcal{F}^{(0)}_* - \ln o_{\mathrm{LG}} \,, \tag{7.71}$$

we obtain

$$O_{\mathrm{SGL}}(\boldsymbol{x}) = o_{\mathrm{SL}} \, \frac{e^{\mathcal{F}(\boldsymbol{x})}}{e^{\mathcal{F}_*} + \left\langle r^X e^{\mathcal{F}^X(x^X)} \right\rangle_X} \,. \tag{7.72}$$

This reparametrisation shows that $\mathcal{F}_*$ gives the scale of a transition of $O_{\mathrm{SGL}}(\boldsymbol{x})$ between $O_{\mathrm{SG}}(\boldsymbol{x}) \propto e^{\mathcal{F}(\boldsymbol{x})}$ and $O_{\mathrm{SL}}(\boldsymbol{x})$, depending on the values of $\mathcal{F}^X$: The "line-veto term" $\left\langle r^X e^{\mathcal{F}^X} \right\rangle_X$ in Eq. (7.72) only starts to play a role when it is comparable to $e^{\mathcal{F}_*}$. Note, however, that while this transition can be very steep, it is in principle smooth, not a discrete switch between the limiting odds.

As a last step to make this behaviour more explicit, let us again consider the log-odds:

$$\ln O_{\mathrm{SGL}}(\boldsymbol{x}) = \ln o_{\mathrm{SL}} + \mathcal{F}(\boldsymbol{x}) - \mathcal{F}''_{\max}(x) - \ln \left(e^{\mathcal{F}_* - \mathcal{F}''_{\max}} + \left\langle r^X e^{\mathcal{F}^X(x^X) - \mathcal{F}''_{\max}(\boldsymbol{x})} \right\rangle_X \right) ,$$
$$(7.73)$$

where the largest denominator term is

$$\mathcal{F}''_{\max}(\boldsymbol{x}) \equiv \max \left\{ \mathcal{F}_*, \, \mathcal{F}^X(x^X) + \ln r^X \right\} . \qquad (7.74)$$

Again, as in the $\ln O_{\mathrm{SL}}$ case in Eq. (7.50), the logarithmic correction is of order unity. Therefore, $\ln O_{\mathrm{SGL}}$ approximately corresponds to $\ln O_{\mathrm{SL}}$ when $\max\{\mathcal{F}^X + \ln r^X\} > \mathcal{F}_*$, and to $\ln O_{\mathrm{SG}}$ otherwise.

The transition scale $\mathcal{F}_*$ from Eq. (7.71) is mostly determined by the arbitrary prior parameter $\mathcal{F}_*^{(0)}$, and then corrected by the more physically meaningful $\ln o_{\mathrm{LG}}$. Thus, choosing a value for $\mathcal{F}_*^{(0)}$ has a critical influence on the behaviour of O_{SGL}: for high $\mathcal{F}_*^{(0)}$, it becomes more similar to the $\mathcal{F}$-statistic and more sensitive in nearly-Gaussian data; while for low $\mathcal{F}_*^{(0)}$, it becomes more similar to O_{SL} and better in line-heavy data.

Ideally, we would choose this tuning parameter depending on expected signal and noise populations. But there is no such physical guidance, as it derives from the unphysical choice of amplitude priors in Eq. (7.19). Hence, some empirical method has to replace it. I will discuss this issue, and a proposed method, in more detail in Sec. 8.2.

However, outside of this analysis of limiting and transition behaviour, the parametrisation of Eq. (7.68) is preferable to that of Eq. (7.72), mostly because Eq. (7.68) is explicitly of the form

$$O_{\mathrm{SGL}} = o_{\mathrm{SGL}} \, B_{\mathrm{SGL}} . \qquad (7.75)$$

Hence, the function `XLALComputeLRstat()` in the LALSuite software package is implemented to compute, as "LRstat" values, the (decadic) log-Bayes-factor $\log_{10} B_{\mathrm{SGL}}$. Using $\log_{10}$ instead of $\ln$ make the resulting values more intuitive.

Again, consider the difference to a two-stage line-veto approach. In that case, O_{SL} as a veto would be applied only to candidates that are "strong" in terms of $O_{\mathrm{SG}} \propto e^{\mathcal{F}}$, for which the Gaussian-noise hypothesis is already considered unlikely with high confidence. On the other hand, for O_{SGL}, the transition from O_{SG} to O_{SL} is smooth and, more importantly, it depends on the single-detector statistics $\mathcal{F}^X$ rather than the multi-detector $\mathcal{F}$. Thus, even in the limiting cases of strong signals or disturbances, the ranking as determined by O_{SGL} is different than that of a two-stage approach.

7.3 Semi-coherent detection statistics

As discussed in Sec. 5.9, semi-coherent methods are often used when a coherent-in-time analysis of the full data set is prohibitive in terms of computing cost. Now I present the generalisation of our previous results to the semi-coherent case, where the data $\boldsymbol{x}$

is divided into N_{seg} segments of shorter duration, denoted as $\{\boldsymbol{x}_k\}_{k=1}^{N_{\mathrm{seg}}}$. I refer to semi-coherent quantities with a hat: $\widehat{}$.

7.3.1 Semi-coherent $\widehat{\mathcal{F}}$-statistic

In a StackSlide semi-coherent approach, the semi-coherent $\widehat{\mathcal{F}}(\boldsymbol{x};\lambda)$-statistic in a template λ is an *incoherent* combination of the coherent statistics $\mathcal{F}_k(\boldsymbol{x}_k;\lambda)$ in each segment k, typically as a summation over all segments:

$$\widehat{\mathcal{F}}(\boldsymbol{x};\lambda) \equiv \sum_{k=1}^{N_{\mathrm{seg}}} \mathcal{F}_k(\boldsymbol{x}_k;\lambda)\,. \tag{7.76}$$

As before, I consider statistics in a single template, and will therefore mostly simplify the notation by dropping any dependence on the phase-evolution parameters λ.

As shown by PGM11, $\widehat{\mathcal{F}}$ can also be derived in the Bayesian way, similarly to the coherent $\mathcal{F}$ in Sec. 7.2.1, by relaxing the requirement of consistent signal amplitudes $\mathcal{A}$ across different segments. In other words, Eq. (7.7) gets modified to allow for a set of N_{seg} independent amplitude parameters $\mathcal{A}_k$. This defines the semi-coherent signal hypothesis $\widehat{\mathcal{H}}_{\mathrm{S}}$ as

$$\widehat{\mathcal{H}}_{\mathrm{S}} : \boldsymbol{x}_k = \boldsymbol{n}_k + \mathcal{A}_k^\mu\, \boldsymbol{h}_\mu\,, \quad \text{for } k = 1, \ldots N_{\mathrm{seg}}\,, \quad \text{with priors} \quad P\left(\mathcal{A}_k, \lambda | \widehat{\mathcal{H}}_{\mathrm{S}}\right)\,. \tag{7.77}$$

For the per-segment amplitude priors $P\left(\mathcal{A}_k | \widehat{\mathcal{H}}_{\mathrm{S}}\right)$, we reuse the amplitude prior given by Eq. (7.19). Hence, by marginalisation as in Eq. (7.17), we obtain the posterior

$$P\left(\widehat{\mathcal{H}}_{\mathrm{S}} | \boldsymbol{x}\right) = \widehat{o}_{\mathrm{SG}}\, P\left(\widehat{\mathcal{H}}_{\mathrm{G}} | \boldsymbol{x}\right) c_*^{-N_{\mathrm{seg}}}\, \mathrm{e}^{\widehat{\mathcal{F}}(\boldsymbol{x})}\,. \tag{7.78}$$

For Gaussian noise, the segment boundaries are just a formality, and there is no actual difference between semi-coherent and coherent hypotheses: $\widehat{\mathcal{H}}_{\mathrm{G}} = \mathcal{H}_{\mathrm{G}}$. For consistency of notation, I still write $\widehat{\mathcal{H}}_{\mathrm{G}}$ throughout this section. The semi-coherent posterior odds between the signal and Gaussian-noise hypotheses across all N_{seg} segments is

$$\widehat{O}_{\mathrm{SG}}(\boldsymbol{x}) \equiv \frac{P\left(\widehat{\mathcal{H}}_{\mathrm{S}} | \boldsymbol{x}\right)}{P\left(\widehat{\mathcal{H}}_{\mathrm{G}} | \boldsymbol{x}\right)} = \widehat{o}_{\mathrm{SG}}\, c_*^{-N_{\mathrm{seg}}}\, \mathrm{e}^{\widehat{\mathcal{F}}(\boldsymbol{x})}\,. \tag{7.79}$$

Note that the prior cut-off parameter c_* enters to the power of N_{seg}, due to the independent priors in each segment.

7.3.2 Semi-coherent line-veto statistic $\widehat{O}_{\mathrm{SL}}$

Similarly, we can now generalise the single-detector line hypothesis of Eq. (7.30) to the semi-coherent case:

$$\widehat{\mathcal{H}}_{\mathrm{L}} = \left(\widehat{\mathcal{H}}_{\mathrm{L}}^1 \text{ and } \widehat{\mathcal{H}}_{\mathrm{G}}^2 \text{ and } \widehat{\mathcal{H}}_{\mathrm{G}}^3 \dots \right) \text{ or}$$
$$\left(\widehat{\mathcal{H}}_{\mathrm{G}}^1 \text{ and } \widehat{\mathcal{H}}_{\mathrm{L}}^2 \text{ and } \widehat{\mathcal{H}}_{\mathrm{G}}^3 \dots \right) \text{ or } \dots \tag{7.80}$$

The probability of the line hypothesis in detector X across all segments is then

$$P\left(\widehat{\mathcal{H}}_{\mathrm{L}}^X | x^X \right) = P\left(\widehat{\mathcal{H}}_{\mathrm{G}}^X | x^X \right) c_*^{-N_{\mathrm{seg}}} \widehat{o}_{\mathrm{LG}}^X \, \mathrm{e}^{\widehat{\mathcal{F}}^X(x^X)} \,, \tag{7.81}$$

where the semi-coherent line-odds in detector X are given by

$$\widehat{o}_{\mathrm{LG}}^X \equiv \frac{P\left(\widehat{\mathcal{H}}_{\mathrm{L}}^X \right)}{P\left(\widehat{\mathcal{H}}_{\mathrm{G}}^X \right)} \,. \tag{7.82}$$

Similarly to Eq. (7.39), the posterior probability for the full semi-coherent line-hypothesis $\widehat{\mathcal{H}}_{\mathrm{L}}$ is

$$P\left(\widehat{\mathcal{H}}_{\mathrm{L}} | \boldsymbol{x} \right) = P\left(\widehat{\mathcal{H}}_{\mathrm{G}} | \boldsymbol{x} \right) c_*^{-N_{\mathrm{seg}}} \widehat{o}_{\mathrm{LG}} \left\langle \widehat{r}^X \, \mathrm{e}^{\widehat{\mathcal{F}}^X(x^X)} \right\rangle_X \,, \tag{7.83}$$

where the line-prior odds and line weights are defined, in analogy to Eqs. (7.35) and (7.36), as

$$\widehat{o}_{\mathrm{LG}} \equiv \frac{P\left(\widehat{\mathcal{H}}_{\mathrm{L}} \right)}{P\left(\widehat{\mathcal{H}}_{\mathrm{G}} \right)} = \sum_X \widehat{o}_{\mathrm{LG}}^X \,, \tag{7.84}$$

$$\widehat{r}^X \equiv \frac{\widehat{o}_{\mathrm{LG}}^X}{\widehat{o}_{\mathrm{LG}} / N_{\mathrm{det}}} \,. \tag{7.85}$$

As in the coherent case, the odds ratio between signal and line hypotheses gives a, now semi-coherent, line-veto statistic:

$$\widehat{O}_{\mathrm{SL}}(\boldsymbol{x}) \equiv \frac{P\left(\widehat{\mathcal{H}}_{\mathrm{S}} | \boldsymbol{x} \right)}{P\left(\widehat{\mathcal{H}}_{\mathrm{L}} | \boldsymbol{x} \right)} = \widehat{o}_{\mathrm{SL}} \, \frac{\mathrm{e}^{\widehat{\mathcal{F}}(\boldsymbol{x})}}{\left\langle \widehat{r}^X \, \mathrm{e}^{\widehat{\mathcal{F}}^X(x^X)} \right\rangle_X} \,. \tag{7.86}$$

Also, we can define a semi-coherent $\widehat{\mathcal{F}}^{+\mathrm{veto}}$-statistic as

$$\widehat{\mathcal{F}}^{+\mathrm{veto}}(\boldsymbol{x}) \equiv \begin{cases} \widehat{\mathcal{F}}(\boldsymbol{x}) & \text{if } \widehat{\mathcal{F}}(\boldsymbol{x}) \geq \max_X \{ \widehat{\mathcal{F}}^X(x) \} \,, \\ 0 & \text{otherwise} \,. \end{cases} \tag{7.87}$$

with the same relation to $\widehat{O}_{\mathrm{SL}}$ and the $\mathcal{F}$-statistic consistency veto as discussed in Sec. 7.2.2 for the coherent case.

7.3.3 Semi-coherent line-robust statistic $\widehat{O}_{\mathrm{SGL}}$

Combining Gaussian noise and semi-coherent line hypotheses, we arrive again at an extended noise hypothesis,

$$\widehat{\mathcal{H}}_{\mathrm{GL}} \equiv \left(\widehat{\mathcal{H}}_{\mathrm{G}} \text{ or } \widehat{\mathcal{H}}_{\mathrm{L}} \right) , \tag{7.88}$$

with a posterior probability given by

$$P\left(\widehat{\mathcal{H}}_{\mathrm{GL}} | \boldsymbol{x} \right) = P\left(\widehat{\mathcal{H}}_{\mathrm{G}} | \boldsymbol{x} \right) \left(1 + c_*^{-N_{\mathrm{seg}}} \widehat{o}_{\mathrm{LG}} \left\langle \widehat{r}^X \mathrm{e}^{\widehat{\mathcal{F}}^X(x^X)} \right\rangle_X \right) . \tag{7.89}$$

From this follows a semi-coherent line-robust detection statistic as

$$\widehat{O}_{\mathrm{SGL}}(\boldsymbol{x}) \equiv \frac{P\left(\widehat{\mathcal{H}}_{\mathrm{S}} | \boldsymbol{x} \right)}{P\left(\widehat{\mathcal{H}}_{\mathrm{GL}} | \boldsymbol{x} \right)} = \left[\widehat{O}_{\mathrm{SG}}^{-1}(\boldsymbol{x}) + \widehat{O}_{\mathrm{SL}}^{-1}(\boldsymbol{x}) \right]^{-1} , \tag{7.90}$$

which we can write explicitly as

$$\widehat{O}_{\mathrm{SGL}}(\boldsymbol{x}) = \widehat{o}_{\mathrm{SGL}} \frac{\mathrm{e}^{\widehat{\mathcal{F}}(\boldsymbol{x})}}{(1 - \widehat{p}_{\mathrm{L}}) \, e^{\widehat{\mathcal{F}}_*^{(0)}} + \widehat{p}_{\mathrm{L}} \left\langle \widehat{r}^X \mathrm{e}^{\widehat{\mathcal{F}}^X(x^X)} \right\rangle_X} . \tag{7.91}$$

Here,

$$\widehat{p}_{\mathrm{L}} \equiv P\left(\widehat{\mathcal{H}}_{\mathrm{L}} | \widehat{\mathcal{H}}_{\mathrm{GL}} \right) = \frac{\widehat{o}_{\mathrm{LG}}}{1 + \widehat{o}_{\mathrm{LG}}} \ \in \ [0,1] \tag{7.92}$$

is the prior line probability, with single-detector versions

$$\widehat{p}_{\mathrm{L}}^X \equiv \frac{P\left(\widehat{\mathcal{H}}_{\mathrm{L}}^X \right)}{P\left(\widehat{\mathcal{H}}_{\mathrm{GL}}^X \right)} = \frac{\widehat{o}_{\mathrm{LG}}^X}{1 + \widehat{o}_{\mathrm{LG}}^X} \tag{7.93}$$

and inverse relations

$$\widehat{o}_{\mathrm{LG}} = \frac{\widehat{p}_{\mathrm{L}}}{1 - \widehat{p}_{\mathrm{L}}} , \quad \widehat{o}_{\mathrm{LG}}^X = \frac{\widehat{p}_{\mathrm{L}}^X}{1 - \widehat{p}_{\mathrm{L}}^X} . \tag{7.94}$$

Also, in analogy to Eq. (7.67), the prior cut-off was reparametrised as

$$\widehat{\mathcal{F}}_*^{(0)} \equiv \ln c_*^{N_{\mathrm{seg}}} . \tag{7.95}$$

Similarly to Eq. (7.72), we can thus write the semi-coherent line-robust statistic as

$$\widehat{O}_{\mathrm{SGL}}(\boldsymbol{x}) = \widehat{o}_{\mathrm{SL}} \frac{\mathrm{e}^{\widehat{\mathcal{F}}(\boldsymbol{x})}}{\mathrm{e}^{\widehat{\mathcal{F}}_*} + \left\langle \widehat{r}^X \mathrm{e}^{\widehat{\mathcal{F}}^X(x^X)} \right\rangle_X} , \tag{7.96}$$

defining a semi-coherent transition scale $\widehat{\mathcal{F}}_*$ as

$$\widehat{\mathcal{F}}_* \equiv \widehat{\mathcal{F}}_*^{(0)} - \ln \widehat{o}_{\mathrm{LG}} , \tag{7.97}$$

which generalises Eq. (7.71). Hence, we find that $\widehat{O}_{\mathrm{SGL}}(\boldsymbol{x})$ transitions from the standard semi-coherent statistic $\widehat{O}_{\mathrm{SG}}(\boldsymbol{x}) \propto \mathrm{e}^{\widehat{\mathcal{F}}}$ to the line-veto statistic $\widehat{O}_{\mathrm{SL}}(\boldsymbol{x})$ when

$$\left\langle \widehat{r}^X \mathrm{e}^{\widehat{\mathcal{F}}^X} \right\rangle_X \sim \mathrm{e}^{\widehat{\mathcal{F}}_*} . \tag{7.98}$$

Again, as in the coherent case, the previous parametrisation from Eq. (7.91) has the advantage of being in the

$$\widehat{O}_{\mathrm{SGL}} = \widehat{o}_{\mathrm{SGL}} \, \widehat{B}_{\mathrm{SGL}} \tag{7.99}$$

form, so that the log-Bayes-factor is

$$\ln \widehat{B}_{\mathrm{SGL}}(\boldsymbol{x}) = \widehat{\mathcal{F}}(\boldsymbol{x}) - \widehat{\mathcal{F}}''_{\max}(\boldsymbol{x}) \tag{7.100}$$
$$- \ln \left((1 - \widehat{p}_{\mathrm{L}}) \, \mathrm{e}^{\widehat{\mathcal{F}}_*^{(0)} - \widehat{\mathcal{F}}''_{\max}(\boldsymbol{x})} + \widehat{p}_{\mathrm{L}} \left\langle \widehat{r}^X \mathrm{e}^{\widehat{\mathcal{F}}^X(x^X) - \widehat{\mathcal{F}}''_{\max}(\boldsymbol{x})} \right\rangle_X \right) ,$$

with the denominator maximum

$$\widehat{\mathcal{F}}''_{\max}(\boldsymbol{x}) \equiv \max \left\{ \widehat{\mathcal{F}}_*^{(0)} + \ln(1 - \widehat{p}_{\mathrm{L}}), \, \widehat{\mathcal{F}}^X(x^X) + \ln \widehat{r}^X + \ln \widehat{p}_{\mathrm{L}} \right\} . \tag{7.101}$$

Note that, in the semi-coherent case, the numerical values of $\widehat{\mathcal{F}}$ are typically large, due to its definition as a sum over segments in Eq. (7.76). However, the logarithmic correction term is still of order unity. This implies that the transition from $\widehat{O}_{\mathrm{SG}}$ to the line-veto odds $\widehat{O}_{\mathrm{SL}}$ is expected to be sharper than in the coherent case of Eq. (7.73).

7.4 Expectation value of the $\mathcal{F}$-statistic under the line hypothesis $\mathcal{H}_{\mathrm{L}}$

In a small aside from the main direction of this chapter, this section presents the derivation of a quantity which will become useful later on in this thesis: the expectation value of the $\mathcal{F}$-statistic under the hypothesis $\mathcal{H}_{\mathrm{L}}$.

As demonstrated in Sec. 7.2.1, the $\mathcal{F}$-statistic can be obtained from a hypothesis test between $\mathcal{H}_{\mathrm{S}}$ and $\mathcal{H}_{\mathrm{G}}$. Thus, the standard results for the distribution and moments of the $\mathcal{F}$-statistic, as given in Sec. 5.7, translate only to the case of CW signals in purely Gaussian noise.

However, the $\mathcal{F}$-statistic as defined by Eq. (5.46) can also be computed in other cases, and we have used this quantity as the basis for the new detection statistics O_{SL} and O_{SGL}. In most applications, we do not need the full distribution of the $\mathcal{F}$-statistic in an arbitrary data set, but the expectation value under the line hypothesis $\mathcal{H}_{\mathrm{L}}$ is an interesting quantity.

Let us start by considering the more general case of a signal with arbitrary detector-dependent amplitude parameters $\mathcal{A}_X^\mu$. For a real CW signal, amplitudes must be consistent across all detectors, corresponding to the case of $\mathcal{A}_X^\mu = \mathcal{A}^\mu$ for all X. On the other

hand, for a line according to the simple model of Eq. (7.30), amplitudes are non-zero for a single detector Y only. Using here, and in the following, automatic summation only over repeated amplitude-space indices $\mu, \nu, \ldots$ and not over detector indices $X, Y, X', \ldots$, the line case corresponds to $\mathcal{A}_X^\mu = \mathcal{A}_Y^\mu \delta_{XY}$.

The JKS factorisation of Eq. (7.10) allows expressing a general data set of a single detector X, containing Gaussian noise and some harmonic signal-like components, as

$$x^X = n^X + h^X = n^X + \mathcal{A}_X^\mu \, h_\mu^X \,. \tag{7.102}$$

Hence, the projections of the data onto the basis functions, as defined in Eq. (7.13), are

$$x_\mu^X \equiv \left\langle x^X \left| h_\mu^X \right. \right\rangle = n_\mu^X + \mathcal{A}_X^\nu \mathcal{M}_{\mu\nu}^X \,, \tag{7.103}$$

where $n_\mu^X \equiv \left\langle n^X \left| h_\mu^X \right. \right\rangle$. From the definition of the scalar product, Eq. (5.7), it follows that the multi-detector results are simply

$$x_\mu = \sum_X x_\mu^X \,, \quad \text{and} \quad \mathcal{M}_{\mu\nu} = \sum_X \mathcal{M}_{\mu\nu}^X \,. \tag{7.104}$$

Recalling that the $\mathcal{F}$-statistic is given by $2\mathcal{F} = x_\mu \mathcal{M}^{\mu\nu} x_\nu$ and noting that the antenna-pattern matrix components $\mathcal{M}^{\mu\nu}$ do not depend on the data, the expectation value in general reduces to

$$E\left[2\mathcal{F}\right] = \mathcal{M}^{\mu\nu} E\left[x_\mu \, x_\nu\right] \,. \tag{7.105}$$

Then, we can use Eq. (7.103) to expand

$$
\begin{aligned}
E\left[x_\mu x_\nu\right] &= \sum_{XX'} E\left[x_\mu^X \, x_\nu^{X'}\right] \\
&= \sum_{XX'} E\left[n_\mu^X n_\nu^{X'}\right] + \sum_{XX'} E\left[n_\mu^X \mathcal{A}_{X'}^\beta \, \mathcal{M}_{\beta\nu}^{X'}\right] \\
&\quad + \sum_{XX'} E\left[n_\nu^{X'} \mathcal{A}_X^\alpha \, \mathcal{M}_{\alpha\mu}^X\right] + \sum_{XX'} E\left[\mathcal{A}_X^\alpha \, \mathcal{M}_{\alpha\mu}^X \, \mathcal{M}_{\nu\beta}^{X'} \, \mathcal{A}_{X'}^\beta\right] \,.
\end{aligned} \tag{7.106}
$$

Further using the noise expectation values $E\left[n_\mu^X n_\nu^{X'}\right] = \mathcal{M}_{\mu\nu}^X \delta^{XX'}$ (for uncorrelated noise between detectors) and $E\left[n_\mu^X\right] = 0$ (assuming zero-mean noise n^X) as well as the data-independence of $\mathcal{M}$ and $\mathcal{A}$, this reduces to

$$E\left[x_\mu x_\nu\right] = \mathcal{M}_{\mu\nu} + \sum_{XX'} \mathcal{A}_X^\alpha \, \mathcal{M}_{\alpha\mu}^X \mathcal{M}_{\nu\beta}^{X'} \, \mathcal{A}_{X'}^\beta \,. \tag{7.107}$$

Next, with the well-known result that $\mathcal{M}^{\mu\nu}\mathcal{M}_{\mu\nu} = 4$ (see Sec. 5.6), the general result for the expectation value of the $\mathcal{F}$-statistic under arbitrary amplitude parameters is

$$E\left[2\mathcal{F}\right] = 4 + \mathcal{M}^{\mu\nu} \sum_{XX'} \mathcal{A}_X^\alpha \, \mathcal{M}_{\alpha\mu}^X \mathcal{M}_{\nu\beta}^{X'} \, \mathcal{A}_{X'}^\beta \,. \tag{7.108}$$

From this, we obtain the standard result for a CW signal with SNR $\rho_{\rm S}$, as given in Sec. 5.7, by specialising to consistent amplitudes in all detectors, i.e., $\mathcal{A}_X^\alpha = \mathcal{A}^\alpha$:

$$E\left[2\mathcal{F}\right]_{\mathcal{H}_{\rm S}} = 4 + \rho_{\rm S}^2\,, \quad \text{with} \quad \rho_{\rm S}^2 = \mathcal{A}^\mu\,\mathcal{M}_{\mu\nu}\,\mathcal{A}^\nu\,. \tag{7.109}$$

On the other hand, under the line hypothesis $\mathcal{H}_{\rm L}$ the amplitudes are $\mathcal{A}_X^\mu = \mathcal{A}_Y^\mu\,\delta_{XY}$, and thus the expectation value is

$$E\left[2\mathcal{F}\right]_{\mathcal{H}_{\rm L}} = 4 + \mathcal{M}^{\mu\nu}\,\mathcal{A}_Y^\alpha\,\mathcal{M}_{\alpha\mu}^Y\,\mathcal{M}_{\nu\beta}^Y\,\mathcal{A}_Y^\beta\,. \tag{7.110}$$

To get a better feeling for this unwieldy result, consider the special case of identical antenna-pattern matrices for all detectors, i.e. $\mathcal{M}_{\mu\nu}^X = \mathcal{M}_{\mu\nu}^Y$. The multi-detector antenna-pattern matrix is then $\mathcal{M}_{\mu\nu} = N_{\rm det}\,\mathcal{M}_{\mu\nu}^Y$, and therefore $\mathcal{M}^{\mu\nu} = \frac{1}{N_{\rm det}}\,\mathcal{M}_Y^{\mu\nu}$. Hence, the expectation value in this case is

$$E\left[2\mathcal{F}\right]_{\mathcal{H}_{\rm L}} = 4 + \frac{1}{N_{\rm det}}\,\rho_{\rm L}^2\,, \tag{7.111}$$

with the (single-detector) "line SNR" in detector Y given by

$$\rho_{\rm L}^2 \equiv \mathcal{A}_Y^\mu\,\mathcal{M}_{\mu\nu}^Y\,\mathcal{A}_Y^\nu\,. \tag{7.112}$$

This result shows that a CW-like disturbance with SNR $\rho_{\rm L}$ in a single detector is not completely suppressed in the multi-detector $\mathcal{F}$-statistic, but is only reduced to an effective multi-detector SNR of approximately $\rho_{\rm L}/\sqrt{N_{\rm det}}$.

In general, the scaling of Eq. (7.111) will not hold exactly; but as the antenna-pattern matrices $\mathcal{M}_{\mu\nu}^X$ are typically not very different between detectors, it should remain approximately true. However, cases of large differences in antenna patterns and in per-detector sensitivity are the topic of Sec. 12.

8 Choice of prior parameters

During the derivation, in Sec. 7, of the new detection statistics $\widehat{O}_{\mathrm{SL}}$ ("line-veto statistic") and $\widehat{O}_{\mathrm{SGL}}$ ("line-robust statistic"), I have briefly mentioned the ill-constrained prior parameters which appear explicitly in the final expressions Eq. (7.86) and Eq. (7.91) for these statistics.

In this section, I will further investigate their impact on the statistics' behaviour, and introduce two simple methods to choose values for these parameters. There is no guarantee that these procedures are optimal, and the priors are unphysical anyway. However, I will demonstrate good performance of these parameter choices through the numerical simulations presented in Sec. 9 and Sec. 10.

Regarding notation, let me note at this point that the coherent statistics described in Sec. 7.2 are simply special cases of the semi-coherent expressions given in Sec. 7.3 for a single segment, i.e. for $N_{\mathrm{seg}} = 1$. Hence, in the following I use the semi-coherent notation, without loss of generality.

First, consider the pure line-veto statistic $\widehat{O}_{\mathrm{SL}}$ of Eq. (7.86). For data from N_{det} detectors, it depends on N_{det} values of the prior line weights $\widehat{r}^X$. So it seems, at first glance, that $\widehat{O}_{\mathrm{SL}}$ has N_{det} free parameters. However, the normalisation condition Eq. (7.37) on the $\widehat{r}^X$ corresponds to a sum constraint, reducing the effective number of free parameters to $N_{\mathrm{det}} - 1$.

Interestingly, the $\widehat{r}^X$ can be computed from the prior odds $\widehat{o}_{\mathrm{LG}}^X$ (or prior line probabilities $\widehat{p}_{\mathrm{L}}^X$), but the overall prior odds $\widehat{o}_{\mathrm{LG}}$ (or, equivalently, $\widehat{p}_{\mathrm{L}}$) do not actually appear in $\widehat{O}_{\mathrm{SL}}$. Gaussian noise is not considered at all in this hypothesis test, so that only relative line probabilities in the different detectors are relevant.

The situation is more complicated for the line-robust statistic $\widehat{O}_{\mathrm{SGL}}$, which in addition to $\widehat{r}^X$ also depends on the total prior line probability $\widehat{p}_{\mathrm{L}}$ and on the amplitude-prior cut-off parameter c_*. Notably, these are not just prefactors, which would be irrelevant for the performance as a detection statistic, but enter into the functional form of $\widehat{O}_{\mathrm{SGL}}$. Thus, a naive count gives $N_{\mathrm{det}} + 2$ parameters. However, the reparametrisation of $\widehat{O}_{\mathrm{SGL}}$ given in Eq. (7.96) demonstrates that the transitioning behaviour is actually determined by the combination

$$\widehat{\mathcal{F}}_* \equiv \widehat{\mathcal{F}}_*^{(0)} - \ln \widehat{o}_{\mathrm{LG}} = \widehat{\mathcal{F}}_*^{(0)} - \ln \left(\frac{\widehat{p}_{\mathrm{L}}}{1 - \widehat{p}_{\mathrm{L}}} \right) . \tag{8.1}$$

Hence, a change in $\widehat{p}_{\mathrm{L}}$ could also be compensated by changing $\widehat{\mathcal{F}}_*^{(0)}$, and vice versa, and the two parameters are not independent. The argument about the sum constraint on the $\widehat{r}^X$ also still applies. Thus, $\widehat{O}_{\mathrm{SGL}}$ effectively has N_{det} free parameters.

Interpreting these prior parameters is not very straightforward. The line probability $\widehat{p}_{\mathrm{L}}$ and the weights $\widehat{r}^X$ have clear intuitive interpretations as the prior estimate for the prevalence of lines in total, and in a given detector, respectively. This immediately suggests determining these parameters from previous experience with the detectors, or from independent measures of the data quality. In Sec. 8.1, I present a simple approach to this kind of "adaptive tuning".

Less clear is the meaning of the prior amplitude cut-off parameter c_*, and the parameter $\widehat{\mathcal{F}}_*^{(0)}$ derived from it, as defined in Eq. (7.95). This parameter results from the rather unphysical choice of the amplitude prior in Eq. (7.19), as discussed in more detail by PK09 and PGM11. There is no known way to give a physics- or experience-motivated estimate for this parameter.

Instead, empirical "tuning" will be required to determine a reasonable value for $\widehat{\mathcal{F}}_*^{(0)}$, based on probing a range of values on a limited subset of data and picking the one for which $\widehat{O}_{\mathrm{SGL}}$ performs best. I will discuss this approach in Sec. 8.2 and give arguments as to why a value obtained that way should be "safe", though not necessarily optimal, for the full data set.

8.1 Simple estimate of prior line probabilities from the data

In the absence of any prior information on line prevalence in the detectors, maximally uninformative line-priors are appropriate: $\widehat{r}^X = 1$ and $\widehat{p}_{\mathrm{L}} = 0.5$. In terms of the other parameters used so far, these correspond to $\widehat{p}_{\mathrm{L}}^X = \frac{1}{1+N_{\mathrm{det}}}$, $\widehat{o}_{\mathrm{LG}}^X = \frac{1}{N_{\mathrm{det}}}$ and $\widehat{o}_{\mathrm{LG}} = 1$. Such a choice means to consider the presence of lines, over the whole multi-detector data set, as just as likely as pure Gaussian noise, and each detector as equally likely to be affected by lines.

A more informed choice should be based on prior characterisation of the detectors, either from previous data-taking runs, engineering and commissioning knowledge or even from an analysis of the current data set which is sufficiently independent from the actual $\widehat{\mathcal{F}}$-statistic based CW analysis. Existing line catalogues usually make no claims to completeness, see Sec. 6.3.

Thus, we intend to judiciously use the observed data $\boldsymbol{x}$ itself for a simple "proxy" estimate of the per-detector prior line probabilities $\widehat{p}_{\mathrm{L}}^X$. It seems convenient to adapt one of the established simple line-vetoing procedures reviewed in Sec. 6.5. Indeed, empirical results are promising when adopting the line-flagging method of Wette (2009), based on outliers in the normalised SFT power.

8.1.1 Line flagging through Fourier power

In short, the method works as follows: First, for a set of search templates spanning a contiguous frequency band (and the full associated parameter space in spin-down parameters and sky positions), one works out the full data-span in terms of frequency bins which potentially contribute to the detection statistics for these templates. Then, one computes the time-averaged normalised power over these bins and counts how many of them exceed a pre-determined threshold. Finally, the measured fraction of such outliers is used as a proxy estimate for the prior line probability.

More specifically, recall from Sec. 5.3 that the data for $\widehat{\mathcal{F}}$-statistic based CW searches is usually prepared in the form of *Short Fourier Transforms* (SFTs) of the original time-domain data. For these, the data is most often split into stretches of $T_{\mathrm{SFT}} = 1800\,\mathrm{s}$ (e.g., see Krishnan et al. 2004), though different T_{SFT} are used for specialised searches, too.

For a single-detector SFT, the *normalised average SFT power* $\mathcal{P}^X(f)$ as a function of frequency f is given by (e.g., see Abbott et al. 2004b, Wette 2009)

$$\mathcal{P}^X(f) \equiv \frac{2}{N_{\mathrm{SFT}}\, T_{\mathrm{SFT}}} \sum_{\alpha=1}^{N_{\mathrm{SFT}}} \frac{\left|\widetilde{x}_\alpha^X(f)\right|^2}{S_\alpha^X(f)} \,, \tag{8.2}$$

where the sum goes over all SFTs in the data set from the detector X, totalling a number of N_{SFT}. For each SFT α and frequency bin, $\widetilde{x}_\alpha^X(f)$ denotes the Fourier-transformed data and $S_\alpha^X(f)$ is the noise PSD.

In well-behaved noise, the normalised SFT power is expected to have a smooth distribution with few outliers. Specifically, in pure Gaussian noise, the quantity $2N_{\mathrm{SFT}}^X \mathcal{P}^X$ follows a χ^2-distribution with $k = 2N_{\mathrm{SFT}}^X$ degrees of freedom, so that the expectation value is

$$E\left[\mathcal{P}^X\right] = \frac{E\left[2N_{\mathrm{SFT}}^X \mathcal{P}^X\right]}{2N_{\mathrm{SFT}}^X} = \frac{k}{2N_{\mathrm{SFT}}^X} = 1\,, \tag{8.3}$$

with standard deviation

$$\sigma\left(\mathcal{P}^X\right) = \frac{\sigma\left(2N_{\mathrm{SFT}}^X \mathcal{P}^X\right)}{2N_{\mathrm{SFT}}^X} = \frac{\sqrt{2k}}{2N_{\mathrm{SFT}}^X} = \frac{1}{\sqrt{N_{\mathrm{SFT}}^X}}\,. \tag{8.4}$$

For large N_{SFT}^X, we can also approximate this by a Gaussian distribution for $\mathcal{P}^X(f)$ with unit mean and standard deviation $\sigma = 1/\sqrt{N_{\mathrm{SFT}}^X}$. In practice, this limit is almost always valid for CW purposes.

An excess of $\mathcal{P}^X(f)$ outliers above the statistically expected level of fluctuations is thus a sign for non-Gaussian contamination of the data band. For long-baseline CW searches, such contaminations are mostly lines or "forests" of narrow line-like features. Hence, counting such outliers gives a rough proxy of line contamination.

8.1.2 Outlier counts as prior estimator

The specific algorithm proposed here is to count the number $N^X_{\mathcal{P}>\mathcal{P}_{\mathrm{thr}}}$ of bins for which $\mathcal{P}^X(f)$ crosses a given threshold $\mathcal{P}^X_{\mathrm{thr}}$, with $N^X_{\mathcal{P}>\mathcal{P}_{\mathrm{thr}}} \in [0, N_{\mathrm{bins}}]$. Then, the estimated prior line-probability $\widehat{p}^X_{\mathrm{L}}$ for that frequency band is

$$\widehat{p}^X_{\mathrm{L}} \equiv \frac{N^X_{\mathcal{P}>\mathcal{P}_{\mathrm{thr}}}}{N_{\mathrm{bins}}} \,. \tag{8.5}$$

The total data range associated with a search band (taking into account Doppler modulation and NS spin-down) depends on the search setup. For most of the examples and applications in this thesis (e.g. the $50\,\mathrm{mHz}$-wide physical search bands in Sec. 10), it is of the order of $100\,\mathrm{mHz}$, corresponding to a few hundred bins for a typical SFT bin-width of $\Delta f = 1/T_{\mathrm{SFT}} \approx 5.6 \times 10^{-4}\,\mathrm{Hz}$.

In order to avoid many false alarms in line flagging, the threshold $\mathcal{P}^X_{\mathrm{thr}}$ has to be safely above the typical noise fluctuations in the data. We can fix a certain acceptable false-alarm probability $p_{\mathrm{FA},\mathcal{P}}$ and use the Gaussian distribution of $\mathcal{P}^X$ to determine $\mathcal{P}^X_{\mathrm{thr}}$. As the width $\sigma = 1/\sqrt{N_{\mathrm{SFT}}}$ of the distribution depends on the number of SFTs used per detector, the thresholds $\mathcal{P}^X_{\mathrm{thr}}$ can in general be different for each detector, as typical data selection procedures for CW searches (e.g. see Sec. 5.2.2 of Shaltev 2013) do not guarantee data sets of equal length.

In comparison, Wette (2009) and Abadie et al. (2010b) used a fixed and detector-independent threshold of $\mathcal{P}_{\mathrm{thr}} = 1.5$. With $N_{\mathrm{SFT}} \sim 500$ for each detector, this is rather high, corresponding to an extremely small false-alarm probability, equivalent to an $\sim 11\sigma$ deviation. This conservative choice was made because, in that analysis, any frequency bands flagged as line-affected through this method were completely excluded from all following analysis steps, which was desirable only for very strong artefacts.

On the other hand, the proposal here is to use the $\mathcal{P}^X$-based line-flagging only to estimate priors for how heavily a given template λ *may* be affected by lines. At the same time, we also want to include weaker lines, to make the method more powerful. This allows for a significantly lower false-alarm level. For the $\mathcal{P}^X$ distributions of typical "quiet" bands of LIGO data, $p_{\mathrm{FA},\mathcal{P}} = 10^{-9}$ turns out to work well. Examples can be found in a later part of this thesis, see Figs. 10.3–10.6.

Finally, the per-detector line weights $\widehat{r}^X$ and the overall line probability $\widehat{p}_{\mathrm{L}}$ follow from the $\widehat{p}^X_{\mathrm{L}}$ by Eqs. (7.85), (7.92) and (7.94).

8.1.3 Validity and limitations of the estimator

As stressed before, this proxy-estimate method is not a classical way of determining priors, as it does not strictly rely on information independent from the present analysis. Thus, it might at first appear that such a data-dependent prior estimation could be

prone to the "sample re-use fallacy", as discussed in Sec. 8.12.1 of (Jaynes 2003): Using the same data twice in a Bayesian inference procedure cannot improve the posterior estimates. This is obvious when one just repeats the probability-updating step with Bayes' theorem twice, using an identical copy of the data. But Jaynes also showed that a "data-dependent prior" can very often be reformulated as just such a step, proving that generating prior estimates from the *same* data set (or a strictly dependent one) is usually pointless.

However, this argument does not apply in this case, as we actually use different subsets of what I sloppily call "the data set" for the prior estimation and for the main analysis, which only have a small overlap. This becomes clear by demonstrating that the proxy estimate for $\widehat{p}_{\mathrm{L}}^{X}$ is *sufficiently independent* from the posterior for the line hypothesis $\mathcal{H}_{\mathrm{L}}$: On the one hand, the simple line hypothesis $\mathcal{H}_{\mathrm{L}}$ used throughout this work is based on the signal hypothesis $\mathcal{H}_{\mathrm{S}}$ and thus for each template describes a narrow-band signal, which over the duration of each 1800s-SFT is confined to a few bins (though it slowly moves through the frequency range with time). For the current $\widehat{\mathcal{F}}$-statistic implementation (see Prix 2011b), only 16 frequency bins per SFT are used to construct the detection statistic, and they are very heavily weighted toward a few central ones. On the other hand, the line-flagging prior estimate determines the line prevalence in a whole frequency band, using $\sim \mathcal{O}\left(100-200\right)$ frequency bins over the full observation time, each counting equally in the estimate.

Thus, the small overlap of the two data subsets may lead to a minor reduction in the prior-estimation effectiveness, but not to a full negation via the sample re-use fallacy. And as we do not claim the method to be optimal, but just easy and convenient, this should be enough for the purpose at hand. An actual gain in detection probabilities, i.e. posterior information, is demonstrated by the results in Sec. 10, as well as safety in the presence of (injected) signals.

The latter point is important because strong signals can also produce outliers in $\mathcal{P}^{X}$, which will then be counted as lines by the flagging procedure. However, the flagging is only used to shift prior weight between $\mathcal{H}_{\mathrm{G}}$ and $\mathcal{H}_{\mathrm{L}}$, while any data containing such strong signals will generally provide so much evidence for $\mathcal{H}_{\mathrm{S}}$ that this slight shift is irrelevant.

A final modification to the tuning procedure becomes necessary because the line-flagging proxy cannot be considered as a direct estimator of $\widehat{p}_{\mathrm{L}}^{X}$. Rather, it provides only an indication for the presence of lines, based on spectral features that can be robustly identified. It could miss other types of lines, or identify features that may not map directly to actual disturbances in $\widehat{\mathcal{F}}$-statistic searches. This is again due to the different spectral width of the estimator's and the detection statistic's supports on the data set.

Specifically, the time evolution of signal templates and lines has to be considered: For example, a weak "wandering" line, with a frequency that decreases over time, may not show up as an outlier in $\mathcal{P}^{X}$, but it may severely affect a signal template with similar spin-down behaviour. The opposite effect, in a long-integration-time search, would be a

monochromatic but very narrow line that produces a $\mathcal{P}^X$ outlier, but may actually be harmless for the $\widehat{\mathcal{F}}$-statistic of a template with rapid frequency evolution, as the affected frequency bin only contributes a negligible amount of power to the template.

Hence, observing no threshold crossings in the average SFT power $\mathcal{P}^X$ does not necessarily imply that the $\widehat{\mathcal{F}}$-statistic could not be affected by instrumental artefacts, while seeing many outliers in $\mathcal{P}^X$ does not always yield high values of $\widehat{\mathcal{F}}$. Therefore, we want to avoid values of $\widehat{p}_{\mathrm{L}}^X$, or equivalently $\widehat{o}_{\mathrm{LG}}^X$, which suggest more confidence than seems justifiable. This is achieved by truncating the estimator's range. In principle, the truncation rule introduces additional "meta-tuning parameters", but as long as the boundaries are low/high enough, the difference in the effect on O_{SGL} or O_{SL} is small. A somewhat flexible rule is to truncate $\widehat{p}_{\mathrm{L}}^X$ to an interval

$$\widehat{p}_{\mathrm{L}}^X \in \left[\frac{N_{\mathrm{trunc}}}{N_{\mathrm{bins}}}, \ 1 - \frac{N_{\mathrm{trunc}}}{N_{\mathrm{bins}}} \right] , \tag{8.6}$$

where $N_{\mathrm{trunc}} < 1$ ensures that the minimum (or maximum) corresponds to less than one outlier bin (or one undisturbed bin) in the whole band, respectively. In current Einstein@Home runs, this rule is used with $N_{\mathrm{trunc}} = 0.1$, see Sec. 11. For example, for $N_{\mathrm{bins}} = 100$, this gives $\widehat{o}_{\mathrm{LG}}^X \in [\approx 0.001001, \ 999]$.

In the following examples and application studies (in Sec. 10), $N_{\mathrm{bins}} \sim \mathcal{O}(100)$ is typically the case and the tuning stays very similar when using a simpler, fixed-interval rule

$$\widehat{o}_{\mathrm{LG}}^X \in [0.001, \ 1000] . \tag{8.7}$$

8.1.4 Example on simulated data

To illustrate the method, I provide an example of a simulated data set. It was produced using the `Makefakedata_v4` code from LALSuite (see Sec. 5.11). I have simulated a $60\,\mathrm{mHz}$ wide band over 50 contiguous SFTs of $T_{\mathrm{SFT}} = 1800\,\mathrm{s}$ each for two detectors $X \in \{\mathrm{H1, L1}\}$, where H1 and L1 stand for the LIGO detectors at Hanford and Livingston, respectively. The data set contains white Gaussian noise with a PSD of $S^X = 3 \cdot 10^{-22}\,\mathrm{Hz}^{-1/2}$ in both detectors. In addition, a monochromatic stationary line of amplitude $h_0 = 2 \cdot 10^{-23}\,\mathrm{Hz}^{-1/2}$ at $50\,\mathrm{Hz}$ is injected in H1 only. Fig. 8.1 shows spectra of $\mathcal{P}^X(f)$ for this data set.

In this example, the line-prior estimation proceeds as follows: For the given number of SFTs, the fixed false-alarm probability of $p_{\mathrm{FA},\mathcal{P}} = 10^{-9}$ corresponds to a threshold $\mathcal{P}_{\mathrm{thr}}^{\mathrm{H1}} = \mathcal{P}_{\mathrm{thr}}^{\mathrm{L1}} = \mathcal{P}_{\mathrm{thr}}(p_{\mathrm{FA},\mathcal{P}} = 10^{-9}, N_{\mathrm{SFT}} = 50) \approx 1.84$, identical for both detectors. There are $N_{\mathrm{bins}} = 127$ frequency bins in the band. As also shown by the per-detector histograms of $\mathcal{P}^X$ in Fig. 8.2, the distribution in L1 is compatible with Gaussian noise, while there is a single bin crossing $\mathcal{P}_{\mathrm{thr}}$ in H1. Hence, I can estimate the line priors as

$$\widehat{o}_{\mathrm{LG}}^{\mathrm{H1}} = \max \left\{ 0.001, \tfrac{1/127}{1 - 1/127} \right\} \approx 0.008$$
$$\widehat{o}_{\mathrm{LG}}^{\mathrm{L1}} = \max \left\{ 0.001, \tfrac{0/127}{1 - 0/127} \right\} = 0.001 . \tag{8.8}$$

Figure 8.1: Example of the normalised SFT power $\mathcal{P}^X(f)$ as a function of frequency f for LIGO H1 (solid blue) and L1 (dashed red) for simulated Gaussian data containing a line in H1. The horizontal line shows the threshold $\mathcal{P}_{\text{thr}}$ at a false-alarm level of $p_{\text{FA},\mathcal{P}} = 10^{-9}$.
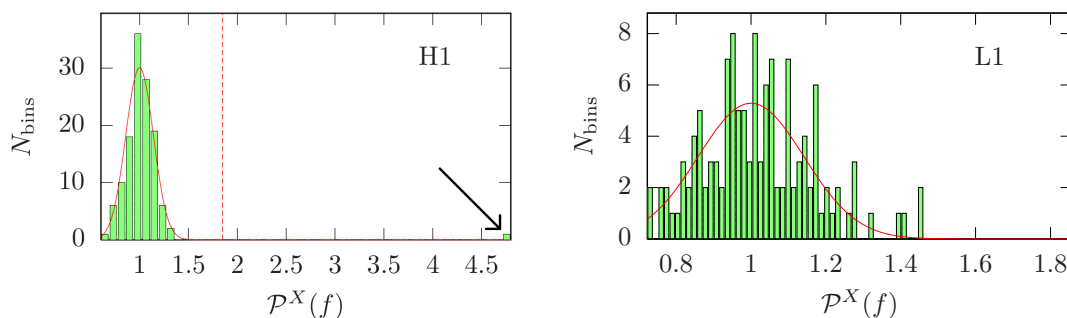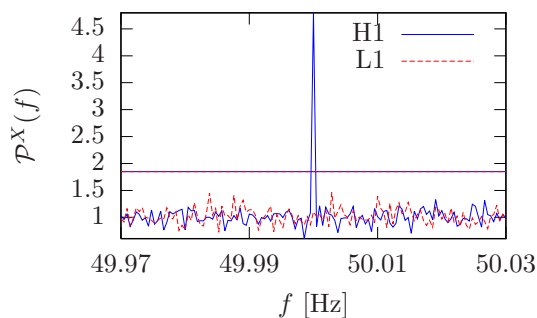

Figure 8.2: Example histograms of the normalised SFT power $\mathcal{P}^X$ for LIGO H1 and L1 for simulated Gaussian data containing a line in H1. The red, solid curves give the theoretical expectation from a $\mathcal{N}(1, 1/\sqrt{50})$ distribution and the red, dashed, vertical lines show the threshold $\mathcal{P}_{\text{thr}}$ at a false-alarm level of $p_{\text{FA},\mathcal{P}} = 10^{-9}$.
The simulated line in H1 is visible as a single bin at $\mathcal{P}^{\text{H1}} > 4.5$, indicated by an arrow.

More realistic and diverse examples will be provided with the tests on LIGO data presented in Sec. 10.

8.2 Empirical choice of transition-scale parameter $\widehat{\mathcal{F}}_*^{(0)}$

While the adaptive tuning of the prior line weights $\widehat{r}^X$ is sufficient to fix the line-veto statistic $\widehat{O}_{\text{SL}}$, and while for the line-robust statistic $\widehat{O}_{\text{SGL}}$, as expressed in Eq. (7.91), the same procedure also delivers an estimator for $\widehat{p}_{\text{L}}$, there is an additional free parameter in $\widehat{O}_{\text{SGL}}$, namely $\widehat{\mathcal{F}}_*^{(0)}$.

As discussed in Sec. 7.2.3, $\widehat{\mathcal{F}}_*^{(0)}$ set, together with $\widehat{p}_{\text{L}}$ through the relation (7.97), a scale which any $\widehat{\mathcal{F}}^X$ values must reach for the transition of $\widehat{O}_{\text{SGL}}$ from the signal-versus-Gaussian-noise odds $\widehat{O}_{\text{SG}} \propto \mathrm{e}^{\widehat{\mathcal{F}}}$ to the signal-versus-line odds $\widehat{O}_{\text{SL}}$.

Hence, we can interpret $\widehat{\mathcal{F}}_*^{(0)}$ as the transition scale in the case of indecisive prior information on line prevalence, i.e. $\widehat{p}_{\mathrm{L}} = 0.5$. The data-dependent effect of $\widehat{p}_{\mathrm{L}}$, obtained from the estimation method described in the previous section, is then to shift the transition scale up or down from this baseline, depending on whether the "prior" knowledge gives lines lower or higher odds, respectively.

As the parameter $\widehat{\mathcal{F}}_*^{(0)}$ ultimately goes back to the unphysical amplitude prior from Eq. (7.19), introduced to re-obtain the $\widehat{\mathcal{F}}$-statistic from the Bayesian approach, there is no physical insight available to choose a value for it. Nor is there a direct, deterministic way to obtain it from the complex composite population of Gaussian noise, signal and line distributions.

Therefore, an empirical approach is required, choosing $\widehat{\mathcal{F}}_*^{(0)}$ in a way that delivers good detection performance of $\widehat{O}_{\mathrm{SGL}}$. Even if it were computationally feasible, it would not be admissible to try all possible values (or a representative subset) on the whole data set and then to choose the one yielding the highest detection probabilities: This would constitute pure post-hoc tuning of the detection statistic, invalidating the statistical significance of any results, as they could just be the result of a single-realisation fluctuation.

Instead, $\widehat{\mathcal{F}}_*^{(0)}$ can be tuned on a small "training set" of data. Constructing such a set that is representative for the whole distribution of line-affected data would be very difficult. But luckily, this is not necessary, because an additional requirement on our detection statistic suggests using a much simpler approach.

In introducing a new detection statistic (a tuned $\widehat{O}_{\mathrm{SGL}}$) which can be used over a whole LIGO data set (as opposed to $\widehat{O}_{\mathrm{SL}}$, which would be appropriate only in strongly disturbed bands), we want to be *conservative* in the sense that any gains in disturbed bands must not be countered by significant losses in the more prevalent quiet, nearly Gaussian bands when compared to the plain $\widehat{\mathcal{F}}$-statistic. This is because in typical CW searches, most of the data is approximately Gaussian – as discussed in Sec. 5.1. Hence, a non-conservative tuning of $\widehat{O}_{\mathrm{SGL}}$ would be worse than keeping the $\widehat{\mathcal{F}}$-statistic for most bands, and only using $\widehat{O}_{\mathrm{SL}}$ or a tuned $\widehat{O}_{\mathrm{SGL}}$ for the disturbed bands.

Due to this argument, we can tune $\widehat{\mathcal{F}}_*^{(0)}$ on a simple training set consisting only of Gaussian noise plus signal injections, without lines, by requiring it to reproduce the performance of the $\widehat{\mathcal{F}}$-statistic on that set.

It is a good approximation to ignore the smoothness of $\widehat{O}_{\mathrm{SL}}$ around $\widehat{\mathcal{F}}_*$ and consider it simply as a threshold on the $\widehat{\mathcal{F}}^X$ values. Then, for Gaussian noise, we can express $\widehat{\mathcal{F}}_*^{(0)}$ in terms of a false-alarm probability

$$p_{\mathrm{FA}*}^{(0)} \equiv P\left(\widehat{\mathcal{F}}^X > \widehat{\mathcal{F}}_*^{(0)} | \mathcal{H}_{\mathrm{G}}\right) . \tag{8.9}$$

As introduced for the $\widehat{\mathcal{F}}$-statistic in general in Sec. 5.7, this follows a central χ^2-distribution with $4N_{\mathrm{seg}}$ degrees of freedom. To remove the N_{seg}-dependence, we can fix a single value for $p_{\mathrm{FA}*}^{(0)}$ and use it to determine $\widehat{\mathcal{F}}_*^{(0)}\left(p_{\mathrm{FA}*}^{(0)}, N_{\mathrm{seg}}\right)$.

In practice, we want to set $\widehat{\mathcal{F}}_*^{(0)}$ low enough ($p_{\mathrm{FA}*}^{(0)}$ high enough) to suppress even weak lines (when applied, later on, to disturbed bands outside of the training set), but not so low as to compromise the performance in Gaussian noise. Thus, a reasonable choice is to use the lowest $\widehat{\mathcal{F}}_*^{(0)}$ (highest $p_{\mathrm{FA}*}^{(0)}$) that does not yet adversely affect the detection power in Gaussian noise.

I will demonstrate this approach for synthetic data in Sec. 9.3.2. For practical use on real detector data, as described in Sec. 10, I will perform Monte-Carlo simulations on a small set of Gaussian data to determine the highest $p_{\mathrm{FA}*}^{(0)}$ with near-$\widehat{\mathcal{F}}$ performance. Additional Monte Carlos on a few disturbed bands will verify that this conservative tuning still yields a significant improvement over $\widehat{\mathcal{F}}$.

Note that the relation Eq. (8.9) between $\widehat{\mathcal{F}}_*^{(0)}$ and $p_{\mathrm{FA}*}^{(0)}$ only makes sense for $\widehat{\mathcal{F}}_*^{(0)} > 0$, while the parameter can take on negative values, and $\widehat{O}_{\mathrm{SL}}$ even corresponds to the limit of $\widehat{O}_{\mathrm{SGL}} \Rightarrow -\infty$. However, as it turns out – see Sec. 9.3.2 and Sec. 10 – the tuning method usually does result in positive values.

9 Tests with synthetic draws

For the first set of tests of the new detection statistics O_{SL} and O_{SGL}, I will use completely *synthetic* draws of detection statistics. These are removed one step further from the analysis of real detector data than typical studies on *simulated data*: No full GW-strain time-series and SFTs are generated and passed through an $\mathcal{F}$-statistic based pipeline. Instead, the synthesis algorithm introduced by PK09 and PGM11 directly generates random draws of the various statistics of interest from the underlying noise and signal distributions.

In the following, I will first describe the algorithm in some detail (Sec. 9.1), then present results on Gaussian noise in Sec. 9.3 and on noise containing disturbances in Sec. 9.4. I will also compare the results of tuned and untuned statistics in Sec. 9.5. In this chapter, for simplicity, I consider the coherent case only, i.e. the statistics as derived in Sec. 7.2.

9.1 Synthesis algorithm

As stated in Sec. 5.7, the $\mathcal{F}$-statistic follows a central χ^2-distribution in pure Gaussian noise, and a non-central χ^2-distribution in the presence of a CW signal. However, simply drawing the multi-detector $\mathcal{F}$-statistic from its distribution would not be sufficient to test the line-veto and line-robust statistics, as they also require the single-detector values $\mathcal{F}^X$. These are of course not statistically independent from the multi-detector $\mathcal{F}$. Hence, random draws must be done for more fundamental quantities that contain all the probabilistic information. After optionally adding the deterministic signal information, these will allow computation of the full set of statistics $\left\{ \mathcal{F}, \mathcal{F}^X, O_{\mathrm{SL}}, O_{\mathrm{SGL}} \right\}$.

An appropriate algorithm has been described by PK09 and PGM11 and is implemented in the `LALpulsar-SynthesizeCWDraws` module of LALSuite, which for my purposes I have wrapped in the application `lalapps_SynthesizeLVStats`.

In the definition of the $\mathcal{F}$-statistic from Eq. (5.46), $2\mathcal{F}(\boldsymbol{x}) = x_\mu \, \mathcal{M}^{\mu\nu} \, x_\nu$, the antenna-pattern matrix $\mathcal{M}_{\mu\nu} = \langle \boldsymbol{h}_\mu | \boldsymbol{h}_\nu \rangle$ is a purely deterministic object depending on the basis functions only. The randomness is all inside the projected data components $x_\mu = \langle \boldsymbol{x} | \boldsymbol{h}_\mu \rangle$.

Hence, the algorithm generates random draws of four noise components $n^X_{\mu,\alpha}$ per detector and SFT from a multivariate Gaussian distribution, with the antenna-pattern matrix as the covariance matrix:

$$ n^X_{\mu,\alpha} \sim \mathcal{N}(0, \mathcal{M}^X_{\mu\nu,\alpha}) \, . \tag{9.1} $$

These are used to compute the so-called "$\mathcal{F}$-statistic atoms", introduced before in Eq. (5.52), through the relations

$$F_{\mathrm{a,n}}^X \equiv \sum_{\alpha=1}^{N_{\mathrm{SFT}}^X} \left(n_{1,\alpha}^X - \mathrm{i}n_{3,\alpha}^X \right) \quad \text{and} \quad F_{\mathrm{b,n}}^X \equiv \sum_{\alpha=1}^{N_{\mathrm{SFT}}^X} \left(n_{2,\alpha}^X - \mathrm{i}n_{4,\alpha}^X \right) . \tag{9.2}$$

A signal, parametrised by its amplitudes $\mathcal{A}^\mu$ as

$$s_\mu^X = \left\langle s^X \left| h_\mu^X \right. \right\rangle = \left\langle h_\nu^X \left| h_\mu^X \right. \right\rangle A^\nu = \mathcal{M}_{\mu\nu}^X \mathcal{A}^\nu , \tag{9.3}$$

can be added through

$$F_{\mathrm{a}}^X = F_{\mathrm{a,n}}^X + \sum_{\alpha=1}^{N_{\mathrm{SFT}}^X} \left(s_1^X - \mathrm{i}s_3^X \right) \quad \text{and} \quad F_{\mathrm{b}}^X = F_{\mathrm{b,n}}^X + \sum_{\alpha=1}^{N_{\mathrm{SFT}}^X} \left(s_2^X - \mathrm{i}s_4^X \right) . \tag{9.4}$$

Internally, the codes in `LALpulsar-SynthesizeCWDraws` perform the computation in Eq. (9.3) under the assumption of unit noise PSDs, $S^X = \mathcal{S} = 1$, to make it numerically more stable. The correct scaling of the atoms is done in a subsequent step.

In fact, as long as the S^X are equal for all X, the absolute scaling by $\mathcal{S}$ does not affect the statistics output at all – as long as the signal strength is scaled appropriately, with the relevant quantity being $h/\sqrt{S}$. Thus, $\mathcal{S} = 1$ can be assumed in general for the synthesis approach. However, unequal per-detector sensitivities S^X, as studied later in Sec. 12, do affect the results. These are handled through noise-weighting the antenna pattern matrix, see Sec. 5.5.

In the next step, the atoms and the antenna-pattern matrix elements A^X, B^X, C^X and determinant D^X are used to compute the per-detector $\mathcal{F}^X$-statistics through the relation

$$2\mathcal{F}^X = \frac{2}{DN_{\mathrm{SFT}}^X} \left(B|F_{\mathrm{a}}^X|^2 + A|F_{\mathrm{b}}^X|^2 - 2C \,\Re\left(F_{\mathrm{a}}^X F_{\mathrm{b}}^{X*} \right) \right) . \tag{9.5}$$

For the multi-detector statistic, the atoms and matrix elements from all detectors are summed up, as in Eq. (5.50b). Computing O_{SL} and O_{SGL} is then straightforward, using Eqs. (7.44) and (7.68).

In the following, I refer to each draw of $\{x_\mu^X\}$, together with the resulting statistics, as a *candidate*. Note that, for a general CW signal, the synthetic statistics depend on the four amplitude parameters $\{h_0, \cos\iota, \psi, \phi_0\}$ through the $\mathcal{A}^\nu$ in Eq. (9.3) and on the sky location (α, δ) through $\mathcal{M}_{\mu\nu}$ (see expressions in Sec. 5.6), but not on the other phase-evolution parameters $\{f, \dot{f}, \ddot{f}, \dots\}$. Hence, results from studies on synthetic statistics should be representative for any frequency band of interest, as long as the noise spectra S^X are chosen appropriately, which for equal-sensitivity detectors only influences the scaled amplitude $h_0^{\mathcal{S}} \equiv h_0/\sqrt{\mathcal{S}[1/\mathrm{Hz}]}$.

In all the synthetic studies presented in this thesis, three of the signal amplitude parameters are drawn uniformly from their full support, i.e. $\cos\iota \in [-1, 1]$, $\psi \in [-\pi/4, \pi/4]$

116

and $\phi_0 \in [0, 2\pi]$. The set is completed with either a fixed value of $h_0^{\mathcal{S}}$ or a fixed (multi-detector) *signal-to-noise ratio* ρ_{S}, defined as in Eq. (5.49). The latter is directly related to the expectation value of the $\mathcal{F}$-statistic as $E[2\mathcal{F}]_{\mathcal{H}_{\mathrm{S}}} = 4 + \rho_{\mathrm{S}}^2$ (see Sec. 5.7) and the two quantities are related through Eq. (5.53). The sky position is drawn isotropically over the sky, unless otherwise noted.

In this approach, lines are simulated exactly according to $\mathcal{H}_{\mathrm{L}}$ of Eq. (7.30): as a CW signal in a single detector. Specifically, the amplitude parameters are drawn from the same prior distributions as for the signal case, but then used only for a single set of $\mathcal{A}^{X\nu}$, while $\mathcal{A}^{Y\nu} = 0$ for $Y \neq X$. As shown in Sec. 7.4, the expectation value of the multi-detector $\mathcal{F}$-statistic in this case is approximately

$$E\left[2\mathcal{F}\right]_{\mathcal{H}_{\mathrm{L}}} \approx 4 + \frac{1}{N_{\mathrm{det}}}\,\rho_{\mathrm{L}}^2 \ \ \text{with} \ \ \rho_{\mathrm{L}}^2 \equiv \mathcal{A}_Y^\mu \mathcal{M}_{\mu\nu}^Y \mathcal{A}_Y^\nu\,, \tag{9.6}$$

with a (single-detector) "line SNR" ρ_{L}.

9.2 Notes on studies with synthetic draws

The following studies require both a set of *noise draws*, including pure Gaussian noise and, possibly, line-affected candidates, and a set of signal candidates. For the noise draws, in each detector a fraction f_{L}^X of draws contains a line and the remaining fraction $1 - f_{\mathrm{L}}^X$ are pure Gaussian noise. I will also refer to f_{L}^X as the *line contamination*.

In analysing these data sets, I use the noise draws to estimate, for each statistic, a threshold corresponding to a particular false-alarm probability p_{FA}. Applying this threshold to the signal candidates yields, for each statistic, the detection probability $p_{\mathrm{det}}(p_{\mathrm{FA}})$ at that false-alarm level p_{FA}. This is known as the *receiver-operating characteristic* (ROC).

Unless otherwise noted, candidates are generated for a network consisting of two detectors, LIGO H1 and L1, assuming identical sensitivity. Lines are only injected into H1, without loss of generality under the non-coincident line hypothesis $\mathcal{H}_{\mathrm{L}}$. A total data length of $T = 25\,\mathrm{h}$, corresponding to $N_{\mathrm{SFT}}^X = 50$ and $N_{\mathrm{SFT}} = 100$, is usually used.

Finally, note that for synthetic statistics the line-prior estimation method for o_{LG}^X of Sec. 8.1 cannot be used, as no SFTs are ever generated and therefore no $\mathcal{P}^X$ values are available. Instead, the proportion of Gaussian and line candidates in the noise sample is exactly known, so that I can simply assume "perfect-knowledge tuning": In pure Gaussian noise examples, I set $o_{\mathrm{LG}}^{\mathrm{H1}} = o_{\mathrm{LG}}^{\mathrm{L1}} = 0.001$, corresponding to the truncation rule from Eq. (8.7). In the presence of lines, I use $p_{\mathrm{L}}^{\mathrm{H1}} = f_{\mathrm{L}}^{\mathrm{H1}}$, so that $o_{\mathrm{LG}}^{\mathrm{H1}} = \frac{f_{\mathrm{L}}^{\mathrm{H1}}}{1 - f_{\mathrm{L}}^{\mathrm{H1}}}$, and $o_{\mathrm{LG}}^{\mathrm{L1}} = 0.001$, as no lines were injected into L1.

9.3 Behaviour for Gaussian draws

9.3.1 Example ROCs

Let me begin the presentation of results from the synthesis approach with the detection performance of various statistics in pure Gaussian noise. ROC curves for different signal populations and statistics are shown in Fig. 9.1 for fixed SNRs of $\rho_S \in \{2, 4, 6\}$ and in Fig. 9.2 for fixed scaled amplitudes $h_0^S \in \{0.025, 0.05, 0.075\}$. The fixed-$h_0^S$ candidates have similar average SNRs as the fixed-SNR populations: using Eq. (5.53), and averaging over the $N_{\mathrm{draws}} = 10^7$ candidates with uniformly distributed $\cos\iota$, ψ and ϕ_0, these are $\bar{\rho}_S \left(h_0^S = 0.025 \right) \approx 2$, $\bar{\rho}_S \left(h_0^S = 0.05 \right) \approx 4$ and $\bar{\rho}_S \left(h_0^S = 0.075 \right) \approx 6$.

In both figures, the left-hand column shows ROC curves for the $\mathcal{F}$-statistic, the $\mathcal{F}^{+\mathrm{veto}}$-statistic, O_{SL} and $O_{\mathrm{SGL}}(\mathcal{F}_*^{(0)} = 10)$, as well as the analytical Gaussian-noise expectation from a χ^2-distribution of the $\mathcal{F}$-statistic. In the right-hand column, these are contrasted with ROCs for O_{SGL}, using several values of $\mathcal{F}_*^{(0)}$.

These results confirm the expectation that the multi-detector $\mathcal{F}$-statistic should be (close to) optimal in pure Gaussian noise (see Sec. 5.7 and JKS98, PK09). Its detection probabilities closely follow the prediction from a χ^2-distribution with 4 degrees of freedom and non-centrality parameter ρ_S^2.

The ROCs for fixed scaled amplitude h_0^S deviate from the χ^2 expectation for the corresponding $\bar{\rho}_S$. For example, in the $h_0^S = 0.05$ population, there is a deficit of p_{det} at high p_{FA} and an excess at low p_{FA}. With the individual signal candidates covering a range in ρ_S and therefore a wider range in $\mathcal{F}$ than for the fixed-ρ_S population, the lower outliers can fall even below the low threshold corresponding to a high p_{FA}; while the higher outliers remain detectable at much lower p_{FA} (high thresholds). For a demonstration, see the comparison of the $2\mathcal{F}$ histogram to that for fixed $\rho_S = 4$ in Fig. 9.3.

In all examples, the $\mathcal{F}^{+\mathrm{veto}}$-statistic performs very similarly to plain $\mathcal{F}$ at low p_{FA}, as most Gaussian and signal candidates pass the veto step unmodified. At higher p_{FA}, the ROC curve for $\mathcal{F}^{+\mathrm{veto}}$ slants away from that for $\mathcal{F}$. This is due to intrinsic upper bounds on the achievable p_{FA} and p_{det}, as a result of vetoing a finite fraction of candidates. At the highest p_{FA}, the curve vanishes, as $\mathcal{F}^{+\mathrm{veto}}$ never reaches these values. For practical CW searches, where low p_{FA} are required, this behaviour is not particularly relevant.

O_{SL}, on the other hand, is notably less powerful in these examples. It suffers from the bad fit between the lines-only noise model $\mathcal{H}_{\mathrm{L}}$ and the purely Gaussian actual noise population. The effect of this can be seen in a scatter plot of the $2\mathcal{F}$ and O_{SL} values for all noise and signal candidates, shown for the $\rho_S = 4$ case in Fig. 9.4.

As shown in the right-hand column of Figs. 9.1 and 9.2, the line-robust statistics O_{SGL} increasingly approach the $\mathcal{F}$-statistic performance with increasing $\mathcal{F}_*^{(0)}$. In particular, at $\mathcal{F}_*^{(0)} \approx 10$, there are no appreciable losses in detection probability p_{det} over the analysed false-alarm range $p_{\mathrm{FA}} \in [10^{-6}, 1]$.
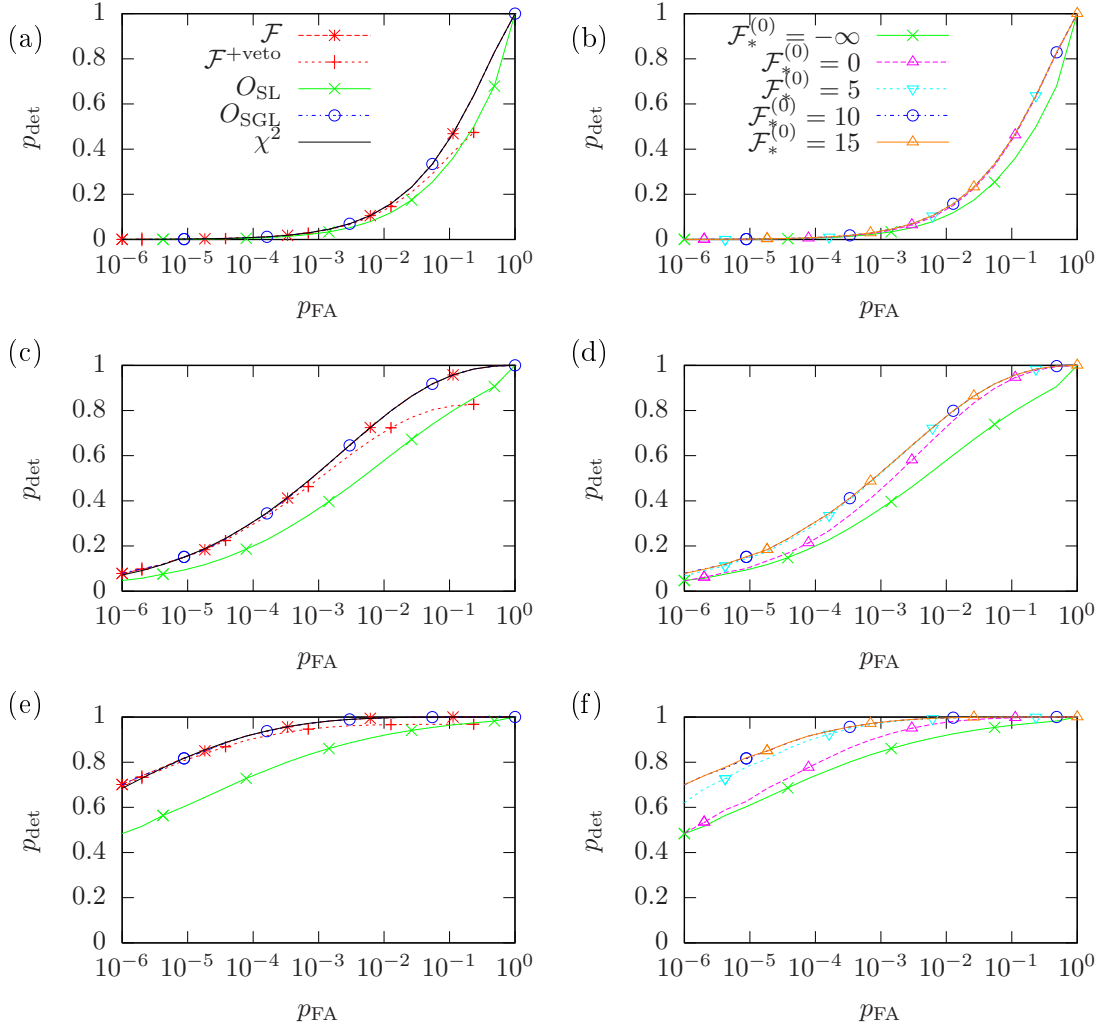
Figure 9.1: Detection probability p_det as a function of false-alarm probability p_FA of different synthetic statistics, for pure Gaussian noise and signal populations with $\rho_\mathrm{S} = 2$ (first row), $\rho_\mathrm{S} = 4$ (second row), $\rho_\mathrm{S} = 6$ (third row).

Each column shows ROCs for the statistics listed in the legend of the respective top panel: with the first column comparing $\mathcal{F}$, $\mathcal{F}^{+\mathrm{veto}}$, O_SL, $O_\mathrm{SGL}(\mathcal{F}_*^{(0)} = 10)$ (labelled simply O_SGL) and the theoretical expectation for $\mathcal{F}$ (labelled χ^2); and the second column comparing O_SGL with several $\mathcal{F}_*^{(0)}$ values.

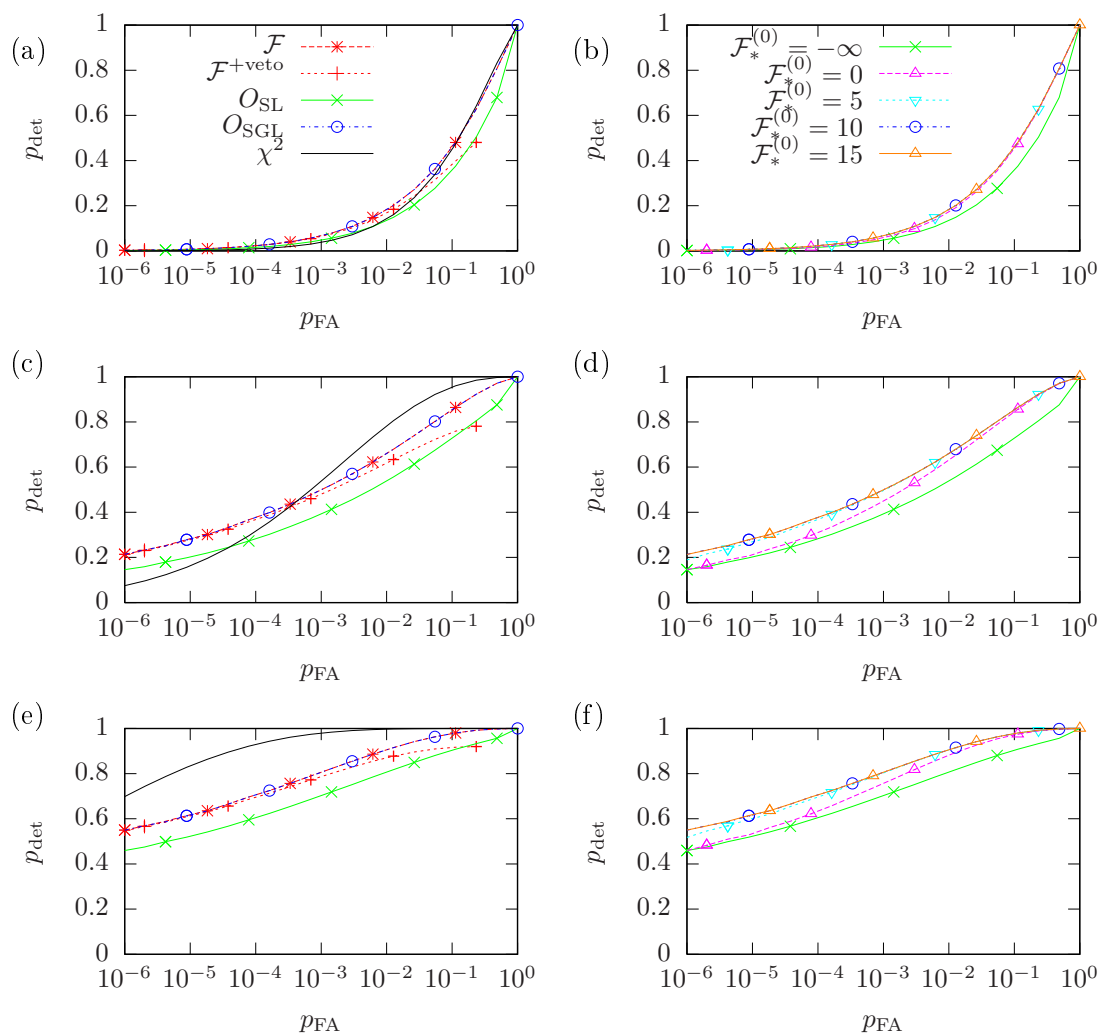Statistical errors are not drawn; for $N_\mathrm{draws} = 10^7$ these are similar to the line widths.

Figure 9.2: Detection probability p_{det} as a function of false-alarm probability p_{FA} of different synthetic statistics, for pure Gaussian noise and signal populations with fixed scaled signal amplitudes $h_0^{\mathcal{S}} = 0.025 \Rightarrow \bar{\rho}_{\mathrm{S}} \approx 2$ (first row), $h_0^{\mathcal{S}} = 0.05 \Rightarrow \bar{\rho}_{\mathrm{S}} \approx 4$ (second row), $h_0^{\mathcal{S}} = 0.075 \Rightarrow \bar{\rho}_{\mathrm{S}} \approx 6$ (third row).

See the caption of Fig. 9.1 and the legends in the top row for further details. Here, the χ^2 expectation is computed using the average SNRs.

Figure 9.3: Comparison of $2\mathcal{F}$ histograms for signals with fixed $\rho_S = 4$ (blue) and with fixed $h_0^S = 0.05$ (red). The two vertical lines give the thresholds corresponding to $p_{FA} = 10^{-4}$, where $p_{\det,\rho_S} < p_{\det,h_0^S}$, and to $p_{FA} = 0.1$, where $p_{\det,\rho_S} > p_{\det,h_0^S}$.

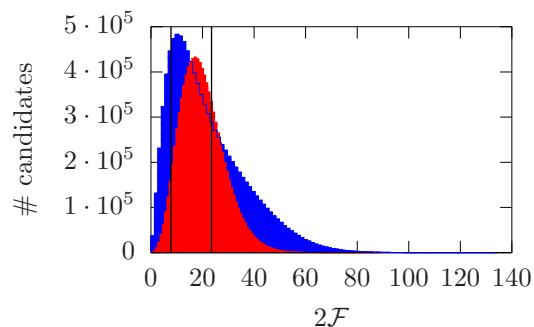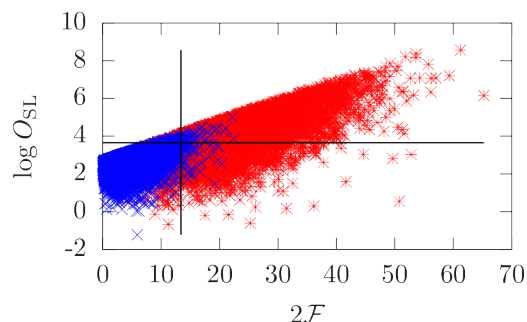
Figure 9.4: Comparison of $2\mathcal{F}$ and $\log O_{SL}$ values for 10^4 candidates from Gaussian noise (blue crosses) and from signals with $\rho_S = 4$ (red stars). The vertical and horizontal lines give the respective $p_{FA} = 0.01$ thresholds for both statistics.

9.3.2 Optimisation of transition-scale parameter $\widehat{\mathcal{F}}_*^{(0)}$

The Gaussian-noise ROCs have already indicated an "optimum" value of $\mathcal{F}_*^{(0)} \approx 10$ for the data sets considered here. However, I will now assess this question more quantitatively, with a variant of the optimisation scheme discussed in Sec. 8.2.

To that end, I have synthesised signal populations with 21 different fixed SNRs, $\rho_S \in [0, 12]$. To save on computation time, only 10^6 candidates were drawn for each population. The very simple optimisation algorithm consists of starting with a high $\mathcal{F}_*^{(0)}$, comparing the detection probabilities for $O_{SGL}(\mathcal{F}_*^{(0)})$ and $2\mathcal{F}$ and accepting the value if the difference is below a certain tolerance τ. The two panels of Fig. 9.5 show the resulting optimum $\mathcal{F}_*^{(0)}$ as a function of p_{FA} for tolerances of 1% and 2.5%, respectively. Values below $\mathcal{F}_*^{(0)} = 0$ were not considered, so that the white areas possibly allow for even lower values.

I find in Fig. 9.5 that the constraint on $\mathcal{F}_*^{(0)}$ comes from a band at intermediate ρ_S. At high ρ_S, both $p_{\det}(2\mathcal{F})$ and $p_{\det}(O_{SGL}(\mathcal{F}_*^{(0)}))$ go towards 1, so that the absolute difference becomes negligible; the same happens at low ρ_L with both going to 0. So at the extremes, any value of $\mathcal{F}_*^{(0)}$ is accepted, and the same would hold true even for the limiting case $O_{SL} = O_{SGL}\left(\mathcal{F}_*^{(0)} = -\infty\right)$.

Meanwhile, in the intermediate regime, low p_{FA} values require high $\mathcal{F}_*^{(0)}$ values, in keeping with the individual ROC results seen before. A value of $\mathcal{F}_*^{(0)} = 10$ is good down
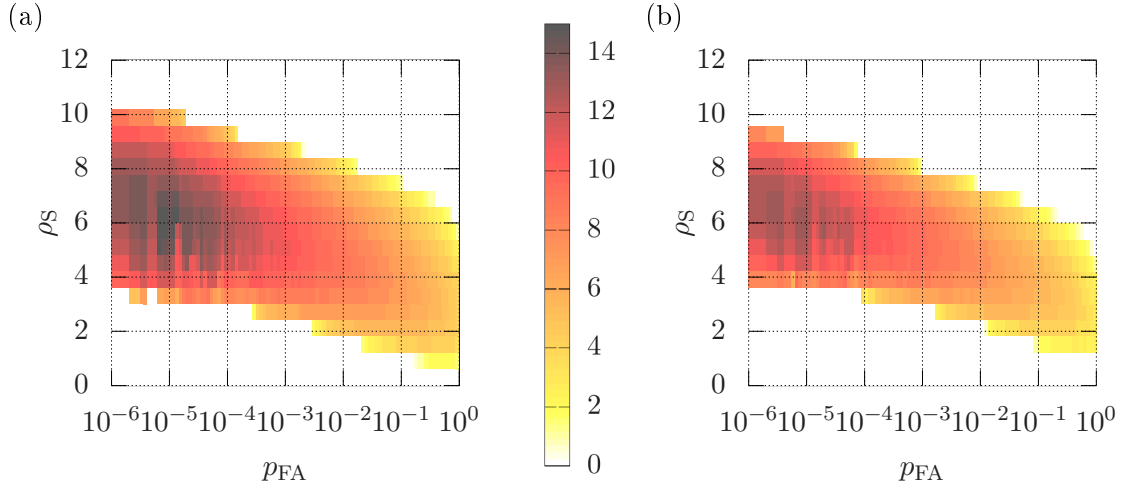
(a) (b)

Figure 9.5: Optimisation results for $\mathcal{F}_*^{(0)}$ in synthetic Gaussian noise. Shown are the lowest $\mathcal{F}_*^{(0)}$ values that still satisfy $p_{\text{det}}\left(2\mathcal{F}\right) - p_{\text{det}}\left(O_{\text{SGL}}\left(\mathcal{F}_*^{(0)}\right)\right) < \tau$, where the tolerance is $\tau = 0.01$ in panel (a) and $\tau = 0.025$ in panel (b). 21 values for ρ_{S} with 10^6 draws each, 100 logarithmic steps in p_{FA} and a resolution of 0.5 in $\mathcal{F}_*^{(0)}$ were used.

to $p_{\text{FA}} \sim 10^{-3}$ for $\tau = 0.01$ and down to $p_{\text{FA}} \sim 10^{-4}$ for $\tau = 0.025$, while at $p_{\text{FA}} \sim 0.1$ already $\mathcal{F}_*^{(0)} \approx 4 - 5$ is enough in both cases.

9.4 Behaviour for draws with disturbances

9.4.1 Example ROCs

For the next set of ROCs, I consider only one signal population, with fixed $\rho_{\text{S}} = 6$. Meanwhile, I change from pure Gaussian noise to noise populations with 90% Gaussian candidates and 10% lines, of the $\mathcal{H}_{\text{L}}$ type defined in Eq. (7.30), in H1: i.e., 10% line contamination, $f_{\text{L}}^{\text{H1}} = 0.1$. I consider three data sets, where the lines have strengths $\rho_{\text{L}} \in \{6, 9, 15\}$. While the signals have an expected multi-detector $\mathcal{F}$-statistic value of $E\left[2\mathcal{F}(\rho_{\text{S}} = 6)\right]_{\mathcal{H}_{\text{S}}} = 40$, Eq. (9.6) gives for the multi-detector expectation of the line candidates:
$E\left[2\mathcal{F}(\rho_{\text{L}} = 6)\right]_{\mathcal{H}_{\text{L}}} \approx 22$, $E\left[2\mathcal{F}(\rho_{\text{L}} = 9)\right]_{\mathcal{H}_{\text{L}}} \approx 44.5$ and $E\left[2\mathcal{F}(\rho_{\text{L}} = 15)\right]_{\mathcal{H}_{\text{L}}} \approx 116.5$.

In these studies, I use perfect-knowledge line priors, i.e. $p_{\text{L}}^{\text{H1}} = f_{\text{L}}^{\text{H1}} = 0.1 \Rightarrow o_{\text{LG}}^{\text{H1}} = 1/9$ and, since no lines were injected into L1, $o_{\text{LG}}^{\text{L1}} = 0.001$ (according to the truncation rule from Eq. (8.7)). The results, for the same set of statistics as before in the Gaussian case, are shown in Fig. 9.6.
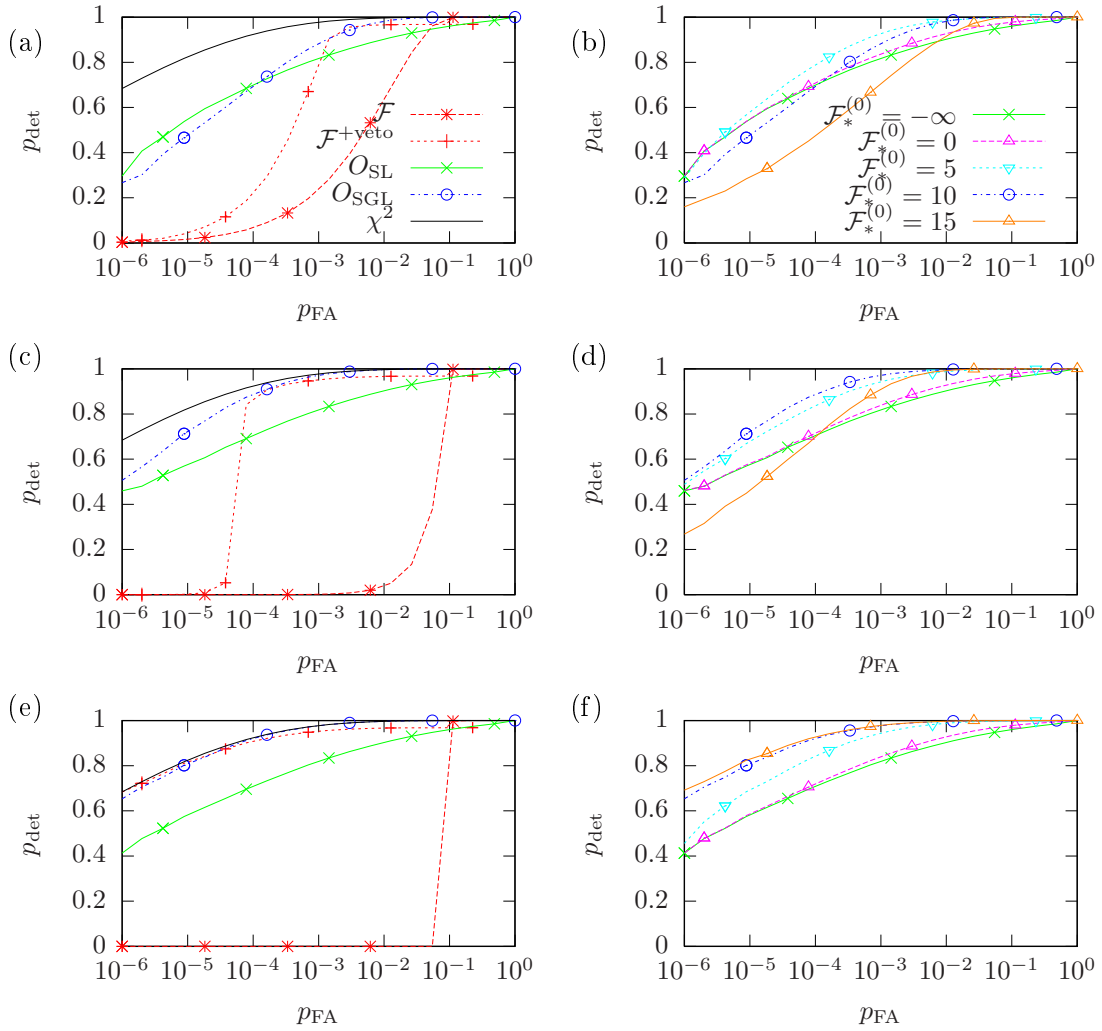
Figure 9.6: Detection probability p_{det} as a function of false-alarm probability p_{FA} of different synthetic statistics, for signals with $\rho_{\mathrm{S}} = 6$ and noise that is 90% Gaussian with 10% line contamination, with line strengths $\rho_{\mathrm{L}} = 6$ (first row), $\rho_{\mathrm{L}} = 9$ (second row), $\rho_{\mathrm{L}} = 15$ (third row). See the caption of Fig. 9.1 and the legends in the top row for further details.

Here the $\mathcal{F}$-statistic performs substantially worse than in Gaussian noise at all false-alarm probabilities below $p_{\mathrm{FA}} \lesssim 0.1$. This already happens in the $\rho_{\mathrm{L}} = 6$ case, where the expected $\mathcal{F}$-statistic of the lines is still smaller than that of the signal, because a few strong outliers dominate the setting of a threshold at low p_{FA} – as can be seen in the $2\mathcal{F}$-O_{SGL} scatter plot in Fig. 9.7. Then, at higher ρ_{L}, the slope of $p_{\det}(\mathcal{F})$ becomes very steep, as crossing the $\mathcal{F}$-values of the bulk and even the lower outliers of the noise populations becomes very difficult ($\rho_{\mathrm{L}} = 9$) and then almost impossible (for $\rho_{\mathrm{L}} = 15$) for the signal candidates.
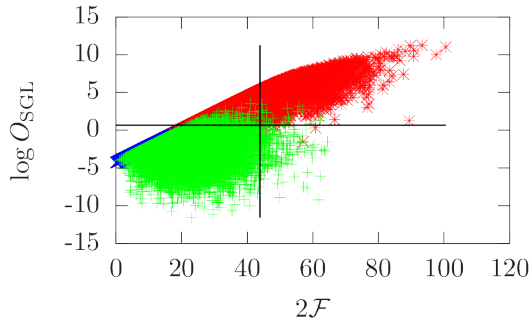

Figure 9.7: Comparison of $2\mathcal{F}$ and $\log O_{\mathrm{SGL}}(\mathcal{F}_*^{(0)} = 10)$ values for 10^4 candidates from Gaussian noise (blue crosses), lines with $\rho_{\mathrm{L}} = 6$ (green plus signs) and signals with $\rho_{\mathrm{S}} = 6$ (red stars). The vertical and horizontal lines give the respective $p_{\mathrm{FA}} = 0.01$ thresholds for both statistics.

Meanwhile, the $\mathcal{F}^{+\mathrm{veto}}$-statistic stays close to the Gaussian-noise-only performance if p_{FA} is high or the lines are strong, while it is bad at distinguishing weak lines from signals at low p_{FA}. Let us look at this effect in more detail for the $\rho_{\mathrm{L}} = 9$ example. The veto step itself is independent of p_{FA}, which instead influences the threshold on the resulting $\mathcal{F}^{+\mathrm{veto}}$ statistic. Here, a fraction of $\sim 6 \times 10^{-4}$ of line candidates survive the veto. Given that lines are present in 10% of the noise cases, this means that still a fraction of $\sim 6 \times 10^{-5}$ of all noise candidates are line candidates which have survived the consistency veto, though sometimes only marginally. Given that these still have their high $\mathcal{F}$-statistic values according to the ρ_{L} distribution, any signal candidates can hardly surpass them, and thus the detection probability drops toward zero at $p_{\mathrm{FA}} \lesssim 6 \times 10^{-5}$. This effect is also visible in the $2\mathcal{F}^{+\mathrm{veto}} - O_{\mathrm{SL}}$ scatter plot of Fig. 9.8, where a few outliers move the $2\mathcal{F}^{+\mathrm{veto}}$ threshold at $p_{\mathrm{FA}} = 10^{-5}$ far to the right.
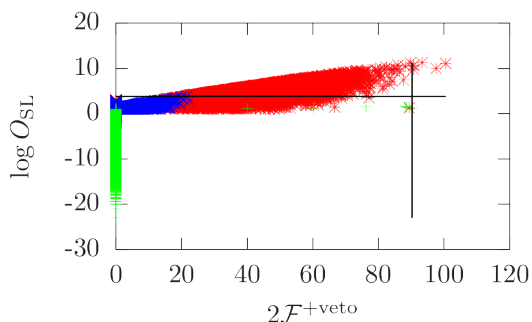
Figure 9.8: Comparison of $2\mathcal{F}^{+\mathrm{veto}}$ and $\log O_{\mathrm{SL}}$ values for 10^4 candidates from Gaussian noise (blue crosses), lines with $\rho_{\mathrm{L}} = 9$ (green plus signs) and signals with $\rho_{\mathrm{S}} = 6$ (red stars). The vertical and horizontal lines give the respective $p_{\mathrm{FA}} = 10^{-5}$ thresholds for both statistics. Note the four line outliers pushing the $2\mathcal{F}^{+\mathrm{veto}}$ threshold far to the right.

This "failure threshold" of the $\mathcal{F}^{+\mathrm{veto}}$-statistic is a function of line strength: For $\rho_{\mathrm{L}} = 6$,

it already happens at $p_{\text{FA}} \sim 10^{-3}$, for $\rho_{\text{L}} = 12$ at $p_{\text{FA}} \lesssim 10^{-6}$ and for $\rho_{\text{L}} = 15$ it is too low to be resolvable by 10^7 random draws.

In comparison, O_{SL} performs better in the sense that it is almost independent of ρ_{L}, and much better than the $\mathcal{F}$-statistic, in all these line-affected examples. However, it still loses 10-20% compared to the Gaussian noise optimum performance, and similarly compared to the $\mathcal{F}^{+\text{veto}}$-statistic above its "failure threshold". This is not surprising, given that at most 10% of noise draws contain a line, while O_{SL} would only be optimal for a noise population consisting exclusively of lines.

Indeed, these shortcomings can be remedied by using a properly-tuned line-robust statistic O_{SGL}, as seen in the second column of Fig. 9.6. Again, the behaviour depends on the choice of transition scale. For the two stronger-line cases, $\mathcal{F}_*^{(0)} = 10$ yields a performance similar to the $\mathcal{F}^{+\text{veto}}$-statistic at high p_{FA}, but loosing less towards the low end, thus staying close to the Gaussian-noise optimum. At first glance, it might be surprising that the low-ρ_{L} case is the most difficult detection problem, in the sense that even O_{SGL} cannot match its performance in pure Gaussian noise. However, this makes sense, as stronger lines are easier to separate from signals, while for $\rho_{\text{S}} \approx \rho_{\text{L}}$ the two populations have a certain overlap in all statistics. O_{SGL} still outperforms both O_{SL} and $\mathcal{F}^{+\text{veto}}$ in this case, as well.

9.4.2 Dependence on population parameters

After having highlighted the most important features of the new detection statistics in the selected ROC curves shown so far, I will now explore their dependence on the signal and noise parameters more systematically by considering p_{det} of the four statistics $\mathcal{F}$, $\mathcal{F}^{+\text{veto}}$, O_{SL} and $O_{\text{SGL}}(\mathcal{F}_*^{(0)} = 10)$ over a wide range of signal and noise populations. In Fig. 9.9, I have plotted these over a 2-D-grid of ρ_{L} and ρ_{S} at fixed line contamination $f_{\text{L}}^{\text{H1}} = 0.1$ and false-alarm probability $p_{\text{FA}} = 0.001$, with both O_{SL} and O_{SGL} using $o_{\text{LG}}^{\text{H1}} = 1/9$, $o_{\text{LG}}^{\text{L1}} = 0.001$. The Gaussian-noise case corresponds to the $\rho_{\text{L}} = 0$ limit at the left edge of each plot.

While the $\mathcal{F}$-statistic needs rapidly increasing ρ_{S} to achieve the same p_{det} when ρ_{L} rises, the other three statistics seem almost immune against these disturbances. The only exception is a region with $2 \lesssim \rho_{\text{S}} \lesssim 6$ and $3 \lesssim \rho_{\text{L}} \lesssim 7$, where $\mathcal{F}^{+\text{veto}}$ and O_{SGL} lose some power compared to O_{SL}. This is just where $E\left[2\mathcal{F}\right]_{\mathcal{H}_{\text{L}}} \approx E\left[2\mathcal{F}\right]_{\mathcal{H}_{\text{S}}}$.

For one such parameter combination, $\rho_{\text{L}} = 6$ and $\rho_{\text{S}} = 3$, histograms of O_{SL} and $O_{\text{SGL}}(\mathcal{F}_*^{(0)} = 10)$ are shown in Fig. 9.10. There are large overlaps between the Gaussian, line and signal populations for both detection statistics. However, O_{SL} achieves a cleaner separation between line and signal candidates in this case.

The kind of plot shown in Fig. 9.9 is not ideally suited for direct comparisons of detection statistics. Therefore, I also show differences of p_{det} for $O_{\text{SGL}}(\mathcal{F}_*^{(0)} = 10)$ compared to the other statistics in Fig. 9.11, at three different p_{FA} values.
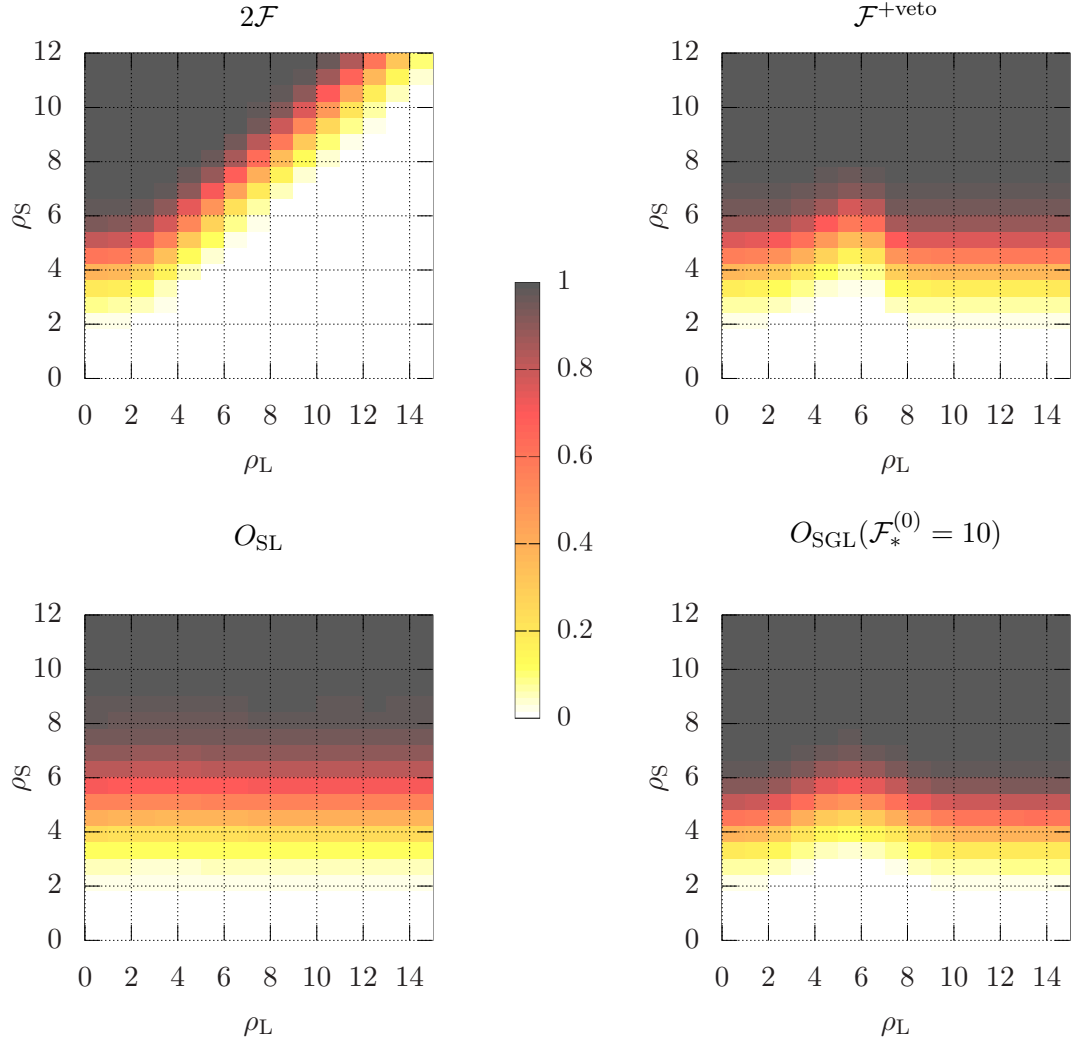
Figure 9.9: Detection probability p_{det} as a function of ρ_{L} and ρ_{S}, at fixed line contamination $f_{\mathrm{L}}^{\mathrm{H1}} = 0.1$ and false-alarm probability $p_{\mathrm{FA}} = 0.001$. The panels show different synthetic statistics: $2\mathcal{F}$, $\mathcal{F}^{+\mathrm{veto}}$, O_{SL} and $O_{\mathrm{SGL}}(\mathcal{F}_*^{(0)} = 10)$.
Both O_{SL} and O_{SGL} use $o_{\mathrm{LG}}^{\mathrm{H1}} = 1/9$, $o_{\mathrm{LG}}^{\mathrm{L1}} = 0.001$.
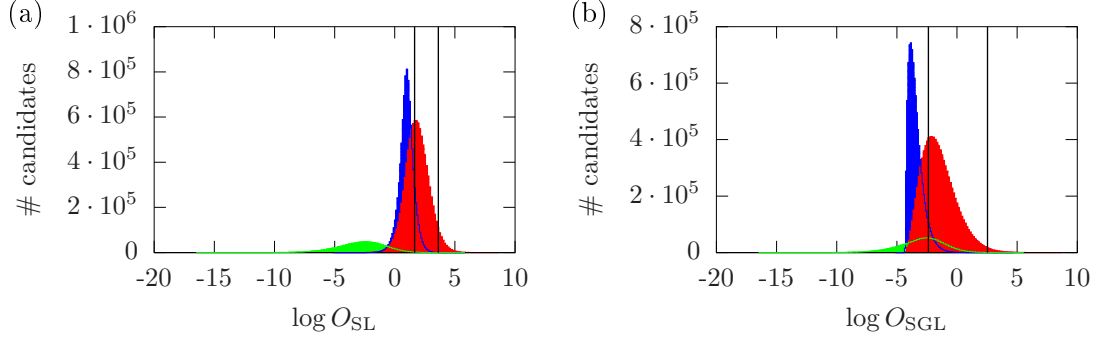
Figure 9.10: Detection-statistic histograms for Gaussian noise (blue), signals with fixed $\rho_{\mathrm{S}} = 3$ (red) and lines with fixed $\rho_{\mathrm{L}} = 6$ (green). Panel (a): O_{SL}, panel (b): $O_{\mathrm{SGL}}(\mathcal{F}_*^{(0)} = 10)$. In each panel, the two vertical lines are thresholds corresponding to $p_{\mathrm{FA}} = 10^{-4}$ and to $p_{\mathrm{FA}} = 0.1$.

Against $2\mathcal{F}$, the improvement is clear, reaching $\Delta p_{\mathrm{det}} \sim 0.8$ for high ρ_{L}. The region of largest differences shifts towards lower ρ_{S} with increasing p_{FA} simply because the $p_{\mathrm{det}} \approx 1$ regime cannot not yield big differences.

Against $\mathcal{F}^{+\mathrm{veto}}$ and O_{SL}, the interesting behaviour in the $E\left[2\mathcal{F}\right]_{\mathcal{H}_{\mathrm{L}}} \approx E\left[2\mathcal{F}\right]_{\mathcal{H}_{\mathrm{S}}}$ region is visible, again. Still, considered as an integral over the whole $(\rho_{\mathrm{L}}, \rho_{\mathrm{S}})$ parameter space and p_{FA} range, it is clear that $O_{\mathrm{SGL}}(\mathcal{F}_*^{(0)} = 10)$ is the most robust and most efficient detection statistic of the set.

Yet, the full parameter space of the $\mathcal{H}_{\mathrm{S}}, \mathcal{H}_{\mathrm{G}}, \mathcal{H}_{\mathrm{L}}$ models has more dimensions. In Fig. 9.12 and Fig. 9.13, I show the same kind of graphs as in the last two figures, but now along the x-axis the variable is $f_{\mathrm{L}}^{\mathrm{H1}}$ instead of ρ_{L}, at fixed $\rho_{\mathrm{L}} = 9$.

Here, I find a qualitatively similar picture, with all statistics except the pure $\mathcal{F}$-statistic performing decently towards high f_{L}, with some intermediate cases where $\mathcal{F}^{+\mathrm{veto}}$ or O_{SL} are slightly better than O_{SGL}, but with the latter clearly being the most robust over the whole parameter space and p_{FA} range.

As a result of these studies, I can conclude that O_{SGL} with a properly chosen $\mathcal{F}_*^{(0)}$ (which in this case turns out as $\mathcal{F}_*^{(0)} \approx 10$, although this value may depend on the data set) is a very robust detection statistic over a wide range of signal and noise populations. However, the behaviour of all the statistics studied here, depending on population parameters and p_{FA}, is non-trivial, and picking a detection statistic for any well-defined detection problem can still require detailed studies of this kind.
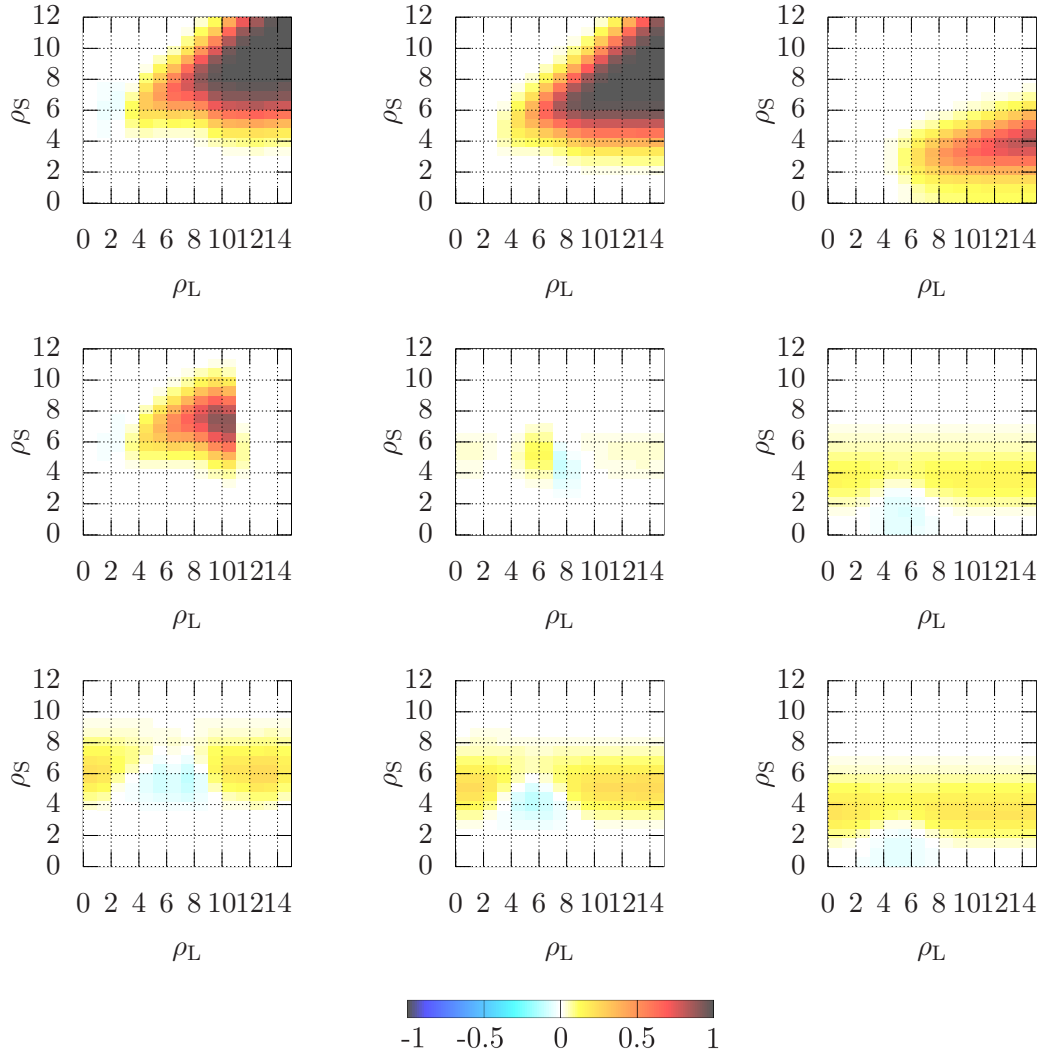
Figure 9.11: Difference of detection probabilities $p_{\text{det}}(O_{\text{SGL}}(\mathcal{F}_*^{(0)} = 10))$ and $p_{\text{det}}(\mathcal{F})$ as a function of ρ_{L} and ρ_{S}, at fixed line contamination $f_{\text{L}}^{\text{H1}} = 0.1$. The three column are for false-alarm probability of $p_{\text{FA}} \in \{10^{-5}, 10^{-3}, p_{\text{FA}} = 0.1\}$.
First row: compared with $p_{\text{det}}(\mathcal{F})$, second row: $p_{\text{det}}(\mathcal{F}^{+\text{veto}})$, third row $p_{\text{det}}(O_{\text{SL}})$.
Both O_{SL} and O_{SGL} use $o_{\text{LG}}^{\text{H1}} = 1/9$, $o_{\text{LG}}^{\text{L1}} = 0.001$.
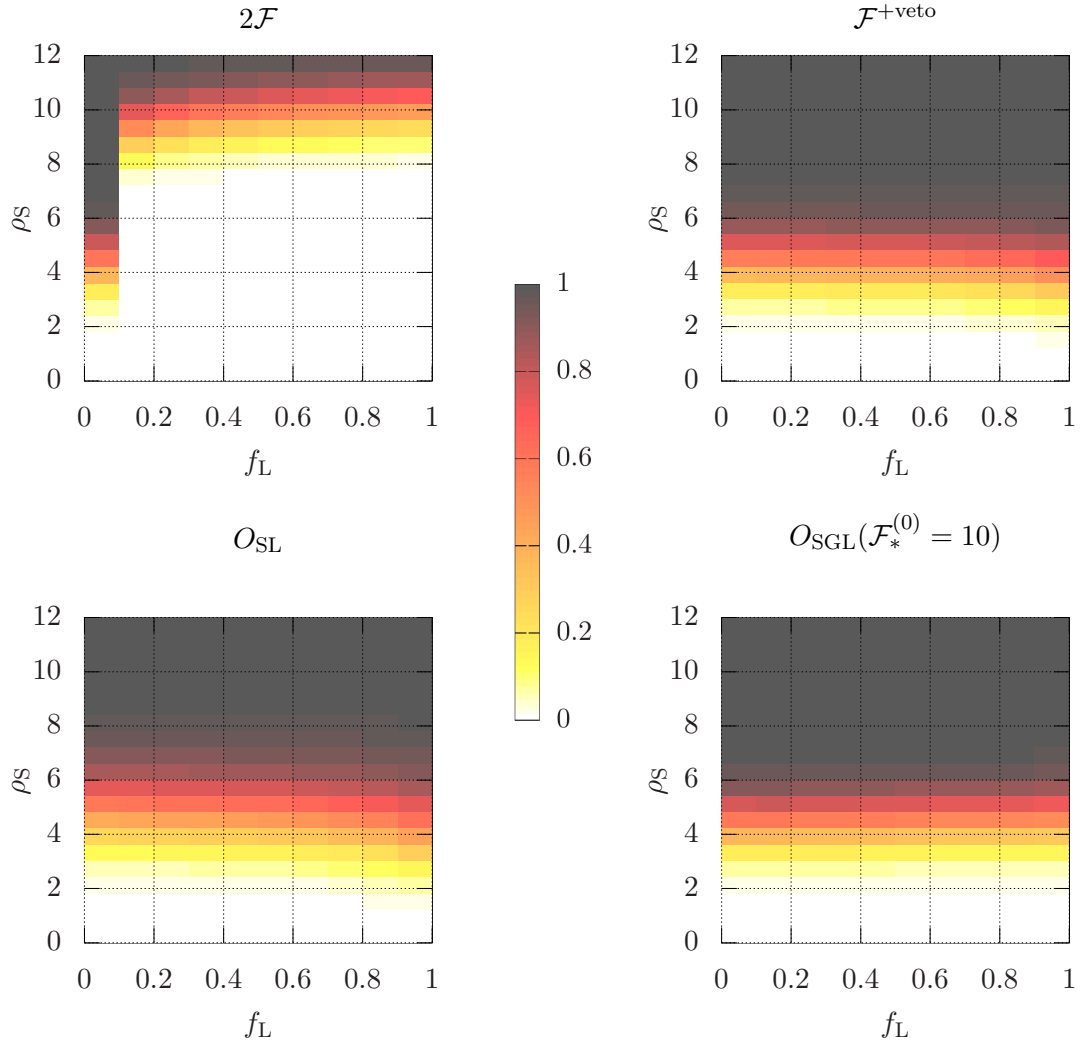
Figure 9.12: Detection probability p_{det} as a function of $f_{\mathrm{L}}^{\mathrm{H1}}$ and ρ_{S}, at fixed line strength $\rho_{\mathrm{L}} = 9$ and false-alarm probability $p_{\mathrm{FA}} = 0.001$. The panels show different synthetic statistics: $\mathcal{F}$, $\mathcal{F}^{+\mathrm{veto}}$, tuned O_{SL} and tuned $O_{\mathrm{SGL}}(\mathcal{F}_*^{(0)} = 10)$.

Though $f_{\mathrm{L}}^{\mathrm{H1}}$ changes over the x-axis, here for convenience I have kept fixed $o_{\mathrm{LG}}^{\mathrm{H1}} = o_{\mathrm{LG}}^{\mathrm{L1}} = 0.5$.
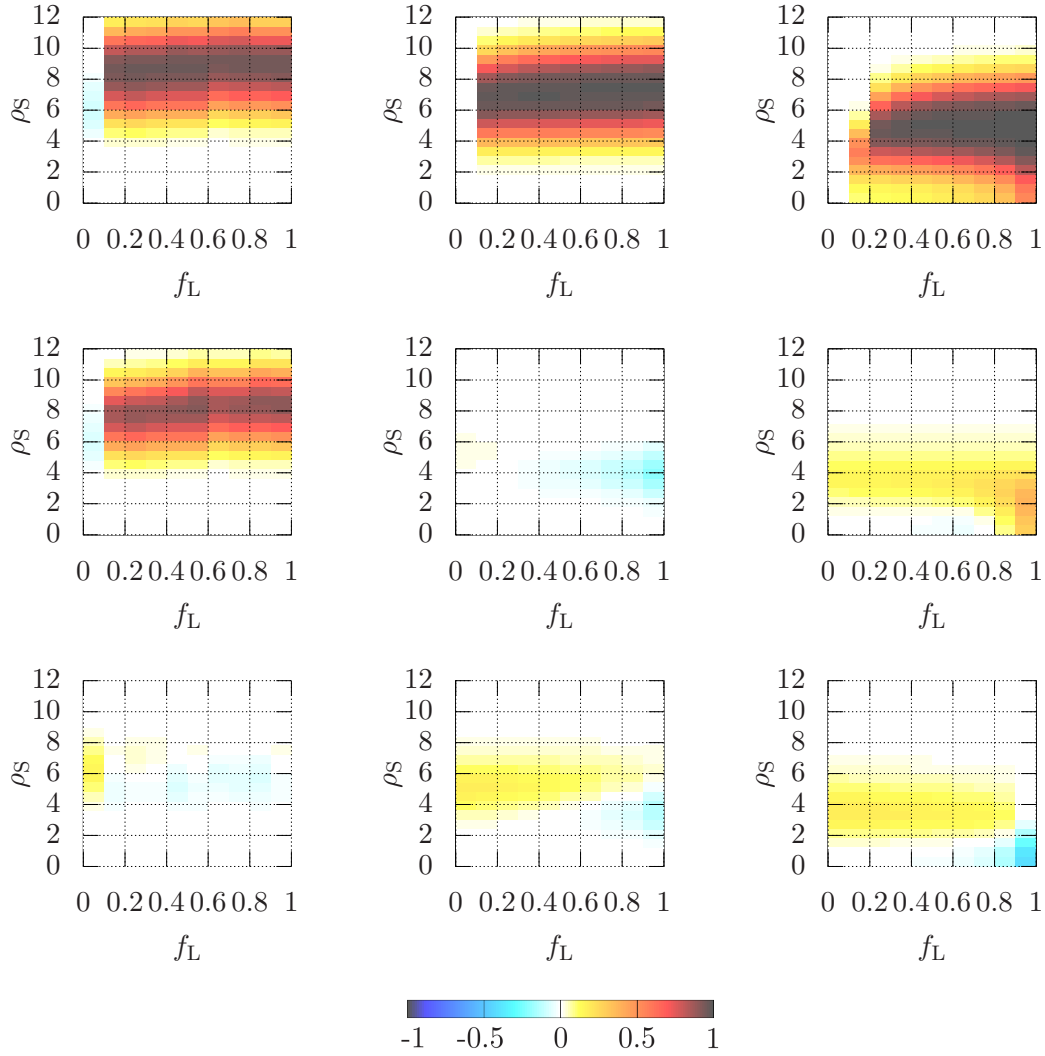
Figure 9.13: Differences of detection probabilities $p_{\mathrm{det}}(O_{\mathrm{SGL}}(\mathcal{F}_*^{(0)} = 10))$ to other statistics as a function of $f_{\mathrm{L}}^{\mathrm{H1}}$ and ρ_{S}, at fixed line strength $\rho_{\mathrm{L}} = 9$. The three column are for false-alarm probabilities of $p_{\mathrm{FA}} \in \{10^{-5}, 10^{-3}, 0.1\}$.
First row: compared with $p_{\mathrm{det}}(\mathcal{F})$, second row: $p_{\mathrm{det}}(\mathcal{F}^{+\mathrm{veto}})$, third row $p_{\mathrm{det}}(O_{\mathrm{SL}})$.
Though $f_{\mathrm{L}}^{\mathrm{H1}}$ changes over the x-axis, here for convenience I have kept fixed equal-odds line priors $o_{\mathrm{LG}}^{\mathrm{H1}} = o_{\mathrm{LG}}^{\mathrm{L1}} = 0.5$.

9.5 Effectiveness of line-prior tuning

In all of the previous studies, I have computed the line-veto and line-robust statistics with "perfect-knowledge tuning" of the line priors: $o_{LG}^{H1} = o_{LG}^{L1} = 0.001$ in Sec. 9.3 and, in Sec. 9.4, $p_L^{H1} = f_L^{H1} = 0.1 \Rightarrow o_{LG}^{H1} = 1/9$ and $o_{LG}^{L1} = 0.001$ (no lines injected into L1). Here, I will compare this tuning to the equal-odds prior $o_{LG}^{H1} = o_{LG}^{L1} = 0.5$, for which I write the statistics as $O_{SL}^{(0)}$ and $O_{SGL}^{(0)}$.

First, Fig. 9.14 shows the influence in Gaussian noise, for the $\rho_S = 6$ case. Note that here, where $o_{LG}^{H1} = o_{LG}^{L1}$ holds also in the perfect tuning case, the behaviour of O_{SL} is not influenced by scaling o_{LG}^X with a common factor, as any such O_{SL} are equivalent detection statistics. However, I find that O_{SGL}, at fixed $\mathcal{F}_*^{(0)}$, can improve due to the tuning by up to 10% over some ranges in p_{FA}.

Another way of interpreting this finding is that a tuning of o_{LG}^X to low values allows to use a lower $\mathcal{F}_*^{(0)}$ value. In this example, $\mathcal{F}_*^{(0)} = 10$ yields results equal to the $\mathcal{F}$-statistic expectation only if $o_{LG}^{H1} = o_{LG}^{L1} = 0.001$, while for the equal-odds prior a higher $\mathcal{F}_*^{(0)}$ is necessary. That would, in turn, reduce the performance of such a statistic in perturbed data. Hence, the tuning allows for a more robust statistic in general.

Figure 9.14: Synthetic ROCs for signals with $\rho_S = 6$ and pure Gaussian noise. The dashed lines are for "untuned", equal-odds line priors, $o_{LG}^{H1} = o_{LG}^{L1} = 0.5$, and the solid lines for "perfect-knowledge" priors, $o_{LG}^{H1} = o_{LG}^{L1} = 0.001$. Statistics with the same $\mathcal{F}_*^{(0)}$, but different line priors, share the same symbols. The χ^2 expectation for the $\mathcal{F}$-statistic is given for comparison.
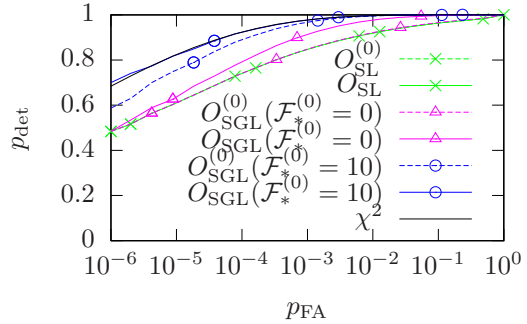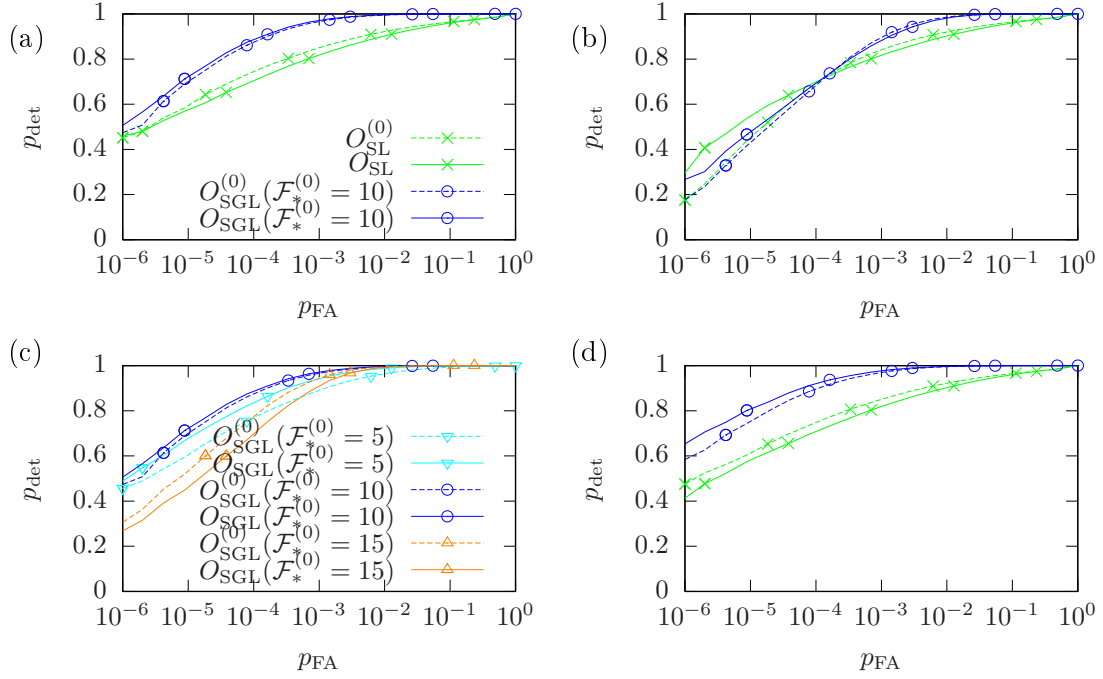
Figure 9.15: Synthetic ROCs for signals with $\rho_{\mathrm{S}} = 6$ and noise that is 90% Gaussian with 10% line contamination, with different line strengths. Panels (a) and (c) have $\rho_{\mathrm{L}} = 9$, but two different sets of statistics, where again dashed lines are for "untuned", equal-odds line priors, $o_{\mathrm{LG}}^{\mathrm{H1}} = o_{\mathrm{LG}}^{\mathrm{L1}} = 0.5$, the solid lines are for "perfect-knowledge" priors, $o_{\mathrm{LG}}^{\mathrm{H1}} = o_{\mathrm{LG}}^{\mathrm{L1}} = 0.001$. Statistics with the same $\mathcal{F}_*^{(0)}$, but different line priors, share the same symbols.

Panels (b) and (d) use the same statistics as (a), but for $\rho_{\mathrm{L}} = 6$ (b) and $\rho_{\mathrm{L}} = 15$ (c).

Next, Fig. 9.15 shows similar results for line-affected candidates. These demonstrate that the o_{LG}^X-tuning can sometimes actually *decrease* the detection power. However, this is the case only when the statistic is badly matched to the noise population, as seen here for O_{SL} and for O_{SGL} with a badly chosen $\mathcal{F}_*^{(0)}$, e.g. for $\mathcal{F}_*^{(0)} = 15$ with lines of SNR $\rho_{\mathrm{L}} = 9$. Still, applied to O_{SGL} with $\mathcal{F}_*^{(0)}$ chosen for good Gaussian noise performance ($\mathcal{F}_*^{(0)} = 10$ in these examples), the tuning of o_{LG}^X can yield gains in detection power of 5–10%, particularly at low p_{FA}.

Considering a large parameter space of ρ_{L} and ρ_{S} in Fig. 9.16, the results are similar to the ROCs. It also becomes clear that the effect of tuning depends strongly on the chosen p_{FA}: At $p_{\mathrm{FA}} = 10^{-3}$, the improvements for $O_{\mathrm{SGL}}(\mathcal{F}_*^{(0)} = 10)$ are very small ($\sim 1\%$) and limited to those parts of the parameter space where not $E\left[2\mathcal{F}\right]_{\mathcal{H}_{\mathrm{L}}} \approx E\left[2\mathcal{F}\right]_{\mathcal{H}_{\mathrm{S}}}$ – in that region, there are actually losses of up to 6%. For O_{SL}, the picture is reversed. On the other hand, at $p_{\mathrm{FA}} = 10^{-5}$, tuning brings improvements of 2-8% over a large part of the parameter space for $O_{\mathrm{SGL}}(\mathcal{F}_*^{(0)} = 10)$, and O_{SL} even has improvements of 5-10% at intermediate ρ_{L}, with only mild losses elsewhere.
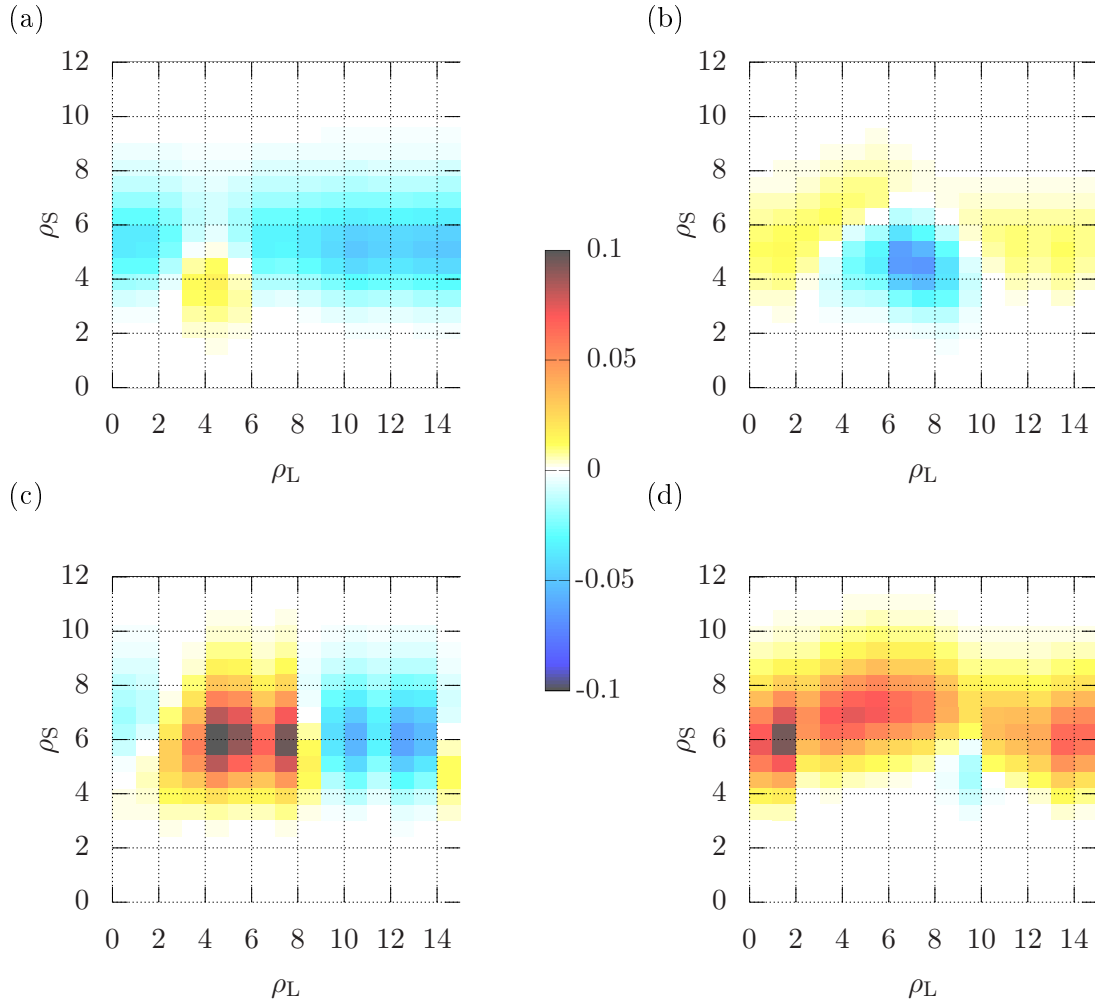
Figure 9.16: Comparison of tuned and untuned O_{SL}, in the left-hand column, and $O_{\mathrm{SGL}}(\mathcal{F}_*^{(0)} = 10)$, in the right-hand column, at fixed $f_{\mathrm{L}}^{\mathrm{H1}} = 0.1$ over varying line and signal strengths ρ_{L} and ρ_{S}.
The first row is for $p_{\mathrm{FA}} = 10^{-3}$, and the second row for $p_{\mathrm{FA}} = 10^{-5}$.

The result of these studies is that o_{LG}^{X} tuning is a valid method to improve the performance of the line-robust statistics, but must be combined with a good $\mathcal{F}_*^{(0)}$ tuning appropriate to the chosen p_{FA}.

10 Tests with LIGO S5 data

In this chapter, I extend the tests of the line-robust statistics to data sets and analysis methods which are closer to those used in current CW searches, such as those on Einstein@Home. To that end, I take several small subsets of data from the fifth science run of the LIGO detectors, or S5 for short (see Sec. 2.6.3). These have been analysed by the LIGO scientific collaboration before, without finding any CW signals (Abbott et al. 2009c, Abadie et al. 2012b, Aasi et al. 2013b). Hence, I consider them as *pure-noise* sets for the injection of simulated signals, searching for those with established codes from LALSuite (see Sec. 5.11).

The goal is to assess improvements in sensitivity due to the new statistics, expressed in terms of the weakest signal h_0 detectable with a certain confidence p_{det}. Therefore, the injection and detection procedures are modelled after those commonly employed for estimating upper limits on h_0 in CW searches (e.g., see Aasi et al. 2013a,b).

For each frequency band of data, I have performed two analyses: one over approximately one year of data using a semi-coherent approach and with the corresponding statistics from Sec. 7.3, and one over a stretch of $25\,\mathrm{h}$ of data, with the fully-coherent statistics from Sec. 7.2.

The semi-coherent results are the main point of this chapter, and the coherent part should be considered mostly as a sanity check, and to bridge the gap from the coherent synthetic tests in Sec. 9. Hence, statements about the particular characteristics of each band of data are mostly geared towards the larger data set, and the coherently analysed subsets may differ slightly in some cases.

In the following, I will first describe the data-selection procedure in Sec. 10.1. Next, Secs. 10.2 and 10.3 describe the set-up of the search pipeline, including template banks, search parameter space, injection procedure and the definition of a detection criterion. After describing the set of tested statistics in Sec. 10.4, I present results for the coherent statistics in Sec. 10.5 and for the semi-coherent ones in Sec. 10.6.

10.1 Data selection

A first data set, in the following labelled (a), consists of simulated pure Gaussian noise. It is used to check the injection and analysis pipeline in a controlled environment. In addition, I use five narrow frequency bands of real interferometer-strain data from the

first year of S5, using segments from the "S5R3" Einstein@Home run (Aasi et al. 2013b), from both the LIGO detectors at Hanford (H1) and Livingston (L1).

The five real-data bands were selected to be representative of different degrees of disturbance from lines, based on by-eye inspection of $\mathcal{P}^X(f)$ spectra (shown in Figs. 10.1 and 10.2):

(b) a "quiet" band where the distribution of the data is very close to Gaussian,

(c) a band with a single, slightly broadened line in L1,

(d) a band with a single line in L1, narrower than in (c),

(e) a band with a broad disturbance feature in L1,

(f) a band with multiple disturbances in H1.

This wide diversity of disturbances is used to check the robustness of the new detection statistics even in cases like (e) and (f) which are not obviously compatible with the narrow-line model $\mathcal{H}_\mathrm{L}$ from Eq. (7.30).

Data for bands (b-f) covers $N_\mathrm{seg} = 84$ segments, while $N_\mathrm{seg} = 121$ for the simulated band (a, S5R5 selection from Aasi et al. 2013b). [1] In both cases, each segment spans $T = 25\,\mathrm{h}$.

All of the coherent searches use data sets spanning $T = 25\,\mathrm{h}$, corresponding to a single segment of the semi-coherent data selection. Since some of the line features seen in the full data set occur only sporadically over time, I have selected a different segment for each band, so that each 25 h-stretch has a similar line-characteristic to that of the corresponding full set.

These time spans, along with the frequency ranges and some additional information, for each of the sample frequency bands are given in Tbls. 10.1 and 10.2 for the coherent and semi-coherent cases, respectively. Note that in these tables and in the following figures, I have extended the notation for coherent and semi-coherent quantities to labels for the example bands, i.e. ($\tilde{\mathrm{a}}$) is the coherent simulated noise example and ($\hat{\mathrm{a}}$) is the corresponding semi-coherent example. A label like (a) is used when referring to common properties of the band in both cases.

There are two kinds of width associated with each frequency band: Physical CW template frequencies are placed in Δf_inj for the injection step, while the search requires data from a wider range Δf_SFT. This is due to Doppler modulation and the spin-down evolution of the signal, as well as the algorithmic requirements of the $\mathcal{F}$-statistic implementation `LALDemod` (see Prix 2011b) and the `HierarchSearchGCT` search code.

---

[1] The corresponding Gaussian test data for the S5R3 segment selection was unusable due to bugs in its generation. Instead of generating a new 84-segment set, the S5R5 set was chosen to minimise the potential for introducing new errors.

Label	Δf_{inj} [Hz]	Δf_{SFT} [Hz]	t_{start} [s]	$\sqrt{S}\,[\mathrm{Hz}^{-1/2}]$	$\max 2\mathcal{F}_{\mathrm{noise}}$	Detector X	N^X_{SFT}	$\sqrt{S^X}\,[\mathrm{Hz}^{-1/2}]$	$\mathcal{P}^X_{\mathrm{thr}}$	o^X_{LG}
$(\widetilde{\mathrm{a}})$	$[60.00, 60.05]$	$[59.99, 60.06]$	852443819	2.50×10^{-22}	36.30	H1	45	2.43×10^{-22}	1.894	0.001
						L1	35	2.57×10^{-22}	2.014	0.001
$(\widetilde{\mathrm{b}})$	$[54.20, 54.25]$	$[54.19, 54.26]$	835120582	1.80×10^{-22}	38.04	H1	47	2.51×10^{-22}	1.875	0.001
						L1	39	1.48×10^{-22}	1.960	0.001
$(\widetilde{\mathrm{c}})$	$[66.50, 66.55]$	$[66.49, 66.56]$	844876223	1.28×10^{-22}	81.68	H1	47	1.19×10^{-22}	1.875	0.001
						L1	36	1.41×10^{-22}	2.000	0.073
$(\widetilde{\mathrm{d}})$	$[69.70, 69.75]$	$[69.69, 69.76]$	821912087	1.42×10^{-22}	122.54	H1	46	1.35×10^{-22}	1.884	0.001
						L1	40	1.50×10^{-22}	1.948	0.015
$(\widetilde{\mathrm{e}})$	$[53.20, 53.25]$	$[53.19, 53.26]$	826439677	3.77×10^{-22}	50.36	H1	42	3.12×10^{-22}	1.925	0.001
						L1	38	5.13×10^{-22}	1.973	0.085
$(\widetilde{\mathrm{f}})$	$[58.50, 58.55]$	$[58.49, 58.56]$	827366996	2.48×10^{-22}	104.46	H1	48	2.58×10^{-22}	1.866	0.585
						L1	40	2.40×10^{-22}	1.948	0.001

Table 10.1: Data sets used for tests of the coherent statistics. Band $(\widetilde{\mathrm{a}})$ is simulated Gaussian noise, while bands $(\widetilde{\mathrm{b}})$-$(\widetilde{\mathrm{f}})$ are LIGO data from the first year of the S5 run. CW signals are injected with frequencies $f \in \Delta f_{\mathrm{inj}}$, while Δf_{SFT} denotes the data range used for the search and the line-prior estimation. Each data set starts at a GPS time of t_{start} and contains N^X_{SFT} SFTs of duration $T_{\mathrm{SFT}} = 1800\,\mathrm{s}$ from each detector. The multi-detector noise PSD S and per-detector S^X are harmonic means over SFTs and arithmetic means over frequency bins. The column labelled $\max 2\mathcal{F}_{\mathrm{noise}}$ shows the highest multi-detector $2\mathcal{F}$ value without injections.
The column $\mathcal{P}^X_{\mathrm{thr}}$ gives the threshold on the normalised SFT power $\mathcal{P}^X$ at $p_{\mathrm{FA},\mathcal{P}} = 10^{-9}$ for the estimation of the line-priors o^X_{LG}.

For the six coherent and six semi-coherent data sets, I have used `lalapps_ComputePSD` to compute the per-detector and multi-detector power spectra (PSD) $S^X(f)$ and $S(f)$. The code also computes the normalised SFT power $\mathcal{P}^X(f)$, as defined in Eq. (8.2). Plots of this quantity are shown in Fig. 10.1 for the coherent case, and in Fig. 10.2 for the semi-coherent case.

From these plots, it is apparent that the "quiet" band (b) is very similar in character to the simulated Gaussian noise of (a). The maximum $\mathcal{P}^X$ values observed in the two (near-)Gaussian cases, $\max(\mathcal{P}^X) \approx 1.5$ for a single segment and $\max(\mathcal{P}^X) \approx 1.05$ for the semi-coherent cases, are in accordance with theoretical expectations from a Gaussian distribution.

The same is true for the full distributions, as shown by the histograms in Figs. 10.3–10.6. A slight bias of $\Delta \mathcal{P}^X \propto N^{-1}_{\mathrm{rngmed}} \approx 0.01$ exists due to the fact that $E\left[\frac{1}{x}\right] \neq \frac{1}{E[x]}$ when normalising by the estimated noise PSD (see Sec. 5.4). The same effect for the $\mathcal{F}$-statistic is discussed in (Prix 2011a). This is only visible in the semi-coherent Gaussian-noise examples $(\widehat{\mathrm{a}})$+$(\widehat{\mathrm{b}})$, and unproblematic in comparison with the thresholds $\mathcal{P}^X_{\mathrm{thr}}$.

These distributions are also used to determine the line-flagging thresholds at $p_{\mathrm{FA},\mathcal{P}} = 10^{-9}$, as introduced in Sec. 8.1: the horizontal lines in the spectra, or equivalently the vertical lines in the histograms, give the corresponding thresholds, which are evidently above the bulk of the Gaussian distributions.
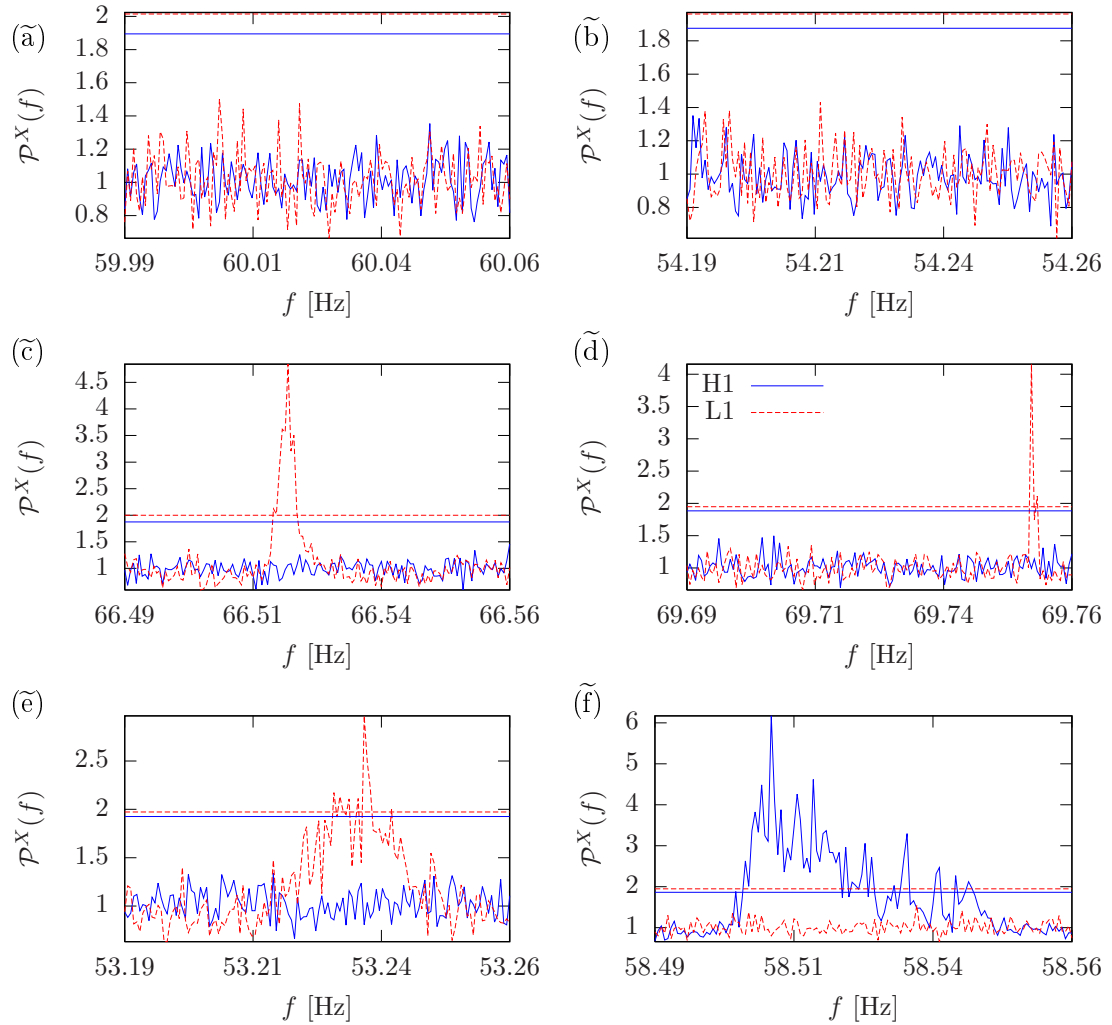
Figure 10.1: Normalised average SFT power $\mathcal{P}^X(f)$ of Eq. (8.2) as a function of frequency f for LIGO H1 (solid blue) and L1 (dashed red), from data used in the coherent searches. The horizontal lines mark, for each detector, the threshold $\mathcal{P}^X_{\text{thr}}$ at $p_{\text{FA},\mathcal{P}} = 10^{-9}$, as used in the line prior estimation.

The panels show: $(\widetilde{a})$ simulated Gaussian noise, $(\widetilde{b})$ a quiet band, $(\widetilde{c})+(\widetilde{d})$ two bands with comparatively narrow lines in L1, $(\widetilde{e})$ a band with a broad disturbance in L1, $(\widetilde{f})$ a band with multiple disturbances in H1.

See Tbl. 10.1 for more details on these data sets.
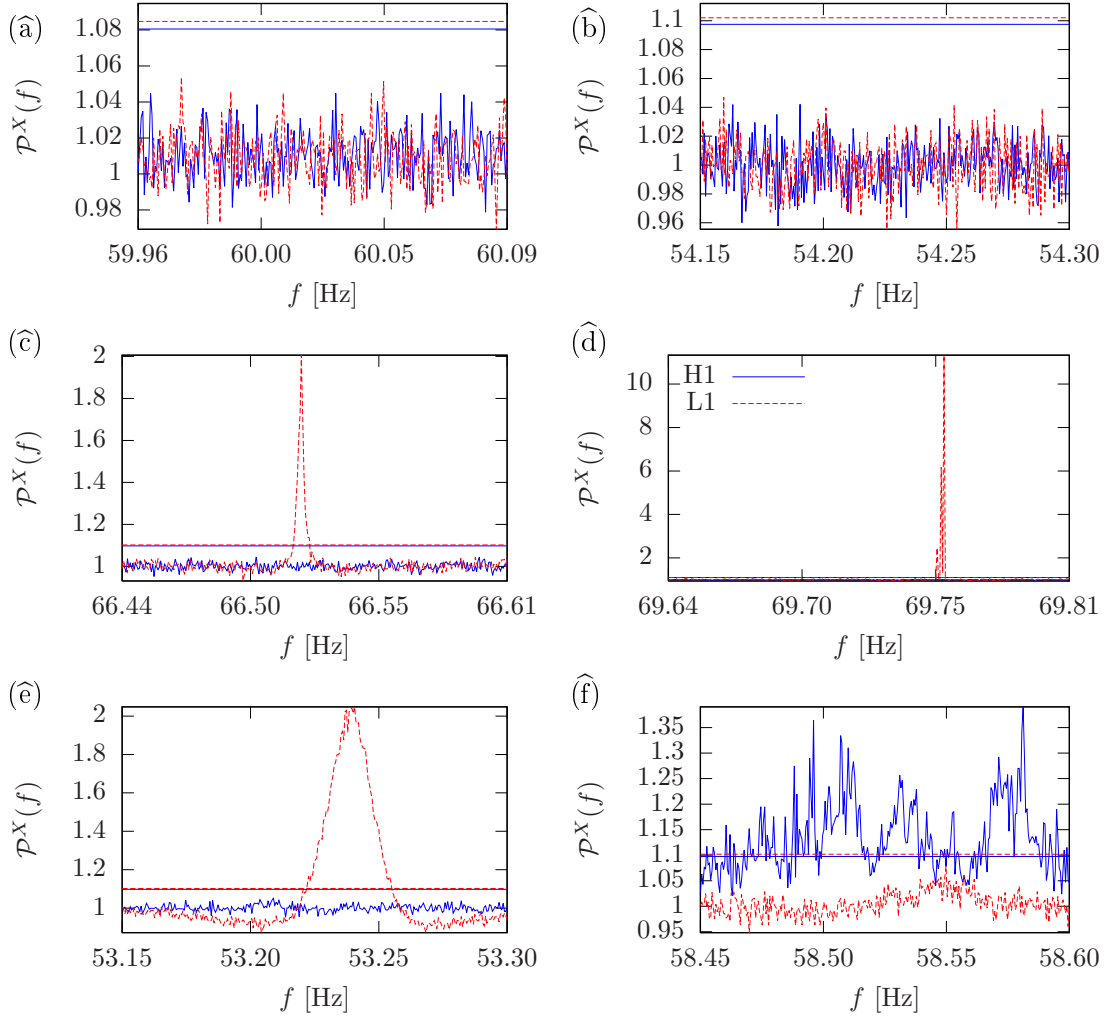
Figure 10.2: Normalised average SFT power $\mathcal{P}^X(f)$ of Eq. (8.2) as a function of frequency f for LIGO H1 (solid blue) and L1 (dashed red), from data used in the semi-coherent searches. The horizontal lines mark, for each detector, the threshold $\mathcal{P}^X_{\mathrm{thr}}$ at $p_{\mathrm{FA},\mathcal{P}} = 10^{-9}$, as used in the line prior estimation.

The panels show: $(\widehat{a})$ simulated Gaussian noise, $(\widehat{b})$ a quiet band, $(\widehat{c})+(\widehat{d})$ two bands with comparatively narrow lines in L1, $(\widehat{e})$ a band with a broad disturbance in L1, $(\widehat{f})$ a band with multiple disturbances in H1.

See Tbl. 10.2 for more details on these data sets.

139
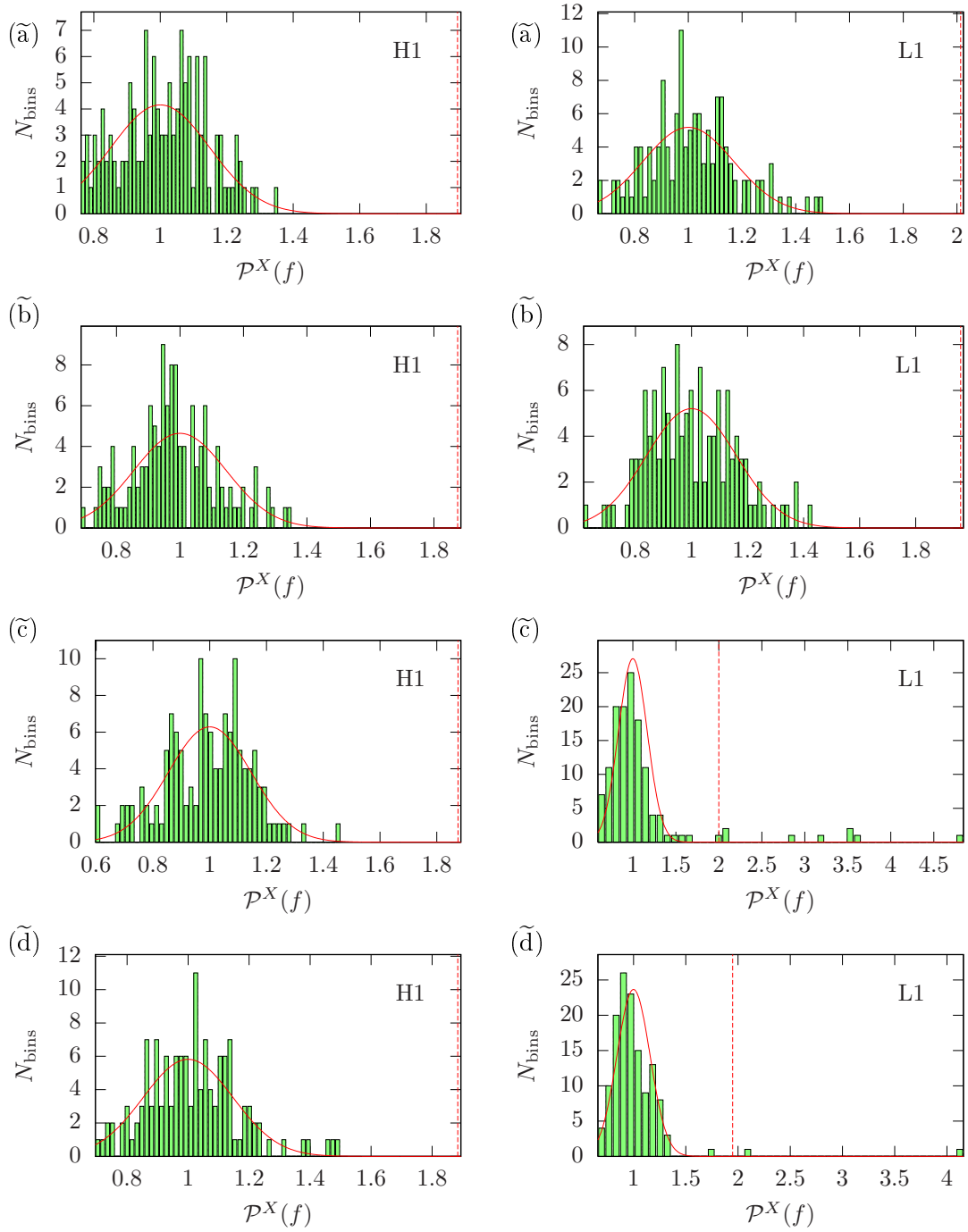
Figure 10.3: Histograms of normalised average SFT power $\mathcal{P}^X(f)$ for the first four single-segment bands from Tbl. 10.1 and Fig. 10.1. The solid curves gives the expected Gaussian distributions, and the dashed vertical lines are the threshold $\mathcal{P}^X_{\text{thr}}$ at $p_{\text{FA},\mathcal{P}} = 10^{-9}$.
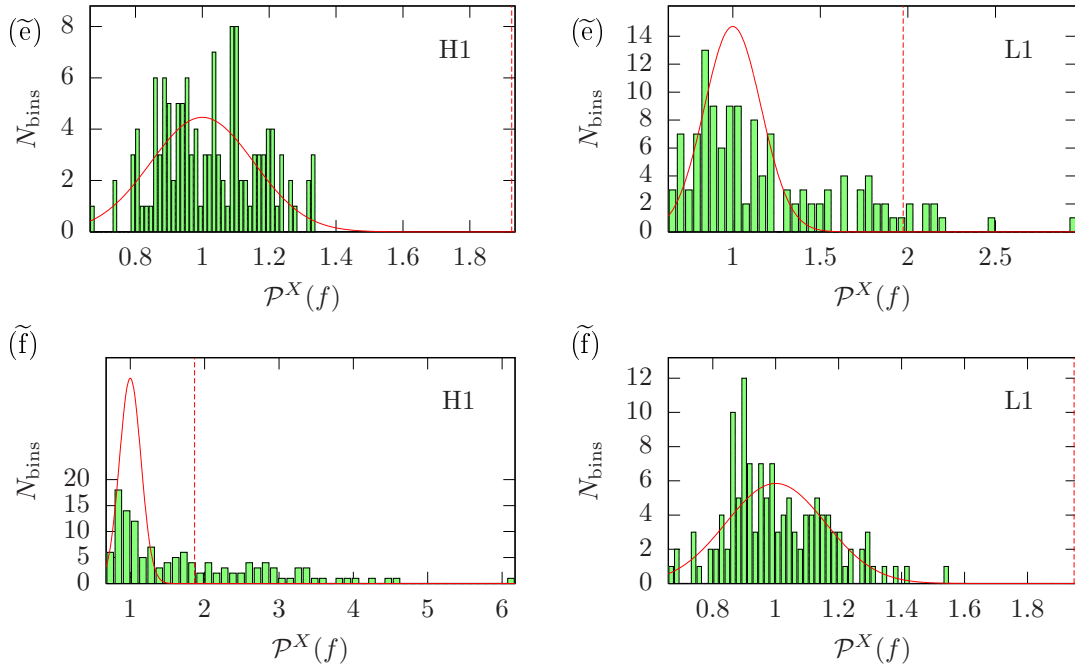
Figure 10.4: Histograms of normalised average SFT power $\mathcal{P}^X(f)$ for the remaining two single-segment bands from Tbl. 10.1 and Fig. 10.1.
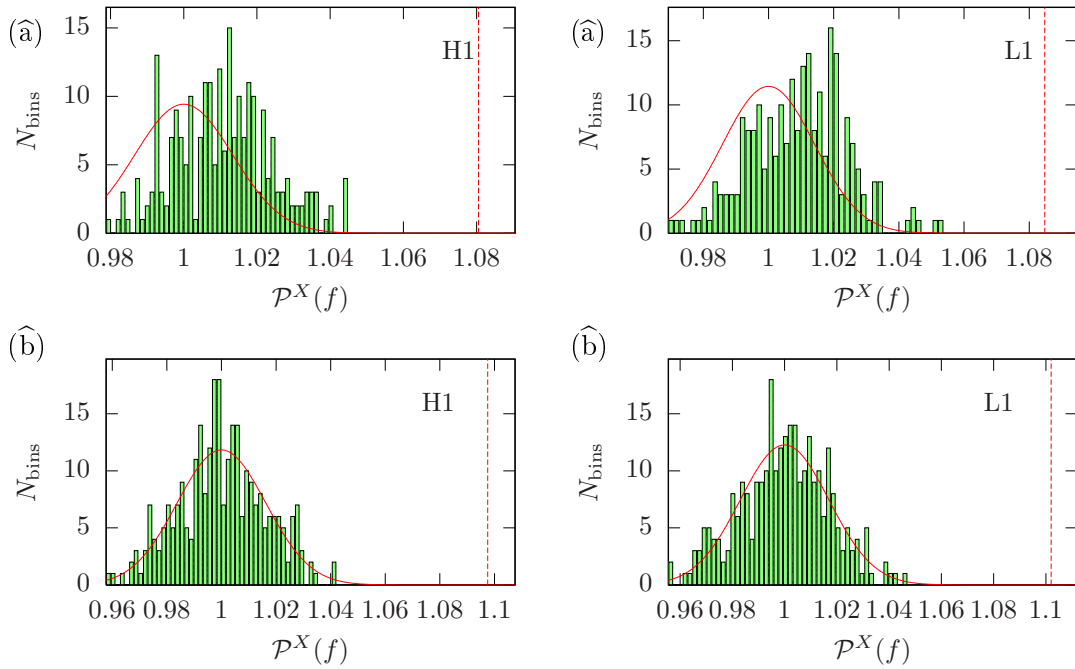
Figure 10.5: Histograms of normalised average SFT power $\mathcal{P}^X(f)$ for the first two semi-coherent bands from Tbl. 10.2 and Fig. 10.2.
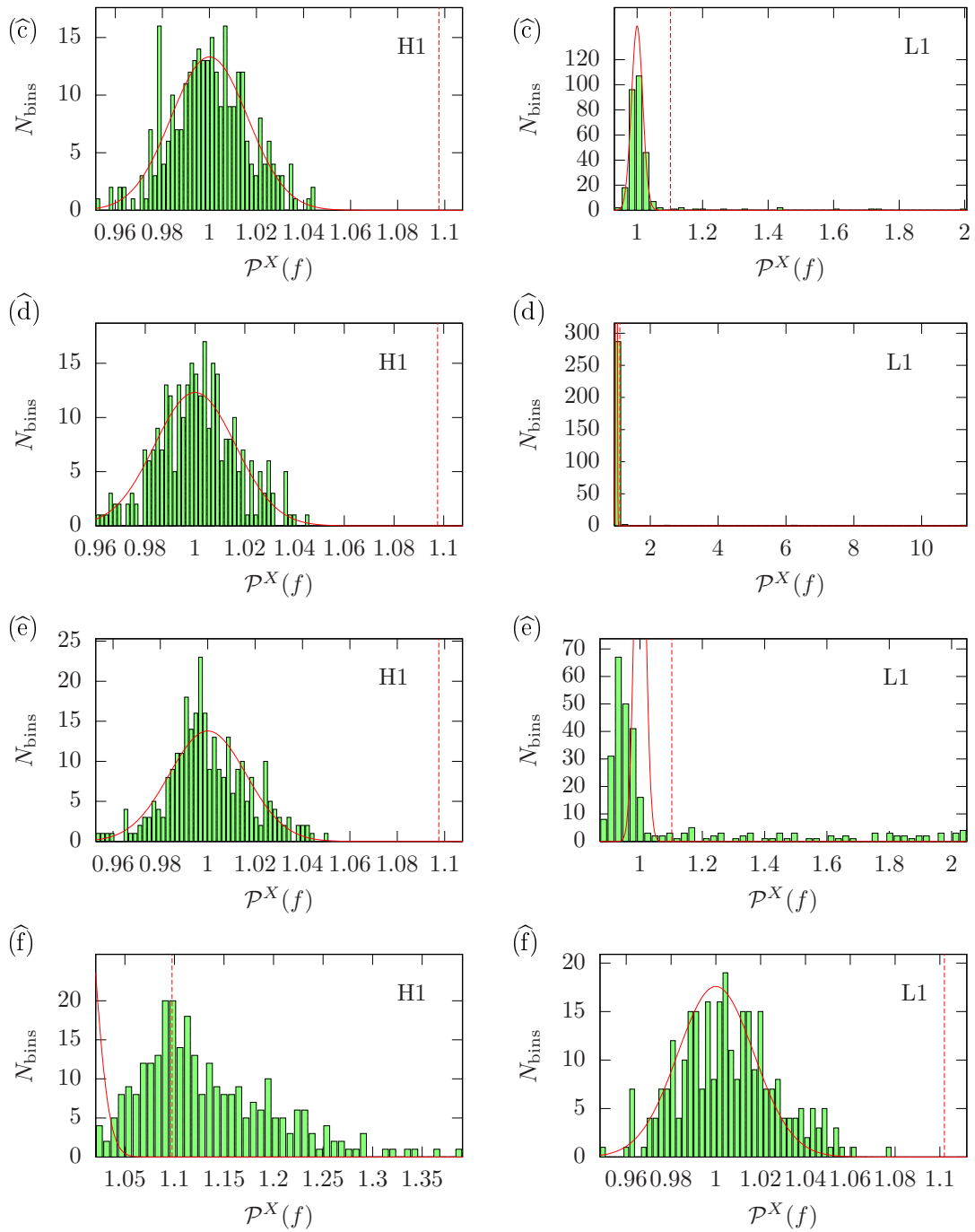
Figure 10.6: Histograms of normalised average SFT power $\mathcal{P}^X(f)$ for the remaining four 84-segment bands from Tbl. 10.2 and Fig. 10.2.

Label	Δf_{inj} [Hz]	Δf_{SFT} [Hz]	t_{start} [s]	N_{seg}	$\sqrt{S}$ [Hz$^{-1/2}$]	$\max 2\overline{\mathcal{F}}_{\text{noise}}$	Detector X	N_{SFT}^X	$\sqrt{S^X}$ [Hz$^{-1/2}$]	$\mathcal{P}_{\text{thr}}^X$	$\widehat{o}_{\text{LG}}^X$
$\widehat{a}$	[60.00, 60.05]	[59.96, 60.09]	852443819	121	1.96×10^{-22}	6.03	H1	5550	1.65×10^{-22}	1.081	0.001
							L1	5010	2.54×10^{-22}	1.085	0.001
$\widehat{b}$	[54.20, 54.25]	[54.15, 54.30]	818845553	84	2.09×10^{-22}	6.51	H1	3781	2.54×10^{-22}	1.098	0.001
							L1	3456	1.81×10^{-22}	1.102	0.001
$\widehat{c}$	[66.50, 66.55]	[66.44, 66.61]	818845553	84	1.14×10^{-22}	10.83	H1	3781	1.35×10^{-22}	1.098	0.001
							L1	3456	1.00×10^{-22}	1.102	0.047
$\widehat{d}$	[69.70, 69.75]	[69.64, 69.81]	818845553	84	1.01×10^{-22}	83.48	H1	3781	1.15×10^{-22}	1.098	0.001
							L1	3456	9.08×10^{-23}	1.102	0.017
$\widehat{e}$	[53.20, 53.25]	[53.15, 53.30]	818845553	84	2.82×10^{-22}	8.85	H1	3781	2.67×10^{-22}	1.098	0.001
							L1	3456	3.00×10^{-22}	1.102	0.288
$\widehat{f}$	[58.50, 58.55]	[58.45, 58.60]	818845553	84	2.12×10^{-22}	8.35	H1	3781	2.20×10^{-22}	1.098	1.743
							L1	3456	2.05×10^{-22}	1.102	0.001

Table 10.2: Data sets used for tests of the semi-coherent statistics. Data for bands $\widehat{b}$-$\widehat{f}$ corresponds to the Einstein@Home segment selection S5R3 (Aasi et al. 2013b), spanning 381 days and containing $N_{\text{seg}} = 84$ segments, each 25 hours long. For band $\widehat{a}$, the simulated pure Gaussian noise has timestamps corresponding to the S5R5 segment selection.

The column labelled $\max 2\overline{\mathcal{F}}_{\text{noise}}$ refers to the highest multi-detector $\mathcal{F}$-statistic without injections, averaged over segments: $2\overline{\mathcal{F}} = \frac{1}{N_{\text{seg}}} \sum_{k=1}^{N_{\text{seg}}} 2\widetilde{\mathcal{F}}_k$.

The remaining labels are identical to those in Tbl. 10.1.

10.2 Template banks and pure-noise searches

Although I reuse a subset of the data and the segment lists from Aasi et al. (2013b), my search setup is quite different. This is mostly because I use, instead of a search code based on the Hough-transform (Krishnan et al. 2004), the `lalapps_HierarchSearchGCT` code (HSGCT) that is based on the "global correlations" method of Pletsch & Allen (2009), which I have described in Sec. 5.10, HSGCT was first used in an LSC publication in Aasi et al. (2013a) and is also in use for ongoing Einstein@Home searches (Allen et al. 2005a). Hence, it was natural to implement the line-robust statistics in this code, and to use studies very similar to those presented here and in KPPLS14 as preparations for Einstein@Home set-ups, for which see Sec. 11.

Now, let me first describe the search setup for the raw ("pure noise") data without any signal injections. For each of the six frequency bands, I performed a search covering $\Delta f = \Delta f_{\text{inj}} = 50\,\text{mHz}$ (see Tbls. 10.1 and 10.2), the whole sky and a fixed band $[-\Delta\dot{f}, 0]$ in the first spin-down parameter $\dot{f}$, with a width of $\Delta\dot{f} \approx 2.6 \times 10^{-9}\,\text{Hz/s}$. I have not considered higher-order spin-down parameters $\ddot{f}, \dddot{f}, \ldots$ in this study.

The sky coverage was determined by a *grid file* constructed in a similar way to the Einstein@Home runs S5GC1 and S6Bucket, which also use the HSGCT code, but are currently still undergoing post-processing and are not published yet. Such a grid is the union of an all-sky square lattice in the equatorial plane, projected onto both hemispheres, and a uniform grid around the equator over the range $\alpha \in [0, 2\pi]$, $\delta \in [-0.5, 0.5]$. This
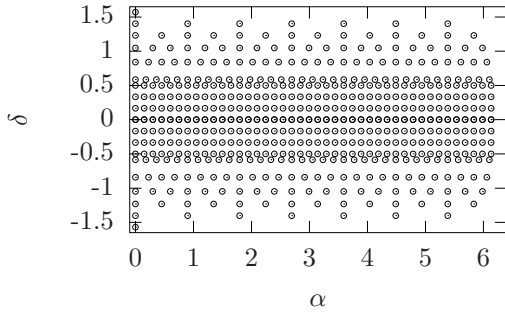
Figure 10.7: Rectangular projection of an example sky-grid at $f = 54\,\mathrm{Hz}$, with $N_{\mathrm{sky}} = 548$. The marker sizes are not indicative of coverage. See the text for details on grid construction.

construction was necessary in order to avoid under-covering of the equatorial region by the HSGCT code. The lattice is constructed with a nominal mismatch of $m_{\mathrm{sky}} = 0.3$, corresponding to an expected relative loss of squared SNR, see Eq. (5.55). The effective angular spacings are approximately $0.15\,\mathrm{rad}$ at $f = 54\,\mathrm{Hz}$.

The sky-template spacings need to scale with frequency as $1/f$ in order to maintain the same mismatch, leading to a quadratically increasing number of sky-grid points. An example sky-grid for $f = 54\,\mathrm{Hz}$, where $N_{\mathrm{sky}} = 548$, is given in Fig. 10.7.

For each band, I have used a grid computed at the next integer-Hz step in frequency. At the highest value considered here, $f = 69\,\mathrm{Hz}$, the grid already has $N_{\mathrm{sky}} = 924$ points. I have selected all example bands at low frequencies ($f < 100\,\mathrm{Hz}$) specifically to avoid searches over much larger sky grids.

Together with grid spacings in frequency and spin-down of $\delta f \approx 1.6 \times 10^{-6}\,\mathrm{Hz}$ and $\delta \dot{f} \approx 5.8 \times 10^{-11}\,\mathrm{Hz}/s$, the full template bank yields empirically measured mismatches of $m \sim 0.6$ in the semi-coherent searches and of $m \lesssim 0.05$ in the coherent searches.

For each sky point, the grid has

$$N_{\mathrm{templ}} = \frac{\Delta f}{\delta f}\frac{\Delta \dot{f}}{\delta \dot{f}} \approx 1.4 \cdot 10^6 \tag{10.1}$$

points in frequency and spin-down. Multiplied with N_{sky}, this is large enough to yield very impractical days-long computing times for the semi-coherent searches. Therefore, I had to split up the search into several jobs submitted to the ATLAS cluster at AEI Hannover, using the Condor parallelisation scheduler (Thain, Tannenbaum & Livny 2005, Thain et al. 2014). For simplicity, jobs were split into a single sky-point each.

I then collected the results from all jobs for a band (coherent and semi-coherent runs separately) and obtained, for each of the statistics under consideration (see Sec. 10.4), the respective loudest noise candidate over the whole template grid. Maximum values for the $\mathcal{F}$-statistic are listed in Tbls. 10.1 and 10.2.
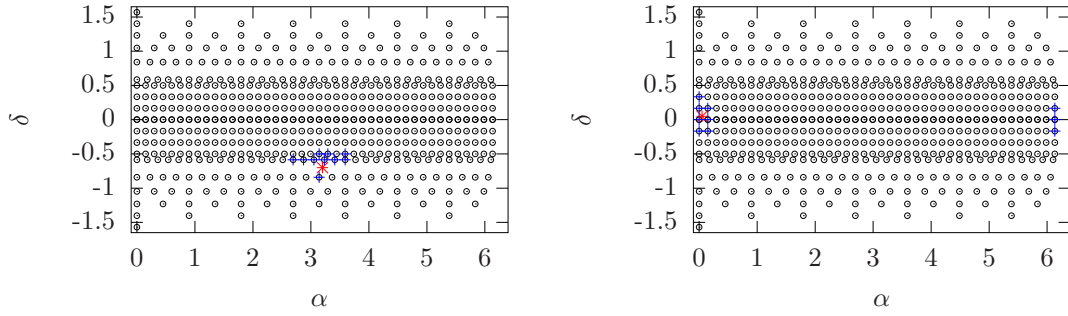
Figure 10.8: Examples of injection points (red stars) on the same $f = 54\,\mathrm{Hz}$, $N_{\mathrm{sky}} = 548$ sky grid as in Fig. 10.7, with the 10 nearest-neighbour grid-points marked with blue crosses. Note how, in the second example, the nearest neighbours wrap around in α.

10.3 Signal injection and detection criterion

To inject CW signals, I used the `lalapps_Makefakedata_v4` code, which can add a deterministic signal waveform, according to the signal model introduced in Sec. 5.2, to the provided noise SFTs.

The Doppler parameters were drawn randomly from uniform distributions, with ranges corresponding to the respective full search range: $\alpha \in [0, 2\pi]$, $\delta \in [-\pi/2, \pi/2]$, $f \in \Delta f_{\mathrm{inj}}$ and $\dot{f} \in [-\Delta \dot{f}, 0]$. Of the amplitude parameters, the inclination angle $\cos\iota \in [-1, 1]$, polarisation angle $\psi \in [-\pi/4, \pi/4]$ and initial phase $\phi_0 \in [0, 2\pi]$ were drawn uniformly from those ranges. The signal strength h_0 was given special treatment: here I chose several discrete values, intended to roughly cover the range of detection probabilities $p_{\mathrm{det}} \in [0, 1]$.

As we only need the loudest candidates, the search-parameter-space volume was then limited to a small region around the signal injection point. This search region consists of a frequency band of $\Delta f = 1\,\mathrm{mHz}$, a spin-down band of $\Delta \dot{f} \approx 2.3 \times 10^{-10}\,\mathrm{Hz/s}$ and of the 10 sky-grid points closest to the injection. To avoid a bias from always having the exact injection values $(f, \dot{f})$ as a grid point, the centre of Δf and $\Delta \dot{f}$ was set to the nearest point of the original pure-noise search grid, instead of centring it on the injection point. For identification of the closest sky-grid points, I used the metric distance (see Sec. 5.8 and Prix 2007b) with the flat "super-sky metric" from Wette & Prix (2013). Two examples for this are shown in Fig. 10.8.

For 1000 injections per band and h_0 value, I have recovered the highest value for each detection statistic. I have counted a signal as *detected* with a given statistic if the highest value found with an injection, exceeds the maximum value from the full pure-noise search. This detection criterion is similar to the common method of setting loudest-event upper limits per $50\,\mathrm{mHz}$ band, as employed for example in Aasi et al. (2013b).

An interesting effect of the small signal-search bands is that, in bands (c), (d) and (e), some of these injection searches do not actually use any of the SFT bins that contain the narrow disturbances. The results from these bands are therefore averages over both disturbed and undisturbed templates. Hence, the performances of detection statistics as evaluated in this chapter do actually apply to the wider class of *bands that contain disturbances*, and not only to *sets of disturbed candidates*.

10.4 Detection statistics used in the tests

The `HSGCT` code, which was originally implemented to compute only the multi-detector $\widehat{\mathcal{F}}$-statistic, has been extended by R. Prix, myself and others to also compute the single-detector $\widehat{\mathcal{F}}^X$ values and the new statistics $\widehat{O}_{\mathrm{SL}}$ and $\widehat{O}_{\mathrm{SGL}}$ from Eqs. (7.86) and (7.91). The code can output two simultaneous toplists (see Sec. 5.12) ordered by different statistics.

To get optimal results for each statistic, I have rerun the code several times to produce toplists ordered by $\widehat{\mathcal{F}}$, $\widehat{O}_{\mathrm{SL}}$ and $\widehat{O}_{\mathrm{SGL}}$ with different $\widehat{\mathcal{F}}_*^{(0)}$ – the latter required for tuning on Gaussian noise, and for sanity checks on the other bands. Furthermore, computing the $\mathcal{F}^{+\mathrm{veto}}$-statistic from the output of $\widehat{\mathcal{F}}$ and $\widehat{\mathcal{F}}^X$ is easy to do in post-processing scripts; for this, I have used the $\widehat{\mathcal{F}}$-sorted toplist.

For $\widehat{O}_{\mathrm{SGL}}$, I have used the tuning of the line priors $\widehat{o}_{\mathrm{LG}}^X$ as described in Sec. 8.1, specifically Eqs. (8.5) and (8.7). I find that the effect of $\widehat{o}_{\mathrm{LG}}^X$ tuning on p_{det} is usually limited to about 5–10%, which is compatible with the synthetic tests in Sec. 9.5. This is lower than typical differences between $\widehat{\mathcal{F}}$ or the $\mathcal{F}^{+\mathrm{veto}}$-statistic and $\widehat{O}_{\mathrm{SGL}}$ in most cases. Thus, I do not explicitly compare tuned and untuned versions in the result plots in this chapter.

Furthermore, the transition-scale parameter $\widehat{\mathcal{F}}_*^{(0)}$ was tuned, as explained in Sec. 8.2, using an extra set of injections on the simulated Gaussian noise set (a). These indicated safe Gaussian-noise performance (in comparison to the $\mathcal{F}$-statistic) for $\mathcal{F}_*^{(0)}(N_{\mathrm{seg}} = 1) \approx 16.7$, $\widehat{\mathcal{F}}_*^{(0)}(N_{\mathrm{seg}} = 84) \approx 237.0$ and $\widehat{\mathcal{F}}_*^{(0)}(N_{\mathrm{seg}} = 121) \approx 323.3$, all corresponding to a false-alarm level of $p_{\mathrm{FA}*}^{(0)} = 10^{-6}$, so that I denote the corresponding statistic as $^{(-6)}\widehat{O}_{\mathrm{SGL}}$.

In summary, I will present results for the following set of statistics: the multi-detector $\widehat{\mathcal{F}}$-statistic; the $\mathcal{F}^{+\mathrm{veto}}$-statistic; $\widehat{O}_{\mathrm{SL}}^{(0)}$ with $\widehat{o}_{\mathrm{LG}}^{\mathrm{H1}} = \widehat{o}_{\mathrm{LG}}^{\mathrm{L1}} = 0.5$; and $^{(-6)}\widehat{O}_{\mathrm{SGL}}$ with $p_{\mathrm{FA}*}^{(0)} = 10^{-6}$ and with $\widehat{o}_{\mathrm{LG}}^X$ determined from $\mathcal{P}^X$.

10.5 Comparison of detection probabilities - coherent case

Here I present results from the injection and search process as detailed above, in the form of *efficiency plots*: the detection efficiency p_{det} as a function of the scaled signal amplitude $h_0^{\mathcal{S}} = h_0/\sqrt{\mathcal{S}[1/\mathrm{Hz}]}$. An important benchmark in this kind of plot is the signal

strength at which p_{det} reaches 95%, corresponding to the typical level at which upper limits are quoted.

The results for the single-segment coherent statistics on the six example bands are shown in Fig. 10.9. When comparing them with those from synthetic draws in Sec. 9, note that the detection criterion defined in Sec. 10.3 – setting the threshold to the highest noise outlier – fixes the false-alarm probability to an extremely low level, on the order of the inverse number of templates.

The results from pure simulated Gaussian noise $(\widetilde{\mathrm{a}})$ and from the quiet band of real data $(\widetilde{\mathrm{b}})$ are very similar, again demonstrating that the data in this band of real LIGO data is very close to Gaussian noise. Here, the detection probabilities demonstrate the expected near-optimality of the unmodified $\mathcal{F}$-statistic. In fact, the line-veto statistic $O_{\mathrm{SL}}^{(0)}$ has noticeably less detection power here, with a 5–10% loss at fixed $h_0^{\mathcal{S}}$ and reaching $p_{\mathrm{det}} = 0.95$ about a factor of 1.5 in $h_0^{\mathcal{S}}$ later. This behaviour is expected, since $\mathcal{H}_{\mathrm{L}}$ does not match the noise population, leading to an inefficient separation of noise and signal candidates when setting thresholds on $O_{\mathrm{SL}}^{(0)}$.

Meanwhile, the conventional $\mathcal{F}^{+\mathrm{veto}}$-statistic is *safer* than $O_{\mathrm{SL}}^{(0)}$ in the sense that it performs just as well as the pure $\mathcal{F}$-statistic. Just as in the purely Gaussian synthetic tests, the line-robust statistic O_{SGL} is also safe in this sense: at $p_{\mathrm{FA}*}^{(0)} = 10^{-6}$, it performs equally well as $\mathcal{F}$ and $\mathcal{F}^{+\mathrm{veto}}$ on this undisturbed data set.

When comparing the results for the disturbed bands $(\widetilde{\mathrm{c}}$–$\widetilde{\mathrm{f}})$ to the Gaussian cases, the first impression is that all statistics lose some detection power, generally reaching $p_{\mathrm{det}} = 0.95$ at higher $h_0^{\mathcal{S}}$. However, they do so to varying degrees. As expected, the pure $\mathcal{F}$-statistic suffers heavy losses in the highly disturbed bands $(\widetilde{\mathrm{d}})$ and $(\widetilde{\mathrm{f}})$, and still performs noticeably worse in the remaining two cases. The $\mathcal{F}^{+\mathrm{veto}}$-statistic is often able to recover most of the losses of the pure $\mathcal{F}$-statistic, but at least in case $(\widetilde{\mathrm{d}})$ it still leaves a lot of room for improvement.

The line-veto statistic $O_{\mathrm{SL}}^{(0)}$ performs similarly to the $\mathcal{F}^{+\mathrm{veto}}$-statistic in case $(\widetilde{\mathrm{c}})$ and yields an improvement over it in cases $(\widetilde{\mathrm{d}})$ and $(\widetilde{\mathrm{f}})$, while in case $(\widetilde{\mathrm{e}})$ it does worse than both $\mathcal{F}$ and $\mathcal{F}^{+\mathrm{veto}}$-statistic – probably because the amplitude of the disturbance is less than in all other cases (see Fig. 10.1) and hence the full noise population is still dominated by candidates from the Gaussian distribution.

The main result is that O_{SGL} is more robust than any of the other statistics, yielding the top performance in all cases. In the clearest example, band $(\widetilde{\mathrm{d}})$ which has a very strong and narrow line in the data, O_{SGL} improves over $\mathcal{F}$ by about 30% at fixed $h_0^{\mathcal{S}}$ and reaches $p_{\mathrm{det}} = 0.95$ almost a factor of 2 earlier. Compared to the $\mathcal{F}^{+\mathrm{veto}}$-statistic, the comparison still yields about 20% and a factor of 1.6.

In summary, the line-robust statistic O_{SGL} consistently shows the best performance over a wide range of data types: it is more robust to varying kinds of disturbances than $\mathcal{F}^{+\mathrm{veto}}$ and safer in Gaussian noise than $O_{\mathrm{SL}}^{(0)}$.
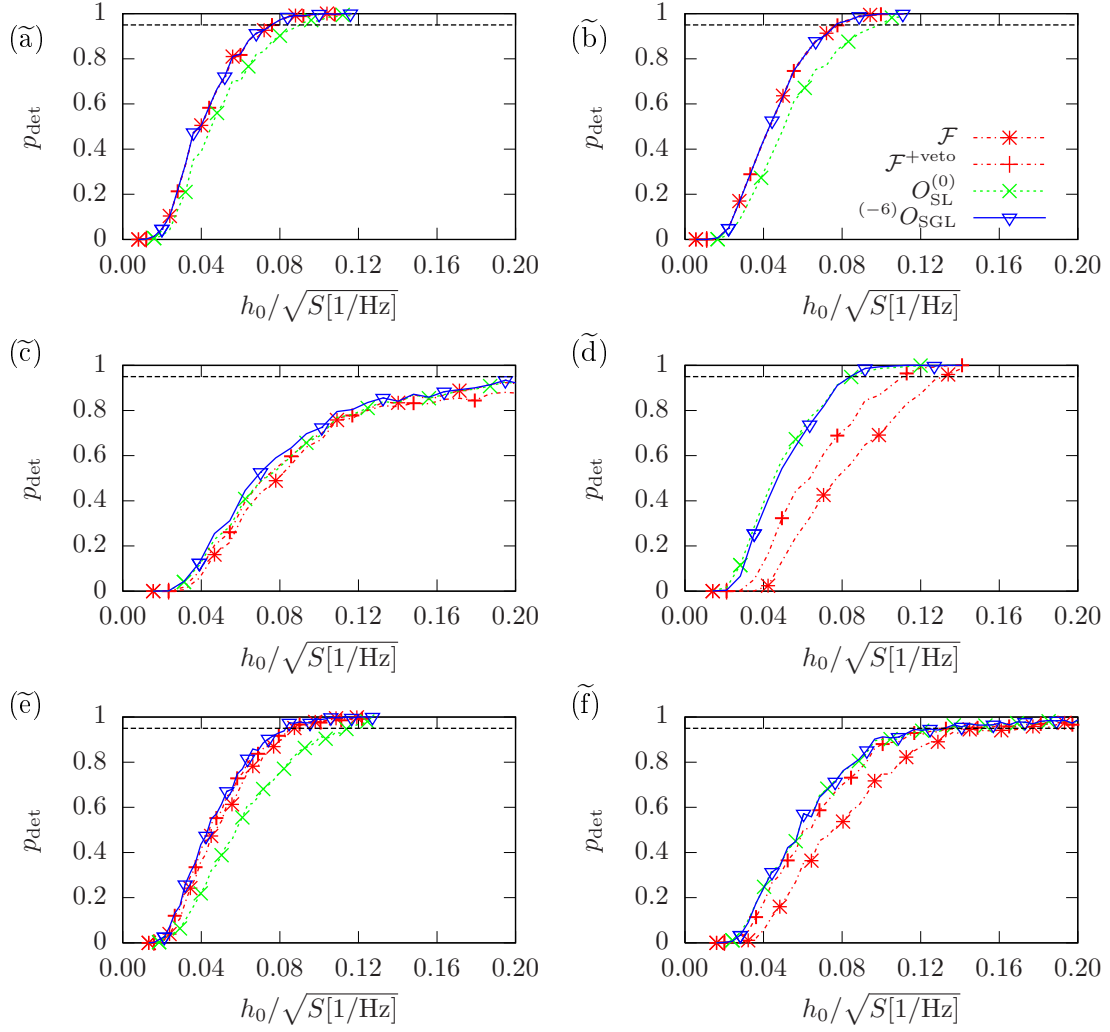
Figure 10.9: Detection efficiency p_{det} as a function of scaled signal amplitude $h_0^{\mathcal{S}} = h_0/\sqrt{S[1/\text{Hz}]}$ for four coherent statistics: $\mathcal{F}$, $\mathcal{F}^{+\text{veto}}$, $O_{\text{SL}}^{(0)}$, and $^{(-6)}O_{\text{SGL}}$. Statistical errors are similar to the size of the symbols. The dashed horizontal line marks the 95% detection probability level.

The panels show: $(\widetilde{\text{a}})$ simulated Gaussian noise, $(\widetilde{\text{b}})$ a quiet band, $(\widetilde{\text{c}})+(\widetilde{\text{d}})$ two bands with comparatively narrow lines in L1, $(\widetilde{\text{e}})$ a band with a broad disturbance in L1, $(\widetilde{\text{f}})$ a band with multiple disturbances in H1.

See Fig. 10.1 and Tbl. 10.1 for more details on these data sets.

10.6 Comparison of detection probabilities – semi-coherent case

Similarly to the coherent results, Fig. 10.10 shows the detection efficiency p_{det} as a function of $h_0^{\mathcal{S}}$ for the semi-coherent statistics over the full, year-long data sets. Qualitatively, I find very similar results as before.

For the quiet bands – simulated Gaussian noise in $(\widehat{\mathrm{a}})$ and real data in $(\widehat{\mathrm{b}})$ – the simple line-veto statistic $\widehat{O}_{\mathrm{SL}}^{(0)}$ again loses a significant fraction of detection power compared to both the $\widehat{\mathcal{F}}$-statistic and to $\widehat{\mathcal{F}}^{+\mathrm{veto}}$, while the line-robust statistic $\widehat{O}_{\mathrm{SGL}}$ does not show any noticeable degradation.

On the other hand, in the bands containing noise disturbances $(\widehat{\mathrm{c}}\text{–}\widehat{\mathrm{f}})$, the $\widehat{\mathcal{F}}$-statistic suffers the most. These examples show the line-robust statistic $\widehat{O}_{\mathrm{SGL}}$ consistently performing better than $\widehat{\mathcal{F}}$ and as well as or better than either $\widehat{O}_{\mathrm{SL}}^{(0)}$ or $\widehat{\mathcal{F}}^{+\mathrm{veto}}$ in all the disturbed bands.

The largest improvement is again in band $(\widehat{\mathrm{d}})$, with a strong and narrow line artefact, which for the longer data set has an even more severe effect on the performance of the other statistics. Here, the signal amplitude required at $95\,\%$ detection probability is nearly two times smaller for $\widehat{O}_{\mathrm{SGL}}$ than for $\widehat{\mathcal{F}}^{+\mathrm{veto}}$. The performance of the unmodified $\widehat{\mathcal{F}}$-statistic in this band is so bad that I refrained from doing injections for such high $h_0^{\mathcal{S}}$ that $p_{\mathrm{det}} = 0.95$ could be reached. Here, $\widehat{O}_{\mathrm{SGL}}$ could give an improvement of an order of magnitude.

Again, the results from this study indicate that a properly tuned $\widehat{O}_{\mathrm{SGL}}$, i.e. in this case $^{(-6)}\widehat{O}_{\mathrm{SGL}}$, can be a reliable universal detection statistic for a wide range of LIGO data with diverse noise characteristics.
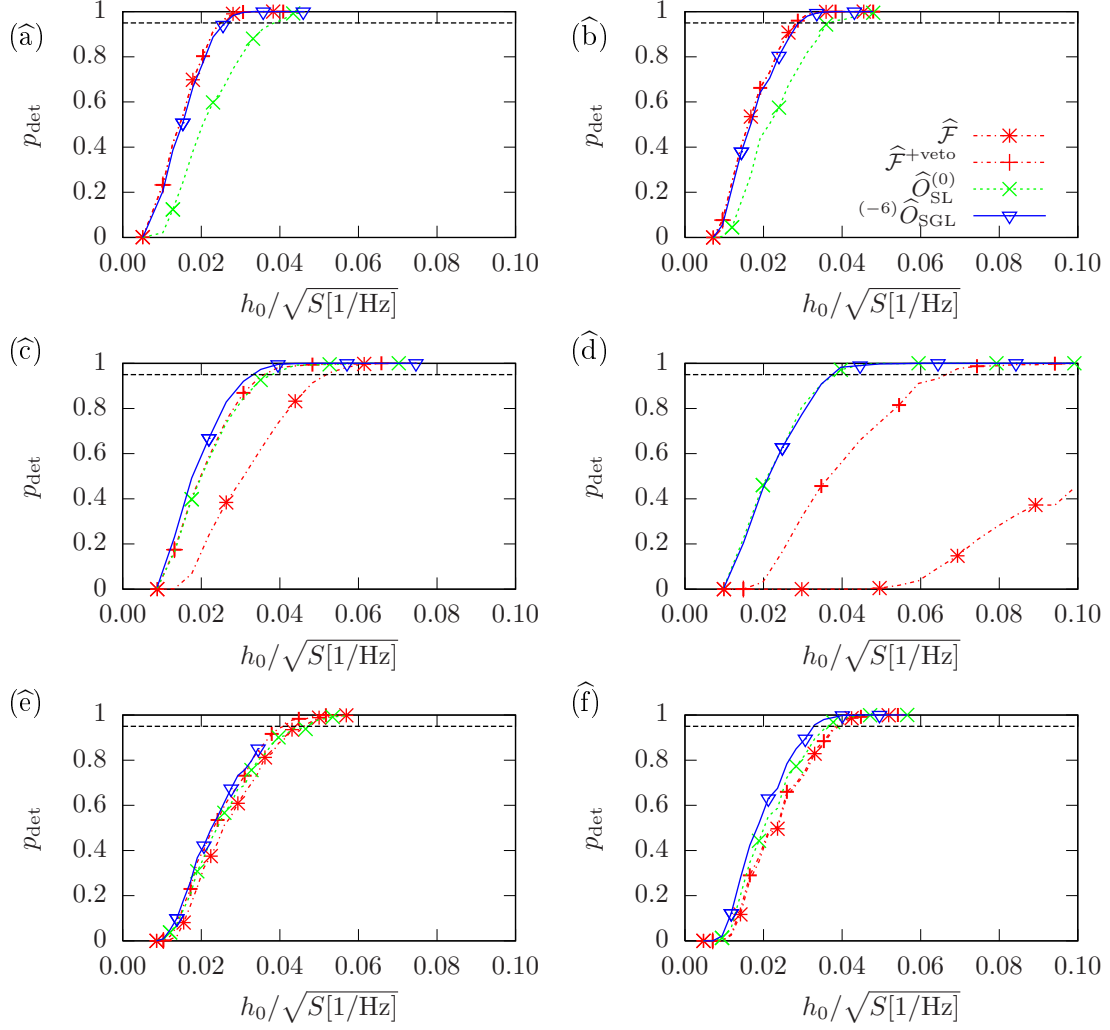
Figure 10.10: Detection efficiency p_{det} as a function of scaled signal amplitude $h_0^{\mathcal{S}} = h_0/\sqrt{S[1/\text{Hz}]}$ for four semi-coherent statistics: $\widehat{\mathcal{F}}$, $\widehat{\mathcal{F}}^{+\text{veto}}$, $\widehat{O}_{\text{SL}}^{(0)}$, and $^{(-6)}\widehat{O}_{\text{SGL}}$. Statistical errors are similar to the size of the symbols. The dashed horizontal line marks the 95% detection probability level.

The panels show: $(\widehat{a})$ simulated Gaussian noise, $(\widehat{b})$ a quiet band, $(\widehat{c})+(\widehat{d})$ two bands with comparatively narrow lines in L1, $(\widehat{e})$ a band with a broad disturbance in L1, $(\widehat{f})$ a band with multiple disturbances in H1.

See Fig. 10.2 and Tbl. 10.2 for more details on these data sets.

11 Application to Einstein@Home

Application to the distributed-computing project Einstein@Home was one of the main drivers behind the developments presented in this thesis. I have given an overview of the project in Sec. 5.12 and will now describe recent progress in the use of line-robust statistics in relation to Einstein@Home.

As of the writing of this thesis, the most recent published CW results from Einstein@Home are those of Aasi et al. (2013b), using data from the fifth LIGO science run (S5, see Sec. 2.6.3). It set the currently most constraining all-sky upper limits for CWs from isolated neutron stars in the 50–1190 Hz range, also shown in Fig. 6.2.

The analysis used the `lalapps_HierarchicalSearch` code based on the Hough transform method (Krishnan et al. 2004). Lines were handled with an initial cleaning step (see Sec. 6.5.1) and application of the $\mathcal{F}$-statistic consistency veto (see Sec. 6.5.3) during post-processing – no results from this thesis were used for this analysis, although I contributed to a `LALApps` progam used in producing the $\widehat{\mathcal{F}}^X$-values for the veto step.

This discussion covers several Einstein@Home *runs*, i.e. separate searches on different parameter spaces and with different set-ups. The results of the runs discussed in Sec. 11.1 are currently undergoing post-processing, while Sec. 11.2 covers searches that are still running or in preparation.

Here, I give only short descriptions of the general search set-ups, focussing mostly on the aspect of line-robust statistics. Detailed descriptions of the data selection, search parameter spaces, analysis procedures and results will be given in upcoming publications of the LIGO Scientific Collaboration and the Virgo Collaboration.

11.1 S6 all-sky searches

With data from the sixth LIGO science run (S6), an Einstein@Home all-sky search has been carried out in three runs, each using the `lalapps_HierarchSearchGCT` (`HSGCT`) code based on the global-correlations method (see Sec. 5.10 and Pletsch 2008, Pletsch & Allen 2009, Pletsch 2010):

- The first run covered 50–450 Hz, corresponding to the best region or "bucket" of the LIGO sensitivity curve, and is therefore called *S6Bucket*. Just as the previous GCT run on S5 data, it used the semi-coherent multi-detector $\widehat{\mathcal{F}}$-statistic as a toplist ordering statistic. No on-host line-vetoing was implemented in this run. However,

for the first time, single-detector $\widehat{\mathcal{F}}^X$-statistics were also computed directly on the host, for use in post-processing.

- A second run covered the same frequency range with an identical search set-up, except for using the semi-coherent line-veto statistic $\widehat{O}_{\mathrm{SL}}$ from Sec. 7.3.2 for toplist ordering, instead of $\widehat{\mathcal{F}}$. This run is called *S6LV1*.

- Finally, the *S6LVE* run ("E" for extension) covered an additional frequency range of 450–510 Hz. The HSGCT code was modified to simultaneously produce two toplists, one ordered by $\widehat{\mathcal{F}}$ and one by $\widehat{O}_{\mathrm{SL}}$. Thus, the results from both the S6Bucket and the S6LV1 runs were extended to higher frequencies.

For the S6Bucket run, the $\widehat{\mathcal{F}}^X$-values were computed in an additional *recalculation* step at the end of each workunit, for the candidates in the final toplist only. The `HSGCT` code uses a coherent coarse grid and a semi-coherent fine grid, as discussed in Sec. 5.9. Each toplist entry corresponds to a candidate at a fine-grid template. According to Eq. (5.57), the semi-coherent $\widehat{\mathcal{F}}$-statistic at a fine-grid point λ is the sum of per-segment $\widetilde{\mathcal{F}}_k$-statistics at the closest coarse-grid point λ_k in each segment k. In the recalculation step, however, the exact fine-grid was used. Hence, both the set of $\{\widehat{\mathcal{F}}, \widehat{\mathcal{F}}^X\}$-values returned by the hosts, and any line-robust statistics computed from them during post-processing, have profited from the increased fine-grid resolution.

For the S6LV1 run, the HSGCT code was modified to directly compute the $\widehat{\mathcal{F}}^X$-values and also $\widehat{O}_{\mathrm{SL}}$ or $\widehat{O}_{\mathrm{SGL}}$ (see Sec. 7.3.3) at each fine-grid point, thus enabling toplist sorting based on those statistics. At the time when the run was set up, the tuning of the free parameters of the line-robust statistic, as described in Sec. 8, had not been developed yet. For this reason, it was decided to use the simple line-veto statistic $\widehat{O}_{\mathrm{SL}}$ instead of the potentially more powerful $\widehat{O}_{\mathrm{SGL}}$. The prior line-odds $\widehat{o}_{\mathrm{LG}}^X$ were set to $\widehat{o}_{\mathrm{LG}}^{\mathrm{H1}} = \widehat{o}_{\mathrm{LG}}^{\mathrm{L1}} = 1$.

From Eqs. (5.50)–(5.52), it is clear that everything needed to compute the $\widehat{\mathcal{F}}^X$-values already exists as intermediate results in the computation of $\widehat{\mathcal{F}}$. Hence, returning these additional numbers from the hosts did require a modification to the code, but comes at a negligible additional computational cost. On the other hand, due to the huge number of templates in an Einstein@Home search, the computation of a new statistic at each fine-grid point is expensive, especially if it includes exponentials and logarithms, as $\widehat{O}_{\mathrm{SL}}$ does. Hence, we chose to save computing power by neglecting the logarithmic correction in the semi-coherent version of Eq. (7.50). In Monte-Carlo studies, this was found to have only a very small effect on detection probabilities.

The two data sets obtained from these runs, one with $2\widehat{\mathcal{F}}$-sorted toplists and one with $\widehat{O}_{\mathrm{SL}}$-sorted toplists, both covering 50–510 Hz, are currently in joint post-processing. This means that a joint set of most significant candidates is created by combining the toplists for each part of the search parameter space. As of the writing of this thesis, the favoured approach is to compute the line-robust statistic $\widehat{O}_{\mathrm{SGL}}$ on all candidates and to use this for a re-ranking of the joint set.

For this purpose, I have computed the required transition-scale-parameter $\widehat{\mathcal{F}}_*^{(0)}$ according to the prescription from Sec. 8.2, using Monte-Carlo studies similar to those presented in Sec. 10, but using S6 data and the same search set-up as the S6LV1 run. I have also estimated prior line-odds $\widehat{o}_{\mathrm{LG}}^X$ for the S6 data set with the SFT-power-based method from Sec. 8.1. These values were then used in Eq. (7.96) to compute $\widehat{O}_{\mathrm{SGL}}$ over all candidates.

11.2 S6 directed searches

The most recent Einstein@Home run, which is currently still running on the host machines, is different from all previous runs because it is not an all-sky search, but directed towards a single sky-position. The run is called *S6CasA* because the target is the supernova remnant (see Sec. 3.1) *Cassiopeia A*.

CasA, at an estimated distance of 3.3 kpc, was originally discovered as one of the first extrasolar radio sources (Ryle & Smith 1948). With an age of around 300 years, it is one of the youngest known SN remnants, and the neutron star identified as its central compact object (de Luca 2008) is one of the most promising candidate CW sources (Aasi et al. 2014f).

It has already been the target of a 12-day coherent analysis of LIGO S5 data (Wette et al. 2008, Wette 2009, Abadie et al. 2010b), setting 95%-confidence upper limits of $h_0 = (0.7–1.2) \cdot 10^{-24}$ in the 100–300 Hz range. A first search for CW emission from CasA with LIGO S6 data (Aasi et al. 2014f) in the 91–573 Hz range, coherently analysing only 8.4 days, already marginally improved over these results, with a best upper limit of $h_0 = 6 \cdot 10^{-25}$.

The semi-coherent Einstein@Home S6CasA run covers the range of 50–1000 Hz and, in contrast to the all-sky searches, searches explicitly not only for the first spin-down term $\dot{f}$, but also for $\ddot{f}$. As in the S6LVE run, dual toplists are produced on the hosts: one sorted by the $\widehat{\mathcal{F}}$-statistic and one according to the fully tuned $\widehat{O}_{\mathrm{SGL}}$. Again, I performed the SFT-power-based tuning of line priors $\widehat{o}_{\mathrm{LG}}^X$ and Gaussian-noise Monte Carlos for the transition scale $\widehat{\mathcal{F}}_*^{(0)}$, both adapted to the new search set-up.

Additional directed searches on S6 data are planned for upcoming Einstein@Home runs, investigating other young and nearby compact objects with unknown rotation frequency that could contain a strong CW emitter. These will probably use a setup similar to the CasA search and primarily use the $\widehat{O}_{\mathrm{SGL}}$-ordered toplists.

12 Line-robust statistics in the case of unequal detector sensitivities

In this chapter, I investigate the behaviour of the line-robust statistics under a set of conditions which have not yet been tested in KPPLS14 nor in chapters 7–10 of this thesis. Since the original submission of this thesis in August 2014, a paper based on this chapter has been published in Class. Quant. Grav. (Keitel & Prix 2015).

The idea of using a comparison between multi- and single-detector statistics, $\mathcal{F}$ and $\mathcal{F}^X$, to distinguish CW signals from (non-coincident) lines implicitly relies on all detectors having similar sensitivities. Indeed, for the synthetic tests in Sec. 9 I explicitly assumed equal noise PSDs S^X, and in the tests on LIGO S5 data in Sec. 10 the largest deviation between the two detectors H1 and L1 was $\sqrt{S^{\mathrm{H1}}}/\sqrt{S^{\mathrm{L1}}} \approx 1.7$ (coherent example $\widetilde{\mathrm{(b)}}$, see Tbl. 10.1). In addition, all tests so far have been for all-sky searches, averaging out the different antenna patterns of the individual detectors.

However, very different sensitivities may make signals and lines difficult to distinguish, which would lead to decreased detection power of our line-robust statistics both in the presence of lines and in pure Gaussian noise. In Sec. 12.1 I will investigate this concern about their *safety* under these generalised conditions, in the sense that they should never have worse detection probabilities than the standard $\mathcal{F}$-statistic. Using synthetic draws, it turns out that this issue only really affects O_{SL} (of Eq. (7.44)) and O_{SGL} (of Eq. (7.68)) with a transition-scale parameter $\mathcal{F}_*^{(0)}$ that is too low. An optimally-tuned O_{SGL} (in the sense of Sec. 8.2) still seems to be safe under most circumstances of practical relevance, though it cannot provide large improvements over $\mathcal{F}$ in extreme cases.

Then, in Sec. 12.2, I discuss an attempt to improve upon this behaviour. Based on changing the amplitude-prior distribution used in Sec. 7, it leads to sensitivity-weighting factors in the detection statistics, taking into account the noise PSDs, amount of data and sky-location-dependent detector responses. Additional synthetic tests in Sec. 12.3 show that this weighting recovers the losses of O_{SL} and O_{SGL} with low $\mathcal{F}_*^{(0)}$, but that it brings no further improvement for an optimally-tuned O_{SGL}.

All numerical results in this chapter are produced with the same synthesis approach as described in Sec. 9.1. O_{SL} and O_{SGL} always use "perfect-knowledge" line priors: $o_{\mathrm{LG}}^X = \max\{0.001, f_{\mathrm{L}}^X/(1 - f_{\mathrm{L}}^X)\}$ for line contaminations f_{L}^X. Receiver-operating characteristic (ROC) curves are based on $N_{\mathrm{draws}} = 10^7$ each for noise and signal populations, while the two-dimensional parameter-space exploration plots have $N_{\mathrm{draws}} = 10^5$ per parameter combination. The discussion in this chapter is limited to coherent quantities,

similarly to Secs. 7.2 and 9. A generalisation to semi-coherent searches along the lines of Sec. 7.3 would be straightforward.

12.1 Investigation of safety concerns at unequal sensitivities

Consider two detectors X and Y, with X being much more sensitive than Y. There may be CW signals that are strong enough to cause a significant outlier in the single-detector $\mathcal{F}^X$-statistic, but fail to do so in $\mathcal{F}^Y$, because the signal is still buried in the higher noise level of detector Y. Also, in this case the multi-detector $\mathcal{F}$-statistic is dominated by the contribution of the more sensitive detector X, so that for a strong line in that detector, $\mathcal{F} \approx \mathcal{F}^X$ holds.

Hence, in this case both an actual astrophysical CW signal and an instrumental line can have very similar signatures in terms of $\{\mathcal{F}, \mathcal{F}^X, \mathcal{F}^Y\}$ values. The line-veto statistic O_{SL} and line-robust statistic O_{SGL}, as given in Eqs. (7.44) and (7.68), are completely determined by this set of values (apart from the prior parameters discussed in Sec. 8). Therefore, it can be expected that these, too, have problems distinguishing lines from signals in such an unequal-sensitivity case, losing detection power due to increased false dismissals.

The line-robust statistics are intended to suppress "signal-like" lines and thus they always include a test of tentative signals against the line hypothesis. If, however, weaker signals appear as "line-like", they receive low odds, and the signal population is less distinct from noise – even in the absence of actual lines – so that fixed-p_{FA} thresholds remove a larger fraction of signal candidates, thus lowering p_{det}.

The approach of tuning O_{SGL} to reproduce the detection performance of the $\mathcal{F}$-statistic, as described in Sec. 9.3.2, should in principle keep us safe from this effect; but whether it actually works under these relaxed assumptions will be tested in the following.

In order to quantify under which conditions a problem may occur, recall the definition of the multi-detector $\mathcal{F}$-statistic from Sec. 5.7:

$$2\mathcal{F}(\boldsymbol{x}, \lambda) \equiv x_\mu \, \mathcal{M}^{\mu\nu}(\lambda) \, x_\nu \,. \tag{12.1}$$

The sensitivity of a detector network is encoded in the antenna-pattern matrix $\mathcal{M}_{\mu\nu}$, discussed in Sec. 5.6. Its scale is given by its determinant,

$$|\mathcal{M}| = \mathcal{S}^{-4} T_{\mathrm{data}}^4 D^2 \,, \tag{12.2}$$

where $\mathcal{S}$ is the multi-detector noise PSD from Eqs. (5.4) and (5.31), T_{data} is the effective amount of data and D quantifies the antenna-pattern-based sensitivity to a particular sky location – see Eqs. (5.17), (5.38) and (5.39).

156
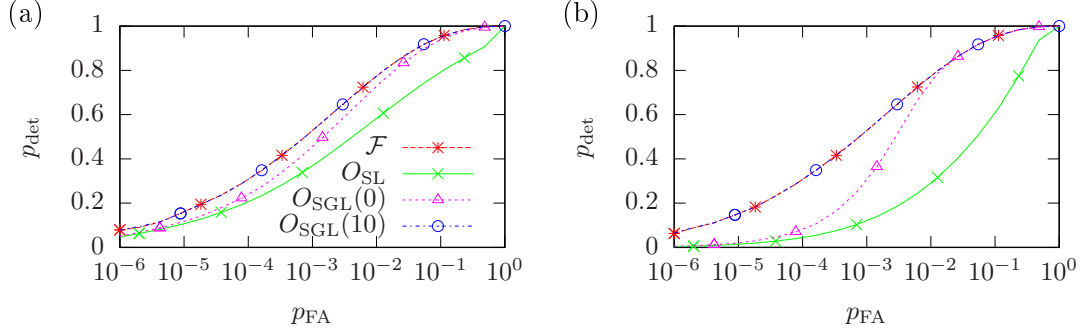
Figure 12.1: Detection probability p_{det} as a function of false-alarm probability p_{FA} for different synthetic statistics, for detectors H1 and H2, a signal population with fixed SNR of $\rho_{\text{S}} = 4$ in Gaussian noise without line contamination. The panels show relative detector sensitivities of (a) $\sqrt{S^{\text{H2}}} = \sqrt{S^{\text{H1}}}$, (b) $\sqrt{S^{\text{H2}}} = 10\sqrt{S^{\text{H1}}}$. For O_{SGL}, different values of $\mathcal{F}_*^{(0)}$ are given in brackets.

Using the same normalisation convention as in Secs. 5.5 and 5.6, the corresponding single-detector quantity is

$$\left|\mathcal{M}^X\right| = \mathcal{S}^{-4} T_{\text{data}}^4 \left(D^X\right)^2 , \tag{12.3}$$

where D^X, through the noise-weighted average from Eq. (5.33), depends quadratically on $(S^X)^{-1}$ and T_{data}^X.

Thus, for two given detectors, their relative sensitivities are given by their noise PSDs S^X, the respective amount of data and the relative sky-position sensitivities D^X. In the following, I will only consider the first and third of these contributions, since T_{data}^X enters to the same power as $\left(S^X\right)^{-1}$ and is therefore equivalent to a corresponding change in that quantity. I first consider the case of two colocated detectors, for example H1 and H2, for different S^X and various noise distributions in Secs. 12.1.1–12.1.3, and then the case of non-colocated detectors H1 and L1 with different D^X in Sec. 12.1.4.

12.1.1 Synthetic tests in Gaussian noise

ROC curves for synthetic draws from a signal population with fixed SNR of $\rho_{\text{S}} = 4$ and pure Gaussian noise without line contamination are shown in Fig. 12.1. In panel (a), both detectors have the same PSD, $\sqrt{S^{\text{H2}}} = \sqrt{S^{\text{H1}}}$. The results are very similar to those from panel (c) of Fig. 9.1 for an H1-L1 network and otherwise identical parameters. O_{SGL} with an optimal tuning of $\mathcal{F}_*^{(0)} = 10$ reproduces the detection probabilities of the $\mathcal{F}$-statistic, while O_{SL} and $O_{\text{SGL}}(\mathcal{F}_*^{(0)} = 0)$ have up to 20% lower p_{det}.

For extremely unequal sensitivities, $\sqrt{S^{\text{H2}}} = 10\sqrt{S^{\text{H1}}}$, as shown in panel (b), the losses of O_{SL} and $O_{\text{SGL}}(\mathcal{F}_*^{(0)} = 0)$ become much more pronounced, due to false dismissals of

157
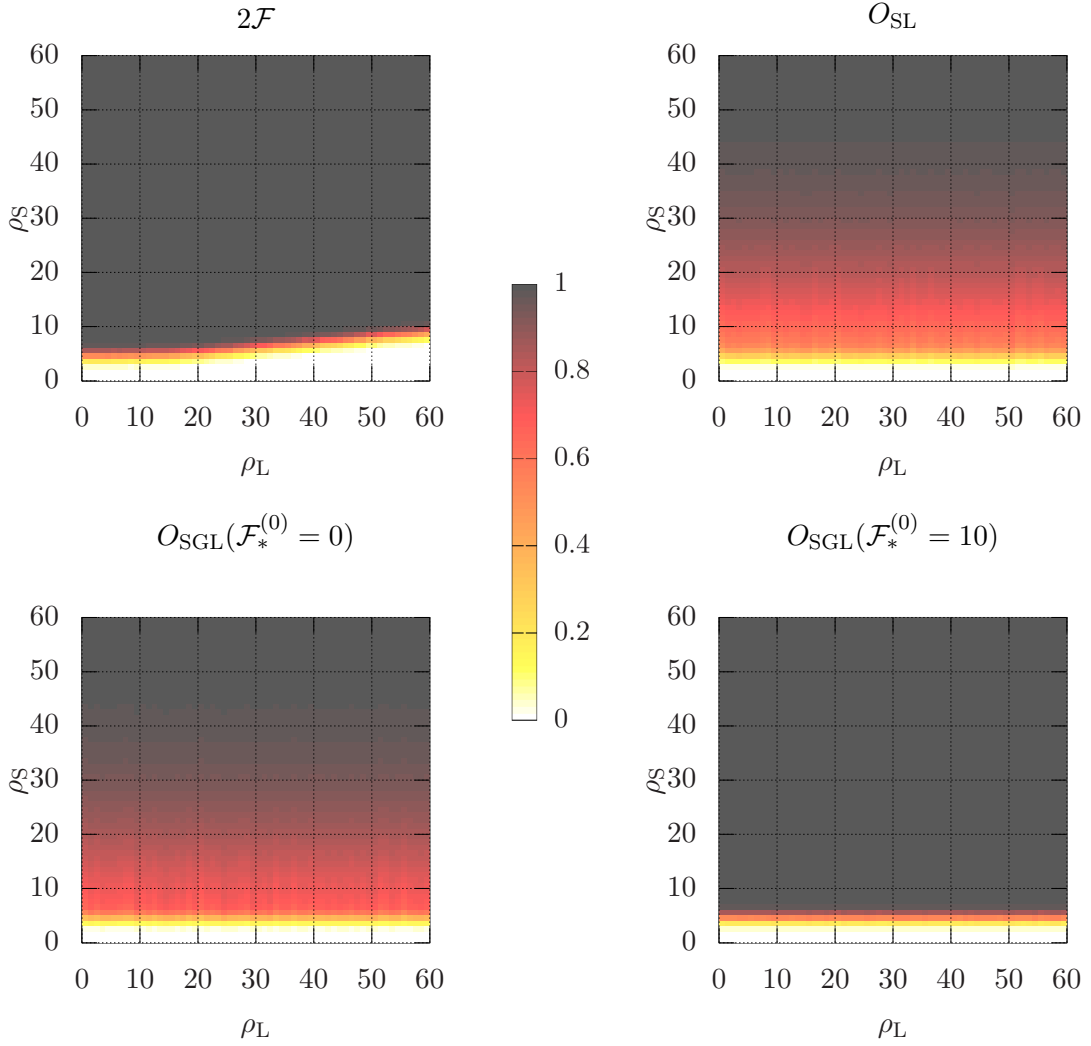
Figure 12.2: Detection probabilities p_{det} of different statistics, for an H1-H2 network with $\sqrt{S^{\text{H2}}} = 10\sqrt{S^{\text{H1}}}$, as a function of line SNR ρ_{L} and signal SNR ρ_{S} at fixed line contamination $f_{\text{L}}^{\text{H2}} = 0.1$ and false-alarm probability $p_{\text{FA}} = 0.001$.

"line-like" signals lowering p_{det} even in the absence of lines. However, $O_{\text{SGL}}(\mathcal{F}_*^{(0)} = 10)$ is *not* affected, because it still lends more weight to the Gaussian-noise hypothesis over the line hypothesis, thus being less likely to confuse signals with lines. This shows that the "safety"-tuning approach of Sec. 8.2 still works even in this extreme example.

12.1.2 Synthetic tests with lines in the less sensitive detector

For the extreme case of $\sqrt{S^{\text{H2}}} = 10\sqrt{S^{\text{H1}}}$, lines in the less sensitive detector H2 are already strongly suppressed in the multi-detector $\mathcal{F}$-statistic, resulting in an $\mathcal{F}$-statistic
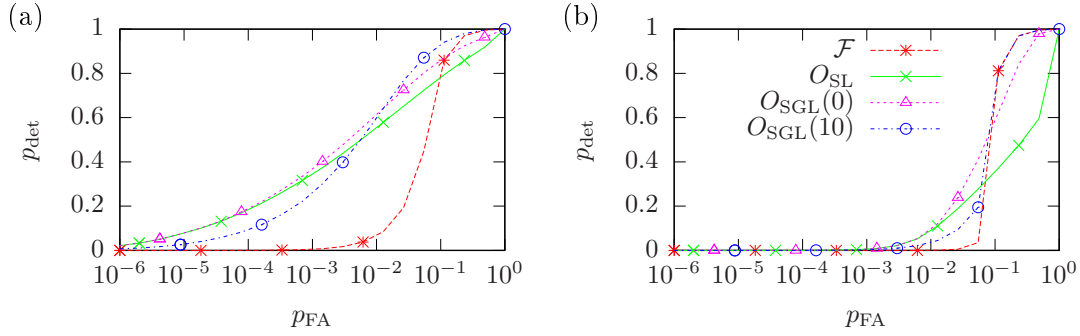
Figure 12.3: Detection probability p_{det} as a function of false-alarm probability p_{FA} for different synthetic statistics, for detectors H1 and H2, a signal population with fixed SNR of $\rho_S = 4$ and noise that is 90% Gaussian with 10% line contamination in H1, with line strength $\rho_L = 6$. The panels show relative detector sensitivities of (a) $\sqrt{S^{\text{H2}}} = \sqrt{S^{\text{H1}}}$, (b) $\sqrt{S^{\text{H2}}} = 10\sqrt{S^{\text{H1}}}$.

noise population that is quite similar to the case of pure Gaussian noise up to high line SNRs ρ_L. Hence, we expect a behaviour similar to the Gaussian-noise ROCs in Fig. 12.1, with losses in sensitivity for O_{SL} and O_{SGL} for low $\mathcal{F}_*^{(0)}$ while $O_{\text{SGL}}(\mathcal{F}_*^{(0)} \approx 10)$ should also be safe in this case.

In Fig. 12.2, detection probabilities at fixed $p_{\text{FA}} = 0.001$ are shown for the statistics $2\mathcal{F}$, $O_{\text{SL}}, O_{\text{SGL}}(\mathcal{F}_*^{(0)} = 0)$ and $O_{\text{SGL}}(\mathcal{F}_*^{(0)} = 10)$ over a wide range in ρ_S and ρ_L and with a line contamination of $f_L^{\text{H2}} = 0.1$. This can be compared to the similar plots for an equal-PSD H1-L1 network in Fig. 9.9.

The results show a very weak dependence on ρ_L. Both the $\mathcal{F}$-statistic and the line-robust $O_{\text{SGL}}(\mathcal{F}_*^{(0)} = 10)$ perform as well as they did in Gaussian noise or for equal sensitivities over most of the range, and the tuned line-robust statistic outperforms the $\mathcal{F}$-statistic only for very high ρ_L.

Meanwhile, O_{SL} and $O_{\text{SGL}}(\mathcal{F}_*^{(0)} = 0)$ show a mostly ρ_L-independent deficiency in detection power, only approaching $p_{\text{det}} = 1$ for extremely high ρ_S of 40 or higher.

12.1.3 Synthetic tests with lines in the more sensitive detector

Next, I consider the case where still $\sqrt{S^{\text{H2}}} = 10\sqrt{S^{\text{H1}}}$, but there is a line contamination of $f_L^{\text{H1}} = 0.1$ in the more sensitive detector. The ROCs in Fig. 12.3 contrast this case (panel b) with the equal-sensitivity case $\sqrt{S^{\text{H2}}} = \sqrt{S^{\text{H1}}}$ (panel a), both for signals with $\rho_S = 4$ and lines with $\rho_L = 6$. As found before in the examples in Sec. 9, all variants of the line-robust statistics give large improvements over the $\mathcal{F}$-statistic in the equal-sensitivity case. However, in panel (b) most of these improvements disappear, though $O_{\text{SGL}}(\mathcal{F}_*^{(0)} = 10)$ is still safe compared to $2\mathcal{F}$ at all p_{FA}.
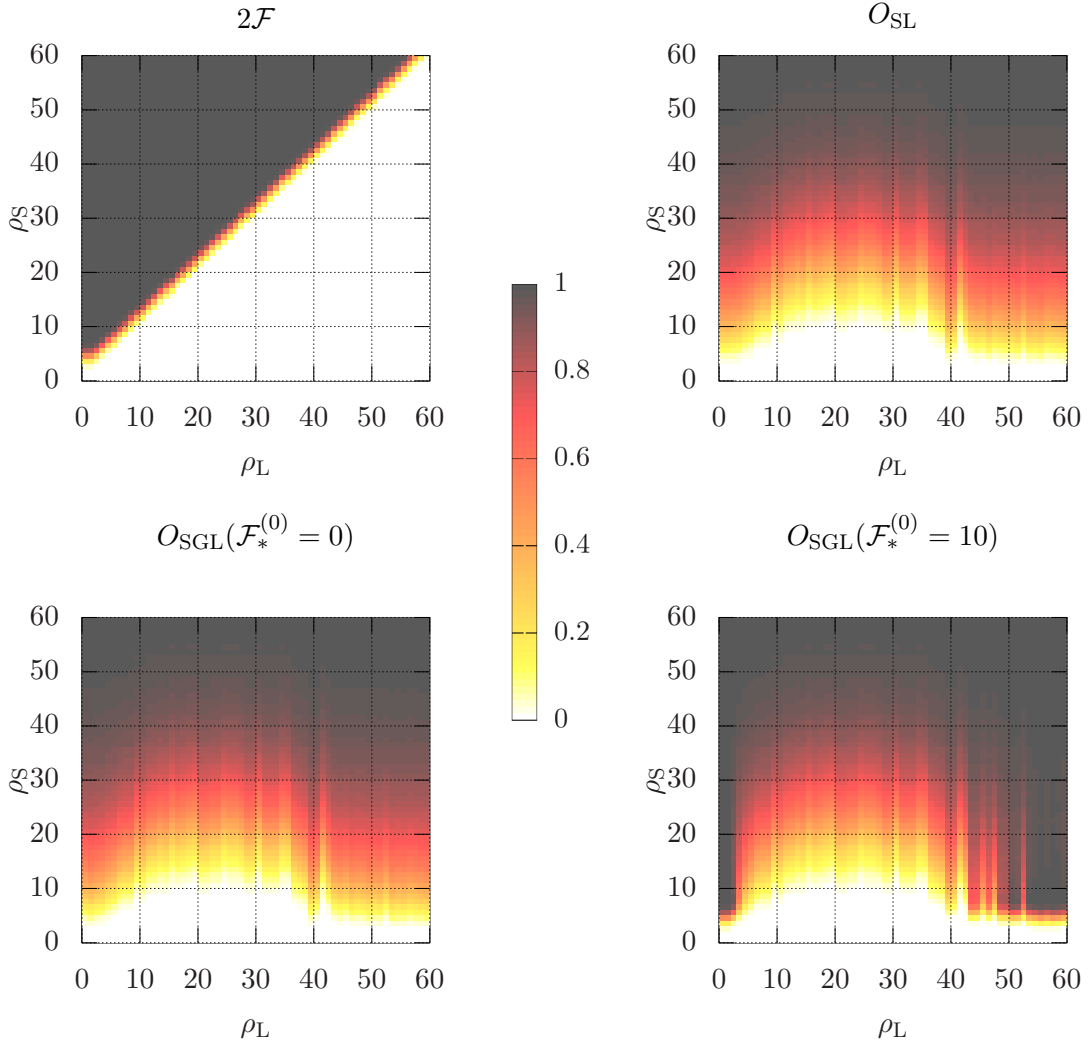
Figure 12.4: Detection probabilities p_{det} of different statistics, for an H1-H2 network with $\sqrt{S^{\text{H2}}} = 10\sqrt{S^{\text{H1}}}$, as a function of line SNR ρ_{L} and signal SNR ρ_{S} at fixed line contamination $f_{\text{L}}^{\text{H1}} = 0.1$ and false-alarm probability $p_{\text{FA}} = 0.001$.

For the same detector network, a systematic investigation of detection probabilities over the same range of ρ_{S} and ρ_{L} as in Fig. 12.2 is shown in Fig. 12.4, at fixed $p_{\text{FA}} = 0.001$. This demonstrates that $O_{\text{SGL}}(\mathcal{F}_*^{(0)} = 10)$ is safe at very low ρ_{L}, where the data is still almost Gaussian, matching the $\mathcal{F}$-statistic for all ρ_{S}. This range also includes the example from Fig. 12.3. At very high ρ_{L}, it performs much better than $\mathcal{F}$ and almost equally well as in the low-ρ_{L} regime.

In parts of the main region of interest, namely for intermediate to high ρ_{L}, $O_{\text{SGL}}(\mathcal{F}_*^{(0)} = 10)$ is *not safe*, performing worse than the $\mathcal{F}$-statistic when $\rho_{\text{S}} > \rho_{\text{L}}$, i.e. just when the detection problem should actually be comparatively easy. However, this is also compensated

Figure 12.5: Detection probability difference $p_{\text{det}}(O_{\text{SGL}}) - p_{\text{det}}(2\mathcal{F})$ with $\mathcal{F}_*^{(0)} = 10$, for an H1-H2 network with $\sqrt{S^{\text{H2}}} = 10\sqrt{S^{\text{H1}}}$, as a function of line SNR ρ_{L} and signal SNR ρ_{S}, at fixed $f_{\text{L}}^{\text{H1}} = 0.1$ and $p_{\text{FA}} = 0.001$.
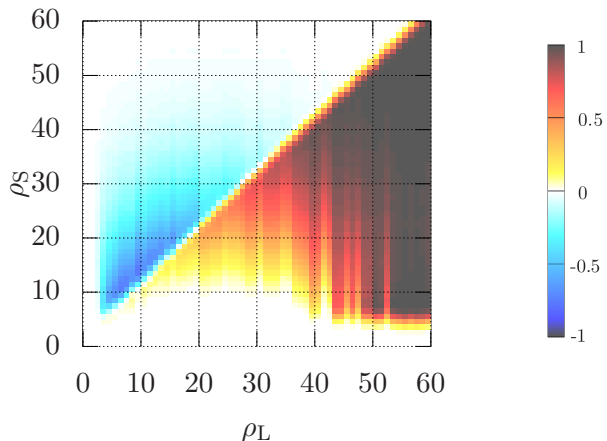
by regions where $O_{\text{SGL}}(\mathcal{F}_*^{(0)} = 10)$ performs better than $2\mathcal{F}$, namely for $\rho_{\text{S}} < \rho_{\text{L}}$.

A direct comparison of p_{det} for these two statistics, $O_{\text{SGL}}(\mathcal{F}_*^{(0)} = 10)$ and $2\mathcal{F}$, is shown in Fig. 12.5. Among the results presented in this section, this plot gives the clearest picture of the potential problem related to the simple line hypothesis introduced in Sec. 7.1.3: whereas the line-robust statistics improve over the $\mathcal{F}$-statistic by suppressing "signal-like lines", the approach can fail when there are also "line-like signals" in the data because of a much less sensitive detector not picking up the signal.

Typical CW searches with ground-based detectors operate in the regime of low signal SNRs ρ_{S}, so that the unsafe region for $O_{\text{SGL}}(\mathcal{F}_*^{(0)} = 10)$ is likely of little practical relevance. On the other hand, gains from O_{SGL} in this case are limited to the high-ρ_{L} range, but such strong lines are still more likely to occur in real data than strong signals are.

12.1.4 Synthetic tests of sky-location dependence

For non-colocated detectors, different antenna patterns lead to sky-location-dependent sensitivity differences, through the determinant factors D^X. From Figs. 5.4 and 5.5, we see that these differences are rather limited, and that they partially average out over longer observation times. For example, the maximum ratio of antenna-pattern determinants between the H1 and L1 detectors and for a 12-hour observation time (starting from a GPS time of 852443819) occurs at a sky location of $(\alpha, \delta) \approx (4.2523, -0.0793)$, where $D^{\text{L1}}/D^{\text{H1}} \approx 5.84$. For a 24-hour observation, this decreases to a maximum ratio of $D^{\text{L1}}/D^{\text{H1}} \approx 2.67$ at $(\alpha, \delta) \approx (2.4117, 0.0159)$.

In comparing this discrepancy in sensitivities to those considered in the preceding tests, the scale of D^X ratios can be translated to an equivalent scale of square-roots of the noise PSDs. Through the noise-weights (see Sec. 5.5), D^X depends on $(S^X)^{-2}$, so that these

maximum ratios would correspond to equivalent square-root-PSD ratios $\sqrt{S^{\mathrm{L1}}}/\sqrt{S^{\mathrm{H1}}}$ of only about 1.55 and 1.28, respectively.

Hence, we expect only a very small effect on detection probabilities from this most extreme case of different antenna patterns, and even less for other sky locations or for all-sky searches. Synthetic-ROC tests at "worst-case" sky positions have confirmed this, resulting in no significant losses in detection power and no safety concerns for either O_{SGL} or even O_{SL}.

12.2 Sensitivity-weighted detection statistics

In this section, I describe an attempt to improve the line-robust statistics in the case of detectors with different sensitivities. The idea is to re-weight the contribution of each detector in the denominators of O_{SL} and O_{SGL} with a factor corresponding to its respective sensitivity, including its PSD, amount of data and sky-location dependence – as seen in Eq. (12.3). By *down-weighting* contributions with higher sensitivity, this should intuitively decrease the chance of considering candidates with unequal $\mathcal{F}^{X}$-statistics as lines, thus decreasing the risk of false dismissals. A simple approach to include such a sensitivity weighting relies on revisiting the amplitude-parameter prior introduced in Sec. 7.1.2.

12.2.1 More on amplitude priors

The derivation of the posterior probability for the signal hypothesis $\mathcal{H}_{\mathrm{S}}$, Eq. (7.25), contains an integral for the marginalisation over amplitude parameters $\mathcal{A}$, namely

$$P\left(\boldsymbol{x}|\mathcal{H}_{\mathrm{S}}\right) = \int P\left(\boldsymbol{x}|\mathcal{H}_{\mathrm{S}}, \mathcal{A}\right) P\left(\mathcal{A}|\mathcal{H}_{\mathrm{S}}\right) \mathrm{d}\mathcal{A} \; . \tag{12.4}$$

As discussed in Sec. 7.1.2, this integral cannot be solved analytically for general parametrisations of $\mathcal{A}$ and prior distributions $P\left(\mathcal{A}|\mathcal{H}_{\mathrm{S}}\right)$. However, as previously demonstrated by PK09 and PGM11, it becomes a simple Gaussian integral for the "JKS factorisation" from Eq. (5.24) and with a uniform prior in the four JKS amplitude parameters $\mathcal{A}^{\mu}$.

Such a uniform prior would be "improper" (non-normalisable), unless we introduce a cut-off. One possibility for such a cut-off was introduced by PGM11 and adapted by KPPLS14, as described in Sec. 7.1.2:

$$P\left(\{\mathcal{A}^{\mu}\}|\mathcal{H}_{\mathrm{S}}\right) = \begin{cases} C & \text{for} \quad h_0^4(\mathcal{A}) < \frac{70\,c_*}{\sqrt{|\mathcal{M}|}} \, , \\ 0 & \text{otherwise} \, , \end{cases} \tag{12.5}$$

with a free parameter $c_* \in (0, \infty)$. Equivalently, it can be written as

$$P\left(\{\mathcal{A}^{\mu}\}|\mathcal{H}_{\mathrm{S}}\right) = \begin{cases} C & \text{for} \quad \widehat{\rho}(\mathcal{A}) < \widehat{\rho}_{\max} \, , \\ 0 & \text{otherwise} \, , \end{cases} \tag{12.6}$$

with an SNR-like quantity $\widehat{\rho} = h_0 \, |\mathcal{M}|^{1/8}$, so that $c_* = \frac{\widehat{\rho}_{\mathrm{max}}^4}{70}$.

However, PK09 originally used a different prior distribution, directly placing a fixed cut-off $h_{0\mathrm{max}} \in (0, \infty)$ on the signal strength parameter h_0:

$$P\left(\{\mathcal{A}^\mu\}|\mathcal{H}_{\mathrm{S}\mathcal{M}}\right) = \begin{cases} C & \text{for} \quad h_0(\mathcal{A}) < h_{0\mathrm{max}}\,, \\ 0 & \text{otherwise}\,. \end{cases} \tag{12.7}$$

Here, I use $\mathcal{H}_{\mathrm{S}\mathcal{M}}$ as a shorthand for the signal hypothesis with modified amplitude prior, the meaning of which will become clear in the next section.

This variant was discarded by PGM11 due to poor performance of the resulting detection statistic on medium-duration "transient CW" signals. However, for classical CW signals, the effect of such a prior has not been explicitly analysed yet, especially not in the context of comparing several detectors for robustness against line artefacts.

12.2.2 Sensitivity weighting for signals in pure Gaussian noise?

Before considering lines, it clarifies matters to first investigate the effect of these prior choices in the simpler case of CW signals in pure Gaussian noise. The difference between the two prior choices is that Eq. (12.5) results in a signal-hypothesis posterior

$$P\left(\mathcal{H}_{\mathrm{S}}|\boldsymbol{x}\right) = o_{\mathrm{SG}} \, c_*^{-1} \, P\left(\mathcal{H}_{\mathrm{G}}|\boldsymbol{x}\right) \, \mathrm{e}^{\mathcal{F}(\boldsymbol{x})} \tag{12.8}$$

and therefore in signal-to-Gaussian-noise odds of

$$O_{\mathrm{SG}}(\boldsymbol{x}) \equiv \frac{P\left(\mathcal{H}_{\mathrm{S}}|\boldsymbol{x}\right)}{P\left(\mathcal{H}_{\mathrm{G}}|\boldsymbol{x}\right)} \propto \mathrm{e}^{\mathcal{F}(\boldsymbol{x})}\,; \tag{12.9}$$

while Eq. (12.7) leads to a signal-hypothesis posterior

$$P\left(\mathcal{H}_{\mathrm{S}\mathcal{M}}|\boldsymbol{x}\right) = o_{\mathrm{S}\mathcal{M}\mathrm{G}} \, \frac{70}{h_{0\mathrm{max}}^4} \, P\left(\mathcal{H}_{\mathrm{G}}|\boldsymbol{x}\right) \, |\mathcal{M}|^{-1/2} \, \mathrm{e}^{\mathcal{F}(\boldsymbol{x})} \tag{12.10}$$

and odds of

$$O_{\mathrm{S}\mathcal{M}\mathrm{G}}(\boldsymbol{x}) \equiv \frac{P\left(\mathcal{H}_{\mathrm{S}\mathcal{M}}|\boldsymbol{x}\right)}{P\left(\mathcal{H}_{\mathrm{G}}|\boldsymbol{x}\right)} \propto |\mathcal{M}|^{-1/2} \, \mathrm{e}^{\mathcal{F}(\boldsymbol{x})}\,. \tag{12.11}$$

As discussed before, the antenna-pattern determinant $|\mathcal{M}|$ is a measure of the overall sensitivity of a network of detectors. I therefore refer, in the following, to any statistic derived from the prior Eq. (12.7), so that it has an explicit factor of $|\mathcal{M}|$ in the odds, as a *sensitivity-weighted statistic*.

Inserting the explicit expression from Eq. (12.2),

$$O_{\mathrm{S}\mathcal{M}\mathrm{G}}(\boldsymbol{x}) \propto \mathrm{e}^{\mathcal{F}(\boldsymbol{x})} \, \mathcal{S}^2 T_{\mathrm{data}}^{-2} D^{-1}\,, \tag{12.12}$$

demonstrates that any candidate coming from a particularly good set of data (low $\mathcal{S}$, large T_{data}), or from a point on the sky where the detector is most sensitive over the observation time (large D), is actually *down-weighted*. Thus, intuitively this statistic should be worse than the pure $\mathcal{F}$-statistic, and in general I will not consider using $\mathcal{H}_{\mathrm{S}\mathcal{M}}$ instead of $\mathcal{H}_{\mathrm{S}}$.

12.2.3 Sensitivity-weighted line-veto statistic

On the other hand, the effect of down-weighting outliers from more sensitive data could be useful in the case of line-vetoing. Consider again two detectors, one much more sensitive than the other (e.g., having lower S^X), and a signal that is strong enough to produce an elevated $\mathcal{F}^X$-statistic in the better detector, but not strong enough to be seen in the other one. This signal is likely to trigger the simple line hypothesis $\mathcal{H}_\mathrm{L}$ from Sec. 7.1.3, as the signature is similar to that of a line in one of two equally sensitive detectors.

When I now introduce the sensitivity-weighting from above in a modified line hypothesis, an outlier in the more sensitive detector will be considered less likely to come from a line. Such a reduction of false positives for the line hypothesis should then lead to less false dismissals of signals by the signal-versus-line odds.

Hence, I define a sensitivity-weighted single-detector line hypothesis $\mathcal{H}_{\mathrm{L}\mathcal{M}}^X$ that uses the single-detector version of the prior from Eq. (12.7):

$$
P\left(\{\mathcal{A}^{X\mu}\}|\mathcal{H}_{\mathrm{L}\mathcal{M}}^X\right) = \left\{ \begin{array}{ll} C & \text{for} \quad h_0(\mathcal{A}^X) < h_{0\mathrm{max}}^X\,, \\ 0 & \text{otherwise}\,. \end{array} \right. \tag{12.13}
$$

The line hypothesis $\mathcal{H}_{\mathrm{L}\mathcal{M}}$ for a non-coincident line in any detector is constructed as in Eq. (7.30). *Sensitivity-weighted line-veto odds* are then given by the unweighted signal hypothesis $\mathcal{H}_\mathrm{S}$ and the weighted $\mathcal{H}_{\mathrm{L}\mathcal{M}}$:

$$
O_{\mathrm{SL}\mathcal{M}}(\boldsymbol{x}) \equiv \frac{P\left(\mathcal{H}_\mathrm{S}|\boldsymbol{x}\right)}{P\left(\mathcal{H}_{\mathrm{L}\mathcal{M}}|\boldsymbol{x}\right)} = o_{\mathrm{SL}\mathcal{M}} \frac{\widehat{\rho}_{\mathrm{max}}^{-4}\,\mathrm{e}^{\mathcal{F}(\boldsymbol{x})}}{\left\langle \left(h_{0\mathrm{max}}^X\right)^{-4} r^X \left|\mathcal{M}^X\right|^{-1/2}\,\mathrm{e}^{\mathcal{F}^X(x^X)} \right\rangle_X}\,, \tag{12.14}
$$

where r^X are the line-prior weights defined in Eq. (7.36).

This expression contains various prior-cut-off parameters: $\widehat{\rho}_{\mathrm{max}}$ from $\mathcal{H}_\mathrm{S}$ and a set of $\{h_{0\mathrm{max}}^X\}$ from $\mathcal{H}_{\mathrm{L}\mathcal{M}}^X$. In Sec. 7, $\widehat{\rho}_{\mathrm{maxS}} = \widehat{\rho}_{\mathrm{maxL}} = \widehat{\rho}_{\mathrm{maxL}}^X$ was assumed for all X, so that any such parameters cancelled out. Here, I first assume $h_{0\mathrm{max}}^X = h_{0\mathrm{max}}$, again for all X, justified by the general absence of detailed physical knowledge about different line-strength populations in different detectors. This reduces the effect of the cut-offs to a common pre-factor to the odds:

$$
O_{\mathrm{SL}\mathcal{M}}(\boldsymbol{x}) = o_{\mathrm{SL}\mathcal{M}} \left(\frac{h_{0\mathrm{max}}}{\widehat{\rho}_{\mathrm{max}}}\right)^4 \frac{\mathrm{e}^{\mathcal{F}(\boldsymbol{x})}}{\left\langle r^X \left|\mathcal{M}^X\right|^{-1/2}\,\mathrm{e}^{\mathcal{F}^X(x^X)} \right\rangle_X}\,. \tag{12.15}
$$

As the only requirement for these cut-offs is that they should be large enough for the marginalisation integral to become Gaussian, I can choose to keep only one of them as a free parameter and to fix the ratio between them. For convenience of notation, I define

$$
\overline{\mathcal{M}} \equiv \left(\frac{\widehat{\rho}_{\mathrm{max}}}{h_{0\mathrm{max}}}\right)^8 = \text{const.} \tag{12.16}
$$

Pulling $\overline{\mathcal{M}}$ into the denominator, the weighted line-veto statistic becomes

$$O_{\mathrm{SL}\mathcal{M}}(\boldsymbol{x}) = o_{\mathrm{SL}\mathcal{M}} \; \frac{\mathrm{e}^{\mathcal{F}(\boldsymbol{x})}}{\left\langle r^X \sqrt{\frac{\overline{\mathcal{M}}}{|\mathcal{M}^X|}} \; \mathrm{e}^{\mathcal{F}^X(x^X)} \right\rangle_X} = o_{\mathrm{SL}\mathcal{M}} \; \frac{\mathrm{e}^{\mathcal{F}(\boldsymbol{x})}}{\left\langle r^X q^X \mathrm{e}^{\mathcal{F}^X(x^X)} \right\rangle_X} , \qquad (12.17)$$

with a per-detector relative *sensitivity-weighting factor*

$$q^X \equiv \sqrt{\frac{\overline{\mathcal{M}}}{|\mathcal{M}^X|}} . \qquad (12.18)$$

Now, let us consider the Bayes factor

$$B_{\mathrm{SL}\mathcal{M}}(\boldsymbol{x}) \equiv \frac{O_{\mathrm{SL}\mathcal{M}}(\boldsymbol{x})}{o_{\mathrm{SL}\mathcal{M}}} . \qquad (12.19)$$

It should give an unbiased answer to the question of how much more likely $\mathcal{H}_{\mathrm{S}}$ becomes in comparison with $\mathcal{H}_{\mathrm{L}\mathcal{M}}$ by considering the data $\boldsymbol{x}$. It should therefore produce numbers on the same scale as for the unweighted $B_{\mathrm{SL}}(\boldsymbol{x})$. Hence, the parameter $\overline{\mathcal{M}}$ should be similar to typical $|\mathcal{M}^X|$ values, making the denominator terms in Eq. (12.17) similar in scale to those in Eq. (7.44).

An obvious choice is to use an average of the determinants $|\mathcal{M}^X(\alpha, \delta)|$ over all detectors X and sky positions (α, δ):

$$\overline{\mathcal{M}} = \left\langle |\mathcal{M}^X(\alpha, \delta)| \right\rangle_{X,\alpha,\delta} = \mathcal{S}^{-4} \left\langle T_{\mathrm{data}}^{X4} \left(D^X(\alpha, \delta) \right)^2 \right\rangle_{X,\alpha,\delta} . \qquad (12.20)$$

There are several possible orderings for taking the averages over X and (α, δ), as well as the noise-weighted average over SFTs that is implicit in the D^X themselves. Due to the non-linearities involved, these averages do not generally commute.

However, as we are only interested in getting the *scale* of $\overline{\mathcal{M}}$ right, I will use a particularly simple prescription. As the sky-dependent variations in D^X, and thus $|\mathcal{M}^X|$, never reach an order of magnitude, I relax the conditions on $\overline{\mathcal{M}}$ and allow it to be a function $\overline{\mathcal{M}}(\alpha, \delta)$ of sky position. This way, only the average over detectors remains:

$$\overline{\mathcal{M}}(\alpha, \delta) \equiv \left\langle |\mathcal{M}^X(\alpha, \delta)| \right\rangle_X = \mathcal{S}^{-4} \left\langle (T_{\mathrm{data}}^X)^4 \left(D^X(\alpha, \delta) \right)^2 \right\rangle_X . \qquad (12.21)$$

12.2.4 Sensitivity-weighted line-robust statistic

Furthermore, I construct an extended noise hypothesis, in analogy to Eq. (7.40), but this time using the modified line-amplitude prior from Eq. (12.13):

$$\mathcal{H}_{\mathrm{GL}\mathcal{M}} : (\mathcal{H}_{\mathrm{G}} \text{ or } \mathcal{H}_{\mathrm{L}\mathcal{M}}) . \qquad (12.22)$$

This gives the *sensitivity-weighted line-robust odds* as an analogue to O_{SGL} of Eq. (7.68):

$$O_{\mathrm{SGL}\mathcal{M}}(\boldsymbol{x}) \equiv \frac{P\left(\mathcal{H}_{\mathrm{S}}|\boldsymbol{x}\right)}{P\left(\mathcal{H}_{\mathrm{GL}\mathcal{M}}|\boldsymbol{x}\right)} = o_{\mathrm{SGL}\mathcal{M}} \frac{\mathrm{e}^{\mathcal{F}(\boldsymbol{x})}}{(1-p_{\mathrm{L}})\,\mathrm{e}^{\mathcal{F}_{*}^{(0)}} + p_{\mathrm{L}}\,\left\langle r^{X}q^{X}\mathrm{e}^{\mathcal{F}^{X}(x^{X})}\right\rangle_{X}}\,. \quad (12.23)$$

Here, the transition-scale parameter $\mathcal{F}_{*}^{(0)}$ is unchanged from its definition in Eq. (7.67), as only the per-detector terms are modified.

Comparing the relative scale between the constant term and the per-detector terms, a change in sensitivity-weighting factors q^{X} would only be compensated by a logarithmic change in $\mathcal{F}_{*}^{(0)}$. Since I already defined q^{X} in Eq. (12.18) and $\overline{\mathcal{M}}$ in Eq. (12.16) in such ways as to reduce the numerical range of q^{X}, an empirical tuning of $\mathcal{F}_{*}^{(0)}$, as described in Sec. 8.2, can be expected to yield similar values as for the unweighted O_{SGL}. Numerical tests in analogy to those presented in Sec. 9.3.2 indeed show only small changes in the optimal $\mathcal{F}_{*}^{(0)}$ over typical ranges in false-alarm probabilities.

12.3 Synthetic tests of the sensitivity-weighted statistics

In this section, I present results from synthetic-draw comparisons of the sensitivity-weighted detection statistics $O_{\mathrm{SL}\mathcal{M}}$ and $O_{\mathrm{SGL}\mathcal{M}}$ against their unweighted counterparts O_{SL} and O_{SGL}, covering a similar range of noise populations as in Sec. 12.1.

12.3.1 Gaussian noise

To determine the effect of sensitivity-weighting on the detection performance of the line-robust statistics, I first revisit the same case as covered in Fig. 12.1, but including additional sensitivity ratios. For a colocated network of H1 and H2, signals with $\rho_{\mathrm{S}} = 4$ and pure Gaussian noise, the corresponding set of ROCs is shown in Fig. 12.6.

Panel (a) shows the case of equal sensitivity, where $O_{\mathrm{SL}\mathcal{M}}$ and $O_{\mathrm{SGL}\mathcal{M}}(\mathcal{F}_{*}^{(0)} = 10)$ perform exactly as their unweighted counterparts. This is expected from the analytical expressions in Eqs. (12.17) and (12.23), as in this case $q^{X} = 1$ and so the statistics revert back to the unweighted forms, Eqs. (7.44) and (7.68).

For increasing ratios of $\sqrt{S^{\mathrm{H2}}}/\sqrt{S^{\mathrm{H1}}} \in \{2, 5, 10\}$, there is still no difference between O_{SGL} and $O_{\mathrm{SGL}\mathcal{M}}$ with both at $\mathcal{F}_{*}^{(0)} = 10$. However, p_{det} for the unweighted O_{SL} decreases, while $O_{\mathrm{SL}\mathcal{M}}$ actually improves and approaches the performance of $2\mathcal{F}$ and $O_{\mathrm{SGL}}(\mathcal{F}_{*}^{(0)} = 10)$. ROCs for intermediate values of $\mathcal{F}_{*}^{(0)}$ would fall between the curves for O_{SL} (which corresponds to $\mathcal{F}_{*}^{(0)} \to -\infty$) and $\mathcal{F}_{*}^{(0)} = 10$.
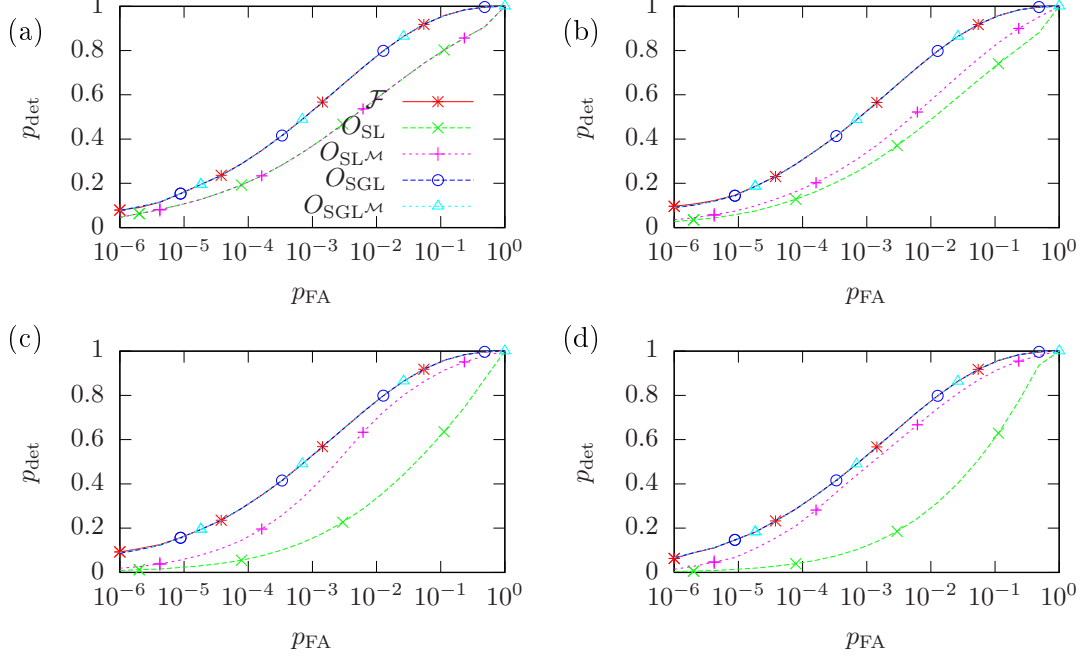
Figure 12.6: Detection probability p_det as a function of false-alarm probability p_FA for different statistics, for a signal population with fixed SNR of $\rho_\mathrm{S} = 4$ in Gaussian noise without line contamination. The panels show relative detector sensitivities of (a) $\sqrt{S^\mathrm{H2}} = \sqrt{S^\mathrm{H1}}$, (b) $\sqrt{S^\mathrm{H2}} = 2\sqrt{S^\mathrm{H1}}$, (c) $\sqrt{S^\mathrm{H2}} = 5\sqrt{S^\mathrm{H1}}$, (d) $\sqrt{S^\mathrm{H2}} = 10\sqrt{S^\mathrm{H1}}$. O_SGL and $O_\mathrm{SGL\mathcal{M}}$ both use $\mathcal{F}_*^{(0)} = 10$.

12.3.2 Lines in the less sensitive detector

The case of an H1-H2 network with $\sqrt{S^\mathrm{H2}} = 10\sqrt{S^\mathrm{H1}}$ and a line contamination $f_\mathrm{L}^\mathrm{H2} = 0.1$ in the weaker detector were considered before in Sec. 12.1.2 for the unweighted statistics, and the results were similar to pure Gaussian noise: significant losses in p_det for O_SL and O_SGL for low $\mathcal{F}_*^{(0)}$, while $O_\mathrm{SGL}(\mathcal{F}_*^{(0)} = 10)$ in this case is still completely safe when compared to the $\mathcal{F}$-statistic.

To illustrate the effect of sensitivity weighting for this noise population, Fig. 12.7 shows differences of p_det between weighted and unweighted statistics over the same range in ρ_S and ρ_L as in Fig. 12.2. Similarly to the Gaussian-noise ROCs in Fig. 12.6, $O_\mathrm{SL\mathcal{M}}$ and $O_\mathrm{SGL\mathcal{M}}(\mathcal{F}_*^{(0)} = 0)$ can regain 20-30% of p_det in comparison to their unweighted counterparts, whereas for high $\mathcal{F}_*^{(0)}$ such as 10 the changes are negligible.
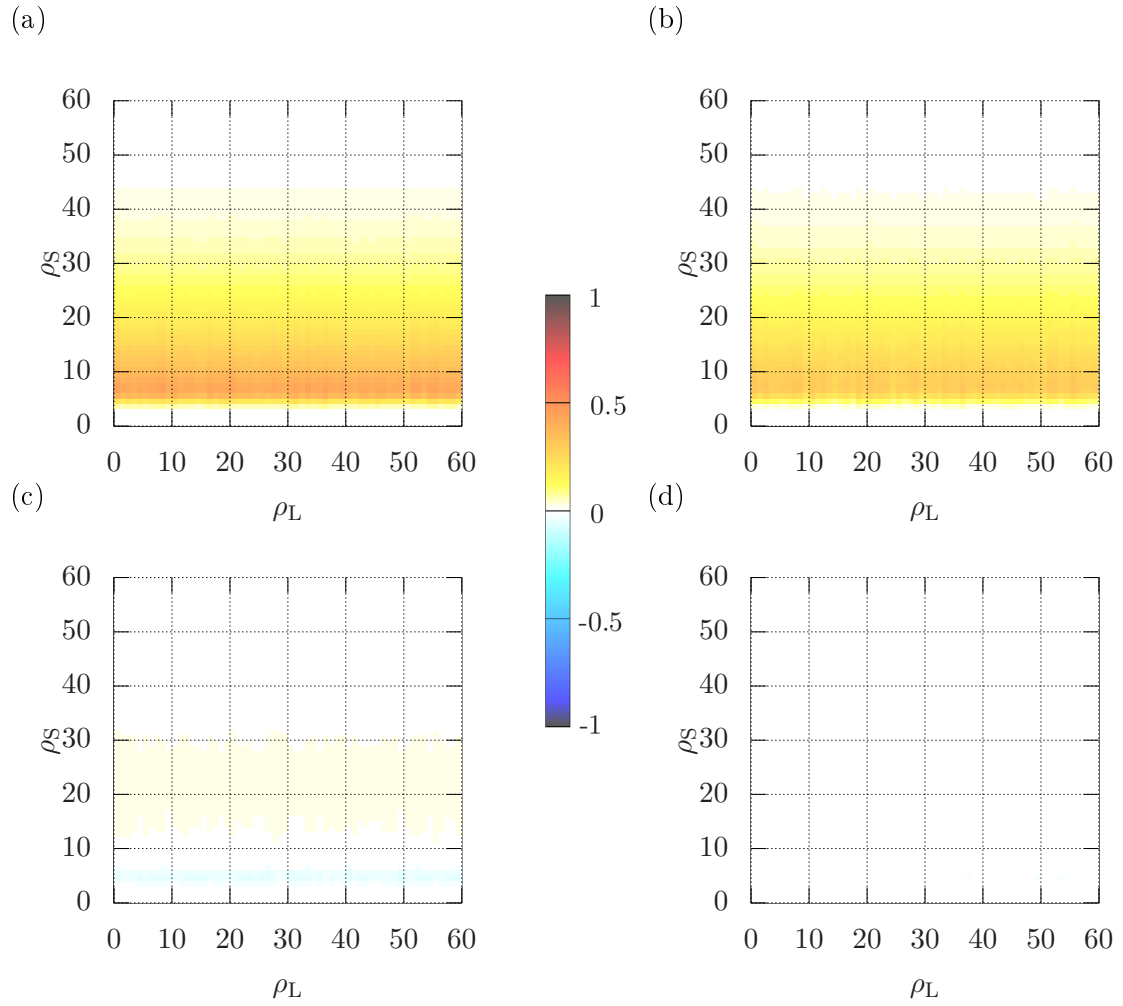
Figure 12.7: Detection probability differences between weighted and unweighted statistics, for an H1-H2 network with $\sqrt{S^{\text{H2}}} = 10\sqrt{S^{\text{H1}}}$, as a function of line SNR ρ_{L} and signal SNR ρ_{S}, at fixed $f_{\text{L}}^{\text{H2}} = 0.1$ and $p_{\text{FA}} = 0.001$.
(a): $p_{\text{det}}(O_{\text{SL}\mathcal{M}}) - p_{\text{det}}(O_{\text{SL}})$,
(b): $p_{\text{det}}(O_{\text{SGL}\mathcal{M}}) - p_{\text{det}}(O_{\text{SGL}})$ at $\mathcal{F}_*^{(0)} = 0$,
(c): $p_{\text{det}}(O_{\text{SGL}\mathcal{M}}) - p_{\text{det}}(O_{\text{SGL}})$ at $\mathcal{F}_*^{(0)} = 4$,
(d): $p_{\text{det}}(O_{\text{SGL}\mathcal{M}}) - p_{\text{det}}(O_{\text{SGL}})$ at $\mathcal{F}_*^{(0)} = 10$.

12.3.3 Lines in the more sensitive detector

On the other hand, as we have already seen in Fig. 12.3, the detection problem is more difficult in general if there are lines present in the more sensitive detector. These can be very hard to distinguish from CW signals using only the information in $\mathcal{F}$ and $\{\mathcal{F}^X\}$.

For the same parameters as in Fig. 12.4, i.e. an H1-H2 network with $\sqrt{S^{\mathrm{H2}}} = 10\sqrt{S^{\mathrm{H1}}}$ and a line contamination of $f_{\mathrm{L}}^{\mathrm{H1}} = 0.1$, changes in p_{det} due to sensitivity-weighting are shown in Fig. 12.8. In these noise populations, the improvements of the sensitivity-weighted counterparts to O_{SL} and O_{SGL} with low $\mathcal{F}_*^{(0)}$ are more modest than in the previous cases, with p_{det} improving only in the low- and high-ρ_{L} regions, and not in the most problematic range in-between. Most importantly, sensitivity weighting again brings no improvement for an optimally-tuned $O_{\mathrm{SGL}}(\mathcal{F}_*^{(0)} = 10)$.

12.3.4 Sky-location dependence

I have also compared synthetic ROCs for the weighted and unweighted statistics for a non-colocated network of H1 and L1 at the "worst-case" different-sensitivity sky locations discussed in Sec. 12.1.4. For $T_{\mathrm{obs}} = 12\,\mathrm{h}$, the differences are already negligible in pure Gaussian noise and small, at most a few percent, in the presence of lines in either detector. All differences are completely negligible for $T_{\mathrm{obs}} = 24\,\mathrm{h}$.

(a)

(b)

(c)

(d)
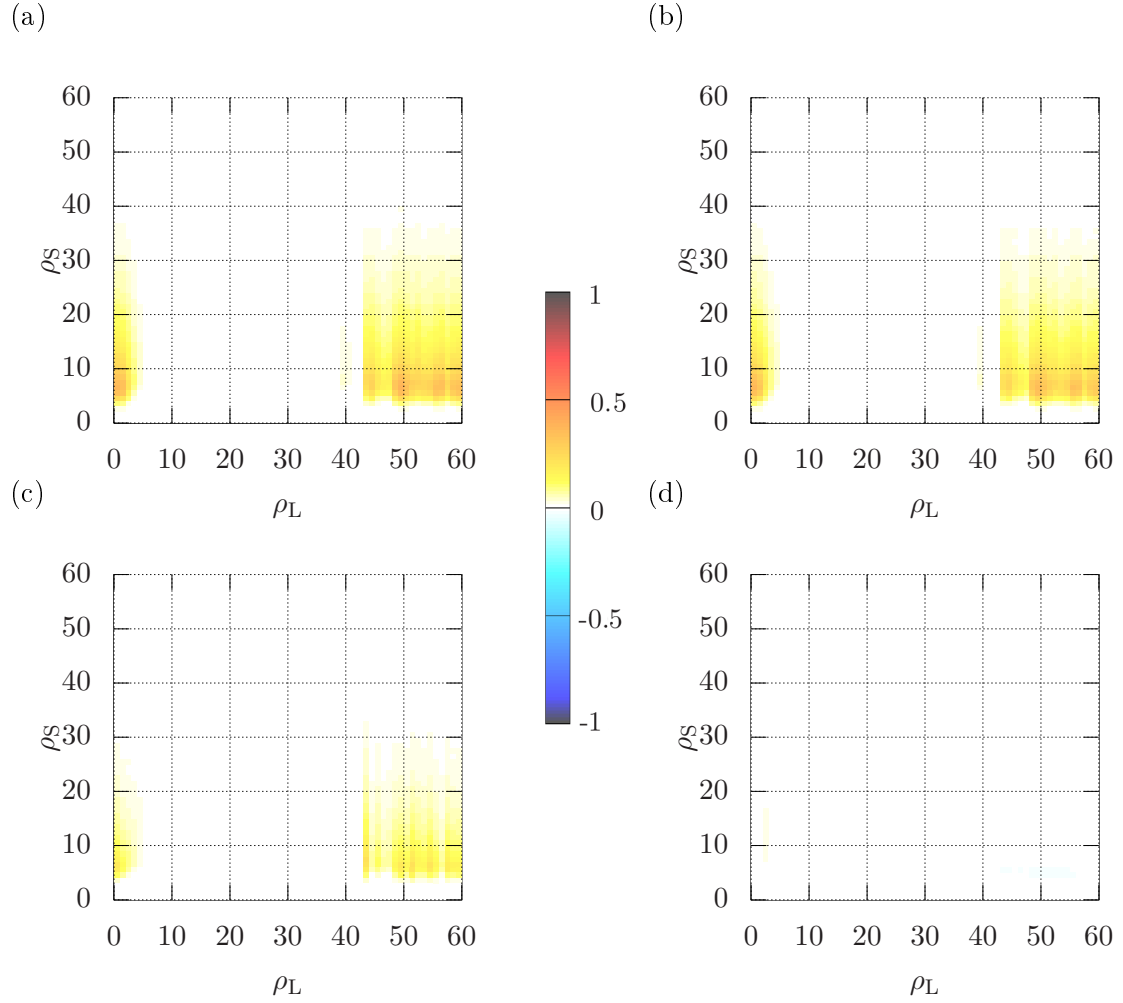
Figure 12.8: Detection probability differences between weighted and unweighted statistics, for an H1-H2 network with $\sqrt{S^{\mathrm{H2}}} = 10\sqrt{S^{\mathrm{H1}}}$, as a function of line SNR ρ_{L} and signal SNR ρ_{S}, at fixed $f_{\mathrm{L}}^{\mathrm{H1}} = 0.1$ and $p_{\mathrm{FA}} = 0.001$.
(a): $p_{\mathrm{det}}(O_{\mathrm{SL}\mathcal{M}}) - p_{\mathrm{det}}(O_{\mathrm{SL}})$,
(b): $p_{\mathrm{det}}(O_{\mathrm{SGL}\mathcal{M}}) - p_{\mathrm{det}}(O_{\mathrm{SGL}})$ at $\mathcal{F}_*^{(0)} = 0$,
(c): $p_{\mathrm{det}}(O_{\mathrm{SGL}\mathcal{M}}) - p_{\mathrm{det}}(O_{\mathrm{SGL}})$ at $\mathcal{F}_*^{(0)} = 4$,
(d): $p_{\mathrm{det}}(O_{\mathrm{SGL}\mathcal{M}}) - p_{\mathrm{det}}(O_{\mathrm{SGL}})$ at $\mathcal{F}_*^{(0)} = 10$.

12.4 Conclusions

The synthetic tests presented in this chapter lead to the following main conclusions about the safety of line-robust statistics for unequally sensitive detectors, and about the simple sensitivity-weighting attempt to improving it:

1. The sky-location-dependent differences in detector sensitivities, due to different antenna patterns, are generally too small to lead to any noticeable effects. Even for a search over a short observation time of 12 h and directed at a location with extreme differences in antenna patterns, the effect on detection probabilities is minimal. Hence, the line-robust detection statistics from Sec. 7 can be considered as just as safe for directed searches as for the all-sky searches tested before, provided the detectors have similar noise PSDs and amounts of data.

2. To notice any effects due to unequal sensitivities, these must be quite pronounced, for example a ratio in $\sqrt{S^X}$ of well over 2, which is larger than typical values encountered for the LIGO H1-L1 network.

3. Even for very unequal sensitivities (for example a factor 10 in $\sqrt{S^X}$), the line-robust statistic O_{SGL} of Eq. (7.68) with an $\mathcal{F}_*^{(0)}$-tuning as described in Sec. 8.2 is still *safe* in Gaussian noise – in the sense of not being worse than the $\mathcal{F}$-statistic – and improves over $\mathcal{F}$ in the presence of strong lines in only a less sensitive detector.

4. The line-veto statistic O_{SL} of Eq. (7.44), as well as O_{SGL} with lower values of $\mathcal{F}_*^{(0)}$, are *not safe* in these cases. Here, sensitivity-weighting can recover some losses. However, there would normally be no reason to use these statistics in place of the tuned O_{SGL}, for which sensitivity-weighting makes no significant difference in any of the cases considered here.

5. For very unequal sensitivities, lines in the most sensitive detector lead to partial losses and partial gains of the tuned O_{SGL} compared to the $\mathcal{F}$-statistic. The cases where O_{SGL} is unsafe (at high signal SNRs) are arguably of less practical relevance than those were it still yields an improvement (for weaker signals and very strong lines). Again, sensitivity-weighting makes no difference to the performance of the tuned O_{SGL}.

Thus, I find that that the sensitivity-weighting approach through the use of a modified amplitude prior, as described in Sec. 12.2, does not seem a promising direction in practice. The "unweighted" but tuned line-robust statistic, as described in KPPLS14 and discussed in the previous chapters, is generally found to be safe even for detectors with highly unequal sensitivities. The remaining weakness for particularly "line-like signals" might be a subject for further work, although the quantitative limits demonstrated here makes this seem less urgent for practical applications.

13 Unmodulated-sinusoid line model

The approach to increased line-robustness in CW searches that I have presented in Secs. 7–12 can in a sense be considered as a Bayesian generalisation of the $\mathcal{F}$-statistic consistency veto described in Sec. 6.5.3. I will now present a preliminary investigation of an alternative approach, which in turn could be considered as a Bayesian generalisation of the S-Veto introduced and studied by Abbott et al. (2008a), Pletsch (2008) and Abbott et al. (2009d) and discussed in Sec. 6.5.2.

The line-robust statistics which I have defined so far are based on a specific non-coincident line hypothesis $\mathcal{H}_{\mathrm{L}}$, defined in Eqs. (7.27) and (7.30). It describes a line with the same model function as a CW signal, but constrained to a single detector in a multi-detector search. While this hypothesis helps against typical non-coincident line disturbances, which are very detrimental for $\mathcal{F}$-statistic searches, this hypothesis also has a few disadvantages.

First, the approach cannot be usefully generalised to coincident lines, as then the only remaining difference between a real CW signal ($\mathcal{H}_{\mathrm{S}}$ in Eq. (7.7)) and a multi-detector version of Eq. (7.30) would be the consistency of amplitude parameters. This would yield only a weak distinction and hence would not produce a useful detection statistic.

Second, the line hypothesis $\mathcal{H}_{\mathrm{L}}$ is itself somewhat unphysical, as we know that one of the actual defining characteristics of lines is that they are *terrestrial* disturbances and that any correspondence with the frequency evolution of astrophysical signals can only be due to random chance.

Therefore, another simple, yet complementary, approach is to model lines as *unmodulated sinusoids*, i.e. as perfectly monochromatic signals. This is not an attempt at a full description of the complex phenomenology of lines in LIGO data, as discussed in Sec. 6. For many lines, though, it should be a better description than the signal-based line hypothesis $\mathcal{H}_{\mathrm{L}}$.

Here, I will present the first steps in an analytical treatment of a "sinusoid-robust statistic". These are, in fact, very similar to the standard Bayesian procedure for the detection of sinusoids in Gaussian noise, as presented by Bretthorst (1988). The novelty lies mainly in the explicit comparison between CW signal model and sinusoids. This approach also naturally leads to the issue of marginalising detection statistics over the phase-evolution parameter-space, which I briefly discuss.

13.1 Single-detector sinusoid hypothesis and probability

Even though this approach should allow for the inclusion of *coincident* lines, these should still have different amplitude and phase-evolution parameters across detectors. Thus, I will start the discussion with the case of a single detector, but for now omitting the index X on most quantities (except for any hypotheses).

A general stationary harmonic function with frequency f can be expressed by

$$u(t, \mathcal{B}, f) \equiv B_1 \sin(ft) + B_2 \cos(ft) \,, \tag{13.1}$$

where $\mathcal{B} \equiv \{B_1, B_2\}$ are the two *amplitude parameters* for such a sinusoid, similar to the four amplitude parameters $\mathcal{A}^\mu$ for a CW signal introduced in Eq. (5.25).

I define a single-detector *unmodulated-sinusoid hypothesis* as

$$\mathcal{H}_\mathrm{U}^X : x(t) = n(t) + u(t, \mathcal{B}, f) \quad \text{with prior} \quad P\left(\mathcal{B}, f \,|\, \mathcal{H}_\mathrm{U}^X\right) , \tag{13.2}$$

where $n(t)$ represents zero-mean Gaussian noise, as described in Sec. 5.1. I will discuss the amplitude prior in a later step, and for now I formally restrict the derivation to a fixed f by using a delta prior

$$P\left(\mathcal{B}, f' \,|\, \mathcal{H}_\mathrm{U}^X\right) = P\left(\mathcal{B} \,|\, \mathcal{H}_\mathrm{U}^X\right) \delta(f' - f) \,, \tag{13.3}$$

and will discuss the issue of wide parameter spaces towards the end of this section.

From $P\left(x \,|\, \mathcal{H}_\mathrm{G}^X\right)$, as in Eq. (7.2), the likelihood for this hypothesis at fixed $\mathcal{B}$ is

$$\begin{aligned} P\left(x \,|\, \mathcal{H}_\mathrm{U}^X, \mathcal{B}, f\right) &= \kappa \, e^{-\frac{1}{2}\langle x(t) - u(t, \mathcal{B}, f) | x(t) - u(t, \mathcal{B}, f) \rangle} \\ &= P\left(x \,|\, \mathcal{H}_\mathrm{G}^X\right) e^{B_1 \langle x | \sin(ft) \rangle + B_2 \langle x | \cos(ft) \rangle - \frac{1}{2} v(t, \mathcal{B}, f)} \,, \end{aligned} \tag{13.4}$$

with all data-independent terms in the exponent collected in

$$\begin{aligned} v(t, \mathcal{B}, f) \equiv (B_1)^2 \langle \sin(ft) | \sin(ft) \rangle + 2 B_1 B_2 \langle \sin(ft) | \cos(ft) \rangle \\ + (B_2)^2 \langle \cos(ft) | \cos(ft) \rangle \,. \end{aligned} \tag{13.5}$$

The scalar products between sine and cosine functions in $v(t, \mathcal{B}, f)$ can be evaluated in closed forms, using the single-detector version of the approximate narrow-band definition of the scalar product from Eq. (5.7). For simplicity, I assume a coherent analysis over a single stretch of data with length T; however, generalisation of these results to sums over SFTs is straightforward, using the scalar product from Eq. (5.27).

For now writing S for the single-detector noise PSD, the sine-sine term is

$$\langle \sin(ft) | \sin(ft) \rangle = \frac{2}{S} \int_0^T \sin^2(f\,t)\,\mathrm{d}t = \frac{1}{S}\left(T - \frac{\sin(2f\,T)}{2f}\right) \approx \frac{T}{S} \,, \tag{13.6a}$$

along with

$$\langle\cos(ft)\,|\,\cos(ft)\rangle = \frac{1}{S}\left(T + \frac{\sin(2fT)}{2f}\right) \approx \frac{T}{S} \tag{13.6b}$$

for the cosine-cosine term and, for the cross terms:

$$\langle\sin(ft)\,|\,\cos(ft)\rangle = \frac{1}{S}\frac{\sin^2(fT)}{f} \approx 0\,. \tag{13.6c}$$

CW searches with ground-based GW detectors are always in the limit of $fT \gg 1$, where the frequency-dependent terms become negligible, as well as the entire cross terms.

I will now introduce a notation that is more complex than really required for the problem at hand, but which is useful in showing parallels to the derivation of the $\mathcal{F}$-statistic. Defining, in analogy with Eq. (5.42), projections of the data onto the basis functions

$$x_{\mathrm{U}1}(f) \equiv \langle x(t)\,|\,\sin(ft)\rangle \quad \text{and} \quad x_{\mathrm{U}2}(f) \equiv \langle x(t)\,|\,\cos(ft)\rangle\,, \tag{13.7}$$

and using an indexing convention where α and β run over the values 1 and 2 only, I can write the likelihood from Eq. (13.4) more compactly as

$$P\left(x\,|\,\mathcal{H}_{\mathrm{U}}^X, \mathcal{B}, f\right) = P\left(x\,|\,\mathcal{H}_{\mathrm{G}}^X\right)\,\mathrm{e}^{B^\alpha x_{\mathrm{U}\alpha}(f) - \frac{1}{2}B^\alpha \gamma_{\alpha\beta}(f)B^\beta}\,, \tag{13.8}$$

where the matrix

$$\gamma_{\alpha\beta} \equiv \frac{1}{S}\begin{pmatrix} \langle\sin(ft)\,|\,\sin(ft)\rangle & \langle\cos(ft)\,|\,\cos(ft)\rangle \\ \langle\sin(ft)\,|\,\cos(ft)\rangle & \langle\cos(ft)\,|\,\sin(ft)\rangle \end{pmatrix} \approx \frac{T}{S}\cdot\mathbb{1} \tag{13.9}$$

is the unmodulated-sinusoid analogue of the CW antenna-pattern matrix from Eq. (5.36). Even for low frequencies, it has only two independent components, as $\gamma_{12} = \gamma_{21}$ and $\gamma_{22} = 2T - \gamma_{11}$. For $fT \gg 1$, the likelihood simplifies to

$$P\left(x\,|\,\mathcal{H}_{\mathrm{U}}^X, \mathcal{B}, f\right) \approx P\left(x\,|\,\mathcal{H}_{\mathrm{G}}^X\right)\,\mathrm{e}^{B^\alpha x_{\mathrm{U}\alpha}(f) - \frac{T}{2S}\left((B_1)^2 + (B_2)^2\right)}\,. \tag{13.10}$$

In analogy with the procedure in Sec. 7.1.2 for the signal-hypothesis likelihood, the next step is to marginalise over the amplitude parameters $\mathcal{B}$. For this, I use a simple prior with a fixed, detector-independent amplitude cut-off:

$$P\left(\{\mathcal{B}\}\,|\,\mathcal{H}_{\mathrm{U}}^X\right) = \begin{cases} \frac{1}{2\pi B_*^2} & \text{for} \quad (B_1)^2 + (B_2)^2 < 2B_*^2\,, \\ 0 & \text{otherwise}\,. \end{cases} \tag{13.11}$$

Here, B_* is an arbitrary cut-off, similar to c_* for the CW amplitude prior in Eq. (7.19). The prior normalisation has been fixed with a 2-D integral over transformed parameters $B \equiv \sqrt{(B_1)^2 + (B_2)^2}$ and $\theta \equiv \arctan\left(-B_2/B_1\right)$.

Using the 2-D version of the Gaussian integral from Eq. (7.21), this leads to a marginalised likelihood

$$P\left(x\,|\,\mathcal{H}_{\mathrm{U}}^X, f\right) = P\left(x\,|\,\mathcal{H}_{\mathrm{G}}^X\right) B_*^{-2}\,|\gamma|^{-1/2}\,\mathrm{e}^{\mathcal{U}(x,f)}\,, \tag{13.12}$$

where I have defined, in analogy with the $\mathcal{F}$-statistic from Eq. (5.46), an *unmodulated-sinusoid statistic*

$$2\mathcal{U}(x,f) \equiv x_{\mathrm{U}\alpha}(f)\,\gamma^{\alpha\beta}(f)\,x_{\mathrm{U}\beta}(f) \approx \frac{S}{T}\left((x_{\mathrm{U}1}(f))^2 + (x_{\mathrm{U}2}(f))^2\right)\,. \qquad (13.13)$$

Here, $\gamma^{\alpha\beta}(f) \approx \frac{S}{T}\cdot\mathbb{1}$ are the components of the inverse matrix to $\gamma_{\alpha\beta}(f)$.

The posterior probability for the unmodulated-sinusoid hypothesis in detector X is thus

$$P\left(\mathcal{H}_{\mathrm{U}}^X \,|\, x, f\right) = o_{\mathrm{UG}}^X\,P\left(x\,|\,\mathcal{H}_{\mathrm{G}}^X\right)B_*^{-2}\,|\gamma|^{-1/2}\,\mathrm{e}^{\mathcal{U}(x,f)} \qquad (13.14\mathrm{a})$$

$$\approx o_{\mathrm{UG}}^X\,P\left(\mathcal{H}_{\mathrm{G}}^X\,|\,x\right)\frac{S}{B_*^2 T}\,\mathrm{e}^{\frac{S}{2T}\left((x_{\mathrm{U}1}(f))^2 + (x_{\mathrm{U}2}(f))^2\right)}\,, \qquad (13.14\mathrm{b})$$

with prior odds between sinusoid and Gaussian-noise hypothesis of

$$o_{\mathrm{UG}}^X \equiv \frac{P\left(\mathcal{H}_{\mathrm{U}}^X\right)}{P\left(\mathcal{H}_{\mathrm{G}}^X\right)}\,. \qquad (13.15)$$

Inserting the projections from Eq. (13.7), I can rewrite the exponent in Eq. (13.14b) as

$$\frac{S}{2T}\left((x_{\mathrm{U}1})^2 + (x_{\mathrm{U}2})^2\right) = \frac{1}{2TS}\left(\left(\int_0^T x(t)\sin(ft)\,\mathrm{d}t\right)^2 + \left(\int_0^T x(t)\cos(ft)\,\mathrm{d}t\right)^2\right)\,, \qquad (13.16)$$

which is just the squared modulus of the Fourier-transformed data $\widetilde{x}$:

$$P\left(\mathcal{H}_{\mathrm{U}}^X\,|\,x,f\right) \approx o_{\mathrm{UG}}^X\,P\left(x\,|\,\mathcal{H}_{\mathrm{G}}^X\right)\frac{S}{B_*^2 T}\,\mathrm{e}^{\frac{1}{2TS}|\widetilde{x}(f)|^2}\,. \qquad (13.17)$$

Hence, in a practical implementation with finite sampling, $P\left(\mathcal{H}_{\mathrm{U}}^X\,|\,x,f\right)$ is related to the periodogram considered in Sec. 4.5 and can be computed by Fast Fourier Transforms (FFTs). In SFT-based CW searches, the "SFT power" from Eq. (8.2), without the running-median normalisation, could be used.

Due to the modulated nature of CW signals, even for a targeted search (with fixed phase-evolution parameters) lines in a certain range of detector-frame frequencies can affect the $\mathcal{F}$-statistic. Hence, it is useful to consider the frequency-marginalised sinusoid posterior over a band $f \in [f_{\min}, f_{\max}]$:

$$P\left(\mathcal{H}_{\mathrm{U}}^X\,|\,x\right) = \int_{f_{\min}}^{f_{\max}} P\left(\mathcal{H}_{\mathrm{U}}^X\,|\,x,f\right)P\left(f\,|\,\mathcal{H}_{\mathrm{U}}^X\right)\,\mathrm{d}f\,. \qquad (13.18)$$

One could choose a uniform prior $P\left(f\,|\,\mathcal{H}_{\mathrm{U}}^X\right)$, or base it on detector-characterisation work as described in Sec. 6.3.

13.2 Multi-detector generalisation

As mentioned before, the unmodulated-sinusoid approach should allow for coincident lines in multiple detectors. Thus, the full multi-detector sinusoid hypothesis $\mathcal{H}_\mathrm{U}$ has to include all possible combinations of $\mathcal{H}_\mathrm{U}^X$ and $\mathcal{H}_\mathrm{G}^X$:

$$
\begin{aligned}
\mathcal{H}_\mathrm{U} \equiv &\left(\mathcal{H}_\mathrm{U}^1 \text{ and } \mathcal{H}_\mathrm{G}^2 \text{ and } \mathcal{H}_\mathrm{G}^3 \ \ldots\right) \text{ or} \\
&\left(\mathcal{H}_\mathrm{G}^1 \text{ and } \mathcal{H}_\mathrm{U}^2 \text{ and } \mathcal{H}_\mathrm{G}^3 \ \ldots\right) \text{ or} \\
&\left(\mathcal{H}_\mathrm{U}^1 \text{ and } \mathcal{H}_\mathrm{U}^2 \text{ and } \mathcal{H}_\mathrm{G}^3 \ \ldots\right) \text{ or } \ldots,
\end{aligned}
\tag{13.19}
$$

or, equivalently:

$$
\mathcal{H}_\mathrm{U} = \left(\mathcal{H}_\mathrm{U}^1 \text{ or } \mathcal{H}_\mathrm{G}^1\right) \text{ and } \left(\mathcal{H}_\mathrm{U}^2 \text{ or } \mathcal{H}_\mathrm{G}^2\right) \text{ or } \ \ldots
\tag{13.20}
$$

This is in contrast with Eq. (7.30) for the non-coincident line hypothesis $\mathcal{H}_\mathrm{L}$. Interestingly, $\mathcal{H}_\mathrm{U}$ manifestly includes the pure Gaussian noise hypothesis as a special case:

$$
\mathcal{H}_\mathrm{G} = \mathcal{H}_\mathrm{G}^1 \text{ and } \mathcal{H}_\mathrm{G}^2 \text{ and } \ \ldots
\tag{13.21}
$$

To obtain the multi-detector posterior probability, I assume independent Gaussian-noise distributions and line-amplitude priors between detectors, and I can neglect the null-set overlaps between $\mathcal{H}_\mathrm{U}^X$ and $\mathcal{H}_\mathrm{G}^X$. Lines in different detectors may have different frequencies f^X. Thus, reintroducing X-indices in Eqs. (13.14a) and (13.17), the posterior probability for a fixed set of these frequencies is

$$
\begin{aligned}
P\left(\mathcal{H}_\mathrm{U} \,|\, \boldsymbol{x}, \{f^X\}\right) &= \prod_{X=1}^{N_\mathrm{det}} \left(P\left(\mathcal{H}_\mathrm{G}^X \,|\, x^X\right) + P\left(\mathcal{H}_\mathrm{U}^X \,|\, x^X, f^X\right)\right) \\
&= P\left(\mathcal{H}_\mathrm{G} \,|\, \boldsymbol{x}\right) \prod_{X=1}^{N_\mathrm{det}} \left(1 + o_\mathrm{UG}^X B_*^{-2} \left|\gamma^X\right|^{-1/2} \mathrm{e}^{\mathcal{U}^X(x^X, f^X)}\right) \\
&\approx P\left(\mathcal{H}_\mathrm{G} \,|\, \boldsymbol{x}\right) \prod_{X=1}^{N_\mathrm{det}} \left(1 + o_\mathrm{UG}^X \frac{S^X}{B_*^2 T} \mathrm{e}^{\frac{1}{2TS^X} \left|\widetilde{x}^X(f^X)\right|^2}\right),
\end{aligned}
\tag{13.22}
$$

and the general frequency-marginalised multi-detector posterior is

$$
P\left(\mathcal{H}_\mathrm{U} \,|\, \boldsymbol{x}\right) \equiv \int\limits_{f_\mathrm{min}}^{f_\mathrm{max}} P\left(\mathcal{H}_\mathrm{U} \,|\, \boldsymbol{x}, \{f^X\}\right) P\left(\{f^X\} \,|\, \mathcal{H}_\mathrm{U}\right) \mathrm{d}^{N_\mathrm{det}} f^X \,.
\tag{13.23}
$$

In the case that there is no prior information about correlations of line-frequencies between detectors, $P\left(\{f^X\}\right) = \prod_{X=1}^{N_\mathrm{det}} P\left(f^X\right)$, the integrals can be pulled through:

$$
P\left(\mathcal{H}_\mathrm{U} \,|\, \boldsymbol{x}\right) \approx P\left(\mathcal{H}_\mathrm{G} \,|\, \boldsymbol{x}\right) \prod_{X=1}^{N_\mathrm{det}} \left(1 + o_\mathrm{UG}^X \frac{S^X}{B_*^2 T} I_\mathrm{U}^X(x^X)\right),
\tag{13.24}
$$

where I have assumed all $P\left(f^X\,|\,\mathcal{H}_{\mathrm{U}}^X\right)$ to be normalised to 1 and, for ease of notation in the following section, I have defined

$$I_{\mathrm{U}}^X(x^X) \equiv \int\limits_{f_{\min}}^{f_{\max}} \mathrm{e}^{\frac{1}{2TS^X}\left|\widetilde{x}^X(f^X)\right|^2} P\left(f^X\,|\,\mathcal{H}_{\mathrm{U}}^X\right)\,\mathrm{d}f^X\;. \tag{13.25}$$

13.3 Sinusoid-robust statistic

A sinusoid-robust statistic can be constructed by comparing the CW-signal hypothesis $\mathcal{H}_{\mathrm{S}}$ from Eq. (7.7) with $\mathcal{H}_{\mathrm{U}}$. $\mathcal{H}_{\mathrm{S}}$ depends on the phase-evolution parameters λ, but for now I focus on a targeted search where these are fixed. Even in this case, an odds ratio should be computed using the marginalised sinusoid posterior from Eq. (13.23), as a signal template can also be triggered by nearby lines. Using the CW-signal posterior from Eq. (7.25), this signal-versus-sinusoid odds ratio is given by

$$O_{\mathrm{SU}}(\boldsymbol{x},\lambda) \equiv \frac{P\left(\mathcal{H}_{\mathrm{S}}\,|\,\boldsymbol{x},\lambda\right)}{P\left(\mathcal{H}_{\mathrm{U}}\,|\,\boldsymbol{x}\right)} \approx \frac{o_{\mathrm{SG}}\,c_*^{-1}\,\mathrm{e}^{\mathcal{F}(\boldsymbol{x},\lambda)}}{\int\limits_{f_{\min}}^{f_{\max}} P\left(\mathcal{H}_{\mathrm{U}}\,|\,\boldsymbol{x},\{f^X\}\right) P\left(\{f^X\}\,|\,\mathcal{H}_{\mathrm{U}}\right)\,\mathrm{d}^{N_{\mathrm{det}}} f^X}\;, \tag{13.26}$$

which for independent f^X-priors becomes

$$O_{\mathrm{SU}}(\boldsymbol{x},\lambda) \approx \frac{o_{\mathrm{SG}}\,c_*^{-1}\,\mathrm{e}^{\mathcal{F}(\boldsymbol{x},\lambda)}}{\prod\limits_{X=1}^{N_{\mathrm{det}}} \left(1 + o_{\mathrm{UG}}^X \frac{S^X}{B_*^2 T}\,I_{\mathrm{U}}^X(x^X)\right)}\;. \tag{13.27}$$

As the multi-detector $\mathcal{H}_{\mathrm{U}}$ in Eq. (13.19) already includes the pure Gaussian case, $\mathcal{H}_{\mathrm{G}}$, this is already the analogue of the full line-robust odds ratio O_{SGL} from Eq. (7.59). A statistic comparable to the line-veto statistic O_{SL} from Eq. (7.44) would require a modification of Eq. (13.19) to explicitly exclude the purely Gaussian case.

To bring this odds ratio into the form of $O_{\mathrm{SU}}(\boldsymbol{x},\lambda) = o_{\mathrm{SU}} B_{\mathrm{SU}}(\boldsymbol{x},\lambda)$, let me first introduce some additional prior odds, namely

$$o_{\mathrm{SU}} \equiv \frac{P\left(\mathcal{H}_{\mathrm{S}}\right)}{P\left(\mathcal{H}_{\mathrm{U}}\right)} = \frac{o_{\mathrm{SG}}}{o_{\mathrm{UG}}} \tag{13.28}$$

and the multi-detector version of Eq. (13.15),

$$o_{\mathrm{UG}} \equiv \frac{P\left(\mathcal{H}_{\mathrm{U}}\right)}{P\left(\mathcal{H}_{\mathrm{G}}\right)} = \frac{\prod\limits_{X=1}^{N_{\mathrm{det}}} \left(P\left(\mathcal{H}_{\mathrm{G}}^X\right) + P\left(\mathcal{H}_{\mathrm{U}}^X\right)\right)}{\prod\limits_{X=1}^{N_{\mathrm{det}}} P\left(\mathcal{H}_{\mathrm{G}}^X\right)} = \prod\limits_{X=1}^{N_{\mathrm{det}}} \left(1 + o_{\mathrm{UG}}^X\right)\;, \tag{13.29}$$

178

as well as single-detector sinusoid probabilities, in analogy to the p_{L}^X from Eq. (7.64):

$$p_{\text{U}}^X \equiv \frac{o_{\text{UG}}^X}{1 + o_{\text{UG}}^X} \,. \tag{13.30}$$

Then, I can rewrite Eq. (13.27) as

$$O_{\text{SU}}(\boldsymbol{x}, \lambda) = o_{\text{SU}} \frac{c_*^{-1} \, e^{\mathcal{F}(\boldsymbol{x}, \lambda)}}{\prod\limits_{X=1}^{N_{\text{det}}} \left(\frac{1}{1 + o_{\text{UG}}^X} + p_{\text{U}}^X \frac{S^X}{B_*^2 T} I_{\text{U}}^X(x^X) \right)} \,, \tag{13.31}$$

so that the Bayes factor is given by

$$B_{\text{SU}}(\boldsymbol{x}, \lambda) = \frac{B_*^{2 N_{\text{det}}}}{c_*} \frac{e^{\mathcal{F}(\boldsymbol{x}, \lambda)}}{\prod\limits_{X=1}^{N_{\text{det}}} \left(\frac{B_*^2}{1 + o_{\text{UG}}^X} + p_{\text{U}}^X \frac{S^X}{T} I_{\text{U}}^X(x^X) \right)} \,. \tag{13.32}$$

Comparing to Eq. (7.68) for the line-robust statistic O_{SGL}, the constant term B_*^2 plays a role similar to the transition-scale parameter $\mathcal{F}_*^{(0)}$ in O_{SGL}. The pre-factor ratio of the two different cut-offs does not influence the performance of B_{SU} as a detection statistic. In the absence of physical knowledge about the relative strengths of signal and line amplitudes, it could be chosen purely on grounds of numerical convenience.

13.4 Outlook: parameter-space marginalisation

The signal-versus-sinusoid Bayes factor from Eq. (13.32) could be used directly for targeted CW searches in line-affected data. For searches over unknown frequency-evolution parameters λ, it would also be possible to use it as a detection statistic, with a threshold purely determined from numerical simulations. However, to directly provide the Bayesian answer to the general question whether a CW signal or stationary lines are a better explanation for the data, another ingredient would be needed: marginalisation over the phase-evolution parameter space.

There are no known analytical solutions to the required integrals over the $\mathcal{F}$-statistic, but they can be approximated by a sum over $B_{\text{SU}}(\boldsymbol{x}, \lambda)$ in all points of a template bank. One could marginalise over the whole parameter space of a search, or over local regions only. A promising approach might be to split the parameter space into regions according to the global correlations (see Sec. 5.10 and Prix & Itoh 2005, Pletsch 2008, Pletsch & Allen 2009), and to marginalise $B_{\text{SU}}(\boldsymbol{x}, \lambda)$ over each of these. Such an approach would give the most natural generalisation of the S-veto method. The question of priors on λ would have to be addressed, however.

14 Concept for an octahedral gravitational-wave detector in space

14.1 Introduction

This chapter is, in essence, a reprint of a research paper titled "Octahedron configuration for a displacement noise-canceling gravitational wave detector in space" by Wang, Keitel, Babak et al. (2013), published in Phys. Rev. D 88.10, 104021. I will refer to this paper as OGO13 from now on.

Here, I reproduce the paper essentially without modifications in content. The only changes are the addition of these introductory statements, as well as the omission of the original Appendix A, which contains mathematical details to which I have not contributed myself.

I will first, in Sec. 14.1.1, give a brief description of the paper, which is a modified version of the original abstract. Next, in Sec. 14.1.2, I give a detailed description of the contributions of the various authors, including my own. The original introduction to the paper follows in Sec. 14.1.3. Note that the references for this paper can be found, along with those for the rest of this thesis, in the common bibliography in Appendix B.

14.1.1 Synopsis

In OGO13 we have presented a study of a three-dimensional octahedron constellation for a space-based gravitational wave (GW) detector. This concept was named the *Octahedral Gravitational Observatory* (OGO). We have shown that it is possible, by combining data from the links between six spacecraft, to remove laser-frequency noise and acceleration disturbances from the GW signal without needing LISA-like drag-free control, thereby simplifying the payloads and placing less stringent demands on the thrusters. We have generalised LISA's time-delay interferometry (TDI) to displacement-noise-free interferometry (DFI) by deriving a set of generators for those combinations of the data streams that cancel laser and acceleration noise.

However, we found that the three-dimensional configuration makes orbit selection complicated. So far, only a halo orbit near the Lagrangian point L1 has been found to be stable enough, and this allows only short arms up to 1400 km. We have derived the

sensitivity curve of OGO with this arm length, resulting in a peak sensitivity of about $2 \cdot 10^{-23} \, \mathrm{Hz}^{-1/2}$ near $100 \, \mathrm{Hz}$.

Using this result, we have compared this short-arm version of OGO to the present generation of ground-based detectors, and to some future detectors. We have also investigated the scientific potential of such a detector, which include observing GWs from compact binary coalescences, the stochastic background and pulsars, as well as the possibility to test alternative theories of gravity. The result of this analysis showed a mediocre sensitivity level for this short-arm-length detector, somewhere between those of initial and advanced ground-based detectors.

Thus, the study suggests that actually building a space-based detector of this specific configuration does not seem efficient. However, we have also demonstrated that if alternative orbits allowing for longer detector arms can be found, a detector with much improved science potential could be constructed using the octahedron configuration and DFI solutions demonstrated in OGO13. Also, since the sensitivity of a DFI detector is limited mainly by shot noise, we have included a discussion on how the overall sensitivity could be improved by using advanced technologies that reduce this particular noise source.

14.1.2 Author contributions

The full list of authors of this paper is, in the original order: Yan Wang, David Keitel, Stanislav Babak, Antoine Petiteau, Markus Otto, Simon Barke, Fumiko Kawazoe, Alexander Khalaidovski, Vitali Müller, Daniel Schütze, Holger Wittel, Karsten Danzmann and Bernard F. Schutz.

As second author of this paper, my main contribution was the estimation of scientific perspectives for several source types, Secs. 14.5.1, 14.5.4 and 14.5.5. I have made no direct contributions to the initial derivation of DFI measurements, as presented in Secs. 14.3 and 14.4.1, as well as in more detail in Appendix A of OGO13, which is not reproduced here; this was solely the work of Y. Wang, S. Babak and A. Petiteau. Neither have I contributed to the selection of candidate orbits, presented in Sec. 14.2, which was mostly the work of V. Müller. Secs. 14.5.2 and 14.5.3 were contributed mostly by Y. Wang and S. Babak. For the remaining sections and the overall structure of the paper, I had a central part in conception and writing.

Furthermore, together with Y. Wang and M. Otto, I had editorial responsibility for the final written version of the whole paper, as well as for a significant rewriting of Sec. 14.4 and other parts of the paper after some important referee comments.

14.1.3 Introduction from the original paper

The search for gravitational waves (GWs) has been carried out for more than a decade by ground-based detectors. Currently, the LIGO and Virgo detectors are being upgraded using advanced technologies (Acernese et al. 2009, Harry 2010). The ground-based detectors are sensitive in quite a broad band from about 10 Hz to a few kHz. In this band possible GW sources include stellar-mass compact coalescing binaries (Abadie et al. 2010c), asymmetric core collapse of evolved heavy stars (Fryer & New 2011), neutron stars with a nonzero ellipticity (Owen, Reitze & Whitcomb 2009) and, probably, a stochastic GW background from the early Universe or from a network of cosmic strings (Allen & Romano 1999, Maggiore 2000a).

In addition, the launch of a space-based GW observatory is expected in the next decade, such as the classic LISA mission concept (Danzmann et al. 2003, or its recent modification known as evolved LISA (eLISA) / NGO, see Amaro-Seoane et al. 2013), and DECIGO (Ando et al. 2010a). LISA has become a mission concept for any heliocentric drag-free configuration that uses laser interferometry for detecting GWs. The most likely first GW observatory in space will be the eLISA mission, which has an arm length of 10^9 m and two arms, with one "mother" and two "daughter" spacecraft exchanging laser light in a V-shaped configuration to sense the variation of the metric due to passing GWs.

The eLISA mission aims at mHz frequencies, targeting other sources than ground-based detectors, most importantly supermassive black hole binaries. In a more ambitious concept, DECIGO is supposed to consist of a set of four smaller triangles (12 spacecraft in total) in a common orbit, leading to a very good sensitivity in the intermediate frequency region between LISA and advanced LIGO (aLIGO).

Here we want to present a concept for another space-based project with quite a different configuration from what has been considered before. The concept was inspired by a three-dimensional interferometer configuration in the form of an octahedron, first suggested by Chen et al. (2006) for a ground-based detector, based on two Mach-Zehnder interferometers.

The main advantage of this setup is the cancellation of timing, laser frequency and displacement noise by combining multiple measurement channels. We have transformed this detector into a space-borne observatory by placing one LISA-like spacecraft (but with four telescopes and a single test mass) in each of the six corners of the octahedron, as shown in Fig. 14.1. Therefore, we call this project the *Octahedral Gravitational Observatory* (OGO).

Before going into the mathematical details of displacement-noise free interferometry (DFI), we first consider possible orbits for a three-dimensional octahedron constellation in Sec. 14.2. As we will find later on, the best sensitivities of an OGO-like detector are expected at very long arm lengths. However, the most realistic orbits we found that can sustain the three-dimensional configuration with stable distances between adjacent
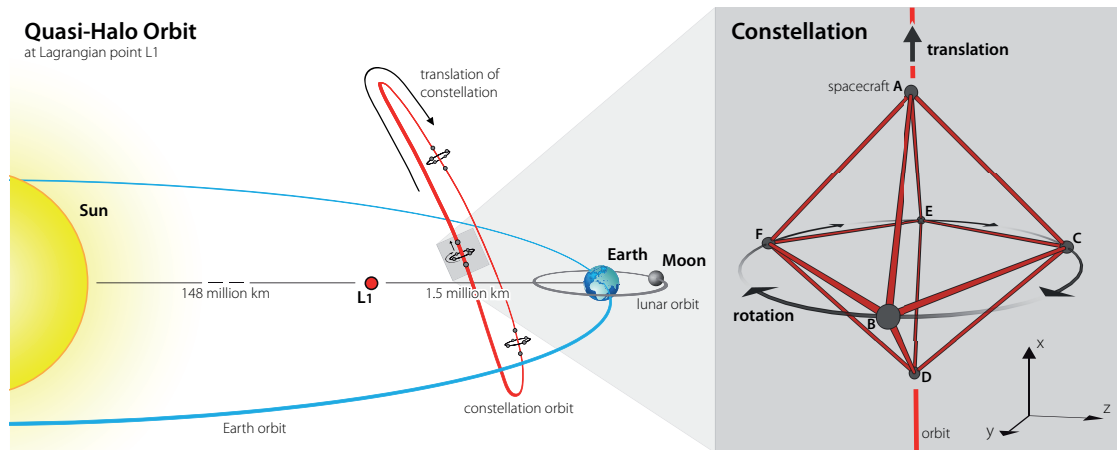
Figure 14.1: Left: Graphical representation of the proposed halo orbit around L1. Right: OGO's spacecraft constellation along the halo orbit, with a radius of $1000\,\mathrm{km}$ and spacecraft separation of $L = \sqrt{2}\,r \approx 1400\,\mathrm{km}$.

spacecraft for a sufficiently long time are so-called "halo" and "quasihalo" orbits around the Lagrange point L1 in the Sun-Earth system.

These orbits are rather close to Earth, making a mission potentially cheaper in terms of fuel and communication, and corrections to maintain the formation seem to be reasonably low. On the other hand, a constellation radius of only $1000\,\mathrm{km}$ can be supported, corresponding to a spacecraft-to-spacecraft arm length of approximately $1400\,\mathrm{km}$.

We will discuss this as the standard configuration proposal for OGO in the following, but ultimately we still aim at using much longer arm lengths. As a candidate, we will also discuss OGO orbits with $2 \times 10^9\,\mathrm{m}$ arm lengths in Sec. 14.2. However, such orbits might have significantly varying separations and would require further study of the DFI technique in such circumstances.

The octahedron configuration gives us 24 laser links, each corresponding to a science measurement channel of the distance (photon flight-time) variation between the test masses on adjacent spacecraft. The main idea is to use a sophisticated algorithm called *displacement-noise free interferometry* (DFI, Kawamura & Chen 2004, Chen & Kawamura 2006, Chen et al. 2006), which proceeds beyond conventional Time-Delay Interferometry techniques (TDI, Tinto & Dhurandhar 2005, Otto, Heinzel & Danzmann 2012), and in the right circumstances can improve upon them.

It can cancel both timing noise and acceleration noise when there are more measurements than noise sources. In three dimensions, the minimum number of spacecraft for DFI is 6, which we therefore use for OGO: this gives $6 - 1$ relative timing (clock) noise sources and $3 \times 6 = 18$ components of the acceleration noise, so that $24 > 5 + 18$ and the DFI requirement is fulfilled. On the one hand, this required number of links increases the complexity of the detector. On the other hand, it provides some redundancy in the

number of shot-noise-only configurations, which could be very useful if one or several links between spacecraft are interrupted.

After applying DFI, we assume that the dominant remaining noise will be shot noise. For the case of an equal-arm-length three-dimensional constellation, we analytically find a set of generators for the measurement channel combinations that cancel simultaneously all timing and acceleration noise. We assume that all deviations from the equal-arm configuration are small and can be absorbed into a low-frequency part of the acceleration noise. We describe the procedure of building DFI combinations in Sec. 14.3. This will also allow us to quantify the redundancy inherent in the six-spacecraft configuration. The technical details of the derivation can be found in Appendix A of OGO13.

In Sec. 14.4, we compute the response functions of the octahedron DFI configuration and derive the sensitivity curve of the detector. We assume the conservative $1400 \, \text{km}$ arm length, a laser power of $10 \, \text{W}$ and a telescope diameter of $1 \, \text{m}$, while identical strain sensitivity is achievable for smaller telescopes and higher power.

Unfortunately, those combinations that cancel acceleration and timing noise also suppress the GW signal at low frequencies. This effect shows up as a rather steep slope $\sim f^2$ in the response function.

We present sensitivity curves for single DFI combinations and find that there are in principle 12 such noise-uncorrelated combinations (corresponding to the number of independent links) with similar sensitivity, leading to an improved network sensitivity of the full OGO detector. We find that the best sensitivity is achieved around $78 \, \text{Hz}$, in a range similar to that of ground-based detectors. The network sensitivity of OGO is better than that of initial LIGO at this frequency, but becomes better than that of aLIGO only below $10 \, \text{Hz}$. The details of these calculations are presented in Sec. 14.4.2.

At this point, in Sec. 14.4.3, we briefly revisit the alternative orbits with a longer arm length, which would result in a sensitivity closer to the frequency band of interest for LISA and DECIGO. For this variant of OGO, we assume LISA-like noise contributions (but without spacecraft jitter) and compare the sensitivity of an octahedron detector using DFI with one using TDI, thus directly comparing the effects of these measurement techniques.

Actually, we find that the $2 \times 10^9 \, \text{m}$ arm length is close to the point of equal sensitivity of DFI and TDI detectors in the limit of vanishing jitter. This implies that DFI would be preferred for even longer arm lengths, but might already become competitive at moderate arm lengths if part of the jitter couples into the displacement noise in such a way that it can also be canceled.

A major advantage of the OGO concept lies in its rather moderate requirement on acceleration noise, as detailed in Sec. 14.4.4. For other detectors, this limits the overall performance, but in this concept it gets canceled out by the DFI combinations. Assuming some improvements in subdominant noise sources, our final sensitivity thus depends only on the shot-noise level in each link.

Hence, we can improve the detector performance over all frequencies by reducing solely the shot noise. This could be achieved, for example, by increasing the power of each laser, by introducing cavities (similar to DECIGO), or with nonclassical (squeezed) states of light. We briefly discuss these possibilities in Sec. 14.4.5.

In Sec. 14.5, we discuss the scientific potentials OGO would have even using the conservative short-arm-length orbits. First, as a main target, the detection rates for inspiraling binaries are higher than for initial LIGO, but fall short of aLIGO expectations. However, joint detections with OGO and aLIGO could yield some events with greatly improved angular resolution. Second, due to the large number of measurement channels, OGO is good for probing the stochastic background. Furthermore, the three-dimensional configuration allows us to test alternative theories of gravity by searching for additional GW polarization modes. In addition, we briefly consider other source types such as pulsars, intermediate mass ($10^2 < M/M_\odot < 10^4$) black hole (IMBH) binaries and supernovae.

Finally, in Sec. 14.6, we summarize the description and abilities of the Octahedral Gravitational Observatory and mention additional hypothetical improvements. In this article, we use geometric units, $c = G = 1$, unless stated otherwise.

14.2 Orbits

The realization of an octahedral constellation of spacecraft depends on the existence of suitable orbits. Driving factors, apart from separation stability, are assumed to be (i) fuel costs in terms of velocity Δv necessary to deploy and maintain the constellation of six spacecraft, and (ii) a short constellation-to-Earth distance, required for a communication link with sufficient bandwidth to send data back to Earth. As described in the introduction, OGO features a three-dimensional satellite constellation. Therefore, using heliocentric orbits with a semimajor axis $a = 1\,\mathrm{AU}$ similar to LISA would cause a significant drift of radially separated spacecraft and is in our opinion not feasible.

However, in the last decades orbits in the nonlinear regime of Sun/Earth-Moon libration points L1 and L2 have been exploited, which can be reached relatively cheaply in terms of fuel (Gomez et al. 1993). A circular constellation can be deployed on a torus around a halo L1 orbit. The radius is limited by the amount of thrust needed for keeping the orbit stable. A realistic Δv for orbit maintenance allows a nominal constellation radius of $r = 1000\,\mathrm{km}$ (Howell & Barden 1999). We assume the spacecraft B, C, E and F in Fig. 14.1 to be placed on such a torus, whereby the out-of-plane spacecraft A and D will head and trail on the inner halo. The octahedron formation then has a base length $L = \sqrt{2}\,r \approx 1400\,\mathrm{km}$. The halo and quasihalo orbits have an orbital period of roughly 180 days and the whole constellation rotates around the A-D line.

We already note at this point that a longer baseline would significantly improve the detector strain sensitivity. Therefore, we also propose an alternative configuration with an approximate average side length of $2 \times 10^9\,\mathrm{m}$, where spacecraft A and D are placed on a

small halo or Lissajous orbit around L1 and L2, respectively. The remaining spacecraft are arranged evenly on a (very) large halo orbit around either L1 or L2. However, simulations using natural reference trajectories showed that this formation is slightly asymmetric and that the variations in the arm lengths (and therefore in the angles between the links) are quite large. Nevertheless, we will revisit this alternative in Sec. 14.4.3 and do a rough estimation of its sensitivity. To warrant a full scientific study of such a long-arm-length detector would first require a more detailed study of these orbits.

Hence, we assume the 1400 km constellation to be a more realistic baseline, especially since the similarity of the spacecraft orbits is advantageous for the formation deployment, because large (and expensive) propulsion modules for each satellite are not required as proposed in the LISA/NGO mission (Danzmann et al. 2011, Jennrich et al. 2012). The 2×10^9 m formation will be stressed only to show the improvement of the detector sensitivity with longer arms.

Formation flight in the vicinity of Lagrange points L1 and L2 is still an ongoing research topic (Folta 2004). Detailed (numerical) simulations have to be performed to validate these orbit options and to figure out appropriate orbit and formation control strategies. In particular the suppression of constellation deformations using non-natural orbits with correction maneuvers and required Δv and fuel consumption needs to be investigated. Remaining deformations and resizing of the constellation will likely require a beam or telescope steering mechanism on the spacecraft.

In addition, the formation will have a varying Sun-incidence angle, leading to further issues for power supply, thermal shielding and blinding of interferometer arms. These points need to be targeted at a later stage of the OGO concept development as well as the effect of unequal arms on the DFI scheme.

14.3 Measurements and noise-canceling combinations

In this section we will show how to combine the available measurement channels of the OGO detector to cancel laser and acceleration noise.

Each spacecraft of OGO is located at a corner of the octahedron, as shown in Fig. 14.1, and it exchanges laser light with four adjacent spacecraft. We consider interference between the beam emitted by spacecraft I and received by spacecraft J with the local beam in J, where $I, J = \{A, B, C, D, E, F\}$ refer to the labels in Fig. 14.1. For the sake of simplicity, we assume a rigid and nonrotating constellation. In other words, all arm lengths in terms of light travel time are equal, constant in time and independent of the direction in which the light is exchanged between two spacecraft. This is analogous to the first generation TDI assumptions (Tinto & Dhurandhar 2005). If the expected deviations from the equal arm configuration are small, then they can be absorbed into the low-frequency part of the acceleration noise. This imposes some restrictions on the orbits and on the orbit correction maneuvers. We also want to note that the overall breathing

of the constellation (scaling of the arm length) is not important if the breathing time scale is significantly larger than the time required for the DFI formation, which is usually true. All calculations below are valid if we take the arm length at the instance of DFI formation, which is the value that affects the sensitivity of the detector.

The measurement of the fractional frequency change for each link is then given by

$$s_{IJ}^{\text{tot}} = h_{IJ} + b_{IJ} + \mathcal{D}p_I - p_J + \mathcal{D}\left(\vec{a}_I \cdot \hat{n}_{IJ}\right) - \left(\vec{a}_J \cdot \hat{n}_{IJ}\right) , \qquad (14.1)$$

where we have neglected the factors to convert displacement noise to optical frequency shifts. Here, we have the following:

 (i) h_{IJ} is the influence of gravitational waves on the link $I \to J$,

 (ii) b_{IJ} is the shot noise (and other similar noise sources at the photo detector and phase meter of spacecraft J) along the link $I \to J$.

(iii) p_I is the laser noise of spacecraft I.

(iv) $\vec{a}_I$ is the acceleration noise of spacecraft I.

 (v) $\hat{n}_{IJ} = (\vec{x}_J - \vec{x}_I)/L$ is the unit vector along the arm $I \to J$ (with length L). Hence, the scalar product $\vec{a}_I \cdot \hat{n}_{IJ}$ is the acceleration noise of spacecraft I projected onto the arm characterized by the unit vector $\hat{n}_{IJ}$.

This is similar to TDI considerations, but in addition to canceling the laser noise p_I, we also want to eliminate the influence of the acceleration noise, that is all terms containing a_I. Following Tinto & Dhurandhar (2005), we have introduced a delay operator $\mathcal{D}$, which acts as

$$\mathcal{D}y(t) = y(t - L) . \qquad (14.2)$$

Note that we use a coordinate frame associated with the center of the octahedron, as depicted in Fig. 14.1.

The basic idea is to find combinations of the individual measurements (Eq. (14.1)) which are free of acceleration noise $\vec{a}_I$ and laser noise p_I. In other words, we want to find solutions to the following equation:

$$\sum_{\text{all } IJ \text{ links}} q_{IJ} \, s_{IJ} = 0 . \qquad (14.3)$$

In Eq. (14.3), q_{IJ} denotes an unknown function of delays $\mathcal{D}$ and s_{IJ} contains only the noise we want to cancel:

$$\begin{aligned} s_{IJ} &\equiv s_{IJ}^{\text{tot}}(b_{IJ} = h_{IJ} = 0) \\ &= \mathcal{D}p_I - p_J + \mathcal{D}\left(\vec{a}_I \cdot \hat{n}_{IJ}\right) - \left(\vec{a}_J \cdot \hat{n}_{IJ}\right) . \end{aligned} \qquad (14.4)$$

If a given q_{IJ} is a solution, then $f(\mathcal{D})q_{IJ}$ is also a solution, where $f(\mathcal{D})$ is a polynomial function (of arbitrary order) of delays. The general method for finding generators of the

solutions for this equation is described in Tinto & Dhurandhar (2005) and we will follow it closely.

Before we proceed to a general solution for Eq. (14.3), we can check that the solution corresponding to Mach-Zehnder interferometers suggested by Chen et al. (2006) also satisfies Eq. (14.3):

$$
\begin{aligned}
Y_1 = {}&[\,(s_{CD} + \mathcal{D}s_{AC}) - (s_{CA} + \mathcal{D}s_{DC}) + (s_{FD} + \mathcal{D}s_{AF}) \\
&- (s_{FA} + \mathcal{D}s_{DF})\,] - [\,(s_{BD} + \mathcal{D}s_{AB}) - (s_{BA} + \mathcal{D}s_{DB}) \\
&+ (s_{ED} + \mathcal{D}s_{AE}) - (s_{EA} + \mathcal{D}s_{DE})\,].
\end{aligned}
\tag{14.5a}
$$

Using the symmetries of an octahedron, we can write down two other solutions:

$$
\begin{aligned}
Y_2 = {}&[\,(s_{CE} + \mathcal{D}s_{BC}) - (s_{CB} + \mathcal{D}s_{EC}) + (s_{FE} + \mathcal{D}s_{BF}) \\
&- (s_{FB} + \mathcal{D}s_{EF})\,] - [\,(s_{AE} + \mathcal{D}s_{BA}) - (s_{AB} + \mathcal{D}s_{EA}) \\
&+ (s_{DE} + \mathcal{D}s_{BD}) - (s_{DB} + \mathcal{D}s_{ED})\,],
\end{aligned}
\tag{14.5b}
$$

$$
\begin{aligned}
Y_3 = {}&[\,(s_{DF} + \mathcal{D}s_{CD}) - (s_{DC} + \mathcal{D}s_{FD}) + (s_{AF} + \mathcal{D}s_{CA}) \\
&- (s_{AC} + \mathcal{D}s_{FA})\,] - [\,((s_{EF} + \mathcal{D}s_{CE}) - (s_{EC} + \mathcal{D}s_{FE}) \\
&+ (s_{BF} + \mathcal{D}s_{CB}) - (s_{BC} + \mathcal{D}s_{FB})\,].
\end{aligned}
\tag{14.5c}
$$

We can represent these solutions as 24-tuples of coefficients for the delay functions q_{IJ}:

$$
\begin{aligned}
q_1 = \{&1, 1, -1, -1, -1, -1, 1, 1, -\mathcal{D}, \mathcal{D}, 0, 0, -\mathcal{D}, \mathcal{D}, 0, 0, \\
&\mathcal{D}, -\mathcal{D}, 0, 0, \mathcal{D}, -\mathcal{D}, 0, 0\},
\end{aligned}
\tag{14.6a}
$$

$$
\begin{aligned}
q_2 = \{&-\mathcal{D}, \mathcal{D}, 0, 0, -\mathcal{D}, \mathcal{D}, 0, 0, 1, 1, -1, -1, -1, -1, 1, 1, \\
&0, 0, \mathcal{D}, -\mathcal{D}, 0, 0, \mathcal{D}, -\mathcal{D}\},
\end{aligned}
\tag{14.6b}
$$

$$
\begin{aligned}
q_3 = \{&0, 0, \mathcal{D}, -\mathcal{D}, 0, 0, \mathcal{D}, -\mathcal{D}, 0, 0, -\mathcal{D}, \mathcal{D}, 0, 0, -\mathcal{D}, \mathcal{D}, \\
&- 1, -1, 1, 1, 1, 1, -1, -1\}.
\end{aligned}
\tag{14.6c}
$$

The order used in the 24-tuples is $\{BA,\ EA,\ CA,\ FA,\ BD,\ ED,\ CD,\ FD,\ AB,\ DB,\ CB,\ FB,\ AE,\ DE,\ CE,\ FE,\ AC,\ DC,\ BC,\ EC,\ AF,\ DF,\ BF,\ EF\}$, so that, for example, the first entry in q_1 represents the s_{BA} coefficient in the Y_1 equation.

These particular solutions illustrate that not all links are used in producing a DFI stream. Multiple zeros in the equations for q_1, q_2, q_3 above indicate those links which do not contribute to the final result, and each time we use only 16 links. We will come back to the issue of "lost links" when we discuss the network sensitivity.

In the following, we will find generators of all solutions. The first step is to use Gaussian elimination (without division by delay operators) in Eq. (14.3), and as a result, we end up with a single (master) equation which we need to solve:

$$
\begin{aligned}
0 = {}&(\mathcal{D} - 1)^2 q_{BC} + (\mathcal{D} - 1)\mathcal{D}q_{CE} + (1 - \mathcal{D})(\mathcal{D} - 1)\mathcal{D}q_{DB} \\
&+ (\mathcal{D} - 1)((1 - \mathcal{D})\mathcal{D} - 1)q_{DC} \\
&+ (\mathcal{D} - 1)q_{DF} + (\mathcal{D} - 1)q_{EF}.
\end{aligned}
\tag{14.7}
$$

In the next step, we want to find the so-called "reduced generators" of Eq. (14.7), which correspond to the reduced set $(q_{BC}, q_{CE}, q_{DB}, q_{DC}, q_{DF}, q_{EF})$. For this we need to compute the Gröbner basis (Buchberger 1970), a set generating the polynomial ideals q_{IJ}. Roughly speaking, the Gröbner basis is comparable to the greatest common divisor of q_{IJ}. Following the procedure from Tinto & Dhurandhar (2005), we obtain seven generators:

$$S_1 = \{0, \mathcal{D}^2 + \mathcal{D}, 0, -\mathcal{D} - \mathcal{D}^2, 1 - \mathcal{D}, \mathcal{D}^2 + 1, -1 + \mathcal{D}, -1 - \mathcal{D}^2, \mathcal{D} - \mathcal{D}^2, 0, -\mathcal{D},$$
$$\mathcal{D}^2, -\mathcal{D}^2 - 1, -\mathcal{D} - 1, 1, 1 + \mathcal{D} + \mathcal{D}^2, -\mathcal{D} + \mathcal{D}^2, 0, \mathcal{D}, -\mathcal{D}^2, \mathcal{D}^2 + 1, 1 + \mathcal{D}, \quad (14.8\text{a})$$
$$-1, -\mathcal{D} - \mathcal{D}^2 - 1\},$$

$$S_2 = \{\mathcal{D} + 1, \mathcal{D} + 1, -\mathcal{D} - 1, -\mathcal{D} - 1, -1 + \mathcal{D}, \mathcal{D} - 1, 1 - \mathcal{D}, 1 - \mathcal{D}, -2\mathcal{D}, 0, \mathcal{D},$$
$$\mathcal{D}, -2\mathcal{D}, 0, \mathcal{D}, \mathcal{D}, 2\mathcal{D}, 0, -\mathcal{D}, -\mathcal{D}, 2\mathcal{D}, 0, -\mathcal{D}, -\mathcal{D}\}, \quad (14.8\text{b})$$

$$S_3 = \{0, \mathcal{D}, -\mathcal{D}, 0, -1, \mathcal{D} - 1, 1 - \mathcal{D}, 1, 1 - \mathcal{D}, 1, -1 + \mathcal{D}, -1, -\mathcal{D}, 0, \mathcal{D}, 0, \mathcal{D},$$
$$0, 0, -\mathcal{D}, \mathcal{D} - 1, -1, 1, -\mathcal{D} + 1\}, \quad (14.8\text{c})$$

$$S_4 = \{\mathcal{D}, -\mathcal{D} + \mathcal{D}^2, \mathcal{D}, -\mathcal{D} - \mathcal{D}^2, 2, -2\mathcal{D} + \mathcal{D}^2 + 2, -2 + 2\mathcal{D}, -2 - \mathcal{D}^2, 2\mathcal{D} - 2 - \mathcal{D}^2,$$
$$-2, 2 - 2\mathcal{D}, 2 + \mathcal{D}^2, \mathcal{D} - \mathcal{D}^2, -\mathcal{D}, -\mathcal{D}, \mathcal{D} + \mathcal{D}^2, -2\mathcal{D} + \mathcal{D}^2, 0, 0, 2\mathcal{D} - \mathcal{D}^2,$$
$$-\mathcal{D} + \mathcal{D}^2 + 2, 2 + \mathcal{D}, -2 - \mathcal{D}, \mathcal{D} - \mathcal{D}^2 - 2\}, \quad (14.8\text{d})$$

$$S_5 = \{0, \mathcal{D}^2 + \mathcal{D}, -\mathcal{D}^2, -\mathcal{D}, 1 - \mathcal{D}, \mathcal{D}^2 + 1, \mathcal{D} - \mathcal{D}^2 - 1, -1, \mathcal{D} - \mathcal{D}^2, 0,$$
$$-\mathcal{D} + \mathcal{D}^2, 0, -1 - \mathcal{D}^2, -\mathcal{D} - 1, 1 + \mathcal{D}^2, 1 + \mathcal{D}, \mathcal{D}^2, \mathcal{D}, 0, -\mathcal{D}^2 - \mathcal{D},$$
$$-\mathcal{D} + \mathcal{D}^2 + 1, 1, \mathcal{D} - 1, -1 - \mathcal{D}^2\}, \quad (14.8\text{e})$$

$$S_6 = \{\mathcal{D} + 2 + \mathcal{D}^2, \mathcal{D} + \mathcal{D}^3 + 2, -\mathcal{D} + \mathcal{D}^2 - 2, -\mathcal{D} - 2 - 2\mathcal{D}^2 - \mathcal{D}^3, -2 + 2\mathcal{D},$$
$$2\mathcal{D} - \mathcal{D}^2 + \mathcal{D}^3 - 2, -2\mathcal{D} + 2\mathcal{D}^2 + 2, 2 - 2\mathcal{D} - \mathcal{D}^2 - \mathcal{D}^3, \mathcal{D}^2 - 4\mathcal{D} - \mathcal{D}^3, 0, \quad (14.8\text{f})$$
$$2\mathcal{D} - 2\mathcal{D}^2, 2\mathcal{D} + \mathcal{D}^2 + \mathcal{D}^3, -3\mathcal{D} - \mathcal{D}^3, \mathcal{D} - \mathcal{D}^2, \mathcal{D} - \mathcal{D}^2, 2\mathcal{D}^2 + \mathcal{D} + \mathcal{D}^3,$$
$$-\mathcal{D}^2 + 2\mathcal{D} + \mathcal{D}^3, -2\mathcal{D}, 0, \mathcal{D}^2 - \mathcal{D}^3, 5\mathcal{D} + \mathcal{D}^3, \mathcal{D} + \mathcal{D}^2, -3\mathcal{D} - \mathcal{D}^2, -3\mathcal{D} - \mathcal{D}^3\},$$

$$S_7 = \{1, 1 + \mathcal{D}, -1, -1 - \mathcal{D}, 0, \mathcal{D}, 0, -\mathcal{D}, -\mathcal{D}, 0, 0, \mathcal{D}, -1 - \mathcal{D},$$
$$-1, 1, 1 + \mathcal{D}, \mathcal{D}, 0, 0, -\mathcal{D}, 1 + \mathcal{D}, 1, -1, -1 - \mathcal{D}\}. \quad (14.8\text{g})$$

As before, these operators have to be applied to s_{IJ}, using the same ordering as given above. All other solutions can be constructed from these generators. A detailed derivation of expressions (14.8a)–(14.8g) is given in Appendix A of OGO13.

Before we proceed, let us make several remarks. The generators found here are not unique, just like in the case of TDI (Tinto & Dhurandhar 2005). The set of generators does not necessarily form a minimal set, and we can only guarantee that the found set of generators gives us a module of syzygies and can be used to generate other solutions. The combinations S_1 to S_7 applied on 24 raw measurements s_{IJ}^{tot} eliminate both laser and displacement noise while mostly preserving the gravitational wave signal. Note that again in those expressions we do not use all links – for example, if the link BA is lost due to some reasons, we still can use S_1, S_3, S_5 to produce DFI streams.

190

14.4 Response functions and sensitivity

In the previous section we have found generators that produce data streams free of acceleration and laser noise. Now we need to apply these combinations to the shot noise and to the GW signal to compute the corresponding response functions.

14.4.1 Shot noise level and noise transfer function

We will assume that the shot noise is independent (uncorrelated) in each link and equal in power spectral density, based on identical laser sources and telescopes on each spacecraft. We denote the power spectral density of the shot noise by $\widetilde{S}_{\mathrm{sn}}$. A lengthy but straightforward computation shows that the spectral noise $\widetilde{S}_{\mathrm{n},i}$ corresponding to the seven combinations S_i, $i = 1, \ldots, 7$ from Eqs. (14.8a)–(14.8g) is given by

$$\widetilde{S}_{\mathrm{n},1} = 16\, \widetilde{S}_{\mathrm{sn}}\, \epsilon^2 \left(9 + 2\cos 2\epsilon + 3\cos 4\epsilon\right), \tag{14.9a}$$

$$\widetilde{S}_{\mathrm{n},2} = 160\, \widetilde{S}_{\mathrm{sn}}\, \epsilon^2, \tag{14.9b}$$

$$\widetilde{S}_{\mathrm{n},3} = 48\, \widetilde{S}_{\mathrm{sn}}\, \epsilon^2 \left(2 - \cos 2\epsilon\right), \tag{14.9c}$$

$$\widetilde{S}_{\mathrm{n},4} = 16\, \widetilde{S}_{\mathrm{sn}}\, \epsilon^2 \left(24 - 13\cos 2\epsilon + 6\cos 4\epsilon\right), \tag{14.9d}$$

$$\widetilde{S}_{\mathrm{n},5} = 16\, \widetilde{S}_{\mathrm{sn}}\, \epsilon^2 \left(9 - 2\cos 2\epsilon + 3\cos 4\epsilon\right), \tag{14.9e}$$

$$\widetilde{S}_{\mathrm{n},6} = 16\, \widetilde{S}_{\mathrm{sn}}\, \epsilon^2 \left(45 - 6\cos 2\epsilon + 17\cos 4\epsilon\right), \tag{14.9f}$$

$$\widetilde{S}_{\mathrm{n},7} = 48\, \widetilde{S}_{\mathrm{sn}}\, \epsilon^2 \left(2 + \cos 2\epsilon\right), \tag{14.9g}$$

where $\epsilon \equiv \omega L/2$, with the GW frequency ω. In the low frequency limit ($\epsilon \ll 1$), the noise $\widetilde{S}_{\mathrm{n},i}$ for each combination S_i is proportional to ϵ^2.

Let us now compute the shot noise in a single link. We consider for OGO a configuration with LISA-like receiver-transponder links and the following parameters: spacecraft separation $L = 1414\,\mathrm{km}$, laser wavelength $\lambda = 532\,\mathrm{nm}$, laser power $P = 10\,\mathrm{W}$ and telescope diameter $D = 1\,\mathrm{m}$. For this arm length and telescope size, almost all of the laser power from the remote spacecraft is received by the local spacecraft. Hence, the shot-noise calculation for OGO is different from the LISA case, where an overwhelming fraction of the laser beam misses the telescope (Danzmann et al. 2011).

For a Michelson interferometer, the sensitivity to shot noise is usually expressed as (Maggiore 2008)

$$\sqrt{\widetilde{S}_h(f)} = \frac{1}{2L} \sqrt{\frac{\hbar c \lambda}{\pi P}} \ [1/\sqrt{\mathrm{Hz}}], \tag{14.10}$$

where we have temporarily restored the speed of light c and the reduced Planck constant $\hbar$. Notice that the effect of the GW transfer function is not included here yet. For a single link $I \to J$ of OGO as opposed to a full two-arm Michelson with dual links, $\sqrt{\widetilde{S}_{h,IJ}}$ is a factor of 4 larger. However, our design allows the following two improvements: (i)

Since there is a local laser in J with power similar to the received laser power from I, the power at the beam splitter is actually $2P$, giving an improvement of $1/\sqrt{2}$. This is also different from LISA, where due to the longer arm length the received power is much smaller than the local laser power. (ii) If we assume that the arm length is stable enough to operate at the dark fringe, then we gain another factor of $1/\sqrt{2}$.

So, we arrive at the following shot-noise-only sensitivity for a single link:

$$\sqrt{\widetilde{S}_{h,IJ}(f)} = \frac{1}{L}\sqrt{\frac{\hbar c\lambda}{\pi P}} \; [1/\sqrt{\text{Hz}}]. \tag{14.11}$$

14.4.2 GW signal transfer function and sensitivity

Next, we will compute the detector response to a gravitational wave signal. We assume a GW source located in the direction $\hat{n} = -\hat{k} = (\sin\theta\cos\phi, \sin\theta\sin\phi, \cos\theta)$ as seen from the detector frame. We choose unit vectors

$$\hat{u} = \begin{bmatrix} \cos\theta\cos\phi \\ \cos\theta\sin\phi \\ -\sin\theta \end{bmatrix}, \quad \hat{v} = \begin{bmatrix} \sin\phi \\ -\cos\phi \\ 0 \end{bmatrix} \tag{14.12}$$

orthogonal to $\hat{k}$ pointing tangentially along the θ and ϕ coordinate lines to form a polarization basis. This basis can be described by polarization tensors $\mathbf{e}_+$ and $\mathbf{e}_\times$, given by

$$\mathbf{e}_+ \equiv \hat{u}\otimes\hat{u} - \hat{v}\otimes\hat{v}\,, \quad \mathbf{e}_\times \equiv \hat{u}\otimes\hat{v} + \hat{v}\otimes\hat{u}\,. \tag{14.13}$$

The single-arm fractional frequency response to a GW is (Estabrook & Wahlquist 1975)

$$h_{IJ} = \frac{H_{IJ}(t - \hat{k}\cdot\vec{x}_I - L) - H_{IJ}(t - \hat{k}\cdot\vec{x}_J)}{2\left(1 - \hat{k}\cdot\hat{n}_{IJ}\right)}, \tag{14.14}$$

where $\vec{x}_I$ is the position vector of the I-th spacecraft, L the (constant) distance between two spacecraft and

$$H_{IJ}(t) \equiv h_+(t)\,\xi_+(\hat{u},\hat{v},\hat{n}_{IJ}) + h_\times(t)\,\xi_\times(\hat{u},\hat{v},\hat{n}_{IJ})\,. \tag{14.15}$$

Here $h_{+,\times}(t)$ are two GW polarizations in the basis (14.13) and

$$\xi_+(\hat{u},\hat{v},\hat{n}_{IJ}) \equiv \hat{n}_{IJ}^{\mathsf{T}}\mathbf{e}_+\hat{n}_{IJ} = (\hat{u}\cdot\hat{n}_{IJ})^2 - (\hat{v}\cdot\hat{n}_{IJ})^2\,,$$
$$\xi_\times(\hat{u},\hat{v},\hat{n}_{IJ}) \equiv \hat{n}_{IJ}^{\mathsf{T}}\mathbf{e}_\times\hat{n}_{IJ} = 2(\hat{u}\cdot\hat{n}_{IJ})(\hat{v}\cdot\hat{n}_{IJ})\,. \tag{14.16}$$

In order to find the arm response for arbitrary incident GWs, we can compute the single arm response to a monochromatic GW with Eq. (14.14) and then deduce the following general response in the frequency domain,

$$
\begin{aligned}
h_{IJ}(f) = \epsilon \operatorname{sinc}\left[\epsilon(1 - \hat{k} \cdot \hat{n}_{IJ})\right] &\mathrm{e}^{-\mathrm{i}\epsilon[\hat{k}\cdot(\vec{x}_I + \vec{x}_J)/L + 1]} \\
&\times \left[\xi_+(\hat{n}_{IJ})h_+(f) + \xi_\times(\hat{n}_{IJ})h_\times(f)\right],
\end{aligned}
\tag{14.17}
$$

where we used the normalized sinc function, conventionally used in signal processing: $\operatorname{sinc}(x) := \sin(\pi x)/(\pi x)$.

Hence, the transfer function for a GW signal is

$$
\begin{aligned}
\mathcal{T}_{IJ+,\times}^{\mathrm{GW}}(f) = \epsilon \operatorname{sinc}\left[\epsilon(1 - \hat{k} \cdot \hat{n}_{IJ})\right] &\\
&\times \mathrm{e}^{-\mathrm{i}\epsilon[\hat{k}\cdot(\vec{x}_I + \vec{x}_J)/L + 1]}\xi_{+,\times}(\hat{n}_{IJ}).
\end{aligned}
\tag{14.18}
$$

For the sake of simplicity, we will from now on assume that the GW has "+" polarization only. This simplification will not affect our qualitative end result. Substituting the transfer function for a single arm response into the above 7 generators [Eqs. (14.8a)–(14.8g)], we can get the transfer function $\mathcal{T}_i^{\mathrm{GW}}$ for each combination. The final expressions are very lengthy and not needed here explicitly.

Having obtained the transfer function, we can compute the sensitivity for each combination $i = 1, \ldots, 7$ as

$$
\sqrt{\widetilde{S}_{h,i}} = \sqrt{\frac{\widetilde{S}_{\mathrm{n},i}}{\langle(\mathcal{T}_i^{\mathrm{GW}})^2\rangle}},
\tag{14.19}
$$

where the triangular brackets imply averaging over polarization and source sky location.

We expect up to 12 independent round trip measurements, corresponding to the number of back-and-forth links between spacecraft. It is out of the scope of this work to explicitly find all noise-uncorrelated combinations (similar to the optimal channels A, E, T in the case of LISA (Tinto & Dhurandhar 2005)). However, if we assume approximately equal sensitivity for each combination (which is almost the case for the combinations $S_1, \ldots, S_7$), we expect an improvement in the sensitivity of the whole network by a factor $1/\sqrt{12}$.

Therefore, we simply approximate the network sensitivity of the full detector as

$$
\sqrt{\widetilde{S}_{h,\mathrm{net}}} = \sqrt{\widetilde{S}_{h,5}/12}.
$$

Note that the potential loss of some links would imply that not all generators can be formed. We can lose up to 6 links and still be able to form a DFI stream (but probably only one). The number of lost links (and which links are lost exactly) will affect the network sensitivity. In our estimations below we deal with the idealized situation and assume that no links are lost.
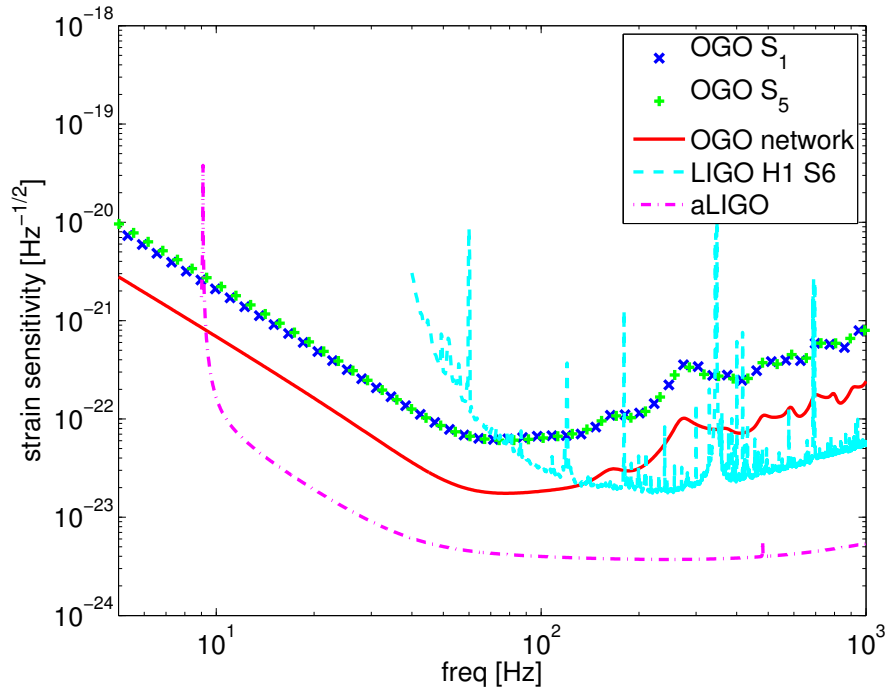
Figure 14.2: Sensitivities for two single DFI combinations (S_1, *blue crosses* and S_5, *green plus signs*) of OGO (with $L \approx 1400\,\mathrm{km}$) and for the full OGO network sensitivity (scaled from S_5, *red solid line*). For comparison, the dashed lines show sensitivities for initial LIGO (H1 during science run S6, from Abadie et al. (2010d), *cyan dashed line*) and aLIGO (design sensitivity for high-power, zero detuning configuration, from Shoemaker et al. (2010), *magenta dash-dotted line*).

We plot the sensitivity curves for individual combinations and the network sensitivity in Fig. 14.2. For comparison we also show the design sensitivity curves of initial LIGO (S6 science run, Abadie et al. 2010d) and advanced LIGO (high laser power configuration with zero detuning of the signal recycling mirror, Shoemaker et al. 2010). Indeed one can see that the sensitivities of the individual OGO configurations are similar to each other and close to initial LIGO. The network sensitivity of OGO lies between LIGO and aLIGO sensitivities. OGO as expected outperforms aLIGO below 10 Hz, where the seismic noise on the ground becomes strongly dominant.

14.4.3 General performance of the DFI scheme

Having derived the full sensitivity curve of the OGO mission design with $L \approx 1400\,\mathrm{km}$ as an exemplary implementation of the three-dimensional DFI scheme in space, let us take a step back and analyze the general performance of a DFI-enabled detector. These features are also what led us to consider the octahedron configuration in the first place.

Specifically, let us look in more detail at the low frequency asymptotic behavior of the transfer functions and sensitivity curves. We consider a LISA-like configuration with two laser noise free combinations: an unequal arm Michelson (TDI-X) and a Sagnac combination (TDI-α). Let us assume for a moment that the only noise source is shot noise, which at low frequencies ($\epsilon \ll 1$) scales as $\sqrt{\widetilde{S}_{\mathrm{n},X}} \sim \epsilon^2$ and $\sqrt{\widetilde{S}_{\mathrm{n},\alpha}} \sim \epsilon^1$ for those two combinations, respectively.

The GW transfer function, for both TDI combinations, scales as $\mathcal{T}_\alpha, \mathcal{T}_X \sim \epsilon^2$; therefore, the sensitivity curves scale as $\sqrt{\widetilde{S}_{h,\alpha}} \sim \sqrt{\widetilde{S}_{\mathrm{n},\alpha}}/\mathcal{T}_\alpha \sim \epsilon^{-1}$ for TDI-α and scale as $\sqrt{\widetilde{S}_{h,X}} \sim \sqrt{\widetilde{S}_{\mathrm{n},X}}/\mathcal{T}_X \sim \epsilon^0$ for TDI-X. We see that a LISA-like TDI-X-combination has a *flat* shot-noise spectrum at low frequencies, corresponding to a flat total detector sensitivity if all other dominant noise sources can be canceled – which looks extremely attractive.

Thus, a naive analysis suggests that the acceleration and laser noise free combinations for an octahedron detector could yield a flat sensitivity curve at low frequencies. Checking this preliminary result with a more careful analysis was the main motivation for the research presented in this article.

In fact, as we have seen in Sec. 14.4.2, the full derivation delivers transfer functions that, in leading order of ϵ, go as $\mathcal{T}_{1,2,\dots,7} \sim \epsilon^3$. This implies that the sensitivity for laser and acceleration noise free combinations behaves as $\sqrt{\widetilde{S}_{h,1,2,\dots,7}}/\mathcal{T}_{1,2,\dots,7} \sim \epsilon^{-2}$, which is similar to the behavior of acceleration noise. In other words, the combinations eliminating the acceleration noise also cancel a significant part of the GW signal at low frequencies.

In fact, we find that a standard LISA-like TDI-enabled detector of the same arm length and optical configuration as OGO could achieve a similar low-frequency sensitivity (at few to tens of Hz) with an acceleration noise requirement of only $\sim 10^{-12}$ m/s$^2 \sqrt{\mathrm{Hz}}$. This assumes negligible spacecraft jitter and that no other noise sources (phase-meter noise, sideband noise, thermal noise) limit the sensitivity, which at this frequency band would behave differently than in the LISA band. In fact, the GOCE mission (Drinkwater et al. 2003) has already demonstrated such acceleration noise levels at mHz frequencies (Sechi et al. 2011), and therefore this seems a rather modest requirement at OGO frequencies. We therefore see that such a short-arm-length OGO would actually only be a more complicated alternative to other feasible mission designs.

In addition, it is hard to see from just the comparison with ground-based detectors in Fig. 14.2 how exactly the DFI method itself influences the final noise curve of OGO, and how much of its shape is instead determined by the geometrical and technical parameters of the mission concept (arm length, laser power, telescope size). Also, the secondary technological noise sources of a space mission in the comparatively high-frequency band of this exemplary OGO implementation are somewhat different from more well-studied missions like LISA and DECIGO.
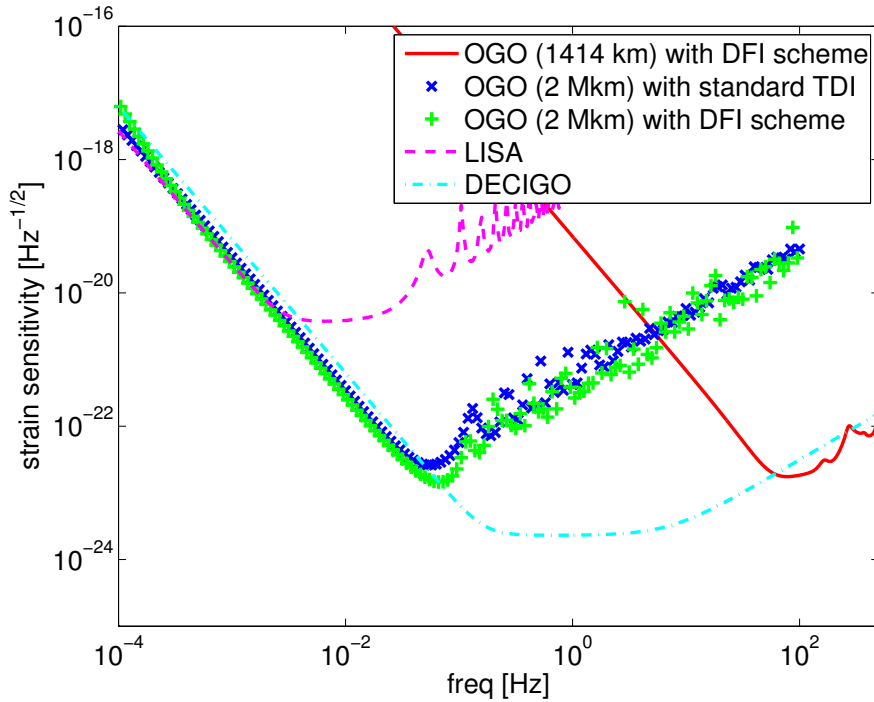
Figure 14.3: Network sensitivities, scaled from S_5, of standard OGO (with DFI, arm length 1414 km, *red solid line*) compared to an OGO-like detector with spacecraft separation of $2 \cdot 10^9$ m, with either full DFI scheme (*blue crosses*) or standard TDI only (*green plus signs*). Also shown for comparison are (classic) LISA ($5 \cdot 10^9$ m, network sensitivity, *magenta dashed line*, from Larson, Hiscock & Hellings 2000) and DECIGO (using the fitting formula Eq. (20) from Yagi 2013, *cyan dash-dotted line*).

Therefore, to disentangle these effects, we will now tentatively study a different version of OGO based on the alternative orbit with an average arm length of $2 \cdot 10^9$ m, as mentioned in Sec. 14.2. It requires further study to determine whether a stable octahedron constellation and the DFI scheme are possible on such an orbit, but assuming they are, we can compute its sensitivity as before.

In Fig. 14.3, we then compare this longer-baseline DFI detector with another detector with the same geometry and optical components, but without the DFI technique, using instead conventional TDI measurements. Here, we are in a similar frequency range as LISA and therefore assume similar values for the acceleration noise of $3 \cdot 10^{-15}$ m/s^2 $\sqrt{\text{Hz}}$ (Danzmann et al. 2011) and secondary noise sources (phase meter, thermal noise, etc.; see Sec. 14.4.4).

However, there is another noise source, spacecraft jitter, which is considered subdominant for LISA, but might become relevant for both the TDI and DFI versions of the $2 \cdot 10^9$ m OGO-like detector. Jitter corresponds to the rotational degrees of freedom between

spacecraft, and its coupling into measurement noise is not fully understood. We have therefore computed both sensitivities without any jitter. It seems possible that at least the part of jitter that couples linearly into displacement noise could also be canceled by DFI, or that an extension of DFI (e.g. more links) could take better care of this, and therefore that the full OGO with DFI would look more favorable compared to the TDI version when nonvanishing jitter is taken into account.

Generally, as one goes for longer arm lengths, the DFI scheme will perform better in comparison to the TDI scheme. At the high-frequency end of the sensitivity curves, both schemes are limited by shot noise and the respective GW transfer functions. Since the shot-noise level does not depend on the arm length, it remains the same for all relevant frequencies. Therefore, as the arm length increases, the high-frequency part of the sensitivity curves moves to the low-frequency regime in parallel (i.e. the corner frequency of the transfer function is proportional to $1/L$). This is the same for both schemes.

On the other hand, in the low-frequency regime of the sensitivity curves the two schemes perform very differently. For TDI, the low-frequency behavior is limited by acceleration noise, while for DFI this part is again limited by shot noise and the GW transfer function. When the arm length increases, the low-frequency part of the sensitivity curve in the TDI scheme moves to lower frequencies in proportion to $1/\sqrt{L}$; while for DFI, it moves in proportion to $1/L$.

Graphically, when the arm length increases, the high-frequency parts of the sensitivity curves in both schemes move toward the lower-frequency regime in parallel, while the low-frequency part of the sensitivity curve for DFI moves faster than for TDI.

Under the assumptions given above, we find that an arm length of $2 \cdot 10^9$ m is close to the transition point where the sensitivities of TDI and DFI are almost equal, as shown in Fig. 14.3. At even longer arm lengths, employing DFI would become clearly advantageous.

Of course, these considerations show that a longer-baseline detector with good sensitivity in the standard space-based detector frequency band of interest would make a scientifically much more interesting case than the default short-arm OGO which we presented first. However, as no study on the required orbits has been done so far, we consider such a detector variant to be highly hypothetical and not worthy of a detailed study of technological feasibility and scientific potential yet. Instead, for the remainder of this paper, we concentrate again on the conservative 1400 km version of OGO. Although the sensitivity curve in Fig. 14.2 already demonstrates its limited potential, we will attempt to neutrally assess its advantages, limitations and scientific reach.

14.4.4 Technological feasibility

Employing DFI requires a large number of spacecraft but on the other hand allows us to relax many of the very strict technological requirements of other space-based GW detector proposals such as (e)LISA and DECIGO. Specifically, the clock noise is canceled by design, so there is no need for a complicated clock tone transfer chain (Barke et al. 2010). Furthermore, OGO does not require a drag-free technology, and the configuration has to be stabilized only as much as required for the equal arm length assumption to hold. This strongly reduces the requirements on the spacecraft thrusters. Also, for the end mirrors, which have to be mounted on the same monolithic structure for all four laser links per spacecraft, it is not required that they are freefalling. Instead, they can be fixed to the spacecraft.

Still, to reach the shot-noise-only limited sensitivity shown in Fig. 14.2, the secondary noise contributions from all components of the measurement system must be significantly below the shot-noise level. Considering a shot-noise level of about $2 \cdot 10^{-17}\,\mathrm{m}/\sqrt{\mathrm{Hz}}$ – which is in agreement with the value derived earlier for the 1400 km version of OGO – this might be challenging.

When actively controlling the spacecraft position and hence stabilizing the distance and relative velocity between the spacecraft, we will be able to lower the heterodyne frequency of the laser beat notes drastically. Where LISA will have a beat note frequency in the tens of MHz, with OGO's short arm length we could be speaking of kHz or less and might even consider a homodyne detection scheme as in LIGO. This might in the end enable us to build a phase meter capable of detecting relative distance fluctuations with a sensitivity of $10^{-17}\,\mathrm{m}/\sqrt{\mathrm{Hz}}$ or below as required by OGO.

As mentioned before, temperature noise might be a relevant noise source for OGO: The relative distance fluctuations on the optical benches due to temperature fluctuations and the test mass thermal noise must be significantly reduced in comparison to LISA. But even though the LISA constellation is set in an environment which is naturally more temperature stable, stabilization should be easier for the higher-frequency OGO measurement band. A requirement of $10^{-17}\,\mathrm{m}/\sqrt{\mathrm{Hz}}$ could be reached by actively stabilizing the temperature down to values of $1\,\mathrm{nK}/\sqrt{\mathrm{Hz}}$ at the corner frequency.

Assuming future technological progress, optimization of the optical bench layout could also contribute to mitigating this constraint, as could the invention of thermally more stable materials for the optical bench. Most likely, this challenge can be solved only with a combination of the mentioned approaches.

The same is true for the optical path length stability of the telescopes. We estimate the required pointing stability to be roughly similar to the LISA mission requirements.

14.4.5 Shot-noise reduction

Assuming the requirements from the previous section can be met, the timing and acceleration noise free combinations of the OGO detector are dominated by shot noise, and any means of reducing the shot noise will lead to a sensitivity improvement over all frequencies. In this subsection, we discuss possible ways to achieve such a reduction.

The most obvious solution is to increase laser power, with an achievable sensitivity improvement that scales with $\sqrt{P}$. However, the available laser power is limited by the power supplies available on a spacecraft. Stronger lasers are also heavier and take more place, making the launch of the mission more difficult. Therefore, there is a limit to simply increasing laser power, and we want to shortly discuss more advanced methods of shot-noise reduction.

One such hypothetical possibility is to build cavities along the links between spacecraft, similar to the DECIGO design (Ando et al. 2010a). The shot noise would be decreased due to an increase of the effective power stored in the cavity. Effectively, this also results in an increase of the arm length. Note, however, that the sensitivity of OGO with cavities cannot simply be computed by inserting effective power and arm length into our previously derived equations. Instead, a rederivation of the full transfer function along the lines of Rakhmanov (2005) is necessary.

Alternatively, squeezed light (Schnabel et al. 2010) is a way to directly reduce the quantum measurement noise, which has already been demonstrated in ground-based detectors (Abadie et al. 2011a, Khalaidovski et al. 2012). However, squeezing in a space-based detector is challenging in many aspects due to the very sensitive procedure and would require further development.

14.5 Scientific perspectives

In this section, we will discuss the science case for our octahedral GW detector (with an arm length of 1400 km) by considering the most important potential astrophysical sources in its band of sensitivity. Using the full network sensitivity, as derived above, the best performance of OGO is at 78 Hz, between the best achieved performance of initial LIGO during its S6 science run and the anticipated sensitivity for advanced LIGO. OGO outperforms the advanced ground-based detectors below 10 Hz, where the seismic noise strongly dominates. In this analysis, we will therefore consider sources emitting GWs with frequencies between 1 Hz and 1 kHz, concentrating on the low end of this range.

Basically, those are the same sources as for ground-based detectors, which include compact binaries coalescences (CBCs), asymmetric single neutron stars (continuous waves, CWs), binaries containing intermediate-mass black holes (IMBHs), burst sources (unmodeled short-duration transient signals), and a cosmological stochastic background.

We will go briefly through each class of sources and consider perspectives of their detection. As was to be expected from the sensitivity curve in Fig. 14.2, in most categories OGO performs better than initial ground-based detectors, but does not even reach the potential of the advanced generation currently under commissioning.

Therefore, this section should be understood not as an endorsement of actually building and flying an OGO-like mission, but just as an assessment of its (limited, but existing) potentials. This demonstrates that an octahedral GW detector employing DFI in space is in principle capable of scientifically interesting observations, even though improving its performance to actually surpass existing detectors or more mature mission proposals still remains a subject of further study.

In addition, we put a special focus on areas where OGO's design offers some specific advantages. These include the triangulation of CBCs through joint detection with ground-based detectors as well as searching for a stochastic GW background and for additional GW modes.

Note that the hypothetical $2 \cdot 10^9$ m variant of OGO (see Secs. 14.2 and 14.4.3) would have a very different target population of astrophysical sources due to its sensitivity shift to lower frequencies. Such a detector would still be sensitive to CBCs, IMBHs, and stochastic backgrounds, probably much more so. But instead of high-frequency sources like CW pulsars and supernova bursts, it would start targeting supermassive black holes, investigating the merging history of galaxies over cosmological scales.

However, as this detector concept relies on an orbit hypothesis not studied in any detail, we do not consider it mature enough to warrant a study of potential detection rates in any detail, and we therefore only refer to established reviews of the astrophysical potential in the frequency band of LISA and DECIGO, e.g. Sathyaprakash & Schutz (2009).

14.5.1 Coalescing compact binaries

Heavy stars in binary systems will end up as compact objects (such as NSs or BHs) inspiralling around each other, losing orbital energy and angular momentum through gravitational radiation. Depending on the proximity of the source and the detector's sensitivity, we could detect GWs from such a system a few seconds up to a day before the merger and the formation of a single spinning object. These CBCs are expected to be the strongest sources of GWs in the frequency band of current GW detectors.

To estimate the event rates for various binary systems, we will follow the calculations outlined in Abadie et al. (2010c). To compare with predictions for initial and advanced LIGO (presented in Abadie et al. 2010c), we also use only the inspiral part of the coalescence to estimate the *horizon distance* (the maximum distance to which we can observe a given system with a given signal-to-noise ratio (SNR)). We use here the same detection threshold on signal-to-noise ratio, a SNR of $\rho = 8$, as in Abadie et al. (2010c) and

	NS-NS	NS-BH	BH-BH
OGO	(0.002, 0.2, 2.2)	(0.001, 0.06, 2.0)	(0.003, 0.1, 9)
LIGO	(2e-4, 0.02, 0.2)	(7e-5, 0.004, 0.1)	(2e-4, 0.007, 0.5)
aLIGO	(0.4, 40, 400)	(0.2, 10, 300)	(0.4, 20, 1000)

Table 14.1: Estimated yearly detection rates for CBC events, given in triplets of the form (lower limit, realistic value, upper limit) as defined in Abadie et al. (2010c).

consider the same fiducial binary systems: NS-NS (with $1.4\,\mathrm{M}_\odot$ each), BH-NS (BH mass $10\,\mathrm{M}_\odot$, NS with $1.4\,\mathrm{M}_\odot$), and BH-BH ($10\,\mathrm{M}_\odot$ each).

For a binary of given masses, the sky-averaged horizon distance is given by

$$D_h = \frac{4\sqrt{5}\, G^{\frac{5}{6}}\, \mu^{\frac{1}{2}}\, M^{\frac{1}{3}}}{\sqrt{96}\, \pi^{\frac{2}{3}}\, c^{\frac{3}{2}}\, \rho} \sqrt{\int_{f_{\min}}^{f_{\mathrm{ISCO}}} \frac{f^{-\frac{7}{3}}}{\widetilde{S}_{\mathrm{h}}(f)}\, \mathrm{d}f}\,. \tag{14.20}$$

Here, $M = M_1 + M_2$ is the total mass and $\mu = M_1 M_2/M$ is the reduced mass of the system. We have used a lower cutoff of $f_{\min} = 1\,\mathrm{Hz}$, and at the upper end the frequency of the innermost stable circular orbit is $f_{\mathrm{ISCO}} = c^3/(6^{3/2}\pi\, G\, M)\,\mathrm{Hz}$, which conventionally is taken as the end of the inspiral.

Now, for any given type of binary (as characterized by the component masses), we obtain the observed event rate (per year) using $\dot{N} = R \cdot N_{\mathrm{G}}$, where we have adopted the approximation for the number of galaxies inside the visible volume from Eq. (5) of Abadie et al. (2010c):

$$N_{\mathrm{G}} = \frac{4}{3}\pi \left(\frac{D_{\mathrm{h}}}{\mathrm{Mpc}}\right)^3 (2.26)^{-3} \cdot 0.0116\,, \tag{14.21}$$

and the intrinsic coalescence rates R per Milky-Way-type galaxy are given in Table 2 of Abadie et al. (2010c).

A single DFI combination S_i has annual rates similar to initial LIGO, and the results for the network sensitivity of full OGO are summarized in Tbl. 14.1. For each binary, we give three numbers following the uncertainties in the intrinsic event rate ("pessimistic", "realistic", "optimistic") as introduced in Abadie et al. (2010c).

From this, we see that OGO achieves detection rates an order of magnitude better than initial LIGO. But we still expect to have only one event in about three years of observation assuming "realistic" intrinsic coalescence rates. The sensitivity of aLIGO is much better than for OGO above 10 Hz, and the absence of seismic noise does not help OGO much because the absolute sensitivities below 10 Hz are quite poor and only a very small fraction of SNR is contributed from the lower frequencies. This is the reason why OGO cannot compete directly with aLIGO in terms of total CBC detection rates, which are about two orders of magnitude lower.

However, OGO does present an interesting scientific opportunity when run in parallel with aLIGO. If OGO indeed detects a few events over its mission lifetime, as the realistic predictions allow, it can give a very large improvement to the sky localization of these sources. Parameter estimation by aLIGO alone typically cannot localize signals enough for efficient electromagnetic follow-up identification. However, in a joint detection by OGO and aLIGO, triangulation over the long baseline between space-based OGO and ground-based aLIGO would yield a fantastic angular resolution. As signals found by OGO are very likely to be picked up by aLIGO as well, such joint detections indeed seem promising. Additionally, the three-dimensional configuration and independent channels of OGO potentially allow a more accurate parameter estimation than a network of two or three simple L-shaped interferometers could achieve.

14.5.2 Stochastic background

There are mainly two kinds of stochastic GW backgrounds (Allen & Romano 1999, Maggiore 2000a): The first is the astrophysical background (sometimes also called astrophysical foreground), arising from unresolved astrophysical sources such as compact binaries (Farmer & Phinney 2003) and core-collapse supernovae (Ferrari, Matarrese & Schneider 1999). It provides important statistical information about distribution of the sources and their parameters. The second is the cosmological background which was generated by various mechanisms in the early Universe (Brustein et al. 1995, Turner 1997, Ananda, Clarkson & Wands 2007). It carries unique information about the very beginning of the Universe ($\sim 10^{-28}\,$s). Thus, the detection of the GW stochastic background is of great interest.

Currently, there are two ways to detect the stochastic GW background. One of them (Hogan & Bender 2001) takes advantage of the null stream (e.g. the Sagnac combination of LISA). By definition, the null stream is insensitive to gravitational radiation, while it suffers from the same noise sources as the normal data stream. A comparison of the energy contained in the null stream and the normal data stream allows us to determine whether the GW stochastic background is present or not. The other way of detection is by cross-correlation (Allen & Romano 1999, Seto 2006) of measurements taken by different detectors. In our language, this uses the GW background signal measured by one channel as the template for the other channel. In this sense, the cross-correlation can be viewed as matched filtering. Both ways require redundancy, i.e. more than one channel observing the same GW signal with independent noise.

Luckily, the octahedron detector has plenty of redundancy, which potentially allows precise background detection. There are in total 12 dual-way laser links between spacecraft, forming 8 LISA-like triangular constellations. Any pair of two such LISA-like triangles that does not share common links can be used as an independent correlation. There are 16 such pairs within the octahedron detector. Within each pair, we can correlate the orthogonal TDI variables A, E and T (as they are denoted in LISA, see Tinto & Dhurandhar 2005). Altogether, there are $16 \times 3^2 = 144$ cross-correlations.

And we have yet more information encoded by the detector, which we can access by considering that any two connected links form a Michelson interferometer, thus providing a Michelson-TDI variable. Any two of these variables that do not share common links can be correlated. There are in total 36 such variables, forming 450 cross-correlations, from which we can construct the optimal total sensitivity.

Furthermore, each of these is sensitive to a different direction on the sky. So the octahedron detector has the potential to detect anisotropy of the stochastic background. However, describing an approach for the detection of anisotropy is beyond the scope of this feasibility study.

Instead, we will present here only an order of magnitude estimation of the total cross-correlation SNR. Usually, it can be expressed as

$$\text{SNR} = \frac{3H_0^2}{10\pi^2}\sqrt{T_{\text{obs}}}\left[2\sum_{k,l}\int_0^\infty \mathrm{d}f\, \frac{\gamma_{kl}^2(f)\Omega_{\text{gw}}^2(f)}{f^6\widetilde{S}_{\text{h},k}(f)\widetilde{S}_{\text{h},l}(f)}\right]^{\frac{1}{2}}, \qquad (14.22)$$

where T_{obs} is the observation time, Ω_{gw} is the fractional energy-density of the Universe in a GW background, H_0 the *Hubble constant*, and $\widetilde{S}_{\text{h},k}(f)$ is the effective sensitivity of the k-th channel. $\gamma_{kl}(f)$ denotes the *overlap reduction function* between the k-th and l-th channels, introduced by Flanagan (1993).

$$\gamma_{kl}(f) = \frac{5}{8\pi}\sum_{p=+,\times}\int \mathrm{d}\hat{\Omega}\, \mathrm{e}^{2\pi \mathrm{i} f\hat{\Omega}\cdot\Delta\mathbf{x}/c}F_k^p(\hat{\Omega})F_l^p(\hat{\Omega}), \qquad (14.23)$$

where $F_k^p(\hat{\Omega})$ is the antenna pattern function. As mentioned in the previous section, there might be 12 independent DFI solutions. These DFI solutions can form $12\times 11/2 = 66$ cross-correlations. According to Allen & Romano (1999), we know $\gamma_{kl}^2(f)$ varies between 0 and 1. As a rough estimate, we approximate $\sum_{k,l}\gamma_{kl}^2(f) \sim 10$; hence, we get the following result for OGO:

$$\text{SNR} = 2.57\left(\frac{H_0}{72\,\frac{\text{km s}^{-1}}{\text{Mpc}}}\right)^2\left(\frac{\Omega_{\text{gw}}}{10^{-9}}\right)\left(\frac{T_{\text{obs}}}{10\,\text{yr}}\right)^{\frac{1}{2}}. \qquad (14.24)$$

Initial LIGO has set an upper limit of $6.9\cdot 10^{-6}$ on Ω_{gw}, and aLIGO will be able to detect the stochastic background at the $1\cdot 10^{-9}$ level (Abbott et al. 2009b). Hence, our naive estimate of OGO's sensitivity to the GW stochastic background is similar to that of aLIGO. Actually, an optimal combination of all the previously-mentioned possible cross-correlations would potentially result in an even better detection ability for OGO.

14.5.3 Testing alternative theories of gravity

In this section we will consider OGO's ability to test predictions of General Relativity against alternative theories. In particular, we will estimate the sensitivity of the proposed detector to all six polarization modes that could be present in (alternative) metric
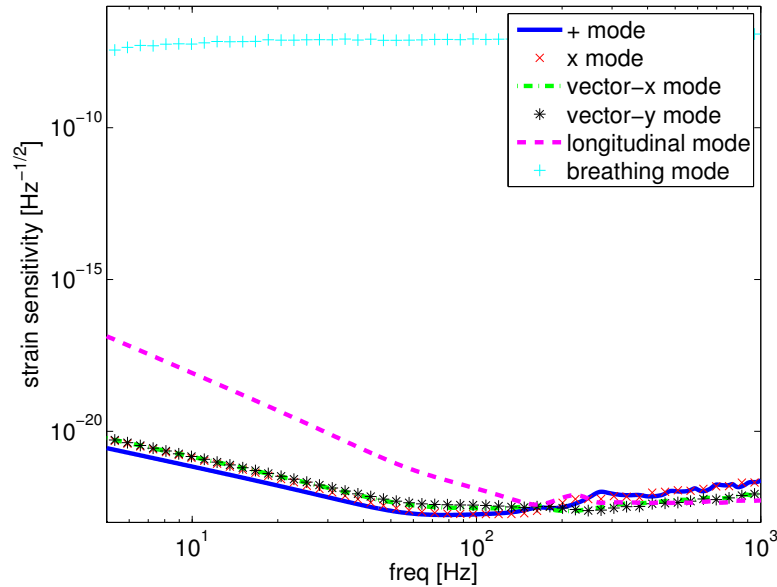
Figure 14.4: Relative sensitivity of the full OGO network (scaled from S5 combination) to alternative polarizations: + mode (*blue solid line*), x mode (*red crosses*), vector-x mode (*green dash-dotted line*), vector-y mode (*black stars*), longitudinal mode (*magenta dashed line*), and breathing mode (*cyan plus signs*).

theories of gravitation (Hohmann 2012). We refer to Eardley, Lee & Lightman (1973) for a discussion on polarization states, which are (i) two transverse-traceless (tensorial) polarizations usually denoted as + and ×, (ii) two scalar modes called breathing (or common) and longitudinal and (iii) two vectorial modes. We also refer to Gair et al. (2013) and Will (2014) for reviews on alternative theories of gravity.

We have followed the procedure for computing the sensitivity of OGO, as outlined above, for the four modes not present in General Relativity, and we compare those sensitivities to the results for the $+, \times$ modes as presented in Fig. 14.2. The generalization of the transfer function used in this paper [Eq. (14.18)] for other polarization modes is given in Chamberlin & Siemens (2012).

We have found that all seven generators show similar sensitivity for each mode. OGO is not sensitive to the common (breathing) mode, which is not surprising as it can be attributed to a common displacement noise, which we have removed by our procedure. The sensitivity to the second (longitudinal) scalar mode scales as ϵ^{-4} at low frequencies and is much worse than the sensitivity to the $+, \times$ polarizations below 200 Hz. However, OGO is more sensitive to the longitudinal mode (by about an order of magnitude) above 500 Hz. The sensitivity of OGO to vectorial modes is overall similar to the $+, \times$ modes: it is by a few factors less sensitive to vectorial modes below 200 Hz and by similar factors more sensitive above 300 Hz. These sensitivities are shown in Fig. 14.4.
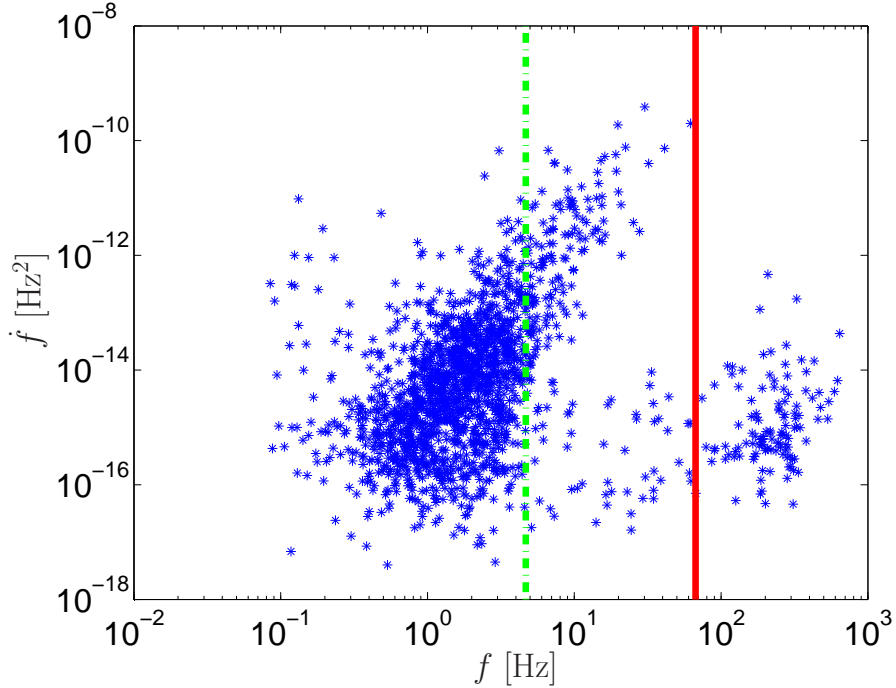
204

Figure 14.5: Population of currently known pulsars in the frequency-spindown plane
(f-$\dot{f}$). OGO could beat initial LIGO left of the red solid line and Advanced LIGO
left of the green dashed line. Data for this plot were taken from Manchester et al.
(2005) on March 2, 2012.

14.5.4 Pulsars – Continuous Waves

CWs are expected from spinning neutron stars with nonaxisymmetric deformations. Spinning NSs are already observed as radio and gamma-ray pulsars. Since CW emission is powered by the spindown of the pulsar, the strongest emitters are the pulsars with high spindowns, which usually are young pulsars at rather high frequencies. Note that the standard emission model (Jaranowski, Królak & Schutz 1998) predicts a gravitational wave frequency $f_{\mathrm{gw}} = 2f$, while alternative models like free precession (Jones & Andersson 2002) and r-modes (Andersson, Kokkotas & Stergioulas 1999) also allow emission at $f_{\mathrm{gw}} = f$ and $f_{\mathrm{gw}} = \frac{4}{3}f$, where f is the NS spin frequency.

OGO has better sensitivity than initial LIGO below 133 Hz, has its best sensitivity around 78 Hz, and is better than aLIGO below 9 Hz. This actually fits well with the current radio census of the galactic pulsar population, as given by the ATNF catalog (Manchester et al. 2005). As shown in Fig. 14.5, the bulk of the population is below ~ 10 Hz, and also contains many low-frequency pulsars with decent spindown values, even including a few down to ~ 0.1 Hz.

We estimate the abilities of OGO to detect CW emission from known pulsars following

the procedure outlined in Abadie et al. (2011b) for analysis of the Vela pulsar. The GW strain for a source at distance D is given as

$$h_0 = \frac{4\pi^2 G I_{zz} \epsilon f^2}{c^4 D} \,, \tag{14.25}$$

where ϵ is the ellipticity of the neutron star and we assume a canonical momentum of inertia $I_{zz} = 10^{38} \, \mathrm{kg\,m^2}$. After an observation time T_{obs}, we could detect a strain amplitude

$$h_0 = \Theta \sqrt{\frac{S_{\mathrm{h}}}{T_{\mathrm{obs}}}} \,. \tag{14.26}$$

The statistical factor is $\Theta \approx 11.4$ for a fully coherent targeted search with the canonical values of $1\,\%$ and $10\,\%$ for false alarm and false dismissal probabilities, respectively (Abbott et al. 2004b). We find that, for the Vela pulsar (at a distance of $290\,\mathrm{pc}$ and a frequency of $f_{\mathrm{Vela,gw}} = 2 \cdot 11.19\,\mathrm{Hz}$), with $T_{\mathrm{obs}} = 30$ days of observation, we could probe ellipticities as low as $\epsilon \sim 5 \cdot 10^{-4}$ with the network OGO configuration. Several known low-frequency pulsars outside the aLIGO band would also be promising objectives for OGO targeted searches.

All-sky searches for unknown pulsars with OGO would focus on the low-frequency range not accessible to aLIGO with a search setup comparable to current Einstein@Home LIGO searches (Aasi et al. 2013b). As seen above, the sensitivity estimate factors into a search setup related part $\Theta/\sqrt{T_{\mathrm{obs}}}$ and the sensitivity $\sqrt{S_{\mathrm{h}}}$. Therefore, scaling a search with parameters identical to the Einstein@Home S5 runs to OGO's best sensitivity at $76\,\mathrm{Hz}$ would reach a sensitivity of $h_0 \approx 3 \cdot 10^{-25}$. This would, for example, correspond to a neutron star ellipticity of $\epsilon \sim 4.9 \cdot 10^{-5}$ at a distance of $1\,\mathrm{kpc}$. Since the computational cost of such searches scales with f^2, low-frequency searches are actually much more efficient and would allow very deep searches of the OGO data, further increasing the competitiveness. Note, however, that for low-frequency pulsars the ellipticities required to achieve detectable GW signals can be very high, possibly mostly in the unphysical regime. On the other hand, for "transient CW"-type signals (Prix, Giampanis & Messenger 2011), low-frequency pulsars might be the strongest emitters, even with realistic ellipticities.

14.5.5 Other sources

Many (indirect) observational evidences exist for stellar mass BHs, which are the end stages of heavy star evolution, as well as for supermassive BHs, the result of accretion and galactic mergers throughout the cosmic evolution, in galactic nuclei. On the other hand, there is no convincing evidence so far for a BH of an intermediate mass in the range of $10^2 - 10^4 \, \mathrm{M_\odot}$. These IMBHs might, however, still exist in dense stellar clusters (Miller & Colbert 2004, Pasquato 2010). Moreover, stellar clusters could be formed as large, gravitationally bound groups, and collision of two clusters would produce inspiralling binaries of IMBHs (Amaro-Seoane & Freitag 2006, Amaro-Seoane, Miller & Freitag 2009).

The ISCO frequency of the second orbital harmonic for a $300\,\mathrm{M}_\odot$-$300\,\mathrm{M}_\odot$ system is about $7\,\mathrm{Hz}$, which is outside the sensitivity range of aLIGO. Still, those sources could show up through the higher harmonics (the systems are expected to have non-negligible eccentricity) and through the merger and ring-down gravitational radiation (Fregeau et al. 2006, Mandel et al. 2008, Yagi 2012). The ground-based LIGO and VIRGO detectors have already carried out a first search for IMBH signals in the $100\,\mathrm{M}_\odot$ to $450\,\mathrm{M}_\odot$ mass range (Abadie et al. 2012c).

With its better low-frequency sensitivity, OGO can be expected to detect a GW signal from the inspiral of a $300\,\mathrm{M}_\odot$-$300\,\mathrm{M}_\odot$ system in a quasicircular orbit up to a distance of approximately $245\,\mathrm{Mpc}$, again using Eq. (14.20). This gives the potential for discovery of such systems and for estimating their physical parameters.

As for other advanced detectors, unmodeled searches (as opposed to the matched-filter CBC and CW searches; see Abadie et al. (2012a) for a LIGO example) of OGO data have the potential for detecting many other types of gravitational wave sources, including, but not limited to, supernovae and cosmic string cusps. However, as in the case for IMBHs, the quantitative predictions are hard to produce due to uncertainties in the models.

14.6 Summary and Outlook

In this paper, we have presented for the first time a three-dimensional gravitational wave detector in space, called the Octahedral Gravitational wave Observatory (OGO). The detector concept employs displacement-noise free interferometry (DFI), which is able to cancel some of the dominant noise sources of conventional GW detectors. Adopting the octahedron shape introduced in Chen et al. (2006), we put spacecraft in each corner of the octahedron. We considered a LISA-like receiver-transponder configuration and found multiple combinations of measurement channels, which allow us to cancel both laser frequency and acceleration noise. This new three-dimensional result generalizes the Mach-Zehnder interferometer considered in Chen et al. (2006).

We have identified a possible halolike orbit around the Lagrange point L1 in the Sun-Earth system that would allow the octahedron constellation to be stable enough. However, this orbit limits the detector to an arm length of ≈ 1400 km.

Much better sensitivity and a richer astrophysical potential are expected for longer arm lengths. Therefore, we also looked for alternative orbits and found a possible alternative allowing for $\approx 2 \cdot 10^9$ m arms, but is is not clear yet if this would be stable enough. Future studies are required to relax the equal-arm-length assumption of our DFI solutions, or to determine a stable, long-arm-length constellation.

Next, we have computed the sensitivity of OGO-like detectors – and have shown that the noise-cancelling combinations also cancel a large fraction of the GW signal at low frequencies. The sensitivity curve therefore has a characteristic slope of f^{-2} at the low-frequency end.

However, the beauty of this detector is that it is limited by a single noise source at all frequencies: shot noise. Thus, any reduction of shot noise alone would improve the overall sensitivity. This could, in principle, be achieved with DECIGO-like cavities, squeezing or other advanced technologies. Also, OGO does not require drag-free technology and has moderate requirements on other components so that it could be realized with technology already developed for LISA Pathfinder and eLISA.

When comparing a DFI-enabled OGO with a detector of similar design, but with standard TDI, we find that at ≈ 1400 km, the same sensitivity could be reached by a TDI detector with very modest acceleration noise requirements.

However, at longer arm lengths DFI becomes more advantageous, reaching the same sensitivity as TDI under LISA requirements but without drag-free technology and clock transfer, at $\approx 2 \cdot 10^9$ m. Such a DFI detector would have its best frequency range between LISA and DECIGO, with peak sensitivity better than LISA and approaching DECIGO without the latter mission concept's tight acceleration noise requirements and with no need for cavities.

Finally, we have assessed the scientific potentials of OGO, concentrating on the less promising, but more mature short-arm-length version. We estimated the event rates for coalescing binaries, finding that OGO is better than initial LIGO, but does not reach the level of advanced LIGO. Any binary detected with both OGO and aLIGO could be localized in the sky with very high accuracy.

Also, the three-dimensional satellite constellation and number of independent links makes OGO an interesting mission for detection of the stochastic GW background or hypothetical additional GW polarizations. Further astrophysically interesting sources such as low-frequency pulsars and IMBH binaries also lie within the sensitive band of OGO, but again the sensitivity does not reach that of aLIGO.

However, we point out that the improvement in the low-frequency sensitivity with increasing arm length happens faster for DFI as compared to the standard TDI. Therefore, searching for stable three-dimensional (octahedron) long-baseline orbits could lead to an astrophysically much more interesting mission.

Regarding possible improvements of the presented setup, there are several possibilities to extend and improve the first-order DFI scheme presented here. One more spacecraft could be added in the middle, increasing the number of usable links. Breaking the symmetry of the octahedron could modify the steep response function at low frequencies. This should be an interesting topic for future investigations.

In principle, the low-frequency behavior of OGO-like detectors could also be improved by more advanced DFI techniques such as introducing artificial time delays (Somiya et al. 2007a,b). This would result in a three-part power law less steep than the shape derived in Sec. 14.4.2. On the other hand, this would also introduce a new source of time delay noise. Therefore, such a modification requires careful investigation.

208

14.7 Acknowledgments for the OGO project

Appendix A: Acknowledgements

Writing this thesis, and doing the research work presented in it, would not have been possible without the help, guidance and support of many people.

Bruce Allen has offered me a place at AEI Hannover, provided an excellent working environment and helpful guidance throughout this project. Reinhard Prix proposed the original ideas leading to most of the work presented here. He also introduced me to all the subtleties of CW data analysis, constantly provided help and suggestions and reviewed my results very carefully. Special thanks to him also for careful and in-depth reading of the drafts for this thesis, leading to significant improvements throughout.

Let me also thank all my collaborators on published papers: Reinhard, Maria Alessandra Papa, Paola Leaci and Maham Siddiqi for the line-robustness paper; Yan Wang, Stas Babak, Markus Otto and others for the OGO paper. For acknowledgements specific to OGO, see Sec. 14.7.

Thanks also to everyone who, in addition to Bruce Allen, agreed to referee this thesis or to sit on my defence committee: Andrzej Królak, Graham Woan, Norbert Dragon, Karsten Danzmann and Holger Pletsch.

In addition to the people already listed, many others make the AEI Hannover such a productive environment. For fruitful scientific discussions, I want to especially thank Karl Wette, Berit Behnke, Miroslav Shaltev, Badri Krishnan, Irene Di Palma, Heinz-Bernd Eggenstein and Bernd Machenschalk, but also everyone else. Thanks also to all my great office mates, past and current: Berit, Benjamin, Pablo, Tito, Jing and Ornella. Furthermore, Carsten Aulbert, Henning Fehrmann and their assistants do a great job at running the ATLAS computing cluster, which I used for the tests presented in Sec. 10.

For providing the LIGO S5 data used in Sec. 10, I gratefully acknowledge the LIGO Scientific Collaboration. I would also like to thank the people from the LSC and from Virgo, especially in the CW group, for providing a fascinating experience of research in a global collaboration: Vladimir Dergachev, Chris Messenger, Keith Riles, Sinéad Walsh, John Whelan and many others.

I also thank the IMPRS on Gravitational Wave Astronomy and the Professor-Rhein-Stiftung of the city of Königswinter for financial support.

On the personal side, thanks to my parents and grandparents for their continuous encouragement of my studies and scientific endeavours. Sadly, my grandfather did not live to see a "Doktor der Naturwissenschaften" in his family. Special thanks also go to my dearest Laura for being at my side all these years, for proof-reading, and, as the saying goes, for "keeping me sane" during the demanding final weeks of writing this thesis.

While preparing the final publication version, I'd like to extend another thank-you to Bruce Allen for his detailed corrections and suggestions.

Appendix B: Bibliography

Abbreviations of common references

JK09   P. Jaranowski & A. Królak (2009). 'Analysis of Gravitational-Wave Data'. Cambridge Monographs on Particle Physics, Nuclear Physics and Cosmology 29. Cambridge University Press.

JKS98   P. Jaranowski, A. Królak & B. F. Schutz (1998). 'Data analysis of gravitational-wave signals from spinning neutron stars: The signal and its detection'. *Phys. Rev. D* 58, 063001. arXiv: `gr-qc/9804014`.

KPPLS14   D. Keitel, R. Prix, M. A. Papa, P. Leaci & M. Siddiqi (2014). 'Search for continuous gravitational waves: Improving robustness versus instrumental artifacts'. *Phys. Rev. D* 89.6, 064023, 064023. arXiv: `1311.5738 [gr-qc]`.

MTW73   C. W. Misner, K. S. Thorne & J. A. Wheeler (1973). 'Gravitation'. W.H. Freeman and Co., San Francisco.

OGO13   Y. Wang, D. Keitel, S. Babak, A. Petiteau, M. Otto et al. (2013). 'Octahedron configuration for a displacement noise-cancelling gravitational wave detector in space'. *Phys. Rev. D* 88.10, 104021, 104021. arXiv: `1306.3865 [gr-qc]`.

PGM11   R. Prix, S. Giampanis & C. Messenger (2011). 'Search method for long-duration gravitational-wave transients from neutron stars'. *Phys. Rev. D* 84, 023007. arXiv: `1104.1704 [gr-qc]`.

PK09   R. Prix & B. Krishnan (2009). 'Targeted search for continuous gravitational waves: Bayesian versus maximum-likelihood statistics'. *Class. Quant. Grav.* 26, 204013. arXiv: `0907.2569 [gr-qc]`.

Full list of references

The following abbreviations are used for collaborations:

LSC: LIGO Scientific Collaboration

LVC: LIGO Scientific Collaboration Virgo Collaboration

VC: Virgo Collaboration

Aasi, J. et al. (2012), LVC. 'The characterization of Virgo data and its impact on gravitational-wave searches'. *Class. Quant. Grav.* 29.15, 155002. arXiv: `1203.5613 [gr-qc]`.

– (2013a), LVC. 'A directed search for continuous Gravitational Waves from the Galactic Center'. *Phys. Rev. D* 88.10, 102002. arXiv: `1309.6221 [gr-qc]`.

– (2013b), LVC. 'Einstein@Home all-sky search for periodic gravitational waves in LIGO S5 data'. *Phys. Rev. D* 87, 042001. arXiv: `1207.7176 [gr-qc]`.

– (2013c), LVC. 'Prospects for Localization of Gravitational Wave Transients by the Advanced LIGO and Advanced Virgo Observatories'. arXiv: `1304.0670 [gr-qc]`.

– (2014a), LSC. 'Advanced LIGO'. arXiv: `1411.4547 [gr-qc]`.

– (2014b), LVC. 'Application of a Hough search for continuous gravitational waves on data from the fifth LIGO science run'. *Class. Quant. Grav.* 31.8, 085014. arXiv: `1311.2409 [gr-qc]`.

– (2014c), LVC. 'Characterization of the LIGO detectors during their sixth science run'. arXiv: `1410.7764`.

– (2014d), LVC. 'First all-sky search for continuous gravitational waves from unknown sources in binary systems'. *Phys. Rev. D* 90.6, 062010. arXiv: `1405.7904 [gr-qc]`.

– (2014e), LVC. 'Gravitational Waves from Known Pulsars: Results from the Initial Detector Era'. *Astrophys. J.* 785, 119. arXiv: `1309.4027 [astro-ph.HE]`.

Aasi, J. et al. (2014f), LVC. 'Searches for continuous gravitational waves from nine young supernova remnants'. arXiv: 1412.5942 [astro-ph.HE].

Abadie, J. et al. (2010a), LSC. 'Calibration of the LIGO gravitational wave detectors in the fifth science run'. *Nucl. Instrum. Meth. Phys. Res. A* 624.1, 223–240.

– (2010b), LSC. 'First Search for Gravitational Waves from the Youngest Known Neutron Star'. *Astrophys. J.* 722, 1504–1513. arXiv: 1006.2535 [gr-qc].

– (2010c), LVC. 'Predictions for the rates of compact binary coalescences observable by ground-based gravitational-wave detectors'. *Class. Quant. Grav.* 27.17, 173001. arXiv: 1003.2480 [astro-ph.HE].

– (2010d), LVC. 'Sensitivity to Gravitational Waves from Compact Binary Coalescences Achieved during LIGO's Fifth and Virgo's First Science Run'. arXiv: 1003.2481 [gr-qc].

– (2011a), LSC. 'A gravitational wave observatory operating beyond the quantum shot-noise limit: Squeezed light in application'. *Nature Phys.* 7, 962–965. arXiv: 1109.2295 [quant-ph].

– (2011b), LVC. 'Beating the Spin-down Limit on Gravitational Wave Emission from the Vela Pulsar'. *Astrophys. J.* 737, 93. arXiv: 1104.2712 [astro-ph.HE].

– (2012a), LVC. 'All-sky search for gravitational-wave bursts in the second joint LIGO-Virgo run'. *Phys. Rev. D* 85, 122007. arXiv: 1202.2788 [gr-qc].

– (2012b), LVC. 'All-sky Search for Periodic Gravitational Waves in the Full S5 LIGO Data'. *Phys. Rev. D* 85, 022001. arXiv: 1110.0208 [gr-qc].

– (2012c), LVC. 'Search for gravitational waves from intermediate mass binary black holes'. *Phys. Rev. D* 85.10, 102004. arXiv: 1201.5999 [gr-qc].

– (2012d), LVC. 'Search for Gravitational Waves from Low Mass Compact Binary Coalescence in LIGO's Sixth Science Run and Virgo's Science Runs 2 and 3'. *Phys. Rev. D* 85, 082002. arXiv: 1111.7314 [gr-qc].

– (2012e), LVC. 'Sensitivity Achieved by the LIGO and Virgo Gravitational Wave Detectors during LIGO's Sixth and Virgo's Second and Third Science Runs'. arXiv: 1203.2674 [gr-qc].

Abbott, B. P. et al. (2004a), LSC. 'Detector description and performance for the first coincidence observations between LIGO and GEO'. *Nucl. Instrum. Meth. Phys. Res. A* 517, 154–179. arXiv: gr-qc/0308043.

– (2004b), LSC. 'Setting upper limits on the strength of periodic gravitational waves from PSR J1939+2134 using the first science data from the GEO 600 and LIGO detectors'. *Phys. Rev. D* 69.8, 082004. arXiv: gr-qc/0308050.

– (2005a), LSC. 'First all-sky upper limits from LIGO on the strength of periodic gravitational waves using the Hough transform'. *Phys. Rev. D* 72.10, 102004. arXiv: gr-qc/0508065.

– (2005b), LSC. 'Search for gravitational waves associated with the gamma ray burst GRB030329 using the LIGO detectors'. *Phys. Rev. D* 72.4, 042002. arXiv: gr-qc/0501068.

– (2005c), LSC. 'Search for gravitational waves from galactic and extra-galactic binary neutron stars'. *Phys. Rev. D* 72.8, 082001. arXiv: gr-qc/0505041.

– (2005d), LSC. 'Upper limits on gravitational wave bursts in LIGO's second science run'. *Phys. Rev. D* 72.6, 062001. arXiv: gr-qc/0505029.

– (2007a), LSC. 'Searches for periodic gravitational waves from unknown isolated sources and Scorpius X-1: Results from the second LIGO science run'. *Phys. Rev. D* 76.8, 082001. arXiv: gr-qc/0605028.

– (2007b), LSC. 'Upper limits on gravitational wave emission from 78 radio pulsars'. *Phys. Rev. D* 76.4, 042001. arXiv: gr-qc/0702039.

– (2008a), LSC. 'All-sky search for periodic gravitational waves in LIGO S4 data'. *Phys. Rev. D* 77.2, 022001. arXiv: 0708.3818 [gr-qc].

– (2008b), LSC. 'Beating the Spin-Down Limit on Gravitational Wave Emission from the Crab Pulsar'. *Astrophys. J. Lett.* 683, L45–L49. arXiv: 0805.4758.

– (2009a), LSC. 'All-Sky LIGO Search for Periodic Gravitational Waves in the Early Fifth-Science-Run Data'. *Phys. Rev. Lett.* 102.11, 111102. arXiv: 0810.0283 [gr-qc].

– (2009b), LVC. 'An upper limit on the stochastic gravitational-wave background of cosmological origin'. *Nature* 460, 990–994. arXiv: 0910.5772 [astro-ph.CO].

– (2009c), LSC. 'Einstein@Home search for periodic gravitational waves in early S5 LIGO data'. *Phys. Rev. D* 80, 042003. arXiv: 0905.1705 [gr-qc].

– (2009d), LSC. 'Einstein@Home search for periodic gravitational waves in LIGO S4 data'. *Phys. Rev. D* 79.2, 022001. arXiv: 0804.1747 [gr-qc].

– (2009e), LSC. 'LIGO: the Laser Interferometer Gravitational-Wave Observatory'. *Rept. Prog. Phys.* 72.7, 076901. arXiv: 0711.3041 [gr-qc].

– (2009f), LSC. 'Search for gravitational-wave bursts in the first year of the fifth LIGO science run'. *Phys. Rev. D* 80, 102001. arXiv: 0905.0020 [gr-qc].

Abdo, A. A. et al. (2009), Fermi-LAT Collaboration. 'A Population of Gamma-Ray Millisecond Pulsars Seen with the Fermi Large Area Telescope'. *Science* 325, 848–852.

– (2013), Fermi-LAT Collaboration. 'The Second Fermi Large Area Telescope Catalog of Gamma-Ray Pulsars'. *Astrophys. J. Suppl. Ser.* 208, 17. arXiv: `1305.4385 [astro-ph.HE]`.

Abernathy, M. et al. (2011). *Einstein gravitational wave Telescope: Conceptual Design Study.* Tech. rep. ET-0106C-10. `https://tds.ego-gw.it/ql/?c=7954`.

Accadia, T. et al. (2012a), VC. 'Noise monitor tools and their application to Virgo data'. *J. Phys. Conf. Ser.* 363.1, 012024.

– (2012b), VC. 'The NoEMi (Noise Frequency Event Miner) framework'. *J. Phys. Conf. Ser.* 363.1, 012037.

Acernese, F. et al. (2007), VC. 'Analysis of noise lines in the Virgo C7 data'. *Class. Quant. Grav.* 24, 433.

– (2008), VC. 'VIRGO: a large interferometer for gravitational wave detection started its first scientific run'. *J. Phys. Conf. Ser.* 120.3, 032007.

– (2009), VC. *Advanced Virgo Baseline Design.* Tech. rep. VIR-027A-09. `https://tds.ego-gw.it/ql/?c=6589`.

– (2015), VC. 'Advanced Virgo: a second-generation interferometric gravitational wave detector'. *Class. Quant. Grav.* 32.2, 024001. arXiv: `1408.3978 [gr-qc]`.

Adam, R. et al. (2014), Planck Collaboration. 'Planck intermediate results. XXX. The angular power spectrum of polarized dust emission at intermediate and high Galactic latitudes'. arXiv: `1409.5738 [astro-ph]`.

Ade, P. A. et al. (2014), BICEP2 Collaboration. 'Detection of B-Mode Polarization at Degree Angular Scales by BICEP2'. *Phys. Rev. Lett.* 112.24, 241101. arXiv: `1403.3985 [astro-ph.CO]`.

Aguiar, O. D. et al. (2002). 'The status of the Brazilian spherical detector'. *Class. Quant. Grav.* 19, 1949–1953.

– (2006). 'The Brazilian gravitational wave detector Mario Schenberg: status report'. *Class.Quant.Grav.* 23, 239.

Alford, M. G., Han, S. & Prakash, M. (2013). 'Generic conditions for stable hybrid stars'. *Phys. Rev. D* 88.8, 083013. arXiv: `1302.4732 [astro-ph.SR]`.

Alford, M. G., Rajagopal, K., Reddy, S. & Steiner, A. W. (2006). 'Stability of strange star crusts and strangelets'. *Phys. Rev. D* 73.11, 114016. arXiv: `hep-ph/0604134`.

Alford, M. G., Schmitt, A., Rajagopal, K. & Schäfer, T. (2008). 'Color superconductivity in dense quark matter'. *Rev. Mod. Phys.* 80, 1455–1515. arXiv: `0709.4635 [hep-ph]`.

Allen, B. (2005). 'χ^2 time-frequency discriminator for gravitational wave detection'. *Phys. Rev. D* 71.6, 062001. arXiv: `gr-qc/0405045`.

Allen, B. et al. (2005a). 'Einstein@Home distributed computing project'. `http://einsteinathome.org/`.

Allen, B., Abbott, B. P. et al. (2005b), LSC. 'Einstein@Home S3 Analysis'. online summary. `http://einstein.phys.uwm.edu/FinalS3Results/`.

Allen, B., Knispel, B., Cordes, J. M., Deneva, J. S., Hessels, J. W. et al. (2013). 'The Einstein@Home Search for Radio Pulsars and PSR J2007+2722 Discovery'. *Astrophys. J.* 773, 91. arXiv: `1303.0028 [astro-ph.IM]`.

Allen, B. & Romano, J. D. (1999). 'Detecting a stochastic background of gravitational radiation: Signal processing strategies and sensitivities'. *Phys. Rev. D* 59.10, 102001. arXiv: `gr-qc/9710117`.

Alpar, M. A., Cheng, A. F., Ruderman, M. A. & Shaham, J. (1982). 'A new class of radio pulsars'. *Nature* 300, 728–730.

Amaro-Seoane, P., Aoudia, S., Babak, S., Binétruy, P., Berti, E. et al. (2013). 'eLISA: Astrophysics and cosmology in the millihertz regime'. *GW Notes* 6, 4–110. arXiv: `1201.3621 [astro-ph.CO]`.

Amaro-Seoane, P. & Freitag, M. (2006). 'Intermediate-Mass Black Holes in Colliding Clusters: Implications for Lower Frequency Gravitational-Wave Astronomy'. *Astrophys. J. Lett.* 653, L53–L56. arXiv: `astro-ph/0610478`.

Amaro-Seoane, P., Miller, M. C. & Freitag, M. (2009). 'Gravitational Waves from Eccentric Intermediate-Mass Black Hole Binaries'. *Astrophys. J. Lett.* 692, L50–L53. arXiv: `0901.0604 [astro-ph.SR]`.

Ananda, K. N., Clarkson, C. & Wands, D. (2007). 'Cosmological gravitational wave background from primordial density perturbations'. *Phys. Rev. D* 75.12, 123518. arXiv: `gr-qc/0612013`.

Anderson, D. P. (2004). 'BOINC: A System for Public-Resource Computing and Storage'. In: *Proc. of the Fifth IEEE/ACM International Workshop on Grid Computing.* Ed. by R. Buyya. IEEE Computer Society, pp. 4–10.

Anderson, D. P., Walton, R., Fenton, C. et al. (2002). 'Berkeley Open Infrastructure for Network Computing'. `http://boinc.berkeley.edu/`.

Andersson, N., Baker, J., Belczynski, K., Bernuzzi, S., Berti, E. et al. (2013). 'The transient gravitational-wave sky'. *Class. Quant. Grav.* 30.19, 193002. arXiv: `1305.0816 [gr-qc]`.

Andersson, N., Comer, G. L. & Prix, R. (2003). 'Are Pulsar Glitches Triggered by a Superfluid Two-Stream Instability?' *Phys. Rev. Lett.* 90.9, 091101. arXiv: `astro-ph/0210486`.

Andersson, N., Kokkotas, K. D. & Stergioulas, N. (1999). 'On the Relevance of the R-Mode Instability for Accreting Neutron Stars and White Dwarfs'. *Astrophys. J.* 516, 307–314. arXiv: `astro-ph/9806089`.

Ando, M. et al. (2010a). 'DECIGO and DECIGO pathfinder'. *Class. Quant. Grav.* 27.8, 084010.

Ando, M., Arai, K., Takahashi, R., Heinzel, G., Kawamura, S. et al. (2001). 'Stable Operation of a 300-m Laser Interferometer with Sufficient Sensitivity to Detect Gravitational-Wave Events within Our Galaxy'. *Phys. Rev. Lett.* 86, 3950–3954. arXiv: `astro-ph/0105473`.

Ando, M., Ishidoshiro, K., Yamamoto, K., Yagi, K., Kokuyama, W. et al. (2010b). 'Torsion-Bar Antenna for Low-Frequency Gravitational-Wave Observations'. *Phys. Rev. Lett.* 105.16, 161101.

Antoniadis, J., Freire, P. C., Wex, N., Tauris, T. M., Lynch, R. S. et al. (2013). 'A Massive Pulsar in a Compact Relativistic Binary'. *Science* 340, 448. arXiv: `1304.6875 [astro-ph.HE]`.

Ashtekar, A. (2014). 'The last 50 years of general relativity and gravitation: from GR3 to GR20 Warsaw conferences'. *Gen. Rel. Grav.* 46, 1706. arXiv: `1312.6425 [gr-qc]`.

Aso, Y., Michimura, Y., Somiya, K., Ando, M., Miyakawa, O. et al. (2013). 'Interferometer design of the KAGRA gravitational wave detector'. *Phys. Rev. D* 88.4, 043007. arXiv: `1306.6747 [gr-qc]`.

Astone, P. et al. (1993). 'Long-term operation of the Rome "Explorer" cryogenic gravitational wave detector'. *Phys. Rev. D* 47, 362–375.

– (1997). 'The gravitational wave detector NAUTILUS operating at T = 0.1 K'. *Astropart. Phys.* 7.3, 231–243.

– (2008). 'EXPLORER and NAUTILUS gravitational wave detectors: a status report'. *Class. Quant. Grav.* 25.11, 114048.

Atwood, W. B. et al. (2009), Fermi-LAT Collaboration. 'The Large Area Telescope on the Fermi Gamma-Ray Space Telescope Mission'. *Astrophys. J.* 697, 1071–1102. arXiv: `0902.1089 [astro-ph.IM]`.

Baade, W. & Zwicky, F. (1934a). 'Remarks on Super-Novae and Cosmic Rays'. *Phys. Rev.* 46, 76–77.

– (1934b). 'Super-Novae and Cosmic Rays'. *Phys. Rev.* 45, 138.

Babak, S. et al. (2013). 'Searching for gravitational waves from binary coalescence'. *Phys. Rev. D* 87.2, 024033. arXiv: `1208.3491 [gr-qc]`.

Balasubramanian, R., Sathyaprakash, B. S. & Dhurandhar, S. V. (1996). 'Gravitational waves from coalescing binaries: Detection strategies and Monte Carlo estimation of parameters'. *Phys. Rev. D* 53, 3033–3055. arXiv: `gr-qc/9508011`.

Ballantini, R., Bernard, P., Chiaveri, E., Chincarini, A., Gemme, G. et al. (2003). 'A detector of high frequency gravitational waves based on coupled microwave cavities'. *Class. Quant. Grav.* 20, 3505–3522.

Ballmer, S., Frolov, V., Lawrence, R., Kells, W., Moreno, G. et al. (2005). *LIGO Thermal Compensation System Description*. Tech. rep. LIGO-T050064-00-R. `https://dcc.ligo.org/LIGO-T050064/public`.

Barke, S., Tröbs, M., Sheard, B., Heinzel, G. & Danzmann, K. (2010). 'EOM sideband phase characteristics for the spaceborne gravitational wave detector LISA'. *Appl. Phys. B* 98, 33–39.

Bass, J. (1966). 'Elements of probability theory'. Academic Press, New York and London.

Baym, G. (1982). 'Neutron stars: the first fifty years'. In: *The Neutron and its Applications*. Ed. by P. Schofield, pp. 45–50.

Baym, G. & Lamb, F. K. (2005). 'Neutron Stars'. In: *Encyclopedia of Physics, 3rd ed.* Ed. by R. G. Lerner & G. L. Trigg. Wiley-VCH. arXiv: `physics/0503245`.

Baym, G., Pethick, C. & Pines, D. (1969). 'Superfluidity in Neutron Stars'. *Nature* 224, 673–674.

Becker, W., ed. (2009). 'Neutron Stars and Pulsars'. Springer Berlin Heidelberg.

Begelman, M. C., Blandford, R. D. & Rees, M. J. (1980). 'Massive black hole binaries in active galactic nuclei'. *Nature* 287, 307–309.

Behnke, B., Papa, M. A. & Prix, R. (2014). 'Postprocessing methods used in the search for continuous gravitational-wave signals from the galactic center'. arXiv: `1410.5997 [gr-qc]`.

Behnke, B. (2013). 'A Directed Search for Continuous Gravitational Waves from Unknown Isolated Neutron Stars at the Galactic Center'. PhD thesis. Fakultät für Mathematik und Physik, Gottfried Wilhelm Leibniz Universität Hannover. `http://opac.tib.uni-hannover.de/DB=1/XMLPRS=N/PPN?PPN=752172840`.

Belczynski, K., Perna, R., Bulik, T., Kalogera, V., Ivanova, N. et al. (2006). 'A Study of Compact Object Mergers as Short Gamma-Ray Burst Progenitors'. *Astrophys. J.* 648, 1110–1116. arXiv: `astro-ph/0601458`.

Benacquista, M. J. & Downing, J. M. B. (2013). 'Relativistic Binaries in Globular Clusters'. *Living Rev. Relativity* 16.4. `http://www.livingreviews.org/lrr-2013-4`.

Bernard, P., Gemme, G., Parodi, R. & Picasso, E. (2001). 'A detector of small harmonic displacements based on two coupled microwave cavities'. *Rev. Sci. Instrum.* 72, 2428–2437. arXiv: `gr-qc/0103006`.

Bildsten, L. (1998). 'Gravitational Radiation and Rotation of Accreting Neutron Stars'. *Astrophys. J. Lett.* 501, L89. arXiv: `astro-ph/9804325`.

Blackburn, L. et al. (2008). 'The LSC glitch group: monitoring noise transients during the fifth LIGO science run'. *Class. Quant. Grav.* 25.18, 184004. arXiv: `0804.0800 [gr-qc]`.

Blackman, R. B. & Tukey, J. W. (1958). 'The measurement of power spectra. From the point of view of communications engineering'. Dover Publications.

Blair, D. G. (1983). 'Resonant bar detectors for gravitational waves'. In: *Gravitational Radiation. Les Houches 1982*. Ed. by N. Deruelle & T. Piran. North-Holland Publishing, pp. 339–385.

Blandford, R. D. (1984). Unpublished argument about the maximum gravitational wave signal from a population of pulsars. See Thorne, K. S. (1987).

Bondi, H. (1957). 'Plane Gravitational Waves in General Relativity'. *Nature* 179, 1072–1073.

– (1960). 'Gravitational Waves in General Relativity'. *Nature* 186, 535.

Bondi, H., Pirani, F. A. & Robinson, I. (1959). 'Gravitational Waves in General Relativity. III. Exact Plane Waves'. *Proc. R. Soc. A* 251, 519–533.

Bondi, H., van der Burg, M. G. & Metzner, A. W. (1962). 'Gravitational Waves in General Relativity. VII. Waves from Axi-Symmetric Isolated Systems'. *Proc. R. Soc. A* 269, 21–52.

Braccini, S., Bradaschia, C., Cobal, M., del Fabbro, R., di Virgilio, A. et al. (1993). 'An improvement in the VIRGO Super Attenuator for interferometric detection of gravitational waves - The use of a magnetic antispring'. *Rev. Sci. Instrum.* 64, 310–313.

Bradaschia, C., Del Fabbro, R., Di Virgilio, A., Giazotto, A., Kautzky, H. et al. (1990). 'The VIRGO Project: A wide band antenna for gravitational wave detection'. *Nucl. Instrum. Meth. Phys. Res. A* 289, 518–525.

Brady, P. R. & Creighton, T. (2000). 'Searching for periodic sources with LIGO. II. Hierarchical searches'. *Phys. Rev. D* 61.8, 082001. arXiv: `gr-qc/9812014`.

Brady, P. R., Creighton, T., Cutler, C. & Schutz, B. F. (1998). 'Searching for periodic sources with LIGO'. *Phys. Rev. D* 57, 2101–2116. arXiv: `gr-qc/9702050`.

Brandt, N. & Podsiadlowski, P. (1995). 'The effects of high-velocity supernova kicks on the orbital properties and sky distributions of neutron-star binaries'. *Mon. Not. R. Astron. Soc.* 274, 461–484.

Bretthorst, G. L. (1988). 'Bayesian Spectrum Analysis and Parameter Estimation'. Lecture Notes in Statistics 48. Springer-Verlag New York.

Brustein, R., Gasperini, M., Giovannini, M. & Veneziano, G. (1995). 'Relic gravitational waves from string cosmology'. *Phys. Lett. B* 361, 45–51. arXiv: `hep-th/9507017`.

Buchberger, B. (1970). 'Ein algorithmisches Kriterium für die Lösbarkeit eines algebraischen Gleichungssystems'. *Aeq. Math.* 4.3, 374–383.

Caballero, I. & Wilms, J. (2012). 'X-ray pulsars: a review.' *Mem. Soc. Astron. Ital.* 83, 230. arXiv: `1206.3124`.

Cameron, R. H. & Martin, W. T. (1944). 'Transformations of Wiener Integrals Under Translations'. *Ann. Math.* Second Series 45.2, 386–396.

Canal, R., Isern, J. & Labay, J. (1990). 'The origin of neutron stars in binary systems'. *Ann. Rev. Astron. Astrophys.* 28, 183–214.

Carilli, C. & Rawlings, S., eds. (2004). 'Science with the Square Kilometre Array'. Vol. 48, Issues 11–12. New Astronomy Reviews, pp. 979–1606.

Carter, B., Langlois, D. & Sedrakian, D. M. (2000). 'Centrifugal buoyancy as a mechanism for neutron star glitches'. *Astron. Astrophys.* 361, 795–802. arXiv: `astro-ph/0004121`.

Cerdonio, M. et al. (1997). 'The ultracryogenic gravitational-wave detector AURIGA'. *Class. Quant. Grav.* 14, 1491–1494.

Chakrabarty, D., Morgan, E. H., Muno, M. P., Galloway, D. K., Wijnands, R. et al. (2003). 'Nuclear-powered millisecond pulsars and the maximum spin frequency of neutron stars'. *Nature* 424, 42–44. arXiv: `astro-ph/0307029`.

Challis, J. (1869). 'The Theory of the Force of Gravity'. In: *Notes on the principles of pure and applied calculation; and applications of mathematical principles to theories of the physical forces.* Cambridge University Press / Deighton, Bell, and Co., pp. 486–505.

Chamberlin, S. J. & Siemens, X. (2012). 'Stochastic backgrounds in alternative theories of gravity: Overlap reduction functions for pulsar timing arrays'. *Phys. Rev. D* 85.8, 082001. arXiv: `1111.5661 [astro-ph.HE]`.

Chandrasekhar, S. (1970). 'Solutions of Two Problems in the Theory of Gravitational Radiation'. *Phys. Rev. Lett.* 24, 611–615.

Chang, J. T. & Pollard, D. (1997). 'Conditioning as disintegration'. *Stat. Neerl.* 51.3, 287–317.

Chen, Y. & Kawamura, S. (2006). 'Displacement- and Timing-Noise-Free Gravitational-Wave Detection'. *Phys. Rev. Lett.* 96.23, 231102. arXiv: `gr-qc/0504108`.

Chen, Y., Pai, A., Somiya, K., Kawamura, S., Sato, S. et al. (2006). 'Interferometers for Displacement-Noise-Free Gravitational-Wave Detection'. *Phys. Rev. Lett.* 97.15, 151103. arXiv: `gr-qc/0603054`.

Christensen, N. (2010), for the LVC. 'LIGO S6 detector characterization studies'. *Class. Quant. Grav.* 27.19, 194010.

Chung, C. T., Melatos, A., Krishnan, B. & Whelan, J. T. (2011). 'Designing a cross-correlation search for continuous-wave gravitational radiation from a neutron star in the supernova remnant SNR 1987A'. *Mon. Not. R. Astron. Soc.* 414, 2650–2663. arXiv: `1102.4654 [gr-qc]`.

Clark, J., Heng, I. S., Pitkin, M. & Woan, G. (2007). 'Evidence-based search method for gravitational waves from neutron star ring-downs'. *Phys. Rev. D* 76.4, 043003. arXiv: `gr-qc/0703138`.

Collins, H. (2004). 'Gravity's shadow: The search for gravitational waves'. University of Chicago Press.

Cooley, J. W. & Tukey, J. W. (1965). 'An algorithm for the machine calculation of complex Fourier series'. *Math. Comp.* 19, 297–301.

Cordes, J. M., Freire, P. C., Lorimer, D. R., Camilo, F., Champion, D. J. et al. (2006). 'Arecibo Pulsar Survey Using ALFA. I. Survey Strategy and First Discoveries'. *Astrophys. J.* 637, 446–455. arXiv: `astro-ph/0509732`.

Coughlin, M. (2010), for the LVC. 'Noise Line Identification in LIGO S6 and Virgo VSR2'. *J. Phys. Conf. Ser.* 243.1, 012010. arXiv: `1109.0330 [gr-qc]`.

Cox, R. T. (1946). 'Probability, Frequency and Reasonable Expectation'. *Am. J. Phys* 14, 1–13.

– (1961). 'Algebra of Probable Inference'. Johns Hopkins University Press.

Culbertson, J. & Sturtz, K. (2014). 'A Categorical Foundation for Bayesian Probability'. *Appl. Categ. Struct.* 22.4, 647–662. arXiv: `1205.1488 [math.CT]`.

Cutler, C., Gholami, I. & Krishnan, B. (2005). 'Improved stack-slide searches for gravitational-wave pulsars'. *Phys. Rev. D* 72.4, 042004. arXiv: `gr-qc/0505082`.

Cutler, C. & Jones, D. I. (2001). 'Gravitational wave damping of neutron star wobble'. *Phys. Rev. D* 63.2, 024002. arXiv: `gr-qc/0008021`.

Cutler, C. & Schutz, B. F. (2005). 'The generalized F-statistic: multiple detectors and multiple gravitational wave pulsars'. *Phys. Rev. D* 72, 063006. arXiv: `gr-qc/0504011`.

Dal Canton, T., Bhagwat, S., Dhurandhar, S. V. & Lundgren, A. (2014). 'Effect of sine-Gaussian glitches on searches for binary coalescence'. *Class. Quant. Grav.* 31, 015016. arXiv: `1304.0008 [gr-qc]`.

Damour, T. & Vilenkin, A. (2001). 'Gravitational wave bursts from cusps and kinks on cosmic strings'. *Phys. Rev. D* 64.6, 064008. arXiv: `gr-qc/0104026`.

Damour, T. (1983). 'Gravitational radiation and the motion of compact bodies'. In: *Gravitational Radiation. Les Houches 1982*. Ed. by N. Deruelle & T. Piran. North-Holland Publishing, pp. 59–144.

Danzmann, K. et al. (2003), LISA Science Team. 'LISA - An ESA cornerstone mission for the detection and observation of gravitational waves'. *Adv. Space Res.* 32.7. Fundamental Physics in Space, 1233–1242.

Danzmann, K., Prince, T. A., Binétruy, P., Bender, P., Buchman, S. et al. (2011). *LISA Assessment Study Report. Unveiling a hidden Universe*. Tech. rep. ESA/SRE(2011)3.
`http://sci.esa.int/lisa/48364-lisa-assessment-study-report-yellow-book/`.

de Luca, A. (2008). 'Central Compact Objects in Supernova Remnants'. In: *40 Years of Pulsars: Millisecond Pulsars, Magnetars and More*. Ed. by C. Bassa, Z. Wang, A. Cumming & V. M. Kaspi. AIP Conf. Ser. Vol. 983, pp. 311–319. arXiv: `0712.2209 [astro-ph]`.

de Waard, A., Gottardi, L., van Houwelingen, J., Shumack, A. & Frossati, G. (2003). 'MiniGRAIL, the first spherical detector'. *Class. Quant. Grav.* 20, 143.

DeGroot, M. H. (1970). 'Optimal Statistical Decisions'. John Wiley & Sons.

Demorest, P. B., Pennucci, T., Ransom, S. M., Roberts, M. S. & Hessels, J. W. (2010). 'A two-solar-mass neutron star measured using Shapiro delay'. *Nature* 467, 1081–1083. arXiv: `1010.5788 [astro-ph.HE]`.

Dergachev, V. (2006). *Description of PowerFlux algorithms and implementation*. Tech. rep. LIGO-T050186.
`https://dcc.ligo.org/LIGO-T050186/public`.

– (2009). 'An all-sky search for continuous gravitational waves'. PhD thesis. University of Michigan.

– (2011). *Description of PowerFlux 2 algorithms and implementation*. Tech. rep. LIGO-T1000272.
`https://dcc.ligo.org/LIGO-T1000272/public`.

Dewdney, P. E., Turner, W., Millenaar, R., McCool, R., Lazio, J. et al. (2013). *Square Kilometer Array System Baseline Design*. Tech. rep. SKA-TEL-SKO-DD-001.

Dhurandhar, S. V. & Vecchio, A. (2001). 'Searching for continuous gravitational wave sources in binary systems'. *Phys. Rev. D* 63.12, 122001. arXiv: `gr-qc/0011085`.

Dhurandhar, S., Krishnan, B., Mukhopadhyay, H. & Whelan, J. T. (2008). 'Cross-correlation search for periodic gravitational waves'. *Phys. Rev. D* 77.8, 082001. arXiv: `0712.1578 [gr-qc]`.

Drever, R. W. P. (1983). 'Interferometric detectors of gravitational radiation'. In: *Gravitational Radiation. Les Houches 1982*. Ed. by N. Deruelle & T. Piran. North-Holland Publishing, pp. 321–338.

Drinkwater, M. R., Floberghagen, R., Haagmans, R., Muzi, D. & Popescu, A. (2003). 'GOCE: ESA's First Earth Explorer Core Mission'. *Space Sci. Rev.* 108, 419–432.

Duncan, R. C. & Thompson, C. (1992). 'Formation of very strongly magnetized neutron stars - Implications for gamma-ray bursts'. *Astrophys. J. Lett.* 392, L9–L13.

Eardley, D. M., Lee, D. L. & Lightman, A. P. (1973). 'Gravitational-Wave Observations as a Tool for Testing Relativistic Gravity'. *Phys. Rev. D* 8, 3308–3321.

Eddington, A. S. (1924). 'The Mathematical Theory of Relativity'. Cambridge University Press.

Einstein, A. (1905). 'Zur Elektrodynamik bewegter Körper'. *Ann. Phys.* 322, 891–921.

– (1915). 'Zur allgemeinen Relativitätstheorie'. *Sitz. König. Preuß. Akad. Wiss. Berl.* 778–786.

– (1916). 'Näherungsweise Integration der Feldgleichungen der Gravitation'. *Sitz. König. Preuß. Akad. Wiss. Berl.* 688–696.

– (1918). 'Über Gravitationswellen'. *Sitz. König. Preuß. Akad. Wiss. Berl.* 154–167.

Estabrook, F. B. & Wahlquist, H. D. (1975). 'Response of Doppler spacecraft tracking to gravitational radiation'. *Gen. Rel. Grav.* 6, 439–447.

Farmer, A. J. & Phinney, E. S. (2003). 'The gravitational wave background from cosmological compact binaries'. *Mon. Not. R. Astron. Soc.* 346, 1197–1214. arXiv: `astro-ph/0304393`.

Ferdman, R. D., van Haasteren, R., Bassa, C. G., Burgay, M., Cognard, I. et al. (2010). 'The European Pulsar Timing Array: current efforts and a LEAP toward the future'. *Class. Quant. Grav.* 27.8, 084014. arXiv: `1003.3405 [astro-ph.HE]`.

Ferrari, V., Matarrese, S. & Schneider, R. (1999). 'Gravitational wave background from a cosmological population of core-collapse supernovae'. *Mon. Not. R. Astron. Soc.* 303, 247–257. arXiv: `astro-ph/9804259`.

Flanagan, E. E. (1993). 'Sensitivity of the Laser Interferometer Gravitational Wave Observatory to a stochastic background, and its dependence on the detector orientations'. *Phys. Rev. D* 48, 2389–2407. arXiv: `astro-ph/9305029`.

Folta, D. (2004). 'Formation Flying Design and Applications in Weak Stability Boundary Regions'. *Ann. N. Y. Acad. Sci.* 1017, 95–111.

Foster, R. S. & Backer, D. C. (1990). 'Constructing a pulsar timing array'. *Astrophys. J.* 361, 300–308.

Fregeau, J. M., Larson, S. L., Miller, M. C., O'Shaughnessy, R. & Rasio, F. A. (2006). 'Observing IMBH-IMBH Binary Coalescences via Gravitational Radiation'. *Astrophys. J. Lett.* 646, L135–L138. arXiv: `astro-ph/0605732`.

Friedman, J. L. & Lockitch, K. H. (1999). 'Gravitational-Wave Driven Instability of Rotating Relativistic Stars'. *Progr. Theor. Phys. Suppl.* 136, 121–134. arXiv: `gr-qc/9908083`.

Friedman, J. L. & Schutz, B. F. (1978). 'Secular instability of rotating Newtonian stars'. *Astrophys. J.* 222, 281–296.

Fryer, C. L. & New, K. C. (2011). 'Gravitational Waves from Gravitational Collapse'. *Living Rev. Relativity* 14.1. http://www.livingreviews.org/lrr-2011-1.

Gair, J. R., Vallisneri, M., Larson, S. L. & Baker, J. G. (2013). 'Testing General Relativity with Low-Frequency, Space-Based Gravitational-Wave Detectors'. *Living Rev. Relativity* 16.7. arXiv: `1212.5575 [gr-qc]`. http://www.livingreviews.org/lrr-2013-7.

Giacconi, R., Gursky, H., Paolini, F. R. & Rossi, B. B. (1962). 'Evidence for x Rays From Sources Outside the Solar System'. *Phys. Rev. Lett.* 9, 439–443.

Glampedakis, K., Andersson, N. & Samuelsson, L. (2011). 'Magnetohydrodynamics of superfluid and superconducting neutron star cores'. *Mon. Not. R. Astron. Soc.* 410, 805–829. arXiv: `1001.4046 [astro-ph.SR]`.

Goetz, E. & Riles, K. (2011). 'An all-sky search algorithm for continuous gravitational waves from spinning neutron stars in binary systems'. *Class. Quant. Grav.* 28.21, 215006. arXiv: `1103.1301 [gr-qc]`.

Gold, T. (1968). 'Rotating Neutron Stars as the Origin of the Pulsating Radio Sources'. *Nature* 218, 731–732.

Gomez, G., Jorba, A., Masdemont, J. & Simo, C. (1993). 'Study of the transfer from the Earth to a halo orbit around the equilibrium point L1'. *Celest. Mech. Dyn. Astron.* 56, 541–562.

Gottardi, L., de Waard, A., Usenko, O., Frossati, G., Podt, M. et al. (2007). 'Sensitivity of the spherical gravitational wave detector MiniGRAIL operating at 5K'. *Phys. Rev. D* 76.10, 102005. arXiv: `0705.0122 [gr-qc]`.

Graham-Smith, F. (2003). 'The radio emission from pulsars'. *Rept. Prog. Phys.* 66, 173–238.

Grote, H. (2010), for the LSC. 'The GEO 600 status'. *Class. Quant. Grav.* 27.8, 084003.

Grote, H., Danzmann, K., Dooley, K. L., Schnabel, R., Slutsky, J. et al. (2013). 'First Long-Term Application of Squeezed States of Light in a Gravitational-Wave Observatory'. *Physical Review Letters* 110.18, 181101. arXiv: `1302.2188 [physics.ins-det]`.

Haensel, P., Potekhin, A. & Yakovlev, D. (2006). 'Neutron Stars 1: Equation of State and Structure'. Springer New York.

Haensel, P. & Proszynski, M. (1982). 'Pion condensation in cold dense matter and neutron stars'. *Astrophys. J.* 258, 306–320.

Harris, F. J. (1978). 'On the Use of Windows for Harmonic Analysis with the Discrete Fourier Transform'. *Proc. IEEE* 66, 51–83.

Harry, G. M. (2010), for the LSC. 'Advanced LIGO: the next generation of gravitational wave detectors'. *Class. Quant. Grav.* 27.8, 084006.

Harry, G. M., Fritschel, P., Shaddock, D. A., Folkner, W. & Phinney, E. S. (2006). 'Laser interferometry for the Big Bang Observer'. *Class. Quant. Grav.* 23, 4887–4894.

Harry, I. W. & Fairhurst, S. (2011). 'Targeted coherent search for gravitational waves from compact binary coalescences'. *Phys. Rev. D* 83.8, 084002. arXiv: `1012.4939 [gr-qc]`.

Hewish, A., Bell, S. J., Pilkington, J. D., Scott, P. F. & Collins, R. A. (1968). 'Observation of a Rapidly Pulsating Radio Source'. *Nature* 217, 709–713.

Hjorth, J. & Bloom, J. S. (2012). 'The Gamma-Ray Burst - Supernova Connection'. In: *Gamma-Ray Bursts.* Ed. by C. Kouveliotou, R. A. J. Wijers & S. Woosley. Cambridge University Press. Chap. 9, pp. 169–190. arXiv: `1104.2274 [astro-ph.HE]`.

Ho, W. C. (2011). 'Evolution of a buried magnetic field in the central compact object neutron stars'. *Mon. Not. R. Astron. Soc.* 414, 2567–2575. arXiv: `1102.4870 [astro-ph.HE]`.

Ho, W. C., Andersson, N. & Haskell, B. (2011). 'Revealing the Physics of r Modes in Low-Mass X-Ray Binaries'. *Phys. Rev. Lett.* 107.10, 101101. arXiv: `1107.5064 [astro-ph.HE]`.

Hobbs, G. et al. (2010). 'The International Pulsar Timing Array project: using pulsars as a gravitational wave detector'. *Class. Quant. Grav.* 27.8, 084013. arXiv: `0911.5206 [astro-ph.SR]`.

Hogan, C. J. & Bender, P. L. (2001). 'Estimating stochastic gravitational wave backgrounds with the Sagnac calibration'. *Phys. Rev. D* 64.6, 062002. arXiv: `astro-ph/0104266`.

Hohmann, M. (2012). 'Propagation of gravitational waves in multimetric gravity'. *Phys. Rev. D* 85.8, 084024. arXiv: `1105.2555 [gr-qc]`.

Hooke, R. (1705). 'Of Comets and Gravity'. In: *The Posthumous Works of Dr. Robert Hooke.* Ed. by R. Waller. Sam. Smith and Benj. Walford, pp. 166–185.

Howell, K. C. & Barden, B. T. (1999). 'Trajectory design and stationkeeping for multiple spacecraft in formation near the Sun-Earth L1 point'. In: *IAF 50th International Astronautical Congress.* International Astronautical Federation, pp. 4–8.

Hulse, R. A. & Taylor, J. H. (1975). 'Discovery of a pulsar in a binary system'. *Astrophys. J. Lett.* 195, L51–L53.

Hurley, K., Boggs, S. E., Smith, D. M., Duncan, R. C., Lin, R. et al. (2005). 'An exceptionally bright flare from SGR 1806-20 and the origins of short-duration γ-ray bursts'. *Nature* 434, 1098–1103. arXiv: `astro-ph/0502329`.

Infeld, L., ed. (1964). 'Proceedings on theory of gravitation: conference in Warszawa and Jablonna, 25-31 July, 1962'. Gauthier-Villars, Paris and PWN, Warszawa.

Infeld, L. & Scheidegger, A. (1951). 'Radiation and gravitational equations of motion'. *Canad. J. Math* 3, 195–207.

Isaacson, R. A. (1968a). 'Gravitational Radiation in the Limit of High Frequency. I. The Linear Approximation and Geometrical Optics'. *Phys. Rev.* 166, 1263–1271.

– (1968b). 'Gravitational Radiation in the Limit of High Frequency. II. Nonlinear Terms and the Effective Stress Tensor'. *Phys. Rev.* 166, 1272–1279.

Itoh, Y., Papa, M. A., Krishnan, B. & Siemens, X. (2004). 'Chi-square test on candidate events from CW signal coherent searches'. *Class. Quant. Grav.* 21, 1667. arXiv: `gr-qc/0408092`.

Jaffe, A. H. & Backer, D. C. (2003). 'Gravitational Waves Probe the Coalescence Rate of Massive Black Hole Binaries'. *Astrophys. J.* 583, 616–631. arXiv: `astro-ph/0210148`.

Janka, H.-T., Langanke, K., Marek, A., Martínez-Pinedo, G. & Müller, B. (2007). 'Theory of core-collapse supernovae'. *Phys. Rep.* 442, 38–74. arXiv: `astro-ph/0612072`.

Jaranowski, P. & Królak, A. (2009). 'Analysis of Gravitational-Wave Data'. Cambridge Monographs on Particle Physics, Nuclear Physics and Cosmology 29. Cambridge University Press.

– (2012). 'Gravitational-Wave Data Analysis. Formalism and Sample Applications: The Gaussian Case'. *Living Rev. Relativity* 15.4. `http://www.livingreviews.org/lrr-2012-4`.

Jaranowski, P., Królak, A. & Schutz, B. F. (1998). 'Data analysis of gravitational-wave signals from spinning neutron stars: The signal and its detection'. *Phys. Rev. D* 58, 063001. arXiv: `gr-qc/9804014`.

Jaynes, E. T. (1987). 'Bayesian Spectrum and Chirp Analysis'. In: *Maximum Entropy and Bayesian Spectral Analysis and Estimation Problems.* Ed. by C. R. Smith & G. J. Erickson. D. Reidel, Dordrecht, pp. 1–37.

– (2003). 'Probability Theory. The Logic of Science'. Cambridge University Press.

Jeffreys, H. (1946). 'An Invariant Form for the Prior Probability in Estimation Problems'. *Proc. R. Soc. A* 186.1007, 453–461.

Jenet, F. A., Hobbs, G. B., Lee, K. J. & Manchester, R. N. (2005). 'Detecting the Stochastic Gravitational Wave Background Using Pulsar Timing'. *Astrophys. J. Lett.* 625, L123–L126. arXiv: `astro-ph/0504458`.

Jenet, F., Finn, L. S., Lazio, J., Lommen, A., McLaughlin, M. et al. (2009). 'The North American Nanohertz Observatory for Gravitational Waves'. *Astro2010 Program Prioritization Panel on Particle Astrophysics and Gravitation.* arXiv: `0909.1058 [astro-ph.IM]`.

Jennrich, O., Binétruy, P., Colpi, M., Danzmann, K., Jetzer, P. et al. (2012). *NGO Assessment Study Report. Revealing a hidden Universe: opening a new chapter of discovery.* Tech. rep. ESA/SRE(2011)19. `http://sci.esa.int/ngo/49839-ngo-assessment-study-report-yellow-book/`.

Johnson-McDaniel, N. K. & Owen, B. J. (2013). 'Maximum elastic deformations of relativistic stars'. *Phys. Rev. D* 88.4, 044004. arXiv: `1208.5227 [astro-ph.SR]`.

Jones, D. I. & Andersson, N. (2002). 'Gravitational waves from freely precessing neutron stars'. *Mon. Not. R. Astron. Soc.* 331, 203–220. arXiv: `gr-qc/0106094`.

Kaplan, D. L. (2004). 'The Diversity of Neutron Stars: Nearby Thermally Emitting Neutron Stars and the Compact Central Objects in Supernova Remnants'. Universal Publishers.

Kawamura, S. et al. (2006). 'The Japanese space gravitational wave antenna DECIGO'. *Class. Quant. Grav.* 23, 125.

– (2011). 'The Japanese space gravitational wave antenna: DECIGO'. *Class. Quant. Grav.* 28.9, 094011.

Kawamura, S. & Chen, Y. (2004). 'Displacement-Noise-Free Gravitational-Wave Detection'. *Phys. Rev. Lett.* 93.21, 211103. arXiv: `gr-qc/0405093`.

Keitel, D. & Prix, R. (2015). 'Line-robust statistics for continuous gravitational waves: safety in the case of unequal detector sensitivities'. *Class. Quant. Grav.* 32.3, 035004. arXiv: `1409.2696 [gr-qc]`.

Keitel, D., Prix, R., Papa, M. A., Leaci, P. & Siddiqi, M. (2014). 'Search for continuous gravitational waves: Improving robustness versus instrumental artifacts'. *Phys. Rev. D* 89.6, 064023. arXiv: `1311.5738 [gr-qc]`.

Kerr, R. P. (1963). 'Gravitational Field of a Spinning Mass as an Example of Algebraically Special Metrics'. *Phys. Rev. Lett.* 11, 237–238.

Khalaidovski, A., Vahlbruch, H., Lastzka, N., Gräf, C., Lück, H. et al. (2012). 'Status of the GEO 600 squeezed-light laser'. *J. Phys. Conf. Ser.* 363.1, 012013. arXiv: `1112.0198 [quant-ph]`.

Khintchine, A. (1934). 'Korrelationstheorie der stationären stochastischen Prozesse'. *Math. Ann.* 109.1, 604–615.

Kiziltan, B., Kottas, A., De Yoreo, M. & Thorsett, S. E. (2013). 'The Neutron Star Mass Distribution'. *Astrophys. J.* 778, 66. arXiv: `1011.4291 [astro-ph.GA]`.

Knispel, B. & Allen, B. (2008). 'Blandford's argument: The strongest continuous gravitational wave signal'. *Phys. Rev. D* 78.4, 044031. arXiv: `0804.3075 [gr-qc]`.

Knispel, B., Allen, B., Cordes, J. M., Deneva, J. S., Anderson, D. et al. (2010). 'Pulsar Discovery by Global Volunteer Computing'. *Science* 329, 1305. arXiv: `1008.2172 [astro-ph.GA]`.

Knispel, B., Eatough, R. P., Kim, H., Keane, E. F., Allen, B. et al. (2013). 'Einstein@Home Discovery of 24 Pulsars in the Parkes Multi-beam Pulsar Survey'. *Astrophys. J.* 774, 93. arXiv: `1302.0467 [astro-ph.GA]`.

Knispel, B., Lazarus, P., Allen, B., Anderson, D., Aulbert, C. et al. (2011). 'Arecibo PALFA Survey and Einstein@Home: Binary Pulsar Discovery by Volunteer Computing'. *Astrophys. J. Lett.* 732, L1. arXiv: `1102.5340 [astro-ph.GA]`.

Kokkotas, K. D. & Schmidt, B. G. (1999). 'Quasi-Normal Modes of Stars and Black Holes'. *Living Rev. Relativity* 2.2. `http://www.livingreviews.org/lrr-1999-2`.

Kolmogorov, A. N. (1933). 'Grundbegriffe der Wahrscheinlichkeitsrechnung'. Springer-Verlag Berlin.

Koop, M. J. & Finn, L. S. (2014). 'Physical response of light-time gravitational wave detectors'. *Phys. Rev. D* 90.6, 062002. arXiv: `1310.2871 [gr-qc]`.

Kramer, M. (2014). 'Precision Tests of Theories of Gravity Using Pulsars'. *Int. J. Mod. Phys. D* 23, 1430004.

Kramer, M., Stairs, I. H., Manchester, R. N., McLaughlin, M. A., Lyne, A. G. et al. (2006). 'Tests of General Relativity from Timing the Double Pulsar'. *Science* 314, 97–102. arXiv: `astro-ph/0609417`.

Kramer, M., Xilouris, K. M., Jessner, A., Lorimer, D. R., Wielebinski, R. et al. (1997). 'Origin of pulsar radio emission. I. High frequency data.' *Astron. Astrophys.* 322, 846–856.

Krishnan, B. (2005), for the LSC. 'Wide parameter search for isolated pulsars using the Hough transform'. *Class. Quant. Grav.* 22, 1265. arXiv: `gr-qc/0506109`.

Krishnan, B., Sintes, A. M., Papa, M. A., Schutz, B. F., Frasca, S. et al. (2004). 'Hough transform search for continuous gravitational waves'. *Phys. Rev. D* 70.8, 082001. arXiv: `gr-qc/0407001`.

Kuroda, K. (1997). '300-m Laser Interferometer Gravitational Wave Detector (TAMA300) in Japan'. In: *Proceedings of the International Conference on Gravitational Waves: Sources and Detectors*. Ed. by I. Ciufolini & F. Fidecaro. World Scientific, pp. 100–107.

Landau, L. D. (1932). 'On the theory of stars'. *Phys. Z. Sowjetunion* 1, 285.

Lander, S. K. (2013). 'Magnetic Fields in Superconducting Neutron Stars'. *Physical Review Letters* 110.7, 071101. arXiv: `1211.3912 [astro-ph.SR]`.

Laplace, P. S. (1805). 'Sur les altérations que le mouvement des planètes et des comètes peut éprouver par la résistance des milieux qu'elles traversent, et par la transmission successive de la pesanteur'. In: *Traité de mécanique céleste*. Vol. IV, Book X. Duprat, Paris. Chap. VII, pp. 313–326.

Larson, M. B. & Link, B. (2002). 'Simulations of glitches in isolated pulsars'. *Mon. Not. R. Astron. Soc.* 333, 613–622. arXiv: `astro-ph/0105461`.

Larson, S. L., Hiscock, W. A. & Hellings, R. W. (2000). 'Sensitivity curves for spaceborne gravitational wave interferometers'. *Phys. Rev. D* 62.6, 062001. arXiv: `gr-qc/9909080`.

Laßwitz, K. (1897). 'Auf zwei Planeten'. Felber, Weimar.

Lattimer, J. M. (2012). 'The Nuclear Equation of State and Neutron Star Masses'. *Ann. Rev. Nucl. Part. Sci* 62, 485–515. arXiv: `1305.3510 [nucl-th]`.

Lattimer, J. M. & Prakash, M. (2001). 'Neutron Star Structure and the Equation of State'. *Astrophys. J.* 550, 426–442. arXiv: `astro-ph/0002232`.

– (2011). 'What a Two Solar Mass Neutron Star Really Means'. In: *From Nuclei to Stars – Festschrift in Honor of Gerald E Brown*. Ed. by S. Lee. World Scientific Publishing. arXiv: `1012.3208 [astro-ph.SR]`.

Lewin, W. H., van Paradijs, J. & Taam, R. E. (1993). 'X-Ray Bursts'. *Space Sci. Rev.* 62, 223–389.

Lifshits, M. (2012). 'Lectures on Gaussian Processes'. Springer Briefs in Mathematics.

Link, B. & Cutler, C. (2002). 'Vortex unpinning in precessing neutron stars'. *Mon. Not. R. Astron. Soc.* 336, 211–216. arXiv: `astro-ph/0108281`.

Littenberg, T. & Cornish, N. (2010). 'Separating gravitational wave signals from instrument artifacts'. *Phys. Rev. D* 82.10, 103007. arXiv: `1008.1577 [gr-qc]`.

Lomb, N. R. (1976). 'Least-squares frequency analysis of unequally spaced data'. *Ast'phys. Space Sci.* 39, 447–462.

Lombardo, U. & Schulze, H.-J. (2001). 'Superfluidity in Neutron Star Matter'. In: *Physics of Neutron Star Interiors.* Ed. by D. Blaschke, N. K. Glendenning & A. Sedrakian. Lecture Notes in Physics, Vol. 578. Springer-Verlag Berlin, p. 30. arXiv: `astro-ph/0012209`.

Loredo, T. (1989). 'From Laplace to Supernova SN 1987A: Bayesian Inference in Astrophysics'. In: *Maximum-Entropy and Bayesian Methods.* Ed. by P. Fougere. Kluwer Academic Publishers, pp. 81–142.

Lorimer, D. R. (2008). 'Binary and Millisecond Pulsars'. *Living Rev. Relativity* 11, 8. arXiv: `0811.0762`. http://www.livingreviews.org/lrr-2008-8.

Lorimer, D. R. & Kramer, M. (2004). 'Handbook of Pulsar Astronomy'. Cambridge University Press.

Lyne, A. G. & Lorimer, D. R. (1994). 'High birth velocities of radio pulsars'. *Nature* 369, 127–129.

Maggiore, M. (2000a). 'Gravitational wave experiments and early universe cosmology'. *Phys. Rep.* 331, 283–367. arXiv: `gr-qc/9909001`.

– (2000b). 'Stochastic backgrounds of gravitational waves'. ICTP 2000 lecture. arXiv: `gr-qc/0008027`.

– (2008). 'Gravitational Waves'. Oxford University Press.

Manca, G. M. et al. (2014). 'GCT code mismatch investigation'. Unpublished.

Manchester, R. N., Hobbs, G. B., Teoh, A. & Hobbs, M. (2005). 'The Australia Telescope National Facility Pulsar Catalogue'. *Astron. J.* 129, 1993–2006. arXiv: `astro-ph/0412641`. http://www.atnf.csiro.au/research/pulsar/psrcat.

Manchester, R. N., Hobbs, G., Bailes, M., Coles, W. A., van Straten, W. et al. (2013). 'The Parkes Pulsar Timing Array Project'. *Publ. Astron. Soc. Austral.* 30, e017. arXiv: `1210.6130 [astro-ph.IM]`.

Manchester, R. N., Lyne, A. G., Camilo, F., Bell, J. F., Kaspi, V. M. et al. (2001). 'The Parkes multi-beam pulsar survey - I. Observing and data analysis systems, discovery and timing of 100 pulsars'. *Mon. Not. R. Astron. Soc.* 328, 17–35. arXiv: `astro-ph/0106522`.

Mandel, I., Brown, D. A., Gair, J. R. & Miller, M. C. (2008). 'Rates and Characteristics of Intermediate Mass Ratio Inspirals Detectable by Advanced LIGO'. *Astrophys. J.* 681, 1431–1447. arXiv: `0705.0285`.

Marple, S. L. (1987). 'Digital Spectral Analysis With Applications'. Prentice Hall.

Mauceli, E., Geng, Z. K., Hamilton, W. O., Johnson, W. W., Merkowitz, S. et al. (1996). 'The Allegro gravitational wave detector: Data acquisition and analysis'. *Phys. Rev. D* 54, 1264–1275. arXiv: `gr-qc/9609058`.

Melatos, A. & Payne, D. J. (2005). 'Gravitational Radiation from an Accreting Millisecond Pulsar with a Magnetically Confined Mountain'. *Astrophys. J.* 623, 1044–1050. arXiv: `astro-ph/0503287`.

Mendell, G. (2002). *Short-Time Fourier Transform (SFT) Specification.* Tech. rep. LIGO-T020043. https://dcc.ligo.org/LIGO-T020043/public.

Mereghetti, S. (2008). 'The strongest cosmic magnets: soft gamma-ray repeaters and anomalous X-ray pulsars'. *Astron. Astrophys. Rev.* 15, 225–287. arXiv: `0804.0250`.

Messenger, C., Prix, R. & Papa, M. A. (2009). 'Random template banks and relaxed lattice coverings'. *Phys. Rev. D* 79.10, 104017. arXiv: `0809.5223 [gr-qc]`.

Michelson, A. A. & Morley, E. (1887). 'On the Relative Motion of the Earth and the Luminiferous Ether'. *Amer. J. Sci.* 34 (203), 333–345.

Miller, M. C. & Colbert, E. J. (2004). 'Intermediate-Mass Black Holes'. *Int. J. Mod. Phys. D* 13, 1–64. arXiv: `astro-ph/0308402`.

Mingarelli, C. M., Sidery, T., Mandel, I. & Vecchio, A. (2013). 'Characterizing gravitational wave stochastic background anisotropy with pulsar timing arrays'. *Phys. Rev. D* 88.6, 062005. arXiv: `1306.5394 [astro-ph.HE]`.

Misner, C. W., Thorne, K. S. & Wheeler, J. A. (1973). 'Gravitation'. W.H. Freeman and Co., San Francisco.

Newton, I. (1687). 'Philosophiae Naturalis Principia Mathematica'. Royal Society, London.

– (1692). 'Third letter to Dr. Bentley, February 25, 1692-3'. In: *Isaaci Newtoni Opera quae exstant Omnia.* Vol. iv. Ed. by S. Horsley. London, 1779-85, p. 438.

Newton, W. G., Gearheart, M. & Li, B.-A. (2013). 'A Survey of the Parameter Space of the Compressible Liquid Drop Model as Applied to the Neutron Star Inner Crust'. *Astrophys. J. Suppl. Ser.* 204, 9. arXiv: `1110.4043 [astro-ph.SR]`.

Neyman, J. & Pearson, E. (1933). 'On the Problem of the Most Efficient Tests of Statistical Hypotheses'. *Phil. Trans. R. Soc. London* 231, 289–337.

Orbanz, P. & Teh, Y. W. (2010). 'Bayesian Nonparametric Models'. In: *Encyclopedia of Machine Learning.* Ed. by C. Sammut & G. I. Webb. Springer US.

Otto, M., Heinzel, G. & Danzmann, K. (2012). 'TDI and clock noise removal for the split interferometry configuration of LISA'. *Class. Quant. Grav.* 29.20, 205003.

Owen, B. J. (1996). 'Search templates for gravitational waves from inspiraling binaries: Choice of template spacing'. *Phys. Rev. D* 53, 6749–6761. arXiv: `gr-qc/9511032`.

– (2000). 'Gravitational waves from the r-modes of rapidly rotating neutron stars'. In: *Gravitational Waves: Third Edoardo Amaldi Conference.* Ed. by S. Meshkov. AIP Conf. Ser. Vol. 523, pp. 55–64. arXiv: `gr-qc/9912065`.

Owen, B. J. & Lindblom, L. (2002). 'Gravitational radiation from the r-mode instability'. *Class. Quant. Grav.* 19, 1247–1253. arXiv: `gr-qc/0111024`.

Owen, B. J., Reitze, D. H. & Whitcomb, S. E. (2009). 'Probing neutron stars with gravitational waves'. In: *astro2010: The Astronomy and Astrophysics Decadal Survey*, p. 229. arXiv: `0903.2603 [astro-ph.SR]`.

Pacini, F. (1967). 'Energy Emission from a Neutron Star'. *Nature* 216, 567–568.

Papa, M. A., Schutz, B. F., Frasca, S. & Astone, P. (1998). 'Detection of Continuous Gravitational Wave Signals: Pattern Tracking with the Hough Transform'. In: *Second International LISA Symposium on the Detection and Observation of Gravitational Waves in Space.* Ed. by W. M. Folkner. AIP Conf. Ser. Vol. 456, pp. 128–134.

Pasquato, M. (2010). 'Croatian Black Hole School 2010 lecture notes on IMBHs in GCs'. arXiv: `1008.4477`.

Pavlov, G. G., Sanwal, D. & Teter, M. A. (2004). 'Central Compact Objects in Supernova Remnants'. In: *Young Neutron Stars and Their Environments.* Ed. by F. Camilo & B. M. Gaensler. IAU Symposium, Vol. 218. Astronomical Society of the Pacific, p. 239. arXiv: `astro-ph/0311526`.

Payne, D. J. & Melatos, A. (2006). 'Frequency Spectrum of Gravitational Radiation from Global Hydromagnetic Oscillations of a Magnetically Confined Mountain on an Accreting Neutron Star'. *Astrophys. J.* 641, 471–478. arXiv: `astro-ph/0510053`.

Pearson, K. (1900). 'On the criterion that a given system of deviations from the probable in the case of a correlated system of variables is such that it can be reasonably supposed to have arisen from random sampling'. *Philos. Mag. Ser. 5* 50.302, 157–175.

Pegoraro, F., Picasso, E. & Radicati, L. A. (1978). 'On the operation of a tunable electromagnetic detector for gravitational waves'. *J. Phys. A* 11, 1949–1962.

Pegoraro, F., Radicati, L. A., Bernard, P. & Picasso, E. (1978). 'Electromagnetic detector for gravitational waves'. *Phys. Lett. A* 68, 165–168.

Perna, R. & Belczynski, K. (2002). 'Short Gamma-Ray Bursts and Mergers of Compact Objects: Observational Constraints'. *Astrophys. J.* 570, 252–263. arXiv: `astro-ph/0201262`.

Pethick, C. J. & Potekhin, A. Y. (1998). 'Liquid crystals in the mantles of neutron stars'. *Phys. Lett. B* 427, 7–12. arXiv: `astro-ph/9803154`.

Phinney, S. et al. (2004). *The Big Bang Observer: Direct detection of gravitational waves from the birth of the Universe to the Present.* Tech. rep. NASA.

Pines, D. & Alpar, M. A. (1985). 'Superfluidity in neutron stars'. *Nature* 316, 27–32.

Pitkin, M., Reid, S., Rowan, S. & Hough, J. (2011). 'Gravitational Wave Detection by Interferometry (Ground and Space)'. *Living Rev. Relativity* 14, 5. arXiv: `1102.3355 [astro-ph.IM]`.
`http://www.livingreviews.org/lrr-2011-5`.

Pletsch, H. J. (2008). 'Parameter-space correlations of the optimal statistic for continuous gravitational-wave detection'. *Phys. Rev. D* 78.10, 102005. arXiv: `0807.1324 [gr-qc]`.

– (2010). 'Parameter-space metric of semicoherent searches for continuous gravitational waves'. *Phys. Rev. D* 82.4, 042002. arXiv: `1005.0395 [gr-qc]`.

– (2011). 'Sliding coherence window technique for hierarchical detection of continuous gravitational waves'. *Phys. Rev. D* 83.12, 122003. arXiv: `1101.5396 [gr-qc]`.

Pletsch, H. J. & Allen, B. (2009). 'Exploiting Large-Scale Correlations to Detect Continuous Gravitational Waves'. *Phys. Rev. Lett.* 103.18, 181102. arXiv: `0906.0023 [gr-qc]`.

Pletsch, H. J., Guillemot, L., Allen, B., Anderson, D., Aulbert, C. et al. (2013). 'Einstein@Home Discovery of Four Young Gamma-Ray Pulsars in Fermi LAT Data'. *Astrophys. J. Lett.* 779, L11. arXiv: `1311.6427 [astro-ph.HE]`.

Pletsch, H. J., Guillemot, L., Allen, B., Kramer, M., Aulbert, C. et al. (2012a). 'Discovery of Nine Gamma-Ray Pulsars in Fermi Large Area Telescope Data Using a New Blind Search Method'. *Astrophys. J.* 744, 105. arXiv: `1111.0523 [astro-ph.HE]`.

Pletsch, H. J., Guillemot, L., Allen, B., Kramer, M., Aulbert, C. et al. (2012b). 'PSR J1838-0537: Discovery of a Young, Energetic Gamma-Ray Pulsar'. *Astrophys. J. Lett.* 755, L20. arXiv: `1207.5333 [astro-ph.HE]`.

Pletsch, H. J., Guillemot, L., Fehrmann, H., Allen, B., Kramer, M. et al. (2012c). 'Binary Millisecond Pulsar Discovery via Gamma-Ray Pulsations'. *Science* 338, 1314–1317. arXiv: `1211.1385 [astro-ph.HE]`.

Podsiadlowski, P., Langer, N., Poelarends, A. J., Rappaport, S., Heger, A. et al. (2004). 'The Effects of Binary Evolution on the Dynamics of Core Collapse and Neutron Star Kicks'. *Astrophys. J.* 612, 1044–1051. arXiv: `astro-ph/0309588`.

Poincaré, H. (1905). 'Sur la dynamique de l'électron'. *C. R. Acad. Sci.* 140, 1504–1508.

Press, W. H., Teukolsky, S. A., Vetterling, W. T. & Flannery, B. P. (2007). 'Numerical recipes 3rd edition: The art of scientific computing'. Cambridge University Press.

Prix, R. (2007a). 'Template-based searches for gravitational waves: efficient lattice covering of flat parameter spaces'. *Class. Quant. Grav.* 24, 481. arXiv: 0707.0428 [gr-qc].

Prix, R. & Itoh, Y. (2005). 'Global parameter-space correlations of coherent searches for continuous gravitational waves'. *Class. Quant. Grav.* 22, 1003. arXiv: gr-qc/0504006.

Prix, R. (2007b). 'Search for continuous gravitational waves: Metric of the multidetector F-statistic'. *Phys. Rev. D* 75.2, 023004. arXiv: gr-qc/0606088.

– (2009), for the LSC. 'Gravitational Waves from Spinning Neutron Stars'. In: *Neutron Stars and Pulsars*. Ed. by W. Becker. Springer Berlin Heidelberg. Chap. 24, pp. 651–686.
https://dcc.ligo.org/LIGO-P060039/public.

– (2011a). *F-statistic bias due to noise-estimator*. Tech. rep. LIGO-T1100551.
https://dcc.ligo.org/LIGO-T1100551/public.

– (2011b). *The F-statistic and its implementation in ComputeFStatistic_v2*. Tech. rep. LIGO-T0900149-v4.
https://dcc.ligo.org/LIGO-T0900149/public.

Prix, R., Giampanis, S. & Messenger, C. (2011). 'Search method for long-duration gravitational-wave transients from neutron stars'. *Phys. Rev. D* 84, 023007. arXiv: 1104.1704 [gr-qc].

Prix, R. & Krishnan, B. (2009). 'Targeted search for continuous gravitational waves: Bayesian versus maximum-likelihood statistics'. *Class. Quant. Grav.* 26, 204013. arXiv: 0907.2569 [gr-qc].

Prix, R. & Shaltev, M. (2012). 'Search for Continuous Gravitational Waves: Optimal StackSlide method at fixed computing cost'. *Phys. Rev. D* 85, 084010. arXiv: 1201.4321 [gr-qc].

Punturo, M. et al. (2010a). 'The Einstein Telescope: a third-generation gravitational wave observatory'. *Class. Quant. Grav.* 27.19, 194002.

– (2010b). 'The third generation of gravitational wave observatories and their science reach'. *Class. Quant. Grav.* 27.8, 084007.

Punturo, M. & Lück, H. (2011). 'Toward a third generation of gravitational wave observatories'. *Gen. Rel. Grav.* 43, 363–385.

Punturo, M., Lück, H. & Beker, M. (2014). 'A Third Generation Gravitational Wave Observatory: The Einstein Telescope'. In: *Advanced Interferometers and the Search for Gravitational Waves*. Ed. by M. Bassan. Springer International Publishing, pp. 333–362.

Punturo, M. & Somiya, K. (2013). 'Underground Gravitational Wave Observatories: KAGRA and ET'. *Int. J. Mod. Phys. D* 22, 1330010.

Rajagopal, M. & Romani, R. W. (1995). 'Ultra–Low-Frequency Gravitational Radiation from Massive Black Hole Binaries'. *Astrophys. J.* 446, 543. arXiv: astro-ph/9412038.

Rakhmanov, M. (2005). *Response of LIGO to Gravitational Waves at High Frequencies and in the Vicinity of the FSR (37.5 kHz)*. Tech. rep. LIGO-T060237-00-D. https://dcc.ligo.org/T060237-x0/public.

Robinson, E. A. (1982). 'A Historical Perspective of Spectrum Estimation'. *Proc. IEEE* 70, 885–907.

Rosado, P. A. (2011). 'Gravitational wave background from binary systems'. *Phys. Rev. D* 84.8, 084004. arXiv: 1106.5795 [gr-qc].

– (2012). 'Gravitational wave background from rotating neutron stars'. *Phys. Rev. D* 86.10, 104007. arXiv: 1206.1330 [gr-qc].

Rosado, P. A. & Sesana, A. (2014). 'Targeting supermassive black hole binaries and gravitational wave sources for the pulsar timing array'. *Mon. Not. R. Astron. Soc.* 439, 3986–4010. arXiv: 1311.0883 [astro-ph.CO].

Ruderman, M. (1969). 'Neutron Starquakes and Pulsar Periods'. *Nature* 223, 597–598.

– (1976). 'Crust-breaking by neutron superfluids and the VELA pulsar glitches'. *Astrophys. J.* 203, 213–222.

Ruderman, M., Zhu, T. & Chen, K. (1998). 'Neutron Star Magnetic Field Evolution, Crust Movement, and Glitches'. *Astrophys. J.* 492, 267–280. arXiv: astro-ph/9709008.

Ryle, M. & Smith, F. G. (1948). 'A New Intense Source of Radio-Frequency Radiation in the Constellation of Cassiopeia'. *Nature* 162, 462–463.

Sancho de la Jordana, L. & Sintes, A. M. (2008). 'A χ^2 veto for continuous gravitational wave searches'. *Class. Quant. Grav.* 25.18, 184014. arXiv: 0804.1007 [gr-qc].

Sathyaprakash, B. et al. (2011). 'Scientific Potential of Einstein Telescope'. In: *Proceedings of the XLVIth Rencontres de Moriond: Gravitational Waves and Experimental Gravity*. Ed. by E. Augé, J. Dumarchez & J. T. T. Vân. Thê Gioi Publishers, pp. 127–136. arXiv: 1108.1423 [gr-qc].

– (2012). 'Scientific objectives of Einstein Telescope'. *Class. Quant. Grav.* 29.12, 124013. arXiv: 1206.0331.

Sathyaprakash, B. S. & Schutz, B. F. (2009). 'Physics, Astrophysics and Cosmology with Gravitational Waves'. *Living Rev. Relativity* 12.2. arXiv: 0903.0338 [gr-qc]. http://www.livingreviews.org/lrr-2009-2.

Saulson, P. R. (1994). 'Fundamentals of Interferometric Gravitational Wave Detectors'. World Scientific Publishing.

Scargle, J. D. (1981). 'Studies in astronomical time series analysis. I - Modeling random processes in the time domain'. *Astrophys. J. Suppl. Ser.* 45, 1–71.

– (1982). 'Studies in astronomical time series analysis. II - Statistical aspects of spectral analysis of unevenly spaced data'. *Astrophys. J.* 263, 835–853.

– (1989). 'Studies in astronomical time series analysis. III - Fourier transforms, autocorrelation functions, and cross-correlation functions of unevenly spaced data'. *Astrophys. J.* 343, 874–887.

– (1990). 'Studies in astronomical time series analysis. IV - Modeling chaotic and random processes with linear filters'. *Astrophys. J.* 359, 469–482.

– (1998). 'Studies in Astronomical Time Series Analysis. V. Bayesian Blocks, a New Method to Analyze Structure in Photon Counting Data'. *Astrophys. J.* 504, 405–418. arXiv: `astro-ph/9711233`.

Schaffner, J. & Mishustin, I. N. (1996). 'Hyperon-rich matter in neutron stars'. *Phys. Rev. C* 53, 1416–1429. arXiv: `nucl-th/9506011`.

Schnabel, R., Mavalvala, N., McClelland, D. E. & Lam, P. K. (2010). 'Quantum metrology for gravitational wave astronomy'. *Nature Commun.* 1, 121.

Schuster, A. (1898). 'On the investigation of hidden periodicities with application to a supposed 26 day period of meteorological phenomena'. *Terrestrial Magnetism* 3.1, 13–41.

Schutz, B. F. (1998). 'Sources of radiation from neutron stars'. In: *Proceedings of the Second Workshop on Gravitational Wave Data Analysis*. Ed. by M. Davier & P. Hello. Editions Frontières. arXiv: `gr-qc/9802020`.

Schutz, B. F. & Papa, M. A. (1999). 'End-to-end algorithm for hierarchical area searches for long-duration GW sources for GEO 600'. In: *Proceedings of Moriond meeting Gravitational Waves and Experimental Gravity*. Ed. by J. Dumarchez. Editions Frontières. arXiv: `gr-qc/9905018`.

Schwarzschild, K. (1916). 'Über das Gravitationsfeld eines Massenpunktes nach der Einsteinschen Theorie'. *Sitz. König. Preuß. Akad. Wiss. Berl.* 189–196.

Searle, A. C. (2008). 'Monte-Carlo and Bayesian techniques in gravitational wave burst data analysis'. arXiv: `0804.1161 [gr-qc]`.

Sechi, G., Buonocore, M., Cometto, F., Saponara, M., Tramutola, A. et al. (2011). 'In-Flight Results from the Drag-Free and Attitude Control of GOCE Satellite'. In: *Preprints of the 18th IFAC World Congress, Milano*. Ed. by S. Bittanti, A. Cenedese & S. Zampieri, pp. 733–740.

Sesana, A. (2013). 'Systematic investigation of the expected gravitational wave signal from supermassive black hole binaries in the pulsar timing band'. *Mon. Not. R. Astron. Soc.* 433, L1–L5. arXiv: `1211.5375 [astro-ph.CO]`.

Sesana, A., Vecchio, A. & Colacino, C. N. (2008). 'The stochastic gravitational-wave background from massive black hole binary systems: implications for observations with Pulsar Timing Arrays'. *Mon. Not. R. Astron. Soc.* 390, 192–209. arXiv: `0804.4476`.

Sesana, A., Vecchio, A. & Volonteri, M. (2009). 'Gravitational waves from resolvable massive black hole binary systems and observations with Pulsar Timing Arrays'. *Mon. Not. R. Astron. Soc.* 394, 2255–2265. arXiv: `0809.3412`.

Seto, N. (2006). 'Correlation analysis of stochastic gravitational wave background around 0.1 1 Hz'. *Phys. Rev. D* 73.6, 063001. arXiv: `gr-qc/0510067`.

Shaltev, M., Leaci, P., Papa, M. A. & Prix, R. (2014). 'Fully coherent follow-up of continuous gravitational-wave candidates: An application to Einstein@Home results'. *Phys. Rev. D* 89.12, 124030. arXiv: `1405.1922 [gr-qc]`.

Shaltev, M. & Prix, R. (2013). 'Fully coherent follow-up of continuous gravitational-wave candidates'. *Phys. Rev. D* 87.8, 084057. arXiv: `1303.2471 [gr-qc]`.

Shaltev, M. (2013). 'Optimization and follow-up of semicoherent searches for continuous gravitational waves'. PhD thesis. Fakultät für Mathematik und Physik, Gottfried Wilhelm Leibniz Universität Hannover. `http://opac.tib.uni-hannover.de/DB=1/XMLPRS=N/PPN?PPN=755483928`.

Shapiro, S. L. & Teukolsky, S. A. (1983). 'Black Holes, White Dwarfs and Neutron Stars: The Physics of Compact Objects'. John Wiley & Sons.

Shearer, A. & Golden, A. (2002). 'Why study pulsars optically?' In: *Proceedings of the 270. WE-Heraeus Seminar on Neutron Stars, Pulsars, and Supernova Remnants*. Ed. by W. Becker, H. Lesch & J. Trümper. MPE Report, Vol. 278, pp. 44–53. arXiv: `astro-ph/0208579`.

Shklovsky, I. S. (1967). 'On the Nature of the Source of X-Ray Emission of SCO XR-1'. *A'phys.J.Lett.* 148, L1.

Shoemaker, D. et al. (2010). *Advanced LIGO anticipated sensitivity curves*. Tech. rep. LIGO-T0900288-v3. `https://dcc.ligo.org/LIGO-T0900288-v3/public`.

– (2011), LSC. *Advanced LIGO Reference Design*. Tech. rep. LIGO-M060056-v2. `https://dcc.ligo.org/M060056-v2/public`.

Sigg, D. (2006), LSC. 'Status of the LIGO detectors'. *Class. Quant. Grav.* 23, 51.

– (2008), LSC. 'Status of the LIGO detectors'. *Class. Quant. Grav.* 25.11, 114041.

Sintes, A. M. & Krishnan, B. (2006). 'Improved Hough search for gravitational wave pulsars'. *J. Phys. Conf. Ser.* 32, 206–211. arXiv: `gr-qc/0601081`.

Somiya, K. (2012). 'Detector configuration of KAGRA – the Japanese cryogenic gravitational-wave detector'. *Class. Quant. Grav.* 29.12, 124007. arXiv: `1111.7185 [gr-qc]`.

Somiya, K., Chen, Y., Goda, K. & Mikhailov, E. E. (2007a). 'Utility investigation of artificial time delay in displacement-noise-free interferometers'. *Phys. Rev. D* 76.2, 022002.

Somiya, K., Goda, K., Chen, Y. & Mikhailov, E. E. (2007b). 'Isolation of gravitational waves from displacement noise and utility of a time-delay device'. *J. Phys. Conf. Ser.* 66.1, 012053. arXiv: `gr-qc/0610117`.

Spruit, H. C. (2008). 'Origin of neutron star magnetic fields'. In: *40 Years of Pulsars: Millisecond Pulsars, Magnetars and More*. Ed. by C. Bassa, Z. Wang, A. Cumming & V. M. Kaspi. AIP Conf. Ser. Vol. 983, pp. 391–398. arXiv: `0711.3650 [astro-ph]`.

Stairs, I. H. (2006). 'Masses of radio pulsars'. *J. Phys. G* 32, 259.

Stergioulas, N. (2003). 'Rotating Stars in Relativity'. *Living Rev. Relativity* 6.3. `http://www.livingreviews.org/lrr-2003-3`.

Strohmaier, E., Simon, H., Dongarra, J. & Meuer, M. (2014). 'Top 500 supercomputer sites - June 2014 list'. `http://top500.org/list/2014/06/`.

Sutton, P. J., Jones, G., Chatterji, S., Kalmus, P., Leonor, I. et al. (2010). 'X-Pipeline: an analysis package for autonomous gravitational-wave burst searches'. *New J. Phys.* 12.5, 053034. arXiv: `0908.3665 [gr-qc]`.

Taylor, J. H. & Weisberg, J. M. (1982). 'A new test of general relativity - Gravitational radiation and the binary pulsar PSR 1913+16'. *Astrophys. J.* 253, 908–920.

– (1989). 'Further experimental tests of relativistic gravity using the binary pulsar PSR 1913 + 16'. *Astrophys. J.* 345, 434–450.

Taylor, W. B. (1877). 'Kinetic Theories of Gravitation'. In: *Annual report of the Board of Regents of the Smithsonian Institution*. Washington Government Printing Office, pp. 205–282.

Thain, D. et al. (2014). 'HTCondor - High Throughput Computing'. `http://research.cs.wisc.edu/htcondor/`.

Thain, D., Tannenbaum, T. & Livny, M. (2005). 'Distributed computing in practice: the Condor experience'. *Conc. Computat. Pract. Exper.* 17.2-4, 323–356.

Thompson, C. & Duncan, R. C. (1993). 'Neutron star dynamos and the origins of pulsar magnetism'. *Astrophys. J.* 408, 194–217.

Thomson, D. J. (1982). 'Spectrum Estimation and Harmonic Analysis'. *Proc. IEEE* 70, 1055–1096.

Thorne, K. S. (1980). 'Multipole expansions of gravitational radiation'. *Rev. Mod. Phys.* 52, 299–340.

– (1987). 'Gravitational radiation'. In: *Three hundred years of gravitation*. Ed. by S. Hawking & W. Israel. Cambridge University Press, pp. 330–458.

Tinto, M. & Dhurandhar, S. V. (2005). 'Time-Delay Interferometry'. *Living Rev. Relativity* 8.4. arXiv: `gr-qc/0409034`. `http://www.livingreviews.org/lrr-2005-4`.

Troja, E., Rosswog, S. & Gehrels, N. (2010). 'Precursors of Short Gamma-ray Bursts'. *Astrophys. J.* 723, 1711–1717. arXiv: `1009.1385 [astro-ph.HE]`.

Tsubono, K. (1995). '300-m Laser Interferometer Gravitational Wave Detector (TAMA300) in Japan'. In: *Gravitational Wave Experiments, Proceedings of the First Amaldi Conference*. Ed. by E. Coccia, G. Pizzella & F. Ronga. World Scientific, pp. 112–114.

Turner, M. S. (1997). 'Detectability of inflation-produced gravitational waves'. *Phys. Rev. D* 55, 435. arXiv: `astro-ph/9607066`.

Ushomirsky, G., Bildsten, L. & Cutler, C. (2000). 'Gravitational waves from low-mass X-ray binaries: A status report'. In: *Gravitational Waves: Third Edoardo Amaldi Conference*. Ed. by S. Meshkov. AIP Conf. Ser. Vol. 523, pp. 65–74. arXiv: `astro-ph/0001129`.

Ushomirsky, G., Cutler, C. & Bildsten, L. (2000). 'Deformations of accreting neutron star crusts and gravitational wave emission'. *Mon. Not. R. Astron. Soc.* 319, 902–932. arXiv: `astro-ph/0001136`.

Van Den Broeck, C. (2005). 'The gravitational wave spectrum of non-axisymmetric, freely precessing neutron stars'. *Class. Quant. Grav.* 22, 1825–1839. arXiv: `gr-qc/0411030`.

Veitch, J. & Vecchio, A. (2010). 'Bayesian coherent analysis of in-spiral gravitational wave signals with a detector network'. *Phys. Rev. D* 81.6, 062003. arXiv: `0911.3820 [astro-ph.CO]`.

Volonteri, M., Haardt, F. & Madau, P. (2003). 'The Assembly and Merging History of Supermassive Black Holes in Hierarchical Models of Galaxy Formation'. *Astrophys. J.* 582, 559–573. arXiv: `astro-ph/0207276`.

Wang, Y., Keitel, D., Babak, S., Petiteau, A., Otto, M. et al. (2013). 'Octahedron configuration for a displacement noise-cancelling gravitational wave detector in space'. *Phys. Rev. D* 88.10, 104021. arXiv: `1306.3865 [gr-qc]`.

Watts, A. L. & Krishnan, B. (2009). 'Detecting gravitational waves from accreting neutron stars'. *Adv. Space Res.* 43, 1049–1054. arXiv: `0901.1680 [astro-ph.SR]`.

Watts, A. L., Krishnan, B., Bildsten, L. & Schutz, B. F. (2008). 'Detecting gravitational wave emission from the known accreting neutron stars'. *Mon. Not. R. Astron. Soc.* 389, 839–868. arXiv: `0803.4097 [astro-ph]`.

Weber, F., Negreiros, R. & Rosenfield, P. (2009). 'Neutron Star Interiors and the Equation of State of Superdense Matter'. In: *Neutron Stars and Pulsars*. Ed. by W. Becker. Springer Berlin Heidelberg. Chap. 10, pp. 213–245.

Weber, F. (2005). 'Strange quark matter and compact stars'. *Prog. Part. Nucl. Phys.* 54, 193–288. arXiv: `astro-ph/0407155`.

Weber, J. (1960). 'Detection and Generation of Gravitational Waves'. *Phys. Rev.* 117, 306–313.

– (1966). 'Observation of the Thermal Fluctuations of a Gravitational-Wave Detector'. *Phys. Rev. Lett.* 17, 1228–1230.

– (1969). 'Evidence for Discovery of Gravitational Radiation'. *Phys. Rev. Lett.* 22, 1320–1324.

– (1970). 'Anisotropy and Polarization in the Gravitational-Radiation Experiments'. *Phys. Rev. Lett.* 25, 180–184.

– (1986). 'Gravitational antennas and the search for gravitational radiation'. In: *Gravitational radiation and relativity*. Ed. by J. Weber & T. M. Karade. Sir Arthur Eddington Centenary Symposium, Vol. 3, pp. 1–77.

Weinberg, S. (1972). 'Gravitation and Cosmology: Principles and Applications of the General Theory of Relativity'. Wiley-VCH.

Weiss, R. (1972). 'Electromagnetically coupled broadband gravitational antenna'. *Q. Prog. Rep., Res. Lab. Electron., MIT* 105, 54–76.

Wen, L. & Schutz, B. F. (2005). 'Coherent network detection of gravitational waves: the redundancy veto'. *Class. Quant. Grav.* 22, S1321. arXiv: `gr-qc/0508042`.

Wette, K. (2012). 'Estimating the sensitivity of wide-parameter-space searches for gravitational-wave pulsars'. *Phys. Rev. D* 85.4, 042003. arXiv: `1111.5650 [gr-qc]`.

Wette, K., Owen, B. J., Allen, B., Ashley, M., Betzwieser, J. et al. (2008). 'Searching for gravitational waves from Cassiopeia A with LIGO'. *Class. Quant. Grav.* 25.23, 235011. arXiv: `0802.3332 [gr-qc]`.

Wette, K. & Prix, R. (2013). 'Flat parameter-space metric for all-sky searches for gravitational-wave pulsars'. *Phys. Rev. D* 88.12, 123005. arXiv: `1310.5587 [gr-qc]`.

Wette, K. (2009). 'Gravitational waves from accreting neutron stars and Cassiopeia A'. PhD thesis. Department of Quantum Science, Research School of Physics and Engineering, Australian National University. `http://hdl.handle.net/1885/7354`.

Weyl, H. (1922). 'Space-time-matter'. Methuen, London.

Whelan, J. T., Prix, R., Cutler, C. J. & Willis, J. L. (2014). 'New coordinates for the amplitude parameter space of continuous gravitational waves'. *Class. Quant. Grav.* 31.6, 065002. arXiv: `1311.0065 [gr-qc]`.

Wiener, N. (1930). 'Generalized harmonic analysis'. *Acta Math.* 55.1, 117–258.

Will, C. M. (2014). 'The Confrontation between General Relativity and Experiment'. *Living Rev. Relativity* 17.4. arXiv: `1403.7377 [gr-qc]`. `http://www.livingreviews.org/lrr-2014-4`.

Williams, P. R. & Schutz, B. F. (2000). 'An efficient matched filtering algorithm for the detection of continuous gravitational wave signals'. In: *Gravitational Waves: Third Edoardo Amaldi Conference*. Ed. by S. Meshkov. AIP Conf. Ser. Vol. 523, pp. 473–476. arXiv: `gr-qc/9912029`.

Woosley, S. E. & Bloom, J. S. (2006). 'The Supernova Gamma-Ray Burst Connection'. *Ann. Rev. Astron. Astrophys.* 44, 507–556. arXiv: `astro-ph/0609142`.

Woosley, S. E. & Weaver, T. A. (1995). 'The Evolution and Explosion of Massive Stars. II. Explosive Hydrodynamics and Nucleosynthesis'. *Astrophys. J. Suppl. Ser.* 101, 181–235.

Woosley, S. & Janka, T. (2005). 'The physics of core-collapse supernovae'. *Nature Phys.* 1, 147–154. arXiv: `astro-ph/0601261`.

Wyithe, J. S. & Loeb, A. (2003). 'Low-Frequency Gravitational Waves from Massive Black Hole Binaries: Predictions for LISA and Pulsar Timing Arrays'. *Astrophys. J.* 590, 691–706. arXiv: `astro-ph/0211556`.

Yagi, K. (2012). 'Gravitational wave observations of galactic intermediate-mass black hole binaries with DECIGO path finder'. *Class. Quant. Grav.* 29.7, 075005. arXiv: `1202.3512 [astro-ph.CO]`.

– (2013). 'Scientific Potential of Decigo Pathfinder and Testing GR with Space-Borne Gravitational Wave Interferometers'. *Int. J. Mod. Phys. D* 22, 1341013. arXiv: `1302.2388 [gr-qc]`.

Yakovlev, D. G., Ho, W. C., Shternin, P. S., Heinke, C. O. & Potekhin, A. Y. (2011). 'Cooling rates of neutron stars and the young neutron star in the Cassiopeia A supernova remnant'. *Mon. Not. R. Astron. Soc.* 411, 1977–1988. arXiv: `1010.1154 [astro-ph.HE]`.

Yakovlev, D. G. & Pethick, C. J. (2004). 'Neutron Star Cooling'. *Ann. Rev. Astron. Astrophys.* 42, 169–210. arXiv: `astro-ph/0402143`.

Zimmermann, M. (1980). 'Gravitational waves from rotating and precessing rigid bodies. II - General solutions and computationally useful formulas'. *Phys. Rev. D* 21, 891–898.

Zimmermann, M. & Szedenits Jr., E. (1979). 'Gravitational waves from rotating and precessing rigid bodies - Simple models and applications to pulsars'. *Phys. Rev. D* 20, 351–355.

Appendix C: Curriculum Vitae

Personal information

Full name:	David Benjamin Keitel
Date of birth:	September 27th, 1985
Place of birth:	Siegburg, Germany

Education and scientific career

1992/07 – 1996/07	primary school, St. Augustin
1996/08 – 1998/06	Rhein-Sieg-Gymnasium, St. Augustin
1998/08 – 2004/06	Gymnasium CJD Königswinter
2004/06	Abitur
2004/10 – 2010/03	Diploma studies of physics and astronomy, Rheinische Friedrich-Wilhelms-Universität Bonn
2007/08 – 2010/03	member of Bonn-Cologne Graduate School (BCGS)
2007/08 – 2007/12	fall term at Stony Brook University (NY, USA), DAAD scholarship
2009-02 – 2010/03	Diploma thesis with Prof. P. Schneider, Argelander-Institut für Astronomie, Bonn: *Constrained probability distributions of correlation functions from Gaussian random fields*
2010/04 – 2010/09	scientific assistant ("Wissenschaftlicher Mitarbeiter"), Argelander-Institut für Astronomie, Bonn
2010/10 – 2014/11	PhD student (IMPRS stipend), Albert-Einstein-Institut, Leibniz Universität Hannover
since 2011/02	member of the LIGO Scientific Collaboration
since 2014/11	Postdoctoral researcher, Albert-Einstein-Institut

Appendix D: List of publications

Publications authored as part of the LIGO scientific collaboration are not listed.

Keitel, D. & Schneider, P. (2011). 'Constrained probability distributions of correlation functions'.
In: *Astron. Astrophys.* 534, A76. arXiv: `1105.3672 [astro-ph.CO]`.

Keitel, D. & Schneider, P. (2012). 'Constrained Probability Distributions of Correlation Functions'.
In: *Proceedings of Statistical Challenges in Modern Astronomy V.*
Ed. by E. D. Feigelson & G. J. Babu. Lecture Notes in Statistics, Vol. 209. Springer New York, pp. 515–517.

Keitel, D., Prix, R., Papa, M. A. & Siddiqi, M. (2012). 'An F-statistic based multi-detector veto for detector artifacts in continuous-wave gravitational wave data'.
In: *Proceedings of Statistical Challenges in Modern Astronomy V.*
Ed. by E. D. Feigelson & G. J. Babu. Lecture Notes in Statistics, Vol. 209. Springer New York, pp. 511–513. arXiv: `1201.5244 [gr-qc]`.

Wang, Y., Keitel, D., Babak, S., Petiteau, A., Otto, M. et al. (2013). 'Octahedron configuration for a displacement noise-cancelling gravitational wave detector in space'.
In: *Phys. Rev. D* 88.10, 104021. arXiv: `1306.3865 [gr-qc]`.

Keitel, D., Prix, R., Papa, M. A., Leaci, P. & Siddiqi, M. (2014). 'Search for continuous gravitational waves: Improving robustness versus instrumental artifacts'.
In: *Phys. Rev. D* 89.6, 064023. arXiv: `1311.5738 [gr-qc]`.

Keitel, D. & Prix, R. (2015). 'Line-robust statistics for continuous gravitational waves: safety in the case of unequal detector sensitivities'.
In: *Class. Quant. Grav.* 32.3, 035004. arXiv: `1409.2696 [gr-qc]`.